NORTHWESTERN UNIVERSITY

In-situ Atomic Scale Studies of Nanoparticle-Solution Interface Processes

A DISSERTATION

SUBMITTED TO THE GRADUATE SCHOOL
IN PARTIAL FULFILLMENT OF THE REQUIREMENTS

for the degree

DOCTOR OF PHILOSOPHY

Field of Materials Science and Engineering

By

Liane M. Moreau

EVANSTON, ILLINOIS

December 2017

ABSTRACT

In-situ Atomic Scale Studies of Nanoparticle-Solution Interface Processes

Liane M. Moreau

While synthesis and transformation processes to produce monodisperse nanoparticles are empirically well-developed, the pathways for these reactions as well as the exact role of synthetic agents and binding characteristics of surface moieties remain poorly understood. This lack of understanding is primarily due to the paucity of information about nanoparticle structural evolution at the atomic scale and an inability to characterize the nanoparticle-solution interface. This thesis addresses such nanoscale processes through use of an approach which combines *in-situ* X-ray atomic scale characterization (XAFS and XRF) with nanoscale morphological parameters derived from electron microscopy and SAXS. These techniques and approach provide significant insight into the chemical pathways that define bimetallic nanoparticle growth and establish a methodology for characterizing nanoparticle structure (both of the inorganic core and molecular species coordinated to its surface) at the atomic scale.

Chapter 1 presents an overview of nanoparticles and the importance of understanding their structure, in addition to outlining current challenges in characterizing the nanoparticle-solution interface and potential methods to address this challenge. This is followed by Chapter 2, a technical background of methods important to the rest of the work in this thesis, including colloidal nanoparticle synthesis and X-ray characterization techniques. In Chapter 3, through pairing XAFS-derived atomic scale information with electron microscopy and SAXS, a pathway for the

transformation of citrate-capped Ag nanospheres into AgAu nanocages is proposed. Following a similar approach, the role of trace Ag in the synthesis of Au nanorods is determined and described in Chapter 4. Namely, it is shown that the anisotropic growth rate of the nanorods is directly proportional to the amount of surface Ag.

In Chapter 5, the structure of CTAB, a common surface species in the synthesis of Au nanoparticles, is investigated through use of XAFS applied to small Au nanoparticles that are primarily composed of surface atoms. In this way, XAFS, a bulk technique, becomes sensitive to the nanoparticle molecular corona. Through combining this approach with molecular-scale techniques used to investigate ligand replacement on nanoparticle surfaces, Chapter 6 explores the exchange of CTAB with ligands believed to have a stronger affinity for Au nanoparticle surfaces, including BSPP and PEG-thiol.

Chapters 3 – 6 each conclude with proposed future work to provide possible directions for project continuation and extension. In addition, a summary of and outlook for the broader impact of understanding nanoparticle-solution interface structure on improving nanoscale processing is also provided as a conclusion.

ACKNOWLEDGEMENTS

I thank my advisors, Professor Michael Bedzyk and Professor Chad Mirkin, for giving me the unique opportunity and resources as a co-advised student to pursue both my passions for nanochemistry and X-ray characterization and learn and develop skills in both research areas. I also thank them both for not only challenging me both be a better scientist and to develop the scientific communication skills necessary to address audiences of varying expertise, but also for their unwavering encouragement and support. I have been exceedingly fortunate to have worked for two renowned experts in their respective fields and to learn so much from them.

Secondly, I thank the other members of my committee, Professor Olvera de la Cruz and Dr. Timothy Fister for their advice and helpful discussion towards improving my thesis work and serving as a source of inspiration. I also give considerable thanks to Dr. Sumit Kewalramani for his mentorship and guidance throughout my graduate career. He is always extremely generous with his time and patience in explaining x-ray theory and answering questions or brainstorming new approaches.

I also acknowledge my funding sources, including support from a National Defense Science and Engineering Graduate (NDSEG) fellowship, support by the AFOSR under Award FA9550-11-1-0275 and also support from the Vannevar Bush Faculty Fellowship program sponsored by the Basic Research Office of the Assistant Secretary of Defense for Research and Engineering, and funded by the Office of Naval Research through grant N00014-15-1-0043. Without this financial support, my graduate research work would not have been possible. I also thank the beamline scientists at the Advanced Photon Source, for their help in acquiring X-ray data, including Dr. Dale

Brewe, John Katsoudas, Dr. Denis Keane, Dr. Qing Ma, Dr. Steven Weigand, and Dr. Joshua Wright.

I acknowledge my collaborators for their help bringing projects through to fulfillment and for their interesting scientific discussion. In particular, I would like to thank Kurinji Krishnamoorthy and Charles Schurman. They are both intelligent and amazing students to work with, and they provided me with a wonderful mentorship opportunity. I also thank my other collaborators, Dr. Mohammad Shahjamali, Dr. Matthew Jones, Eric Roth, Dr. Jinsong Wu, Dr. Matthew O'Brien, Dr. Bor-Rong Chen, James Hedrick, Dr. Daniel Hannah and Dr. Deiter Isheim. Their knowledge and expertise provided valuable insight for the research projects presented in this thesis, and I learned so much from working with them. I also thank all of the members of the Bedzyk and Mirkin research groups, as well as the Materials Science and Engineering Department students, faculty and staff as a whole. They always provided great suggestions and discussion and were a source of friendship and support.

I thank my undergraduate research advisor, Professor Richard Robinson, for giving me the opportunity to research nanoparticles using X-ray methods, which gave me the exposure to nanotechnology and X-ray research that inspired me to pursue a Ph.D. I thank my parents, Lori and Steven Moreau and brothers Eric and Kevin for their support and encouragement. I also thank my boyfriend, Eric Huang, and friends Elizabeth Pogue, Professor Ashwin Shahani, Anirudh Krovi, Alex Sahu and Liza Sobel for their friendship and support throughout my graduate career.

LIST OF ABBREVIATIONS

BSPP	bis(p-sulfonatophenyl)phenylphosphine
CD	circular dichroism
CN	coordination number
CTAB	cetyl trimethyl ammonium bromide
DFT	density functional theory
EDX	energy dispersive X-ray
EM	electron microscopy
EXAFS	extended X-ray absorption fine structure
ICP-MS	inductively coupled plasma-mass spectroscopy
LSPR	localized surface plasmon resonance
MD	molecular dynamics
NMR	nuclear magnetic resonance
NP	nanoparticle
PCA	principal component analysis
PEG	polyethylene glycol
PVP	polyvinylpyrrolidone
UPD	underpotential deposition
SAXS	small-angle X-ray scattering
SDD	silicon drift diode
SEM	scanning electron microscopy
SHE	standard hydrogen electrode

STM	scanning tunneling microscopy
TEM	transmission electron microscopy
XAFS	X-ray absorption fine structure
XANES	X-ray absorption near edge structure
XRD	X-ray diffraction
XRF	X-ray fluorescence
XPS	X-ray photoelectron spectroscopy

TABLE OF CONTENTS

Chapter 1: Introduction 22

Chapter 2: Techniques 29

2.1 Colloidal synthesis of noble metal nanoparticles 29

2.2 UV-vis spectroscopy 30

2.3 Electron microscopy 30

2.4 Small angle X-ray scattering 31

2.5 X-ray fluorescence 32

2.6 X-ray absorption fine structure 35

2.6.1 Physical measurement description 36

2.6.2 XANES 41

2.6.1 EXAFS 42

Chapter 3: How Ag Nanospheres are Transformed into AgAu Nanocages 48

3.1 Abstract 48

3.2 Introduction 48

3.3 Methods 53

3.3.1 Synthesis 53

3.3.2 UV-vis spectroscopy 54

3.3.3 Electron microscopy 54

3.3.4 X-ray scattering 54

3.3.5 XAFS 55

3.3.6 X-ray fluorescence 56

3.4 Results 57

3.4.1 How does the 3D morphology of the nanoparticles evolve as the reaction progresses? 57
3.4.2 How is the nanoparticle reaction initiated? 59
3.4.3 Does the total number of atoms within the nanoparticle increase or decrease? .. 60
3.4.4 Is a homogeneous alloy or local segregation observed? 60
3.4.5 What is the origin of the nanoparticle hollowing process? 62
3.5 Discussion 64
3.5.1 Comparison to Galvanic Exchange and the Nanoscale Kirkendall Effect 64
3.5.2 A Modified Pathway: Nanoscale Galvanic Exchange 65
3.6 Conclusion 68
3.7 Proposed future work 69
3.7.1 Optical properties of AgAu nanoparticle superlattices 69
3.7.2 Investigation of molecular diffusion kinetics of Ag DNA-NP superlattices 70
Chapter 4: The Role of Trace Ag in the Synthesis of Au Nanorods 71
4.1 Abstract 71
4.2 Introduction 71
4.3 Methods 77
4.3.1 Synthesis 77
4.3.2 UV-vis spectroscopy 77
4.3.3 Electron microscopy 77
4.3.4 X-ray photoemission spectroscopy 78
4.3.5 X-ray scattering 78
4.3.6 X-ray fluorescence 78

4.3.7 X-ray absorption spectroscopy 79
4.4 Results 80
4.5 Discussion 87
4.6 Conclusion 93
4.7 Proposed future work 94
4.7.1 Exploring the role of trace Ag in the synthesis of anisotropic nanoparticles 94
4.7.2 The role of trace I^- in the synthesis of Au nanoprisms 95
Chapter 5: Investigating the Structure of CTAB on the Surfaces of Au NPs 96
5.1 Abstract 96
5.2 Introduction 96
5.3 Methods 99
5.3.1 Nanoparticle synthesis 99
5.3.2 XAFS data collection and analysis 100
5.4 Results 101
5.4.1 Determination of nanoparticle size 101
5.4.2 How is the nanoparticle reaction initiated? 102
5.4.3 XANES 103
5.4.4 EXAFS 104
5.5 Discussion 106
5.6 Conclusion 108
5.7 Proposed future work 108
5.7.1 Computational verification of CTAB structure 108
5.7.2 Study of CTAB structure on planar surfaces 109

5.7.3 Study of CTAB structure on faceted nanoparticle surfaces 110
Chapter 6: Towards Understanding CTAB Replacement on Au NP Surfaces 112
6.1 Abstract 112
6.2 Introduction 112
6.3 Methods 115
6.3.1 Synthesis of CTAB-capped particles 115
6.3.2 Functionalization of CTAB-capped particles with BSPP and PEG-thiol 116
6.3.3 XAFS data collection and analysis 116
6.3.4 UV-vis spectroscopy 117
6.3.5 Zeta potential measurements 117
6.3.6 Small angle X-ray scattering 117
6.4 Results 117
6.4.1 Determination of nanoparticle size 117
6.4.2 UV-vis spectroscopy 119
6.4.3 Zeta potential of Au NPs with varying solution ligands 121
6.4.4 XANES 123
6.4.5 EXAFS 124
6.5 Discussion 126
6.6 Conclusion 127
6.7 Proposed future work 128
6.7.1 Computational study of ligand structure on nanoparticle surfaces 128
6.7.2 Determination of ligand binding constant via in-situ XAFS with ligand titration 128

6.7.3 A multi-ligand strategy to maximize DNA loading on CTAB-capped Au NPs . 129
Chapter 7: Summary and Outlook 132
APPENDIX 134
Appendix A: Supporting information for chapters 3-6 134
A.3 Supporting information for chapter 3 134
A.4 Supporting information for chapter 4 202
A.5 Supporting information for chapter 5 245
A.6 Supporting information for chapter 6 247
Appendix B: XAFS data processing and analysis using the IFEFFIT software package ... 254
B.1 Introduction 254
B.2 Downloading the IFEFFIT software package 255
B.3 Data processing using Athena 256
B.4 Data analysis in Artemis 272
B.5 Conclusion and Outlook 294
REFERENCES 296

LIST OF FIGURES

Figure 1.1 Materials Science tetrahedron. This organization schematic outlines the connected areas that form the pillar behind materials science, which include structure, processing, properties and performance. Characterization sits at the center of the tetrahedron, due to the necessity of thorough characterization in understanding how the four pillars are connected……..... 22

Figure 1.2 Nanoscale processing strategies. The two primary approaches to nanoscale processing include top-down (left), where nanoscale features are created from etching bulk and bottom-up (right), where devices are built from individual atom. 23

Figure 2.1 XAFS measurement schematics. XAFS is commonly collected in either transmission (top) or fluorescence (bottom) detection mode. In both cases, the incident X-ray beam passes through an initial ion chamber (blue) with measured intensity I_0 before hitting the sample. In the case of transmission detection, the transmitted X-rays then pass through a second ion chamber (green) with measured intensity I_t. In the case of fluorescence detection, fluorescence intensity for the element of interest (I_f) is collected using an XRF detector (purple). Through the relationships between μ and these measured intensities (equations, right) are used to generate an XAFS spectrum (μ vs. E, right).. 37

Figure 2.2 Model XAFS spectrum and summary of regions. A Co foil spectrum is shown and separated into XANES and EXAFS regions. From the XANES region, within

~50 eV of the elemental absorption edge, electronic structure can be determined and from the EXAFS region, > 50 eV above the absorption edge, the quasi-periodic modulations can be analyzed to extract local structure parameters. 40

Figure 2.3 XAFS spectrum for krypton gas. As can be seen from the spectrum of a monatomic gas (adapted from Scott et al) the XAFS spectrum is featureless for an isolated atom. In this case the probability of creating a core-hole is solely dependent on being above or below the absorption edge. 43

Figure 2.4 Photoelectron wave processes. After a core electron is dissociated, left, it interacts with the surrounding atoms via electron-electron scattering (right). This wave interference results in the quasi-periodic modulations observed in the EXAFS region of the absorption spectrum. 44

Figure 2.5 Background subtraction to extract EXAFS oscillations. After background subtraction according to Eq. 2.20, and conversion from E to k according to Eq. 2.13, the EXAFS oscillations are extracted (right).. 46

Figure 3.1. Galvanic exchange and Kirkendall effect. Two hypothesized bulk processes used to explain the formation of AgAu nanocages from Ag nanoparticle templates include Galvanic exchange (top) and the Kirkendall effect (bottom). 50

Figure 3.2. Synthesis transformation reaction schematic. Polycrystalline citrate-capped Ag nanoparticles (scale bar = 20 nm) starting at room temperature (left) are transformed into AgAu nanocage of a hollow and porous nature (right, 62.9 at% Au) with increasing addition of 0.1 mM $HAuCl_4$. A cartoon representation of the synthesis products are shown (top). As additional $HAuCl_4$ is added, the particles lose their structural integrity.. 52

Figure 3.3. Nanoparticle products as a function of $HAuCl_4$ addition. (Top) TEM images from pure citrate-capped Ag NPs (a) to (b) 4.0 %, (c) 9.8 %, (d) 27.5 % and (e) 62.9 % Au as determined by XRF. All scale bars are 20 nm. (bottom, left) UV-vis spectra reveal LSPR peak shifts to longer wavelengths with additional HAuCl4 (right, inset). (bottom, right) Atomic % Au in the nanoparticles as determined by XRF vs. equivalence Au added into the reaction solution. 57

Figure 3.4. Nanoparticle morphological trends from SAXS modeling, which determines the ensemble averaged inner and outer radii of the hollowed-out NPs. With increasing Au incorporation, the shell thickness (gold) decreases, while the radius of the core (white) increases, as additional Ag atoms are removed from the core. The overall radius of the particle does not significantly change.. 59

Figure 3.5. Nanoparticle coordination number trends from EXAFS modeling. a) Coordination numbers determined from Au L3 edge XAFS. b) Coordination numbers determined from Ag K edge XAFS. Dashed lines represent the theoretical coordination numbers that would be expected from a homogeneous alloy structure. 62

Figure 3.6. EXAFS informs Ag distribution in Ag/Au NPs. a) Ag K-edge Fourier inverted XAFS data for the starting Ag NPs, transformed NPs with 62.9% Au, and a reference sample of Au NPs with trace Ag. b) From Ag K and Au L3 edge EXAFS, the total Ag and Au coordination numbers within the particles as a function of transformation..... 63

Figure 3.7 Schematic of the proposed nanoscale Galvanic exchange pathway. Starting with Ag nanospheres (top-left), the nanoparticles transform into AgAu nanocages

(bottom-left). Alloy composition is shown in a gradient from Ag (gray) to Au (goldenrod). The included numbers reflect the steps in the process outlined in the text..... 67

Figure 4.1 Schematic of possible anisotropic growth pathways in Au nanorod synthesis. 74

Figure 4.2 Timecourse STEM images. Starting from 2 nm Au seeds,STEM images taken from colloidally synthesized Au nanorods quenched with BSPP at timepoints from 2 minutes into growth (top-left) to final product nanorods (bottom-rigtht). The first three images are cryo-STEM of unconcentrated particles. (See section A.4 for details)..... 81

Figure 4.3 Nanoparticle growth and composition. a) EM determined length and diameter growth rates as a function of reaction time, b) UV-vis spectra as a function of reaction time, c) XRF-determined nanoparticle composition and d) XRF and EM determined number of Ag atoms per nanorod…….82

Figure 4.4 Ag K-edge XANES data from 120 min final product nanorods (middle, green) compared to standards with Ag^{+} (top 3) and Ag_0 (bottom 2). A blowup of the near edge region is shown on the right-hand-side for each spectrum..... 84

Figure 4.5 EXAFS results. a) Coordination numbers extracted from Ag K and Au L3 edge XAFS spectra. b) Ag surface coverage, extracted from a combination of XAFS-extracted coordination numbers, EM-determined dimensions and the assumption that Ag on the surface has a CN of 7. 85

Figure 4.6 SEM (top), and EDX maps of Ag and Au at 12 minutes into the reaction where Ag is predominanately at the surface (Fig. 4.5). The bottom schematic shows the

three types of Ag (blue) surface distributions considered. EDX eliminates the case for Ag only on the ends of the nanrods (bottom right). 87

Figure 4.7 Flow chart connecting anisotropic growth hypotheses. The flow chart relates nanorod structural attributes to the appropriate hypothesis for nanorod anisotropic growth. This study provides answers to the questions posed, leading to identification of the UPD hypothesis as the most in line with the reason behind nanorod anisotropic growth. 89

Figure 4.8 Nanorod growth rates vs. Ag surface coverage. Combining the results of XRF, EXAFS and STEM, the diameter growth rate is shown to be unaffected by surface Ag, while the length growth rate is directly correlated. 90

Figure 4.9 Proposed reaction pathway for Au nanorod growth. Starting with ~ 2 nm Au seeds (0 minutes), Ag deposits between 6-8 minutes in the reaction, stabilizing {110} facets and inducing anisotropic growth. By 8 minutes into the reaction, the nanorods are anisotropic with an aspect ratio of 1.5. The final aspect ratio of 3.6 is reached by 12 minutes into the reaction. Over time, Ag deposition slows and incorporated Ag diffuses into the nanorod interior. By 45 minutes into the reaction, Ag surface coverage approaches zero, and the length and diameter nanorod growth rates remain equivalent until reaction completion (120 minutes, final product). . 93

Figure 5.1 Possible nanoparticle-CTAB interface structure configurations. a) The CTA+ headgroup binds to the nanoparticle surface, b) The Br^- counterion binds to the nanoparticle surface and c) Both the CTA^+ headgroup and Br^- counterion adhere to the nanoparticle surface. 98

Figure 5.2 Au L3 edge XAFS spectra of CTAB-capped Au nanoparticles compared with Au foil. Both XANES (left) and EXAFS (right) regions of a bulk Au foil (red) in comparison to 1.7 nm CTAB-capped Au nanoparticles (black) show that the XAFS spectrum is sensitive to nanoparticle interface structure……. 103

Figure 5.3 EXAFS k-space spectrum of CTAB-capped Au nanoparticles (blue) and fitting model (red). The model matches the data in both low k and high k regions. Parameters listed in the table below were extracted from this model..... 105

Figure 5.4 Measurement setup for SEXAFS, adapted from Heald et. al. Using a glancing angle (θ), and placing a fluorescence detector at 90° (I_f), surface sensitivity can be obtained for a planar sample. If an additional detector is placed after the sample (I_r), X-ray reflectivity measurements can also be obtained to investigate sample roughness and electron density. 110

Figure 6.1 Schematic of nanoparticle samples (left) and ligand molecular structures (right). Starting with CTAB-capped Au nanoparticles (top), nanoparticle solutions were brought to equal concentrations of either BSPP (blue) or PEG-thiol (red, n = 4) (middle). Structures where the third ligand was added (bottom) were also investigated, to study which ligand (BSPP or thiol) has a greater affinity to the Au surface. 114

Fig. 6.2 SAXS pattern of CTAB-capped Au NPs. ~2 nm Au nanoparticles subsequent to overgrowth with additional Au were determined to be 14.7 nm in diameter based on SAXS modeling (black line) using a spherical form factor compared to the Au nanoparticle SAXS data (purple circle). 118

Fig. 6.3. UV-vis spectra of 14.7 nm Au nanoparticles with varying surface structure. From UV-vis spectra, it is observed that from the initial CTAB-capped NPs (black), a red-shift is observed when BSPP is introduced into solution (red) and a blue-shift when PEG-thiol is introduced (green). In the case where both BSPP and PEG-thiol are added into solution, a blue-shift characteristic of PEG-thiol is also observed. 120

Figure 6.4. XAFS spectra at the Au L3 edge of nanoparticle samples as a function of ligand species. a) XANES results show drastic differences in the intensity of the white line peak, which is inversely proportional to the occupancy of Au 5d states. b) EXAFS spectra show unique features related to the Au surface coordination when different ligand species are present in solution. Data was collected at a global ligand concentration of 50 mM for all ligand species present in solution. From Figs. A6.2 and A6.3, it is observed that the XANES and EXAFS spectra are nearly identical for the case where 10 mM is used instead of 50 mM..... 124

LIST OF TABLES

Table 5.1 EXAFS modeling parameter summary based on Eq. 5.1……105

Table 6.1 LSPR peak positions 121

Table 6.2 Zeta potential..... 122

Table 6.3 EXAFS-derived parameters. 125

Chapter 1: Introduction

The field of materials science and engineering is based on the concept that materials processing, properties and performance are intimately connected with their structure. To this end, a required thrust area within the field has been developing tools and methodologies to better understand materials structure through characterization. In fact, characterization has found its place at the center of the materials science tetrahedron,[1] the field's fundamental pillar traditionally used to describe its goals (Figure 1.1).

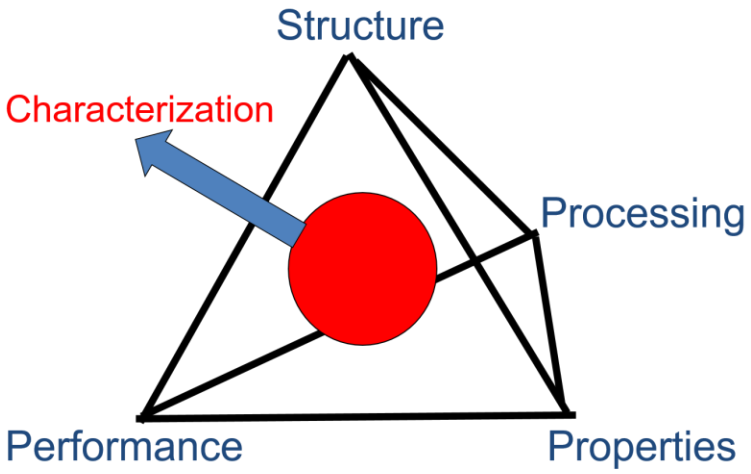

Figure 1.1 Materials Science tetrahedron. This organization schematic outlines the connected areas that form the pillar behind materials science, which include structure, processing, properties and performance. Characterization sits at the center of the tetrahedron, due to the necessity of thorough characterization in understanding how the four pillars are connected.

There are two primary device processing strategies used by materials engineers that each present their own characterization challenges. These include "top-down" and "bottom-up" fabrication (Figure 1.2). Top-down fabrication involves etching and lithography of a larger bulk

material into smaller components. While this has proven a successful approach to device fabrication for many years, particularly in the electronic device industry, a challenge presents itself in that the diffraction limit of visible light limits the feature size attainable using traditional methods.[2-3] Moore's law predicts that as the demand for device performance increases with advances in modern technology, that the required feature size will continue to decrease down to the atomic scale.[4] To this end, bottom-up approaches, where features are controlled from the atomic scale[3] to assemble into larger structures, become increasingly necessary. Nanoparticles (between 1 - 100 nm) have become an increasingly important research area because of this shift.

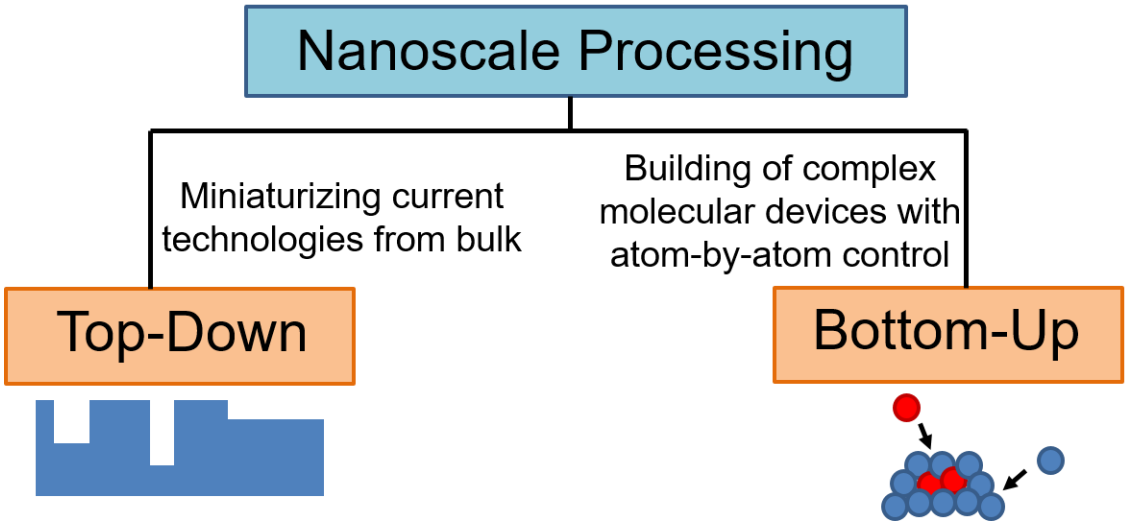

Figure 1.2 Nanoscale processing strategies. The two primary approaches to nanoscale processing include top-down (left), where nanoscale features are created from etching bulk and bottom-up (right), where devices are built from individual atom.

Nanoparticles have proven beneficial over their bulk counterparts due not only to their small size, but also to the properties that emerge as a result of their high surface area to volume ratio. In particular, unique optical,[5] catalytic[6] and electronic[7] phenomena emerge due to their high fraction

of surface atoms. Also, nanoparticles can serve as a scaffold for functional molecules[8-9] and as therapeutic and diagnostic agents due to their capability of passing through the blood-brain barrier.[10] This thesis focuses on noble metal nanoparticles, which have been a subject of particular interest for their facile aqueous-based synthesis methods and their ability to support a localized surface plasmon resonance (LSPR).[5, 11-12]

While the synthesis of colloidal nanoparticles has been empirically well-developed, the pathways underlying their growth and transformation remain elusive and often controversial. In particular, surface molecules and trace synthetic additives have been hypothesized to play a determining role in the size and morphology of nanoparticle products, however, their exact function in the reaction pathway has not yet been established.[13-14] Understanding the pathways behind nanoparticle synthesis and transformation are not only important to further optimize synthetic processes, but also present new and interesting scientific possibilities. While chemical transformations in bulk materials follow well-developed thermochemical kinetic models, nanoparticle systems often display interesting and unpredictable behavior that cannot be explained from standard theory.[15-18] It is therefore necessary to develop a sufficient understanding of nanoparticle transformation pathways to propose theories relevant and useful for this novel length scale.

The lack of understanding behind nanoparticle synthesis and transformation pathways and the role that specific synthetic agents play in these processes stems from the difficulty in characterizing their structure. The small size of nanoparticles results in difficulty in using conventional atomic-scale characterization tools such as X-ray diffraction (XRD), due to broadening of features from their small domain size and amorphous-like surface layers. In addition,

electron microscopy can be destructive to small nanoparticles due to their high reactivity under the electron beam.[19]

Nanoparticles prove a challenging problem to both characterization and modeling due not only to their small size, but also due to the importance of their surfaces. Colloidally-synthesized nanoparticles are in truth composite materials, composed both of an inorganic core material and organic surface species. The binding of these organic species to the nanoparticle surface makes it particularly difficult to characterize nanoparticle interface-structure. Yet given that this interface is where nanoparticle growth and transformation initiates, it becomes necessary to address this characterization challenge. In fact, characterization of nanoparticle interfaces has been identified by forerunners in the field as the key to understanding nanoparticle synthesis processes.[13-14] For example, in a review article concerning the controversy over the synthetic pathway in Au nanorods (which will be addressed in Chapter 3 of this thesis), Murphy et. al addresses the first key challenge that needs to be addressed to achieve progress: "New tools are needed to quantitatively characterize the local chemical environment of nanoparticles in situ with high spatial resolution. 'Local' means both the outer corona of physisorbed molecules and the chemical identity of metal-bound ligands."[13] A key goal of the work in this thesis is to present a methodology to address this characterization gap and utilize this approach to gain a better understanding of poorly understood nanoparticle synthesis and transformation reactions.

Prior to this work, several methods have been used to characterize the nanoparticle-solution interface. Proton Nuclear Magnetic Resonance (NMR) has been used to determine whether a chemical species is present or not present, providing qualitative proof of ligand replacement in nanoparticle systems.[20] Circular Dichroism (CD) has been used to track conformation and secondary structure of surface ligand species.[21] X-Ray techniques such as Photoelectron

Spectroscopy (XPS) and X-Ray Absorption Near Edge Structure (XANES) have been used to track the presence or absence of heavy elements which may be present in surface layers of nanoparticles dried onto substrates[22] as well as the chemical signature, including oxidation states of nanoparticle surface species.[23-24] Another method which can be used to quantitatively track the number of species per particle is Fluorescence Spectroscopy, however this method requires attachment of a fluorophore to the nanoparticle surface ligand, or else that the ligand is stainable using a fluorescent dye, which limits the species which may be probed by this method.[25] In addition, STM (Scanning tunneling microscopy) has been used to track the arrangement of molecules on nanoparticle surfaces, and gain insight into their packing arrangements.[26] While each of the aforementioned techniques gives insight into the nature of the nanoparticle-solution interface, including species present on nanoparticle surfaces, they lack quantitative information concerning the nanoparticle surface composition, in addition to the specific bonds that are formed between the nanoparticle surface and the attachment ligand. In order to extract this information, computational techniques such as Density Functional Theory (DFT) have been employed.[27] Yet even such computational techniques are limited due to the number of atoms required for simulation, proving costly and computationally time consuming, and the difficulty in determining surface energy for nanoscale particles. Thus, to date, an effective methodology to probe nanoparticle surface composition and the binding structure of adhered surface ligands with quantitative specificity, to gain insight into local surface environment has not been established. Alternative approaches to studying the nanoparticle-solution interface need to therefore be established to approach this key problem of understanding the nanoparticle-solution interface.

In designing an approach to probe the nanoparticle-solution interface structure, it is important to consider requirements towards characterizing the interface on multiple length scales. An ideal

technique approach would provide atomic-scale structural information while probing nanoparticles non-destructively in their solution environment, with the potential for *in-situ* analysis. This is particularly important because depositing nanoparticles onto a surface and drying them out disrupts their surface structure as well as the local to global ligand concentration found in solution. In addition, element specificity is required, to provide insight into nanoparticle surface composition, and which species may be binding to the surface or incorporated into surface layers. The technique must also provide surface sensitivity, such that signal from atoms within the nanoparticle core does not dominate the measurement.

These criterion are satisfied through use of X-ray absorption fine structure (XAFS), which presents itself as an advantageous alternative over the aforementioned techniques in its element specificity, ability to probe in-situ, and its sensitivity to both geometric and radial structure of an average core atom.[28] From the near edge XANES region, we can determine the oxidation state of an average atom within the nanoparticle, which will provide information concerning charge transfer between surface atoms and bound ligand species. From the higher energy extended X-ray absorption fine structure (EXAFS) region, we can obtain such specific structural information as which elements are bound and their coordination numbers, interatomic spacings, and structural disorder using ab-initio modeling analysis.[28] When these atomic-scale parameters derived from XAFS are paired with the overall morphological trends which particles undergo in their synthesis and transformation, connections can be made concerning how particular solution components contribute to the reaction pathways. This can be accomplished through studying the structure of nanoparticles stages at aliquots taken at various stages throughout the synthetic reaction, using XAFS to derive atomic scale structure as well as electron microscopy, small angle x-ray scattering (SAXS) and chemical methods to determine how the local nanoparticle corona affects the

morphological evolution of the particles. The rest of this thesis describes how this proposed approach was used in order to propose plausible reaction pathways based on previously elusive atomic-scale structural attributes. The contents contribute valuable information concerning important nanoparticle reactions, and also provides a methodology template to study additional reactions of interest and fill the gap in atomic-scale information required to understand and control the nanoparticle-solution interface.

Chapter 2: Techniques

2.1 Colloidal synthesis of noble metal nanoparticles

The work in this thesis focuses on synthesis and transformation reactions and surface ligand structure of noble metal nanoparticles. Colloidal nanoparticle synthesis requires four main components: 1) A solvent to dissolve reactants and serve as a medium through which these components can diffuse and collide to induce reactions (such as water in the case of aqueous-based synthesis discussed herein); 2) A metal precursor (such as $AgNO_3$ or $HAuCl_4$) that serves as a source of metal ions; 3) A reducing agent (such as $NaBH_4$ or ascorbic acid) which provides a source of electrons to reduce the metal ions into the metallic state; and 4) A surfactant or stabilizing agent, to prevent the nanoparticles from aggregating as a result of their high surface energy.[29]

Given the importance of synthesizing nanoparticles that are uniform in size due to the size-dependence of their novel properties, three general approaches are generally used. In general, it is desirable for fast nucleation is followed by slow and controlled growth.[29-30] An approach which encourages fast nucleation is either via hot injection[31] or by using a strong reducing agent.[32] The other approach is to slow the growth process by using a weaker reducing agent.[33] A third and highly effective approach is to approach is to separate the nucleation and growth processes altogether by inducing growth of pre-synthesized nanoparticle seeds.[34] This "seed-mediated" synthesis has been used in particular in the synthesis of anisotropic Au nanoparticles.[35-36]

Quasi-spherical structures present the lowest energy pathway in the synthesis of noble metal nanoparticles.[37] If additional synthetic agents are introduced into solution, however, anisotropic nanoparticles can be achieved in a wide variety of shapes and sizes.[14, 38-39] It is hypothesized that surface species such as cetyl-trimethyl ammonium bromide (CTAB) or polyvinylpyrrolidone (PVP)

can induce anisotropy by binding preferentially to different surface facets, changing the kinetics of atomic surface addition.[13, 39] Alternatively, trace elemental species, such Ag^+ in the synthesis of Au nanorods,[35] or I^- in the synthesis of Au nanoprisms[40] are thought to serve a similar role. The exact role of these species and pathways behind anisotropic growth, however, are poorly understood, and will be discussed further in chapter 3 of this thesis.

2.2 UV-vis spectroscopy

UV-vis spectroscopy is a particularly useful tool for the case of Ag and Au nanoparticles, due to their ability to produce a localized surface plasmon resonance (LSPR), due to the resonant oscillation of conduction electrons at the nanoparticle surface. Considering that the LSPR peak position is highly sensitive to nanoparticle size, shape and composition, this presents an effective method to evaluate nanoparticle morphology.[5, 11] In addition, the LSPR peak position is also sensitive to species bound to the nanoparticle surface, due to the resulting change in dielectric environment.[23, 41] Since UV-vis measurements are made in solution, these morphological changes can be effectively probed *in-situ*. This is particularly useful when comparing morphological trends to X-ray measurements providing atomic-scale information also *in-situ*.

2.3 Electron microscopy

Electron microscopy including transmission EM (TEM) and scanning EM (SEM) are the most conventional methods to characterize nanoparticle synthesis products. They provide high-resolution images to observe nanoparticle morphology of ex-situ nanoparticle samples. Due to the high energy of the incident electron beam (80 - 200 keV), energy dispersive X-ray (EDX) spectroscopy can be used to map nanoparticle composition as a function of pixel position, since the energy exceeds most X-ray fluorescence energies for elements of interest. These conventional characterization modes are used in this thesis to provide information about nanoparticle

morphology at the nanoscale. These results are then correlated with XAFS-derived atomic scale parameters.

2.4 Small angle x-ray scattering

Small angle X-ray scattering (SAXS) provides a means of determining nanoparticle size, shape and polydispersity. This measurement provides an advantage over electron microscopy in that measurements can be made *in-situ* and also present an ensemble-average of particles, therefore providing morphological trends that are statistically representative of the nanoparticle product. Through use of a thermal flow cell, and short exposure time to minimize beam damage, nanoparticle reactions can be probed throughout the course of a reaction as nanoparticles are being synthesized.[42] In this thesis, SAXS measurements were used to determine nanoparticle morphological parameters *in-situ*, to complement EM images and also to better realize 3D structure in the case of core-shell nanoparticles. The use of SAXS for specific nanoparticle systems is described in detail in Chapters 3, 4 and 6. The theory behind the measurement is described in brief below:

Incident X-rays scatter off of a sample, where q is the magnitude of the scattering vector $\vec{q}$, which is the difference in momentum of the incident and scattered wavevectors and

$$q = \frac{4\pi \sin(\theta)}{\lambda} \tag{1.1}$$

Where λ is the incident photon wavelength and θ is half of the scattering angle 2θ. The resulting scattering amplitude increases with increased difference in the electron density profile of the scattering object compared with the background medium. This makes studying noble metal nanoparticles ideal, due to the high scattering density of the inorganic particle core.

The scattered intensity I(q) is equivalent to

$$I(q) = |F(q)|^2 S(q) \quad (1.2)$$

Where F(q) is the nanoparticle form factor, and S(q) is the structure factor, which in the dilute limit (low particle concentration) can be approximated to 1, as is appropriate in the case of the measurements presented in this thesis. Thus, the scattered intensity can be approximated as $I(q) = |F(q)|^2$. When the form factor integral

$$F(\vec{q}) = \int_v \rho(\vec{r}) s(\vec{r}) e^{i\vec{q}\cdot\vec{r}} d\vec{r} \quad (1.3)$$

Where $\vec{r}$ represents the position vector, $\rho(\vec{r})$ is the electron density and $s(\vec{r})$ is a function specific to the shape of the scattering object is evaluated over volume ν for the case of a solid object (hollow object form factors are discussed in chapter 3), the scattered intensity becomes

$$I(q) = \rho_0^2 v^2 \, e^{\frac{-1}{3} q^2 {R_g}^2} \quad (1.4)$$

Where ρ_0 is the average electron density of the scatterer and R_g is its radius of gyration, which depends on the shape of the scattering object minus the background medium. From the aforementioned relationships, 1-D profiles from obtained from azimuthal averaging over the experimental 2-D scattering pattern can be modeled to extract parameters relevant to the size, shape and polydispersity of solution particles.[43]

2.5 X-ray fluorescence

X-ray fluorescence (XRF) provides a method to determine nanoparticle composition for elements with Z > 12. This method proves advantageous due to its *in-situ* and non-destructive capabilities. Unlike inductively coupled plasma methods, generally used in the nanoparticle community, it is not necessary to dissolve the particles before measurement, where incomplete dissolution or formation of precipitates often occurs.[44] When an internal standard is used, the absolute number of atoms can also be determined. Considering that XAFS data collected for the

purpose of this thesis was obtained in fluorescence mode (see Section 2.6 below) it is convenient and highly useful to collect the full XRF spectrum in addition to the integrated fluorescence from the element of interest.

XRF occurs when the energy of incident x-rays exceeds the energy required to remove an electron from a core electron orbital. This produces a hole that an electron in a higher energy orbital can then fill, returning the atom (now an ion) to its ground state. The decay produced in this process creates characteristic X-ray fluorescence that are element-specific in nature, since the fluorescence energy is equivalent to the binding energy difference between the two electron levels involved in the transition.

There are three types of allowed XRF transitions, K, L and M depending on the electron shell that the core electron was removed from K (n = 1), L (n = 2) and M (n = 3). The transitions are further noted by the higher energy shell (α, β, or γ) and subshell (1, 2 or 3). For example, the $K\alpha_1$ transition is from L_3 to K and the $L\alpha_1$ transition is from M_5 to L_3. A list of these transitions can be found in the database developed by Thompson et al.[45]

In order to determine the compositional atomic ratio $\frac{N_A}{N_B}$ of two elements of interest (A and B) in a sample (or absolute number of atoms when the ratio is found with respect to an internal standard of known concentration), the ratio of the fluorescence yields $\frac{Y_A}{Y_B}$, (obtained from the ratio of the area under the relevant fluorescence peaks, must be normalized according to the following equation

$$\frac{N_A}{N_B} = \frac{Y_A}{Y_B}\ \frac{\sigma_B}{\sigma_A}\ \frac{\eta_B}{\eta_A}\ \frac{T_B}{T_A} \qquad (1.5)$$

Where σ is the element and energy-specific XRF cross-section,[46] η is the detector efficiency at the X-ray fluorescence line energy and T is the transmission factor due to attenuation from species between the sample and detector.

Calculating an accurate transmission factor is particularly important for the case of *in-situ* measurements, since nanoparticles are in a solution environment, necessitating an absorbing media between the nanoparticle and the detector which attenuate the fluorescence signal. The transmission factor can be calculated according to the equation

$$T(E) = e^{-\mu(E)*t} \quad (1.6)$$

Where μ is the linear absorption coefficient of the media or inverse of the absorption length and t is the thickness of the media between the nanoparticle and detector. A transmission factor term $\frac{T_B}{T_A}$ needs to be applied for each XRF species at the relevant energies $T_B(E_B)$ and $T_A(E_A)$. For the cases discussed in this thesis, where XRF measurements were performed on dilute AgAu nanoparticle samples in aqueous solution and placed in 3 nm inner diameter quartz capillaries, transmission factor terms could be neglected for the air between the sample and detector, the capillary walls and the Be window on the fluorescence detector, since these had a < 1 % effect on the fluorescence yield at the energies of interest. Nanoparticle concentrations (μM concentration of atoms) and other solution species were also in the dilute limit (<1 % effect on the fluorescence yield) and were therefore also neglected.

Contributions from the water solvent, however, and any Al foils placed in front of the detector, however, needed to be accounted for. For attenuation due to Al foils (which were used in cases where the Ag concentration in the sample was low, μ and t could simply be input into Eq. 1.6 at the respective energies. For the case of the water, however, an issue arises in that the attenuation

due to water will be different at different spots in the sample capillary where the nanoparticles are suspended. For example, a particle towards the front of the capillary would be attenuated less than a sample towards the side of the capillary that is further from the detector. In order to overcome this, a matrix of points was created at various spots on the capillary that are within the illumination area of the incident beam. The transmission factor T was then calculated and averaged over each of these points with their particular point-to-detector distance. While solid angle correction was explored, this made a <1 % difference in the corrected values due to the large distance between the sample and the detector and was therefore neglected. Applying the matrix of points correction resulted in a ~30 % difference in the corrected yield compared with using a fixed distance at the center of the sample. This approach was verified by comparing the resulting Au Lα to Au Lβ fluorescence intensity ratios within the sample. Through following this procedure, accurate determinations of nanoparticle composition ratios were achieved and enabled the comparison of particle composition to local structure and morphology changes.

2.6 X-ray absorption fine structure

X-ray absorption fine structure (XAFS) was the primary characterization method used throughout this thesis, due to the sensitivity of this technique to element-specific bonding contributions, therefore enabling characterization of nanoparticle structure at the atomic scale. Also, characterization of nanoparticles *in-situ* in their solution environment provides an additional advantage. In addition, unlike XRD, XAFS does not require periodic structure in order to probe inter-atomic contributions, and has been used to obtain molecular structural information from non-crystalline (amorphous) samples.[47] This provides an ideal platform to study nanoparticles due to their small domain size and high concentration of surface atoms that blur periodic features. The

rest of this section will provide a brief overview of this technique and its capabilities as a characterization platform.

2.6.1 Physical measurement description

The basic quantity measured in XAFS is the X-ray absorption coefficient, μ, as a function of incident X-ray energy (E). μ(E) describes how strongly X-rays are absorbed as a function of energy. Generally, μ(E) is proportional $\frac{1}{E^3}$. This is not the case at particular energies, however, since the X-ray absorption spectrum for a given element will exhibit a sharp increase at a photon energy that is equivalent to the ionization potential of a core electron. These absorption edges are named for the electron orbital from which the core electron is removed (K edges for n = 1, L edges for n = 2 and M edges for n = 3). XAFS data is collected through these absorption edges, whose elemental specificity to particular ionization potentials provides it capability to probe the element-specific coordination environment. It should be noted, however, that that XAFS normalization required for EXAFS region analysis is generally difficult for elements where Z ≤ 15, due to the $\frac{1}{E^3}$ energy dependence. In addition, elemental edge energies above 30 keV are also generally difficult to measure. Fortunately, most elements have either K or L edges within an accessible energy range. In particular, this thesis work focuses on XAFS data collected at the Ag K (25.514 keV) and the Au L_3 (11.919 keV) absorption edges.

The absorption coefficient is typically measured via either transmission or fluorescence detection. A schematic of these measurement configurations is shown in Figure 2.1.

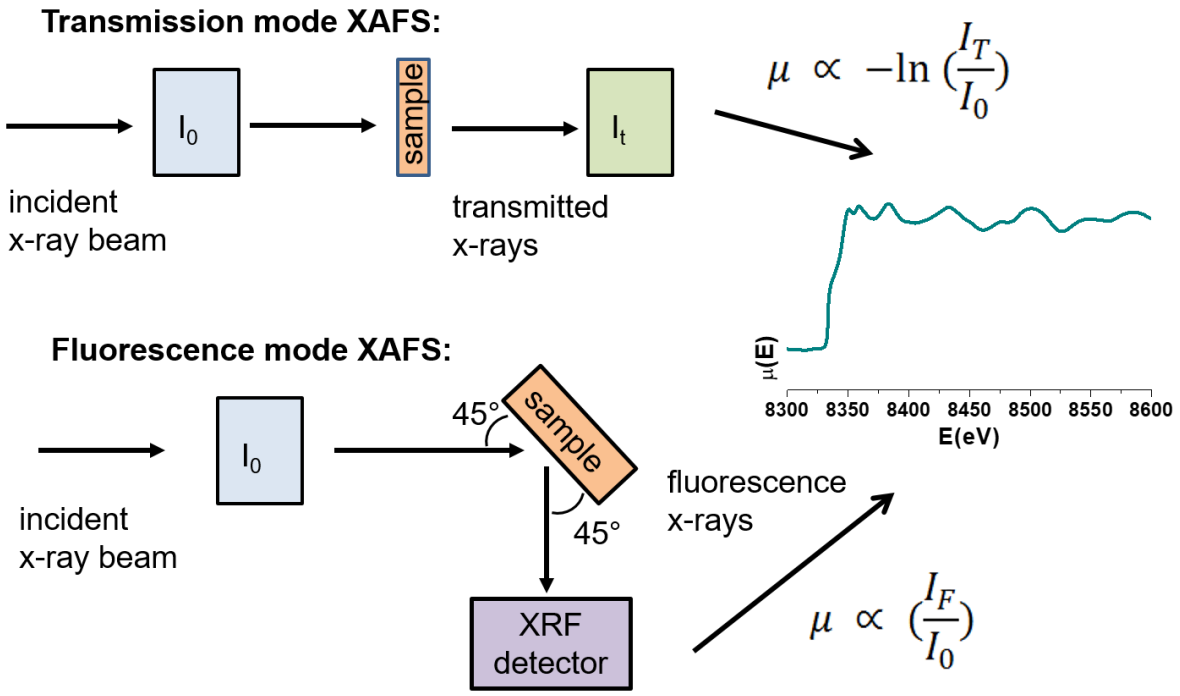

Figure 2.1 XAFS measurement schematics. XAFS is commonly collected in either transmission (top) or fluorescence (bottom) detection mode. In both cases, the incident x-ray beam passes through an initial ion chamber (blue) with measured intensity I_0 before hitting the sample. In the case of transmission detection, the transmitted X-rays then pass through a second ion chamber (green) with measured intensity I_t. In the case of fluorescence detection, fluorescence intensity for the element of interest (I_F) is collected using an XRF detector (purple). Through the relationships between μ and these measured intensities (equations, right) are used to generate an XAFS spectrum (μ vs. E, right).

In transmission mode, the sample is placed between two ion chambers. According to Beer's law, the relationship between the absorption coefficient and the intensity of the x-ray beam through

the first ion chamber (I_0) and the transmitted x-ray intensity through the ion chamber after the sample (I_t) is

$$I_t = I_0\, e^{-\mu(E)t} \tag{2.7}$$

where t is the sample thickness. In this way the absorption coefficient can be extracted as

$$\mu \propto -\ln\left(\frac{I_t}{I_0}\right) \tag{2.8}$$

Using X-ray fluorescence detection, the sample surface is typically placed at a 45° angle both with respect to the XRF detector normal and the incident X-ray beam (i.e., $\theta = \phi = 45°$).[28] Fluorescence mode detection is particularly helpful when the concentration of the element of interest within the sample is sufficiently dilute such that collecting a transmission signal proves difficult due to the high sensitivity of XRF. The XRF photons are generally collected in the horizontal plane with the detector at ~ 90° relative to the incident beam direction to minimize the intensity due to elastically and inelastically scattered X-rays. The relationship between the absorption coefficient and the fluorescence yield collected from the area under the fluorescence line peak from the element of interest (I_F) is

$$\frac{I_f}{I_0} \propto \frac{A}{r^2}\varepsilon_k \frac{\mu(E)}{\mu_{tot}(E)+\mu_{tot}(E_f)\sin\phi sin\theta}\{1-\exp\left[-\left(\frac{\mu_{tot}(E)}{\sin\phi}+\frac{\mu_{tot}(E_f)}{sin\theta}\right)t\right]\} \tag{2.9}$$

Where μ is the portion of the total absorption μ_{tot} due to the element of interest, ε is the probability of producing a photon with energy equivalent to the fluorescence energy E_f, A is the area of the detector at a distance r from the sample, θ is the angle between the sample surface and the detector, ϕ is the angle between the incident beam and the sample and t is the sample thickness. When the sample is sufficiently thick compared to the photon absorption length, then the exponential term can be neglected, making the expression

$$\frac{I_f}{I_0} \propto \frac{A}{r^2}\varepsilon_k \frac{\mu(E)}{\mu_{tot}(E)+\mu_{tot}(E_f)\sin\phi sin\theta} + I_{bkg}(E) \quad (2.10)$$

Where $I_{bkg}(E)$ is the background radiation. When the sample is sufficiently dilute with respect to the element of interest, this decreases the contribution of μ_k to μ_{tot}, causing the $\mu_{tot}(E)$ term to dominate the denominator. This makes it possible to approximate I_f as being proportional to I_0 according to the relationship

$$\mu \propto \frac{I_f}{I_0} \quad (2.11)$$

Based on the aforementioned assumptions required in order to extract this relationship, it should be noted that for samples that are not sufficiently dilute or for the case that the effective thickness of the element of interest is sufficiently thin, that these assumptions break down, resulting in self-absorption effects in the XAFS data.[48] Fortunately, for the case of the XAFS data collected in this thesis, the samples were in the dilute limit, with Au or Ag atoms in the μM concentration in aqueous solution. Therefore, these assumptions were reasonable to use and approximate the absorption coefficient according to Eq. 2.11.

As μ is determined as a function of incident energy E going through an X-ray absorption edge, a spectrum such as that shown in Figure 2.2 results.

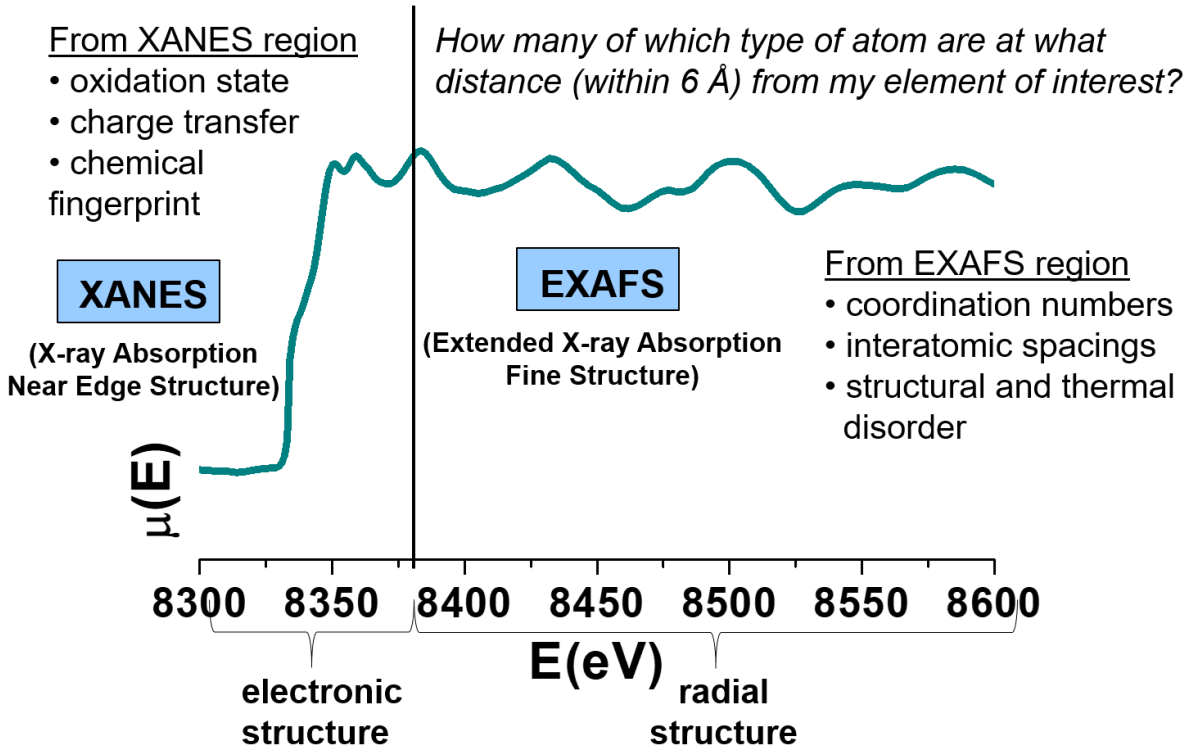

Figure 2.2 Model XAFS spectrum and summary of regions. A Co foil spectrum is shown and separated into XANES and EXAFS regions. From the XANES region, within ~50 eV of the elemental absorption edge, electronic structure can be determined and from the EXAFS region, > 50 eV above the absorption edge, the quasi-periodic modulations can be analyzed to extract local structure parameters.

The sharp increase in the absorption coefficient is the absorption edge previously discussed. The region within 50 eV of this edge is referred to as the X-ray absorption near edge structure (XANES) region. From this region, which is sensitive to the density of states, electronic structure, such as the atomic oxidation state and charge transfer behavior can be derived. This is discussed in greater detail in Section 2.6.2. The quasi-periodic modulations > 50 eV above the absorption

edge is referred to as the Extended XAFS (EXAFS) region. These modulations are sensitive to the presence of atoms surrounding the absorbing atom, enabling local structural parameters including coordination number and interatomic distance in addition to the species of the surrounding atoms to be determined. Effectively, the information obtained from the EXAFS region enables us to answer the question of "How many of which type of atom are at what distance (within ~ 6 Å) from the element of interest?".[47] The details of how these quasi-periodic modulations are generated and how these parameters can be extracted are discussed in Section 2.6.3. Together, these regions of the spectra enable element-specific atomic scale structure to be derived and have proved a useful tool for studying the nanoparticle-solution interface.

2.6.2 XANES

As seen in Figure 2.2, the X-ray absorption edge does not simply occur as a discontinuity in the absorption spectrum. Rather, features can be observed that are related to electronic structure of the absorbing atom site on average within the sample. It should here be noted that from here on when XAFS parameters are discussed, they refer to an ensemble-average of all absorbing -element atoms within a sample. Shoulders or pre-edge features arise from electronic transitions from the core level to valence levels that are just below the continuum. These can be used to gain information about the symmetry of the absorbing level site when appropriate selection rules are applied.[28] Since the position of the absorption edge is related to the potential required to remove a core electron, a shift in the edge position may be indicative of the oxidation state of the absorbing atom. For most cases, a higher edge energy indicates a higher (more positive) oxidation state, since electrostatically, it is more difficult to remove a core electron if the atom is electron-poor.[47] Another general feature indicative of charge transfer is the white line peak, which is the sharp peak that occurs in the proximity of the absorption edge. A sharp white line peak means that an electron

in its final state is highly confined by the surrounding potential.[28] Thus the intensity of this peak has been related to the occupancy of the state. In general, atoms with a higher positive charge exhibit a white line peak with a greater intensity. This is particularly apparent for XAFS data collected at L edges, due to the number and complexity of d-state occupancy.[28]

Few quantitative analysis methods for XANES analysis exist, including principal component analysis (PCA), which in which linear combinations of basis spectra are found and new sets of basis vectors produced, to find the minimum number needed to reproduce the spectrum, and linear combination fitting as a function of multiple known standards.[28] Such methods, while helpful in understanding XANES spectra given their high complexity, are not considered highly accurate. Experts in the field of XAFS have generally advised avoiding quantitative XANES analysis when possible. A more accurate method is qualitatively comparing the spectra to those of known standards. XANES is very sensitive in serving as a chemical fingerprint for individual structures. By comparing XANES spectra to known standards, the oxidation state and electronic environment can be more accurately determined.[28] Thus the XANES analysis presented in this thesis takes this qualitative approach, comparing XANES spectra at the Au L_3 and Ag K absorption edges with relevant standards.

2.6.3 EXAFS

While XANES deals with the core electron excitation itself, the EXAFS region at higher energies involves contributions from surrounding atoms. Without the existence of surrounding atoms, such as is observed for the case of a monatomic gas (Figure 2.3), the absorption spectrum is featureless after the absorption edge, exhibiting the expected $\frac{1}{E^3}$ dependence without modulation.

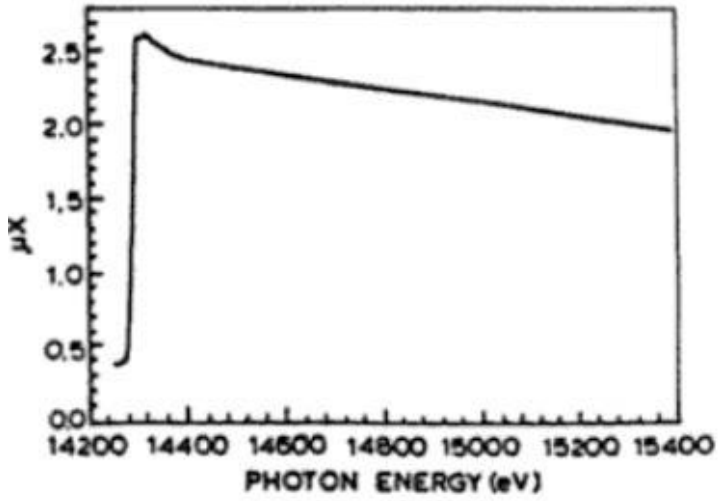

Figure 2.3 XAFS spectrum for krypton gas. As can be seen from the spectrum of a monatomic gas (adapted from Scott et al)[47] the XAFS spectrum is featureless for an isolated atom. In this case the probability of creating a core-hole is solely dependent on being above or below the absorption edge.

A different case is observed, however, when electron-electron scattering results from the presence of surrounding atoms, resulting in quasi-periodic modulations in the EXAFS region of the spectrum. To describe the origin of this effect, it is necessary to introduce the concept of the photoelectron wavevector k. Since it is nonrelativistic,

$$k = \frac{2\pi}{\lambda} = \frac{2\pi m_e v}{h} \qquad (2.12)$$

Where λ is wavelength and m_e is the mass of an electron, v is velocity and h is Planck's constant. k is related to energy E above the absorption edge E_0 by the following relationship

$$k = \sqrt{\frac{8\pi^2 m_e}{h^2}(E - E_0)} \qquad (2.13)$$

Due to electron delocalization, we can describe the dissociated core photoelectron as a spherical wave to describe its trajectory.

$$\psi_{out}(\vec{r}) = \frac{\psi_0 e^{i\vec{k}\cdot\vec{r}}}{r} = \frac{\psi_0 e^{ikr}}{r} \tag{2.14}$$

Where ψ_0 is the incident wave and r is distance from the core atom. A schematic of this dissociation is shown in Figure 2.4.

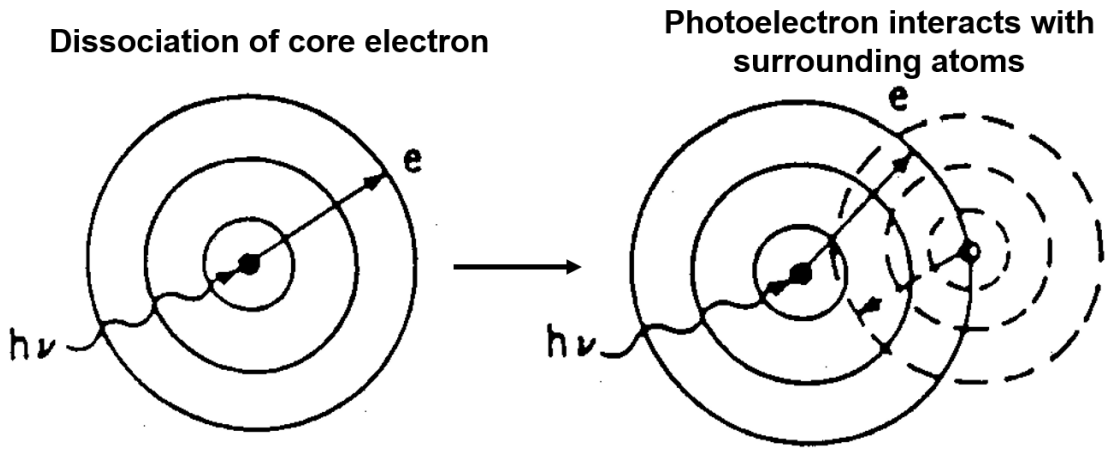

Figure 2.4 Photoelectron wave processes. After a core electron is dissociation, left, it interacts with the surrounding atoms via electron-electron scattering (right). This wave interference results in the quasi-periodic modulations observed in the EXAFS region of the absorption spectrum.

The spherical wave produced by the outgoing photoelectron interferes with the electrons in the surrounding atoms, resulting in a backscattered wave

$$\psi_{scattered}(\vec{r}) = \frac{\psi_{inc.} f e^{i(k|\vec{r}-\vec{R}|+\varphi)}}{|\vec{r}-\vec{R}|} \tag{2.15}$$

Where ψ_{inc} is the wave incident on the scattering atom, f is the scattered fraction, R is the distance travelled by the backscattered wave, and φ is a phase shift that takes into account electrostatic potential.

For the case that $\psi_{inc.} = \psi_{out.}(\vec{r} = \vec{R})$, Eq. 2.15 becomes

$$\psi_{scattered}(\vec{r}) = \frac{\psi_0 e^{ikr}}{r} \frac{f e^{i(k|\vec{r}-\vec{R}|+\varphi)}}{|\vec{r}-\vec{R}|} \quad (2.16)$$

When r = 0, the simplification of this expression is

$$\psi_{scattered}(\vec{r} = 0) = \frac{\psi_0}{R^2} f e^{i(2kr+\varphi)} \quad (2.17)$$

If we consider the total wavefunction $\psi_{tot} = \psi_0 + \psi_{scattered}$,

$$\psi_{total} = \psi_0 + \psi_{scat.} = \psi_0(1 + \frac{f}{R^2} e^{i(2kR+\varphi)}) \quad (2.18)$$

From Eq. 2.18, we can see how the interference between these two waves affects the probability of creating a core-hole, since

$$I = \psi\psi^* \propto 1 + \frac{2f}{R^2}\sin(2kR + \varphi) + \cdots \quad (2.19)$$

Where the sinusoidal term above describes the interference between incoming and outgoing electron waves. This interference effect demonstrates how nearby atoms surrounding an absorbing atom can affect the probability of creating a core hole. Note that as distance R increases, this term becomes negligible, and the quasi-periodic oscillations dampen out. This is one reason why structure can only be determined locally (within ~ 6 Å) from the absorbing atom.

The background can be subtracted from the XAFS spectrum to extract the quasi-periodic modulations as shown in Figure 2.5. Since both the pre-edge and post-edge spectrum have a $\frac{1}{E^3}$ dependence, with the exception of the post-edge modulations that make up only ~1 - 5 % of the overall absorption, the EXAFS modulations can be extracted through background subtraction using the equation

$$\chi(E) = \frac{\mu(E) - \mu_0(E)}{(\Delta\mu)} \quad (2.20)$$

Where γ is the experimental XAFS data, $\mu_0(E)$ is the fit to the post-edge (which is equivalent to the spectrum of an isolate atom, which would appear linear) and $\Delta\mu$ is the difference between fits to the pre- and post-edge regions. The data, pre-edge and post-edge fits are shown in Figure 2.7, left. The data can then be plotted in k space rather than E space through the E to k conversion according to Eq. 2.13.

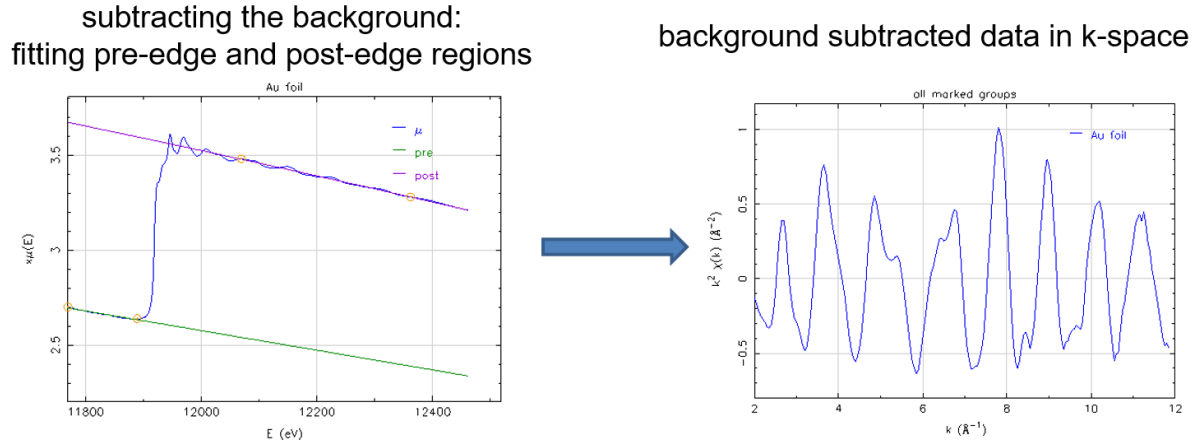

Figure 2.5 Background subtraction to extract EXAFS oscillations. After background subtraction according to Eq. 2.20, and conversion from E to k according to Eq. 2.13, the EXAFS oscillations are extracted (right).

Background subtracted k-space data, such as that shown in Figure 2.5, right, is k-weighted (multiplied by k, k^2 or k^3 as appropriate) in order to emphasize a particular region in k-space, in order to obtain an even oscillation throughout the region of interest. Generally the presence of light-scattering elements corresponds to a lower k-weighting and a heavier-scattering element corresponds to a higher k-weighting.[49] This is discussed further in Appendix B of this thesis.

Due to the quasi-periodic nature of the EXAFS oscillations as described from Eq. 2.19, the spectrum can be modeled according to

$$\chi(k) = \sum_{\Gamma}[\frac{N_{\Gamma}S_0^2F_{\Gamma}(k)}{2kR_{\Gamma}^2}e^{-2k^2\sigma_{\Gamma}^2}e^{-2R_{\Gamma}/\lambda(k)} \times \sin(2kR_{\Gamma} + \phi_{\Gamma}(k))] \quad (2.21)$$

Where Γ is the summation over the individual scattering pathways included in the model, $F_\Gamma(k)$ is the scattering amplitude, λ(k) is the mean free path for inelastic scattering of the photoelectron Φ(k) is the phase shift, which is calculated as a function of the scattering factors of the absorbing and scattering atom, and S_0^2 is the amplitude reduction factor. Degeneracy (or number of neighbors in a given shell of the same type) (N_Γ), interatomic distance (R_Γ), energy shift parameter (E_0), and mean-squared disorder (σ_Γ^2), which includes contributions from structural and thermal disorder to the Debye-Waller factor, are all generally fitting parameters in the model.[47, 50-52] Extraction of these parameters provides knowledge of material structure at the atomic scale, providing valuable insight into their chemical behavior. Further details concerning XAFS data reduction and modeling analysis are provided in Appendix B.

Chapter 3: How Ag Nanospheres are Transformed into AgAu Nanocages

3.1 Abstract

Bimetallic hollow, porous noble metal nanoparticles are of broad interest for biomedical, optical and catalytic applications. The most straightforward method for preparing such structures involves the reaction between $HAuCl_4$ and well-formed Ag particles, typically spheres, cubes, or triangular prisms, yet the mechanism underlying their formation is poorly understood at the atomic scale. By combining *in situ* nanoscopic and atomic-scale characterization techniques (XAFS, SAXS, XRF, and electron microscopy) to follow the process, we elucidate a plausible reaction pathway for the conversion of citrate-capped Ag nanospheres to AgAu nanocages; importantly, the hollowing event cannot be explained by the nanoscale Kirkendall effect, nor by Galvanic exchange alone, two processes that have been previously proposed. We propose a modification of the bulk Galvanic exchange process that takes into account considerations that can only occur with nanoscale particles. This *nanoscale* Galvanic exchange process explains the novel morphological and chemical changes associated with the typically observed hollowing process.

3.2 Introduction

Noble metal nanoparticles are of great interest due to their unusual properties that differ from their bulk counterparts.[39, 53-54] Hollow nanoparticles are of particular interest due to their ability to encapsulate molecular moieties,[55-56] as well as the unique optical properties that emerge from their geometry.[57-59] Bimetallic particles are interesting for their catalytic[60-62] and optical properties.[63] Bimetallic AgAu nanocages synthesized from Ag sacrificial templates through titration with an Au^{3+} salt[64-67] are widely used in photothermal medical applications [59, 68-71] and catalysis,[72-75] as well as in metallic corrosion studies.[76] This general reaction has been used to prepare a wide

variety of hollow particles regardless of geometry.[64, 77-83] In addition, variants of this redox process have been used to prepare bimetallic particles consisting of AgPt,[84-85] AgPd,[85] AuCu,[86] CuPd,[87] CuPt,[87-88] PdPt,[61] CoAu,[89] and PtCo.[90] Despite this versatility and utility, the mechanism underlying these reactions remain elusive.

The reaction converting Ag nanoparticles to Au nanocages is commonly referred to as "Galvanic exchange":

$$3Ag_{(s)} + AuCl^-_{4(aq)} \rightarrow Au_{(s)} + 3Ag^+_{(aq)} + 4Cl^-_{(aq)} \quad (3.1)$$

Specifically, at a surface, the reaction proceeds because the standard reduction potential of the AuCl4-/Au redox pair (0.99 V vs. the standard hydrogen electrode (SHE)) is higher than that of the Ag+/Ag redox pair (0.80 V vs. SHE) (Figure 1, top). The template material becomes a uniformly-porous network as Ag atoms are removed from the template in a 3:1 Ag:Au ratio and vacancies coalesce to reduce surface energy. Due to differences in Ag-Ag, Ag-Au and Au-Au bond energies, the created alloy exhibits local phase segregation with Ag and Au-rich regions.[91] While some have attributed the nanoparticle hollowing to the above described bulk Galvanic exchange effect,[16, 65, 92-94] others have attributed the hollowing process to the Kirkendall effect (Figure 1 bottom).[77, 80, 82, 95-98] In the Kirkendall effect, voids are formed due to a difference in the diffusion rate of the core atoms outward, which exceeds the rate of the added secondary species inward into the nanoparticle core.[15, 98] For the case of AgAu nanoparticle formation, according to this explanation, Ag diffuses more quickly into Au than Au into Ag resulting in a uniform, homogeneous AgAu shell surrounding a hollow core. In this process, no Ag is lost from the nanoparticle with Au addition, resulting in an overall increase in the number of atoms present in the nanoparticle, as seen for other model systems exhibiting the nanoscale Kirkendall effect.[99-101]

Our present study aims to resolve this controversy and elucidate the reaction pathway with atomistic detail.

We explore the conversion from citrate-capped Ag nanospheres to AgAu nanocages and find that the hollowing within the nanoparticles cannot be explained by the nanoscale Kirkendall effect nor Galvanic exchange alone. This conclusion is reached through in-depth nano and atomic scale characterization of the nanoparticles at various stages in their transformation. Overall, we propose a modification of the bulk Galvanic exchange process that takes into account considerations that can only occur with nanoscale particles. We refer to this modified process as "nanoscale Galvanic exchange".

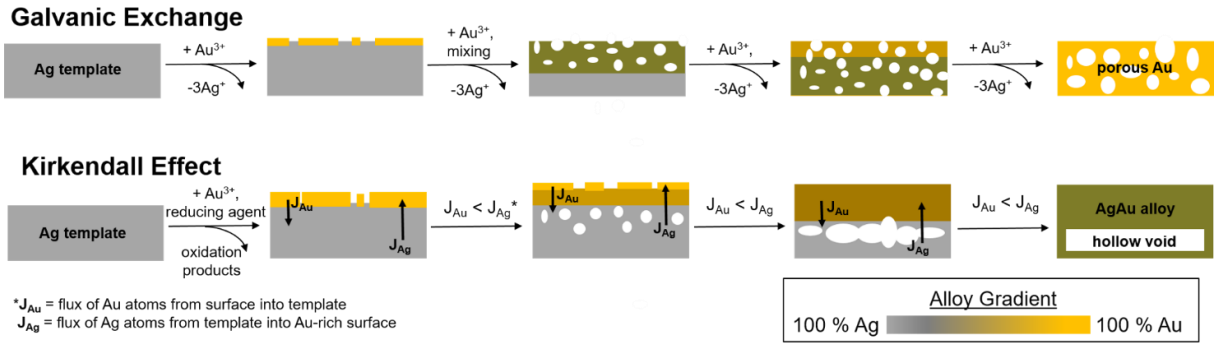

Figure 3.1. Galvanic exchange and Kirkendall effect. Two hypothesized bulk processes used to explain the formation of AgAu nanocages from Ag nanoparticle templates include Galvanic exchange (top) and the Kirkendall effect (bottom)

Before going further, it is important to consider previous studies that provide insight into this particular nanoparticle transformation at the nanoscale. Electron microscopy studies[16, 39, 59, 92, 102] revealed formation of a hollow, porous product and minimal growth of the template particle

attributed to an initial Au surface monolayer formation. Pit formation at the surface provides an active site for Ag oxidation. With additional $HAuCl_4$ incorporation, UV-vis spectroscopy revealed a shift to longer wavelengths in the localized surface plasmon resonance (LSPR) peak throughout the visible regime and into the near-IR, [39, 59] which is expected for a change in morphology towards a hollowed-out structure.[95] The aforementioned features observed are in line with what would be expected for Galvanic exchange, however void formation is observed, which is a structural feature associated with the Kirkendall effect,[99-101] and not with bulk Galvanic exchange, where a uniformly porous network is formed.[91, 103] Electron tomography of single nanoparticles was used to track 3D void and pit formation.[104] Reaction kinetics of void formation were investigated using dark-field scattering,[105] and indicated an abrupt transition into a hollow nanocage structure. Supporting theoretical work[105] concluded that this abrupt transition was due to the energetic favorability of vacancy coalescence into a central void to minimize particle surface area. This provides an alternative explanation for the nanoparticle hollowing process based on nanoscale geometry.

In each of the aforementioned studies, the transformation from Ag nanoparticles to AgAu nanocages was referred to as “Galvanic exchange”, yet there is no atomic-scale information used to inform this conclusion. To this end, we formulate a series of questions that will serve as a foundation for elucidating the chemical pathway and will be addressed in detail through a combination of literature findings and new experimental results: 1) How does the 3D morphology of the nanoparticles evolve as the reaction progresses? 2) How is the nanoparticle reaction initiated? 3) Does the total number of atoms within the nanoparticle increase or decrease? Is there a 3:1 Ag:Au exchange ratio? 4) Is a homogeneous alloy or is local segregation observed? and 5) What is the origin of the nanoparticle hollowing process?

Questions 1 and 2 pertain to nanoparticle structure on the nanometer length scale. In part, these questions have already been answered through use of electron microscopy and tomography.[16, 39, 59, 92, 102, 104] Yet due to a lack of previous atomic-scale characterization, questions 3-5 remain unaddressed. Our experimental contribution to this work fills in this gap in atomic-scale characterization by use of Å-wavelength X-rays. Specifically, we use X-ray absorption fine structure (XAFS) to locally track the atomistic changes as a function of reaction progression. These changes are then correlated with changes in the globally averaged morphological parameters derived from small angle X-ray scattering (SAXS) measurements.

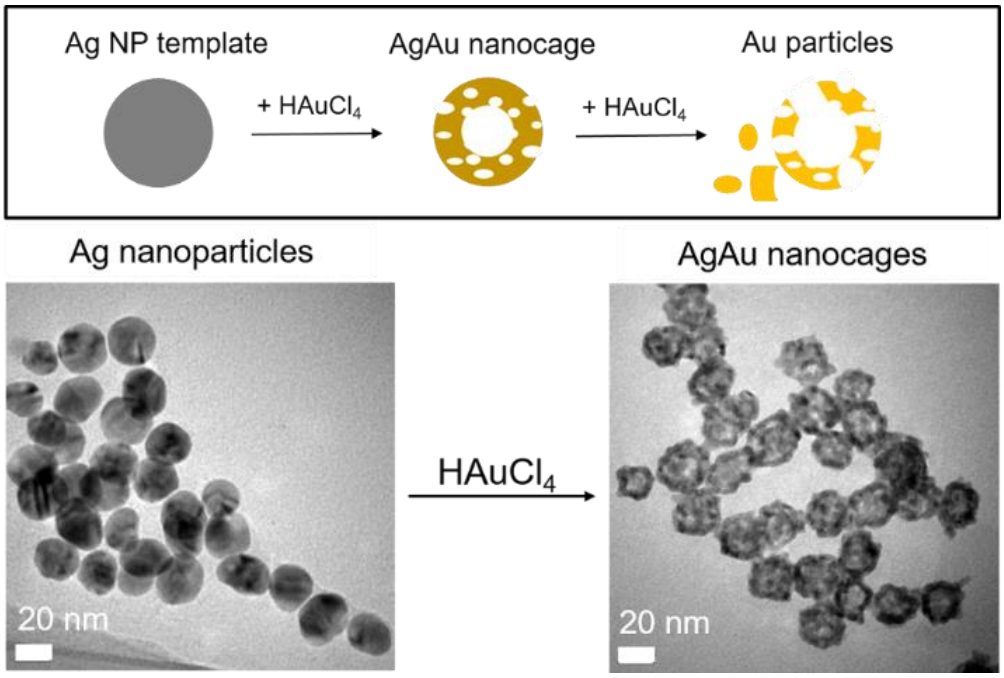

Figure 3.2 Synthesis transformation reaction schematic. Polycrystalline citrate-capped Ag nanoparticles (scale bar = 20 nm) starting at room temperature (left) are transformed into AgAu nanocage of a hollow and porous nature (right, 62.9 at% Au) with increasing addition of 0.1 mM

$HAuCl_4$. A cartoon representation of the synthesis products is shown (top). As additional $HAuCl_4$ is added, the particles lose their structural integrity.

To rule out surface-facet effects on the transformation process as hypothesized elsewhere,[16, 79] citrate-capped polycrystalline Ag nanospheres[106] were chosen as the starting nanoparticle template. These have been previously used to make AgAu nanocages and the reaction has been reported to proceed via Galvanic replacement. [105, 107-109] $HAuCl_4$ was titrated in varying amounts to an aqueous solution of Ag nanosphere templates and the resulting transformed nanoparticles were studied as a function of reaction stage (Figure 3.2). Through characterization with conventional electron microscopy and UV-vis spectroscopy in combination with XAFS, X-ray fluorescence (XRF) and SAXS, local and global atomic and nanoscale trends can be explored in depth, as evidenced by previous studies of Ag and Au alloy nanoparticles using an x-ray focused approach.[42, 110-112] Thus, our characterization toolbox provides us with structural insight into the previously posed questions and enables us to propose a plausible reaction pathway for the transformation from citrate-capped Ag nanospheres to AgAu nanocages.

3.3 Methods

For each of the methods described below, more details can be found in Appendix A.3.

3.3.1 Synthesis

Transformation of Ag nanoparticles into hollow AgAu nanocages was performed using a variation on previous methods.[113] $HAuCl_4$ (Sigma-Aldrich) was dissolved in NANOpure™ water (18.2 MΩ ionic purity) to a concentration of 0.1 mM in solution. This solution (the source of Au^{3+} ions) was then titrated into a vial of 3 pM 18 nm diameter citrate capped silver spheres in aqueous 2 mM sodium citrate solution (Ted Pella) using a syringe pump at a rate of 20 ml/hr at room temperature. $HAuCl_4$ solution was added in different amounts to equal volumes of Ag particles

in order to halt the reaction at different stages of transformation. Transformed particles were then isolated through high-speed centrifugation.

3.3.2 UV-vis spectroscopy

UV-Vis Spectroscopy scans of samples in 1 ml NANOpure^{TM} water were taken using a Cary 5000 UV-vis spectrophotometer across the range of 200-1000 nm at a 1 cm path length.

Inductively Coupled Plasma- Mass Spectroscopy (ICP-MS). Au content in the nanoparticles and supernatant was analyzed using a Thermo Fisher X Series II ICP-MS system at the QBIC Facility at Northwestern University (NU). Particles were dissolved in aqua regia for 24 hours before measurement. Au content in ppb was determined through comparison against a standard curve generated using Au ICP standard (Sigma Aldrich). An internal In standard was also used.

3.3.3 Electron microscopy

Using the NU EPIC Facility, samples were prepared for characterization with electron microscopy by dropcasting on a carbon-coated grid. TEM images were collected using a Hitachi H-8100 TEM at 200 keV. STEM images and EDX maps were collected using a Hitachi HD-2300 Dual EDS S/TEM at 200 keV. Drift correction was used for EDX mapping in order to improve spatial resolution.

3.3.4 X-ray scattering

Small angle X-ray scattering (SAXS) measurements were performed using 10.00 keV X-rays at 5ID-D located at the Advanced Photon Source (APS) at the Argonne National Laboratory (ANL). This is part of the NU operated DND-CAT Facility. The aqueous nanoparticle dispersions were placed in a quartz capillary tube (inner diameter ~ 1.5 mm), which was embedded in a flow cell.

The measured intensity profile $I(q)$ is reasonably described by assuming a spherical core-shell model for the form factor [$F(q)$] of the Ag and Ag/Au bimetallic nanoparticles.[114] Specifically,

$$F(q) = \frac{4\pi}{q^3}[(\rho_c - \rho_s)\{\sin[qR_c] - qR_c\cos[qR_c]\} + (\rho_s - \rho_{sol})\{\sin[q(R_c + T_s)] - q(R_c + T_s)\cos[q(R_c + T_s)]\}] \quad (3.2)$$

Here, R_c is the radius of the hollowed-out core for the Ag/Au alloy nanoparticles. For unalloyed pure Ag nanoparticles, R_c = 0. The electron density ρ_c for the hollowed-out core is assumed equivalent to the water solvent ($\rho_c = \rho_{sol}$ = 334 e^-/nm^3). T_s is the radial thickness of the metallic shell, ρ_s is the electron density for the shell, and

$$I(q) = \frac{N}{V} r_e^2 \langle [F(q)]^2 \rangle + bkg \quad (3.3)$$

To take into account the polydispersity (PD) of nanoparticles, the scattered intensity from an isolated nanoparticle $[F(q)]^2$ is averaged over a Schulz distribution[115] for particle sizes to yield $\langle [F(q)]^2 \rangle$. Here, the ratio of core radius and the shell thickness [R_c/T_s] is assumed to be a constant for all the Ag/Au particles in a given solution. r_e is the classical electron radius and N/V is the number density of nanoparticles in the solution. The constant *bkg* represents any additional background scattering apart from the quartz capillary and water.

3.3.5 XAFS

XAFS spectra at the Au L_3 edge and Ag K edge (11.919 keV and 25.514 keV, respectively) were collected at MR-CAT station 10BM-B located at the APS. Energy scans were taken over a range from -150 eV to 600 eV with respect to the Au or Ag absorption edge using a Si(111) monochromator. XAFS spectra were collected in X-ray fluorescence (XRF) mode using a four-element Vortex Silicon drift-diode (SDD) detector, calibrated with an Au or Ag metal foil standard. Samples were concentrated via centrifugation to micromolar concentrations of Au/Ag atoms and placed in 3 mm inner diameter quartz capillary tubes.

XAFS data was processed using ATHENA and ARTEMIS software, part of the IFEFFIT package.[116] The extended XAFS (EXAFS) regions of the spectra were modeled according to the EXAFS equation:[50-51, 52, 47]

$$\chi(k) = \sum_{\Gamma}[\frac{N_{\Gamma}S_0^2F_{\Gamma}(k)}{2kR_{\Gamma}^2}e^{-2k^2\sigma_{\Gamma}^2}e^{-2R_{\Gamma}/\lambda(k)} \times \sin\left(2kR_{\Gamma} + \phi_{\Gamma}(k)\right) \quad (3.4)$$

Where Γ is the summation over the individual scattering pathways included in the model, *k* is the photoelectron wavevector, $F_\Gamma(k)$ is the scattering amplitude, $\lambda(k)$ is the mean free path of inelastically-scattered photoelectrons and $\Phi(k)$ is the phase shift, which is calculated as a function of the absorbing and scattering atom. S_0^2, the amplitude reduction factor, was set to the value extracted from fitting a bulk Au or Ag foil as applicable. This enables a more accurate determination of the coordination number.[52] Degeneracy (N_Γ), inter-atomic distance (R_Γ), energy shift parameter (E_0), and mean-squared disorder ($\sigma_\Gamma 2$), which includes contributions from structural and thermal disorder (Debye-Waller factor),[50] were adjusted to determine the best fit model.

3.3.6 X-ray fluorescence

X-ray fluorescence spectra (Figure A3.3) were obtained at APS sector 10BM-B using a Vortex four element silicon drift diode detector. Spectra were collected at 26.014 keV (above the Ag K edge energy, 25.514 keV) to determine the Ag-to-Au atomic ratio from the areas under the Au L alpha and Ag K alpha fluorescence lines, with fluorescence peak fits using a Gaussian function. Elemental XRF cross sections, detector efficiency, and attenuation due to solvent media were taken into account in determining the Ag/Au ratio.

3.4 Results

3.4.1 How does the 3D morphology of the nanoparticles evolve as the reaction progresses?

TEM and UV-vis spectroscopy confirm previously observed morphological trends, showing that results from our study are relevant to prior work.[16, 39, 59, 92, 102] These morphological changes are correlated to the amount of Au incorporation (in atomic %) into the NPs determined by XRF (Figure 3.3, bottom-right).

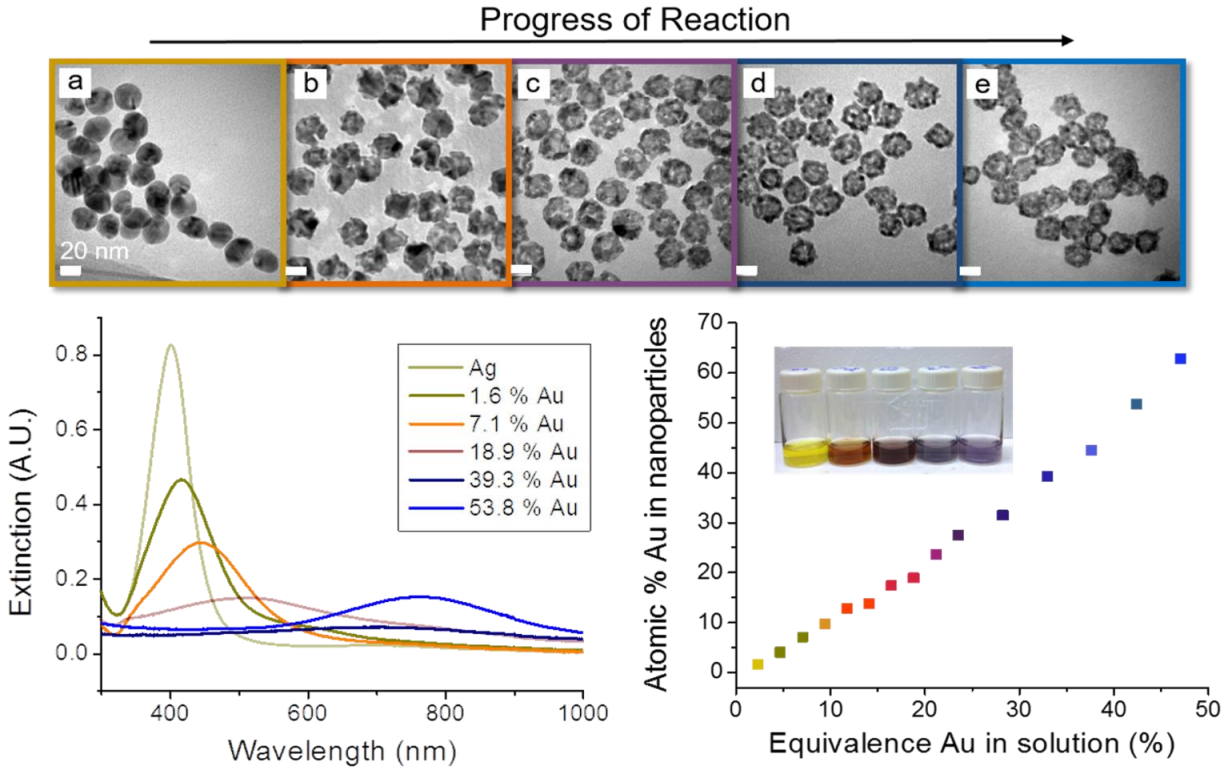

Figure 3.3. Nanoparticle products as a function of $HAuCl_4$ addition. (Top) TEM images from pure citrate-capped Ag NPs (a) to (b) 4.0 %, (c) 9.8 %, (d) 27.5 % and (e) 62.9 % Au as determined by XRF. All scale bars are 20 nm. (bottom, left) UV-vis spectra reveal LSPR peak shifts to longer

wavelengths with additional $HAuCl_4$ (right, inset). (bottom, right) Atomic % Au in the nanoparticles as determined by XRF vs. equivalence Au added into the reaction solution.

TEM (Figure 3.3, top) shows that the initial quasi-spherical Ag nanoparticles are ~ 20 nm in diameter. Pits form at the nanoparticle surface and a hollow center appears. As additional $HAuCl_4$ is added, the interior void in the nanoparticle grows as the shell porosity increases, resulting in hollow and porous nanocages with 62.9 % Au incorporation. As observed previously, above ~ 65 % Au, the particles lose their structural integrity and deteriorate into small, irregular particles.[16, 117] UV-vis spectroscopy (Figure 3, bottom-left) shows that the LSPR peak red-shifts as a function of $HAuCl_4$ addition. This allows for tunable optical properties throughout the visible regime.

SAXS data and model fits based on Eq. 3.2 are shown in Figure A3.6. This analysis enables tracing 3D hollow void formation and shell thickness evolution in a globally statistical manner that is summarized in Figure 3.4. We observe that the hollow core radius increases in size until ~25 % Au, while the shell thickness decreases. Above 25 % Au, we find that these geometrical parameters remain relatively constant, while the porosity of the shell (based on TEM, Figure 3.3, top) continues to increase. Thus, after a critical void size is reached, particle transformation with continued $HAuCl_4$ addition occurs only at the atomic scale. SAXS and local (TEM) analysis of nanoparticle size (Figure A.3.10) both show that within error, the nanoparticles do not change their overall size from the original template structure. This observation is inconsistent with a hollowing process based on the Kirkendall effect, where an increase in size would be expected,[99-101] Figure 3.1.

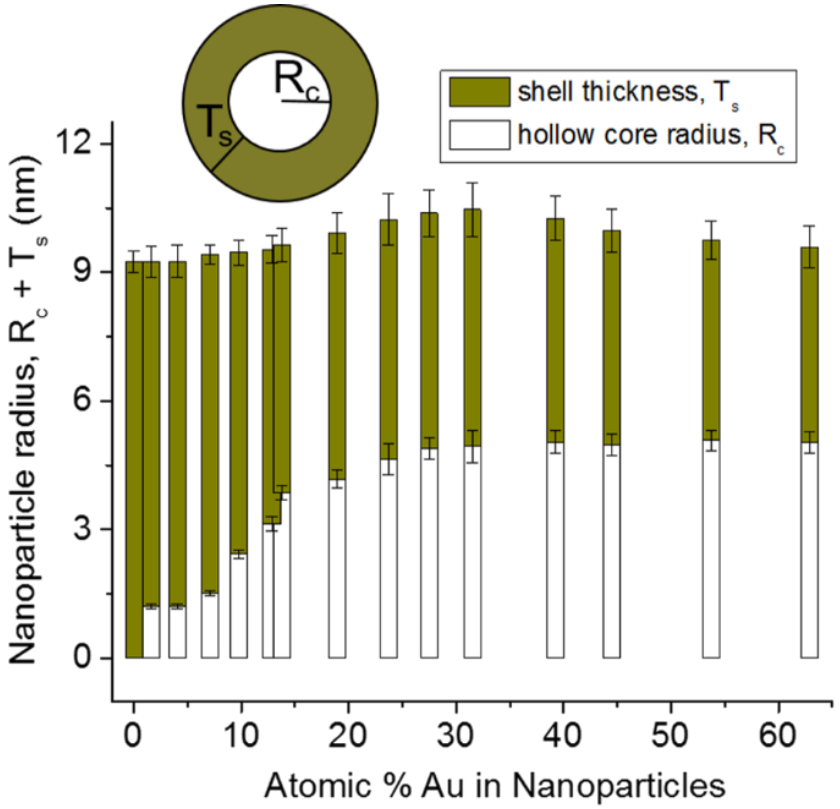

Figure 3.4. Nanoparticle morphological trends from SAXS modeling, which determines the ensemble averaged inner and outer radii of the hollowed-out NPs. With increasing Au incorporation, the shell thickness (gold) decreases, while the radius of the core (white) increases, as additional Ag atoms are removed from the core. The overall radius of the particle does not significantly change.

3.4.2. How is the nanoparticle reaction initiated?

TEM images early in the reaction (Figure 3.3, top) show apparent pits and a non-uniform structure at the nanoparticle surface. This suggests that transformation has occurred at the nanoparticle surface before voids and porosity are observed in the interior. It has previously been suggested that Au(0) coats the nanoparticle surface before transformation occurs.[16, 92] Our ICP and

XRF data at the initial 1.6 % Au shows a Ag:Au replacement ratio (Table A3.1) that is less than unity (0.5 ± 0.1), indicating the addition of 2 Au atoms onto the nanoparticle surface for every Ag atom removed. This means that more Au atoms are added than Ag atoms replaced. If the Au was depositing onto the surface at this initial stage, then the 1.6 % Au and SAXS-determined 18 nm diameter NP would correspond to 0.8 monolayers of Au incorporated in the NP surface atomic layer, assuming bulk-like atomic densities. This observation suggests that at this stage, Ag cannot be the sole reducing agent.

3.4.3 Does the total number of atoms within the nanoparticle increase or decrease?

Is there a 3:1 Ag:Au exchange ratio? Nanoparticle hollowing and increasing porosity suggest that the total number of atoms within the nanoparticles decrease with increasing $HAuCl_4$ addition and this is confirmed through calculation of the Ag:Au exchange ratio (Table A3.1). While after initial Au monolayer deposition the ratio increases to exceed 1:1, meaning an overall loss in the number of atoms within the nanoparticle, the average exchange ratio is significantly less than 3:1. Specifically, at its maximum with 7 % Au incorporation, the exchange ratio reaches the expected 3:1, but decreases quickly and is closer to 2:1 until reaction completion. This also is consistent with the conclusion that more than one reducing agent must be involved in the process, and Galvanic replacement cannot exclusively be used to describe this process.

3.4.4. Is a homogeneous alloy or local segregation observed?

EXAFS analysis reveals differences in the phase shifts and scattering amplitudes of the backscattered photoelectrons from Ag and Au atoms as a function of wavevector k, which enables extraction of Ag-Au and Ag-Ag as well as Au-Ag and Au-Au local structure (see Figure A3.14). EXAFS is a bulk rather than a surface technique, and quantities extracted from analysis are representative of the global average particle structure. As expected, the Au-Au and Ag-Au

coordination increase while Ag-Ag and Au-Ag decrease with increasing Au incorporation (Figure 3.5). Yet if we compare the coordination numbers with those theoretically expected for a homogeneous alloy, (Figure 3.5 dashed lines), we find that there is significant deviation. In particular, in a particle that is 62.9 % Au, the Ag-Ag coordination exceeds Ag-Au. This observation is confirmed in a model-independent manner by observing that Ag K edge XAFS spectra from nanoparticles with 62.9 % Au more closely resembles the spectrum from pure Ag nanoparticles than that from Ag surrounded by Au (Figure 3.6a). This suggests that rather than forming a homogeneous alloy, Ag-rich and Au-rich clusters of atoms are retained throughout the transformation. Such local segregation is expected for bulk systems[91] and has previously been observed in single-particle electron tomography studies of anisotropic nanocages.[104] The size of these clusters was estimated from the amount of reduction in EXAFS coordination numbers compared to bulk,[118] and found to be slightly below 1 nm in the AgAu nanocages (Figure A3.5). The nanoscale nature of this phase segregation was investigated using EDX mapping (Figure A3.4). We find that within the resolution of EDX (~2 nm), Ag and Au are not segregated on this longer length scale. This agrees with EXAFS results and reveals that while the particles are alloyed at the nanoscale, they are compositionally segregated on the atomic scale.

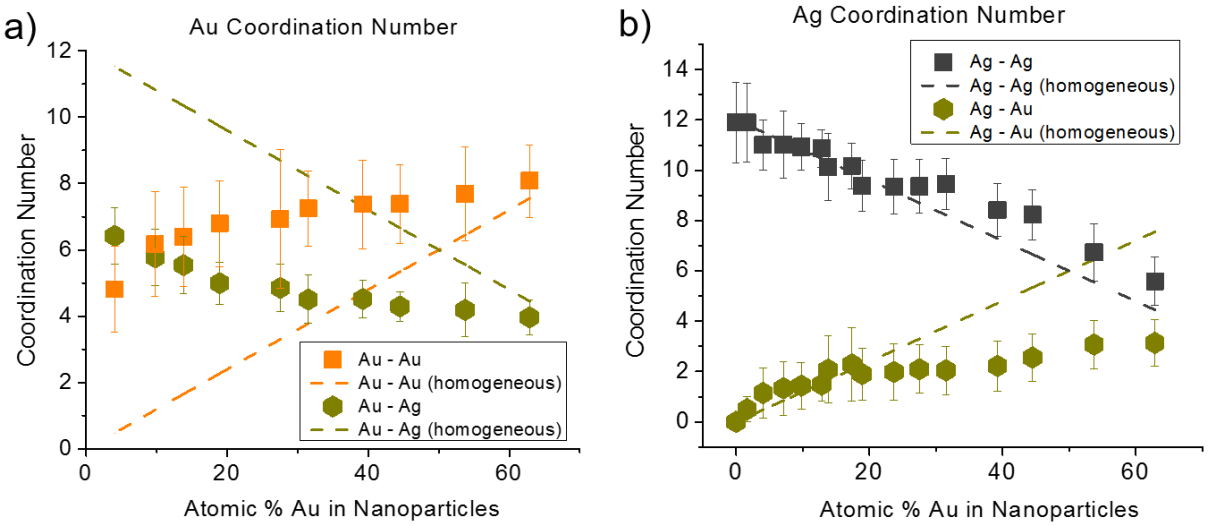

Figure 3.5. Nanoparticle coordination number trends from EXAFS modeling. a) Coordination numbers determined from Au L3 edge XAFS. b) Coordination numbers determined from Ag K edge XAFS. Dashed lines represent the theoretical coordination numbers that would be expected from a homogeneous alloy structure.

Coordination numbers extracted from EXAFS also provide insight into the nanoparticle surface structure. Figure 3.6b shows that above 4 % Au, the overall Au coordination number remains at ~12, as would be expected for fully coordinated atoms, the coordination number for Ag decreases with increasing nanoparticle porosity throughout the transformation. This suggests that spatially, more Ag rather than Au atoms sit in undercoordinated surface sites, even in Au-rich particles.

3.4.5. What is origin of the nanoparticle hollowing process?

Previous EXAFS studies of the nanoscale Kirkendall hollowing process, which occurs in oxide and phosphide nanoparticles,[99-100] revealed formation of an initial phase in nanoparticle

surface layers, after which the diffusion rates of species changed. This leads to faster out-diffusion of the template element than inward diffusion of the secondary element, resulting in nanoparticle hollowing and formation of a new phase, with an entirely different local environment. In our present study, however, the results are not in line with the Kirkendall-system structural changes.

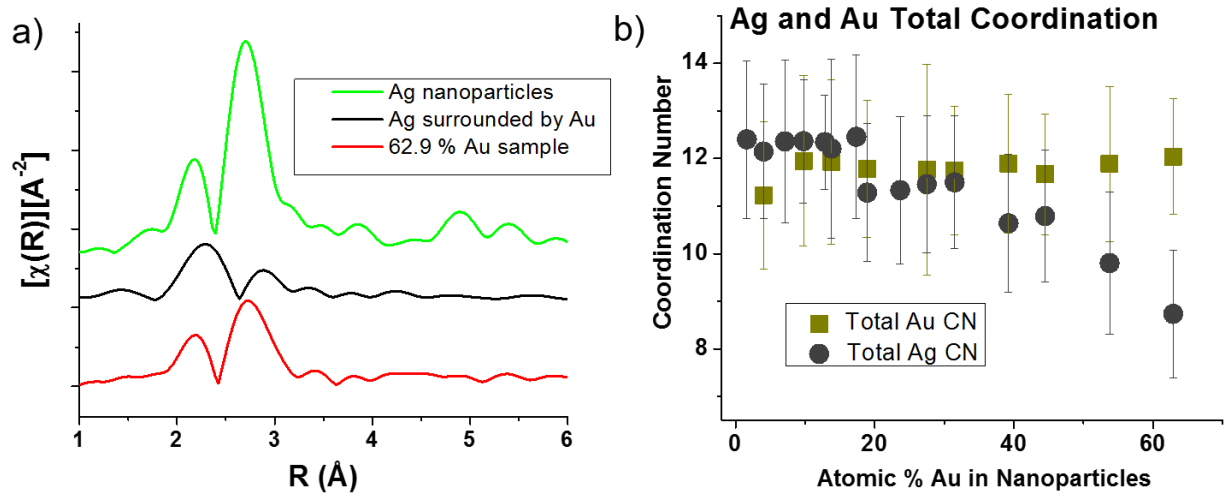

Figure 3.6. EXAFS informs Ag distribution in Ag/Au NPs. a) Ag K-edge Fourier inverted XAFS data for the starting Ag NPs, transformed NPs with 62.9% Au, and a reference sample of Au NPs with trace Ag. b) From Ag K and Au L3 edge EXAFS, the total Ag and Au coordination numbers within the particles as a function of transformation.

EXAFS local structural changes show a consistent trend; Ag-Au and Au-Au coordination numbers increase linearly while Ag-Ag and Au-Ag coordination numbers decrease linearly (Figure 3.5). There is no abrupt change in local structure observed. In addition, Kirkendall hollowing induces an increase in the overall particle size, whereas this is not observed by either TEM or SAXS for our system (Figure A3.10). Rather, our results are in agreement with a previous study which proposed coalescence of vacancies into a critical void in order to reduce the overall surface

area in the nanoparticles.[105] TEM images from particles early in the transformation (Figure 3.3, top) show that either particles exhibit a void or they do not. The void size observed in these particles from SAXS (2 nm, Figure 3.4) is also in good agreement with the critical void size observed from the earlier dark-field scattering study.[105] All of this supports the vacancy-coalescence hollowing pathway previously proposed.[105]

3.5 Discussion

3.5.1 Comparison to Galvanic Exchange and the Nanoscale Kirkendall Effect

Our results confirm many of the characteristic structural changes that would be expected for the case of Galvanic exchange. For example, TEM confirms a porous product, with local Ag and Au segregation (XAFS). In addition, TEM and SAXS results show that the size of the particles remains nearly constant throughout the entire process. However, there are two key deviations from bulk Galvanic exchange: 1) nanoparticle core hollowing is observed rather than the uniformly-porous network that is observed for a bulk film,[91] and 2) while the absolute number of atoms within the nanoparticle does indeed decrease, the Ag:Au exchange ratio deviates substantially from the expected 3:1 ratio.

On the other hand, we do not observe changes in the nanoparticle structure, one would associate with the nanoscale Kirkendall effect. Notably, based on SAXS and TEM analysis, particle size remains nearly constant, and XRF confirms a decrease rather than an increase in the total number of atoms incorporated into the nanoparticle. Our results therefore suggest that the observed hollowing is not the result of the nanoscale Kirkendall effect.

3.5.2 A Modified Pathway: Nanoscale Galvanic Exchange

In order to propose a reaction pathway, we consider deviations the system exhibits from bulk Galvanic exchange. First, nanoparticle hollowing must be accounted for. In bulk films, it is observed that vacancies coalesce to form pores, resulting in a uniformly porous network rather than one larger void.[91] The SAXS results agree with those from a previous study that observe vacancy coalescence into a critical void and describe this process in detail.[105] This, in combination with the lack of structural features expected for Kirkendall hollowing, provides support for the vacancy coalescence hypothesis.[105] Coalescence of vacancies into a hollow void reduces overall surface area in particles for enhanced stability. This variation only occurs on the nanoscale, where particles contain a high surface area to volume ratio.

Second, one must explain why the exchange ratio of Ag:Au is significantly less than 3:1 that defines Galvanic exchange. This implies an additional Au reducing agent. rather than Ag etchant must be contributing; as the etchant would cause the ratio to exceed 3:1. Sodium citrate is known to act as a reducing agent for Au^{3+},[119-120] and in this case serves as the only reasonable electron source for Au^{3+} reduction other than Galvanic exchange.[121]

The concentration of citrate present in the reaction solution (2 mM) provides excess electrons (1.2×10^{19}) compared with the number needed to reduce all Au^{3+} added to solution for the 62.9 % Au sample (5.6×10^{15}), making this plausible simply from an electron counting standpoint. In addition, the high surface energies due to a high number of coordinatively unsaturated surface atoms, lowers the potential for Au reduction on the nanoparticle surface.

Au deposition onto surface sites along with Galvanic exchange, with both Ag and citrate acting as reducing agents, explains why the exchange ratio of Ag:Au is less than the expected 3:1 ratio if it was purely galvanic exchange. It should be noted that in systems where an alternative

particle stabilizing agent (other than citrate) is used or an external reducing agent is introduced, the exchange ratio may differ from those reported here. In fact, it has been previously demonstrated that Au can be deposited on Ag by overcoming the Galvanic exchange pathway through the use of a strong reducing agent such as ascorbic acid[122-123] or by purposefully controlling reaction kinetics even in the case of citrate capped Ag nanoparticles.[120] It should also be noted that anisotropic particles may also induce deviations from the reaction pathway observed in this study due to the introduction of surface-facet specific processes previously proposed. [16, 79] Nevertheless, our study provides unique insights into the transformation of citrate-capped Ag nanospheres into AgAu nanocages, as summarized below.

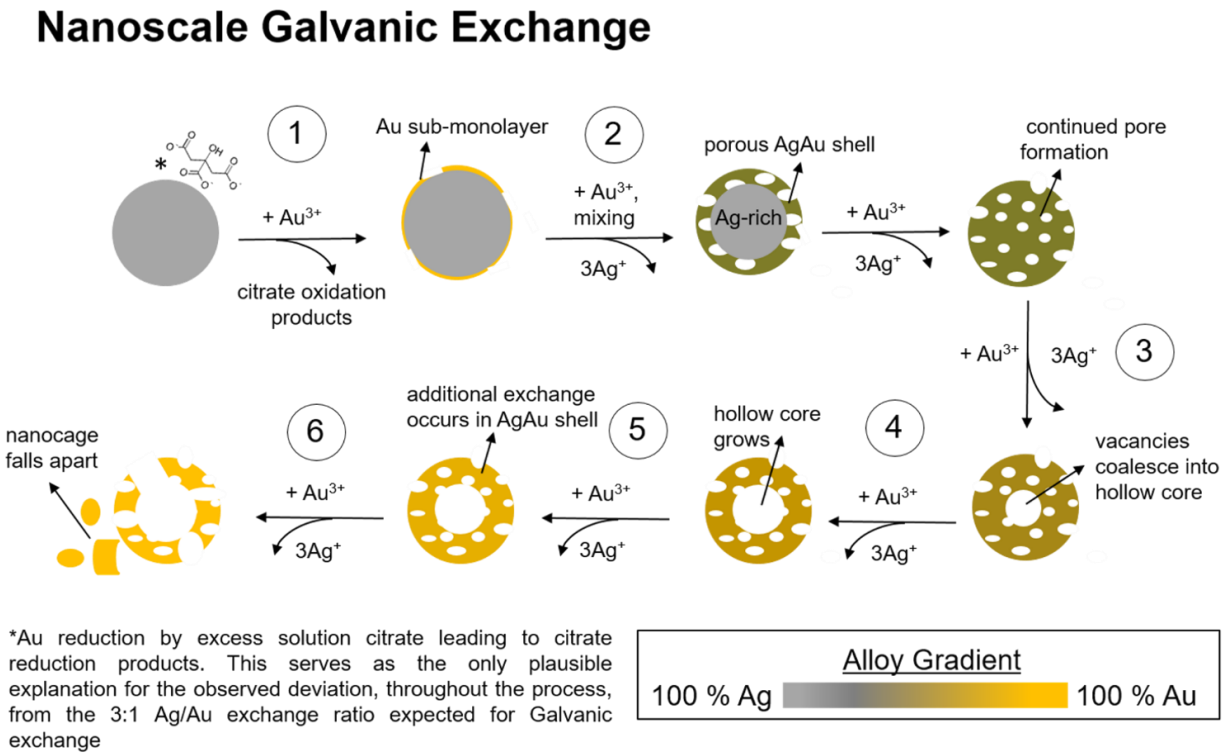

Figure 3.7 Schematic of the proposed nanoscale Galvanic exchange pathway. Starting with Ag nanospheres (top-left), the nanoparticles transform into AgAu nanocages (bottom-left). Alloy composition is shown in a gradient from Ag (gray) to Au (goldenrod). The included numbers reflect the steps in the process outlined in the text.

Through the characterization of the system at both the nanometer and atomic length scales, a plausible reaction pathway can be proposed. Since deviations from bulk Galvanic exchange can be explained as a result of the nanoparticle synthetic environment and high surface area to volume ratio, we propose that the transformation from Ag nanoparticles to Au nanocages proceeds via nanoscale Galvanic exchange (Figure 3.7). The process occurs via six key steps. First, $HAuCl_4$ addition to the polycrystalline Ag nanospheres results in deposition of an Au surface monolayer via citrate reduction of the Au^{3+} on the catalytic Ag particle surface. Second, as additional $HAuCl_4$

is introduced into solution, Galvanic exchange between Ag and Au occurs, resulting in Ag replacement with Au, with concomitant Au deposition via citrate reduction, since in the case of citrate-capped Ag particles, citrate acts as an additional source of Ag reduction. Extraction of more Ag than replacement by Au results in vacancy formation in the particle interior as Ag atoms are removed. Third, at a critical concentration of vacancies formed from unequal atomic replacement, spontaneous central void formation from coalesced vacancies in the nanoparticle becomes energetically favorable, resulting in a hollow core. Fourth, shell thickness deceases while hollow core radius increases with additional exchange. Surface rearrangement occurs such that Ag remains the dominant surface species due to the lower surface energy of Ag vs. Au[124] and facilitates additional exchange. Fifth, as the transformation continues, a bimetallic nanoparticle with locally segregated Ag and Au regions rather than a homogeneous alloy forms. Finally, transformation continues until the nanoparticle loses its structural integrity above ~65 % Au.

3.6 Conclusion

In conclusion, we investigated the key chemical steps responsible for the transformation of citrate-capped Ag nanoparticles into AgAu nanocages in the presence of $HAuCl_4$ and sodium citrate. To this end, we used a combination of local and ensemble average characterization tools both at the nanoscale and atomic scales in order to probe the reaction as a function of $HAuCl_4$ addition. Our findings suggest that that the hollowing process cannot be explained by the nanoscale Kirkendall effect; indeed, the structural features observed during the transformation are not in line with what would be expected for Kirkendall hollowing. Rather, we find that the pathway resembles bulk Galvanic exchange, but with key differences; namely, the formation of a hollow void and the deviation from a 3:1 exchange ratio of Ag:Au, a consequence of citrate in addition to Ag playing a role in the reduction process. The atomic scale structural details elucidated in this study may also

provide insight into how these particles can be used in applications where such structure is critically linked to activity, including catalysis[125] and drug delivery.[59]

3.7 Proposed future work

First, in considering how the proposed mechanism for nanoscale Galvanic exchange could be further evaluated, by using a stabilizing agent other than citrate, it may be considered in a follow-up study whether the 3:1 exchange ratio expected from bulk Galvanic exchange is achieved. This would verify whether or not this deviation from the 3:1 exchange ratio solely results from the capability citrate to act as an additional source of Au^{3+} reduction besides Ag^{+} or if another explanation is required. This may be a complicated problem, however, in that changing the solution environment from using an alternative species my cause additional variables to consider.

Additionally, since from this work it was determined that Ag is the primary surface species, even in Au-rich AgAu nanocages, disulfide functionalization,[126] as has previously been used for Ag nanoparticles, could be applied to preferentially attached DNA to the nanocage surface. Three applications of DNA-functionalized AgAu nanocages are proposed below.

3.7.1 Optical properties of AgAu nanoparticle superlattices

It has been determined that the arrangement of Ag and Au nanoparticles in DNA-NP superlattices greatly affects their optical behavior.[127] Using AgAu nanocages, which have tunable optical properties throughout the visible regime, depending on the reaction stage, would introduce unprecedented tunability into these systems. In addition, by combining AgAu hollow nanocages with solid Ag or Au nanoparticles would also introduce a geometric parameter to investigate in these systems.

3.7.2 Investigation of molecular diffusion kinetics of Ag DNA-NP superlattices

In recent years, the Mirkin group has developed methods to synthesize single-crystal faceted DNA-NP superlattices with well-defined facets.[128] It is unclear, however, how molecular diffusion might occur in these superlattices- would reactions be confined to their surfaces or persist in the superlattice interior layers? In order to approach this question, we consider Galvanic replacement of a Ag DNA-NP superlattice. Through titration of $HAuCl_4$ in varying amounts into a superlattice-containing solution, the superlattice molecular diffusion kinetics could be explored. Through use of cross-sectional TEM, it could be explored whether particles on the superlattice surface are first fully exchanged, or if the superlattice is exchanged uniformly and to what extent this is the case. This, however, would be based on the assumption that nanoparticles embedded in a DNA-NP superlattice could be Galvanically exchanged. This may prove difficult given the high salt concentrations used in these systems, which would greatly affect the system electrostatics.

3.7.3 Biomedical applications of DNA-functionalized AgAu nanocages

DNA-Au NPs have proven effective for gene-regulation therapy.[129] AgAu nanocages have also been used as therapeutic agents, due to their drug encapsulation capacity and demonstrated use in photothermal therapy.[102] If AgAu nanocages were functionalized with DNA, a combinatorial strategy, which involves more than one of these approaches, may be applied. This may prove useful in providing a multi-functional particle for use in new therapy strategies.

Chapter 4: The Role of Trace Ag in the Synthesis of Au Nanorods

4.1 Abstract

The synthesis of high-aspect-ratio, monodisperse Au nanorods from Au spherical seeds has been attributed to the addition of trace Ag. Yet the role that Ag plays in the synthesis process has remained both elusive and controversial. In this study, we correlate the Ag distribution within the nanorods to nanorod growth through timecourse X-ray absorption spectroscopy (XAFS)-derived atomic-coordination paired with electron microscopy nanoscale morphological analysis. Herein, a plausible pathway for the conversion of spherical seeds into Au nanorods is proposed. Evidence shows that the nanorod anisotropic growth is directly related to the Ag surface coverage. Anisotropy is induced early in the reaction when Ag first deposits onto the nanoparticle surface and that later the nanorod grows isotropically as the reaction progresses and Ag diffuses into the nanorod bulk. The results of this investigation and methods employed should be extendable to many anisotropic nanoparticle synthesis reactions that make use of trace elemental species as a synthetic additive.

4.2 Introduction

Control over nanoparticle morphology, including surface faceting, has optimized nanoparticles for use in catalysis due to their preferential faceting,[6] in optics due to their size and shape dependent local surface plasmon resonance (LSPR),[5, 130-131] and in programmable assembly due to their introduction of valency.[132-133] Yet in order to optimize nanoparticles for their intended applications, methods must be developed in order to synthesize anisotropic nanoparticles with uniformity in both size and shape. One such synthetic approach, which has proven successful in producing monodisperse anisotropic Au nanoparticles, begins with colloidal growth from 2 nm Au

seeds in an Au salt solution with trace Ag. The trace Ag has been found to be a necessary reactant in controlling the morphology and aspect ratio of the resulting product.[36, 134] Yet despite the success and reproducibility of these syntheses, the mechanism behind the growth of these particles remains elusive and controversial.

In order to investigate the pathway behind the synthesis of anisotropic Au nanoparticles using trace Ag, the Au nanorods serves as a case study. The nanorod was selected over the other particle morphologies as it was the first to be synthesized by this method[35] and has been the most thoroughly studied. Historically, nanorods originally synthesized colloidally using cetyl trimethylammonium bromide (CTAB) as a surfactant resulted in nanorods which were polydisperse in shape and size.[34, 135] When trace amounts of Ag were added into the reactant solution, however, monodispersity was improved and nanorod aspect ratio could be controlled based on the amount of Ag^+ introduced.[35] This Ag-modified synthesis remains state-of-the-art, and has inspired the synthesis of many additional nanoparticle morphologies using a similar Ag-mediated approach. These results sparked an interest into what role Ag plays in controlling the synthesis product, in addition to the overall mechanism behind anisotropic growth in colloidal nanoparticle systems.

Similar to its bulk counterpart, 2 nm Au nanoparticles have an FCC crystal structure,[19, 37, 136-137] which would normally favor growth of isotropic, quasi-spherical particles. To achieve a non-quasi-spherical product, a process occurs in given *hkl* directions, but not in all symmetrically equivalent directions, to induce asymmetric growth (e.g., growth is inhibited in [101] direction, but not in [011])[19]. Although there are many ideas surrounding nanorod anisotropic growth, two general hypotheses dominate current literature, and are outlined in Figure 4.1: 1) Surfactant CTAB binds preferentially to different *hkl* surface facets, thus limiting the growth of facets they are more

strongly bound to than other facets, leading to anisotropy in facet growth rates[138-139] and 2) Trace Ag binds preferentially to different surface facets, thus slowing the growth on these facets and leading to a nanorod with high aspect ratio.[13] Both hypotheses have indirect evidence which suggests that they might play a role in the synthesis. The argument for CTAB's involvement in anisotropic growth stems from the difficulty of removing CTAB on the sides of the nanorods, whereas the CTAB on the tips of the rods can be easily exchanged with thiolated ligands. This approach has been used to create 1-D assemblies of Au nanorods and suggests that CTAB is bound more strongly to the sides of the rods than the tips, which may result in anisotropic growth.[140-141] For the case of Ag, the preference of Ag for particular surface facets has been explained by the underpotential deposition (UPD) hypothesis,[142] based on the technique commonly used to deposit a metallic monolayer onto the surface of a more noble metal due to a decrease in required reduction potential.[143-144] In bulk systems, the decrease in reduction potential has been determined to be greater for higher-energy surface facets.[143-144] This has led to the hypothesis that in Au nanoparticles, Ag^{+} is preferentially reduced onto higher energy surface facets, leading to anisotropic growth. Yet experimental evidence to support this hypothesis and in particular the Ag distribution within the particles, has yet to be determined.

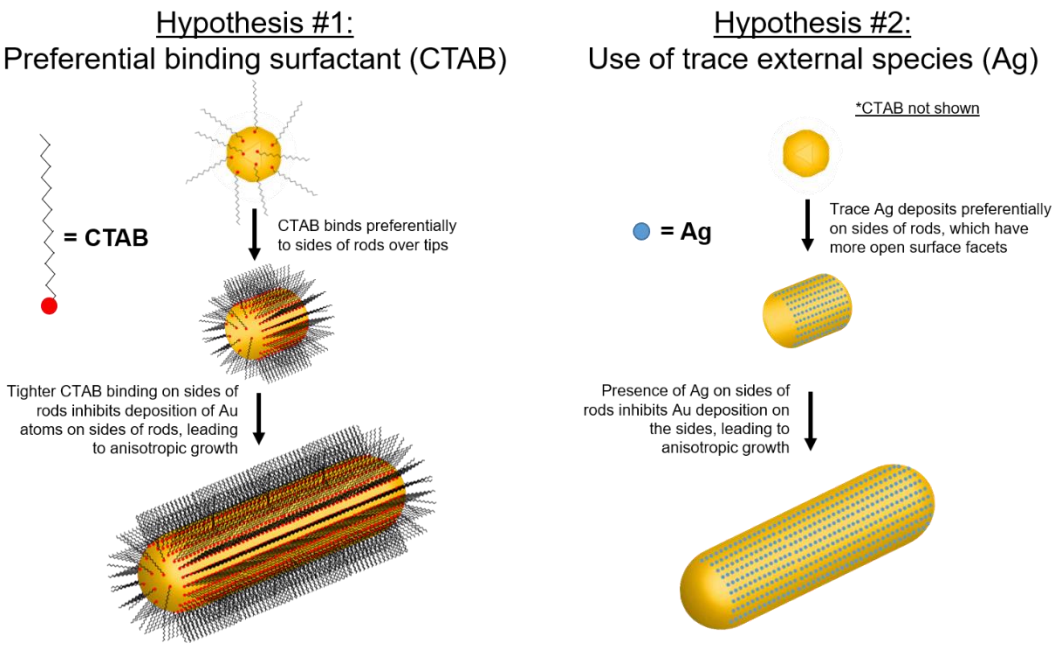

Figure 4.1 Schematic of possible anisotropic growth pathways in Au nanorod synthesis.

Previous investigations into the nanorod synthesis pathway have focused on electron microscopy (EM) results.[35, 142, 145-146] EM images studied as a function of reaction time revealed that nanorods with a high aspect ratio are formed early in the reaction.[146] Based on nano-diffraction, the most commonly reported facets involve the sides of the nanorods as {110} and the tips of the rods as {100}.[142] A few more recent studies, however, have discovered the side facets to be a mixture of {520} and {110} and the tips a mixture of {100} and {111}.[145]

The anisotropy-inducing event was specifically probed using HRTEM on seed particles with and without the presence of trace Ag.[19] Results from this work showed that after reaction for 5 minutes, emergence of {110} facets and anisotropic growth was observed in the presence of Ag. Although the starting Au seeds are most likely icosahedral in shape (and therefore do not exhibit {110} facets), it is hypothesized that due to the similarity of surface energy of {100}, {111} and

{110} facets at small nanoparticle sizes, fluctuations result in random emergence of {110} facets. These facets are only stabilized by the presence of solution Ag, which can deposit preferentially on these open facets.[19] In contrast, multi-twinned particles dominated by {111} faceting were observed in the absence of Ag.[19] A computational study suggests very different results- that there may be formation of an AgBr complex at the start of the reaction which binds preferentially to {100} faces in the seed.[147] In none of these studies, however, was the distribution of Ag, nor its role in the emergence of anisotropy probed directly.

The Ag within the nanorods has been only investigated for the final product nanorods. An earlier XPS study concluded that Ag resides in the surface layers of Au nanoparticles in the final product,[38] yet its exact form and distribution are still unclear. Although EDX results suggest that the final nanorod surfaces showed no facet-bias for the Ag,[148] it is unclear whether this is also the case when Ag first incorporates. Inductively Coupled Plasma-Atomic Emission Spectroscopy (ICP-AES) has shown that the amount of Ag is only a few atomic percent in the final nanorod product.[149] Also, the oxidation state of Ag in the final product nanorods has been probed, however it remains controversial whether the deposited Ag is Ag^0 [142, 149-150] or Ag^+ [149, 151]. In considering the reason for the controversy of the nanorod synthesis process despite the many studies dedicated to gaining insight into this complex problem, a major shortcoming can be easily identified. Although the aforementioned studies provide insight into the structure of the final nanorod product, they attempt to extrapolate the synthesis pathway from only the final product structure. With the exception of a timecourse TEM study,[146] the earlier timepoints in the reaction have not been addressed experimentally. To date there is no knowledge of how the Ag in the nanorod evolves over time. This present study aims to fill in this knowledge gap and relate the structure of Ag within the nanorods to nanorod anisotropic growth.

In this study, the local atomic-scale structure of Ag within the nanorods is probed as a function of reaction time and correlated with the nanorod morphology and anisotropic growth. In particular, use of X-ray absorption fine structure (XAFS) and X-ray fluorescence (XRF) and EDX-mapping allow us to study the Ag contributions within the nanorods specifically. XAFS-derived atomic coordination is used to determine whether Ag is on the nanorod surface or incorporated within the interior and X-Ray Absorption Near Edge Structure (XANES) is used to determine the oxidation state of surface Ag. This can be compared with the atomic % Ag incorporated into the nanorods over time determined from XRF and nanorod morphological changes determined from EM. The emphasis on X-Ray techniques provides the capability to probe nanoparticles *in-situ* in their solution environment and also to achieve a statistically meaningful sample population.

Through use of this structural toolbox to study the Ag within the nanorods over time with atomistic detail, this work distinguishes between the aforementioned hypotheses. Most notably, Ag incorporates onto the nanoparticle surface early in the reaction, which correlates with anisotropic growth. As the reaction progresses, the incorporation rate of Ag slows, such that by ~30 minutes into the 120 minute reaction, very little Ag remains on the nanoparticle surface, but has instead diffused into the nanoparticle bulk. The key observation is that while the diameter growth rate of the nanorods does not depend on the amount of Ag incorporated into the nanoparticle surface, the length growth rate of the nanorods is directly correlated to the amount of surface Ag. This provides support for the underpotential deposition hypothesis of Au nanorod growth. Based on experimental results, a synthetic pathway for nanorod synthesis and the critical role of trace Ag is proposed. These results may be extendable to many of the other anisotropic nanoparticle syntheses which rely on the use of trace species in their syntheses.

4.3 Methods

For each of the methods described below, more details can be found in Appendix A.4.

4.3.1 Synthesis

Au nanorods were synthesized via the procedure established by El-Sayed and co-workers.[35] Briefly, ~2 nm Au seed nanoparticles were synthesized by adding 0.6 mL of 0.01 M ice cold $NaBH_4$ (Sigma-Aldrich) to a stirring solution containing 5 mL 0.2 M CTAB (bioWORLD), 0.25 mL 0.01 M $HAuCl_4$ (Sigma-Aldrich) and 4.75 mL NANOpure^{TM} water (18.2 MΩ ionic purity). In a separate vial, 5 mL 0.2 M CTAB, 0.3 mL 0.004 M $AgNO_3$ (Sigma-Aldrich), 0.5 mL 0.01 M $HAuCl_4$ and 4.5 mL NANOpure^{TM} water were combined and 0.07 mL of 0.078 M ascorbic acid (Sigma-Aldrich) added to reduce Au^{3+} to Au^{+}. 0.012 mL of the as-synthesized seeds were added to this solution and reacted for 120 minutes to form the final nanorod product. In order to quench the reaction at earlier timepoints, an aliquot from the reaction solution was brought to 1 mM bis(*p*-sulfonatophenyl)phenylphosphine (BSPP, Sigma Aldrich), which exchanged with CTAB on the surface of the nanorods and halted further nanorod growth.

4.3.2 UV-vis spectroscopy

UV-Vis Spectroscopy scans of samples in 1 ml NANOpure^{TM} water were taken using a Cary 5000 UV-vis spectrophotometer across the range of 200-1000 nm at a 1 cm path length.

4.3.3 Electron microscopy

Using the NU EPIC Facility, samples were dropcasted on a carbon coated grid for electron microscopy characterization. Scanning transmission electron microscopy (STEM) images were collected using a JEOL JEM-2100 FasTEM at 200 keV. Early timepoint nanorod samples were plunge frozen at different time points on glow discharged 200 mesh lacy carbon grids with an FEI Vitrobot Mark III and loaded into a Gatan Cryo Transfer Holder held at –165C. Image data was

gathered in a Hitachi HD-2300 STEM at 200kV utilizing phase contrast transmission and high angle annular dark field detectors. EDX mapping of 12-minute nanorod samples was performed on an aberration-corrected Hitachi HD-2700 STEM operated at 200 kV accelerated voltage. The image shown in Figure 4.6a is a STEM image collected by the high angle annular dark field detector showing Z-contrast, while the x-ray energy dispersive spectra (EDS) used for mapping is collected by an Oxford x-ray detector and processed by AZtecEnergy software.

4.3.4 X-ray photoelectron spectroscopy

X-ray photoelectron spectra were obtained using a Thermo Scientific ESCALAB 250Xi XPS spectrometer with an Al K alpha (1486.5 eV) anode at 20 kV. Oriented nanorod film samples were prepared by using depletion interactions to dropcast the nanorods onto a silicon substrate with preferred orientation dependent on drying conditions (Appendix A.4).

4.3.5 X-ray scattering

Small angle X-ray scattering (SAXS) patterns were collected using 10.00 keV X-rays at DND-CAT station 5ID-D located at the Advanced Photon Source (APS) at Argonne National Laboratory (ANL). The aqueous nanoparticle dispersions were placed in quartz capillary tubes (inner diameter ~ 1.5 mm, Charles Supper) for measurement. The scattering patterns from ex-situ (BSPP-quenched) and in-situ samples were collected and compared at various stages throughout the timecourse reaction.

4.3.6 X-ray fluorescence

X-ray fluorescence (XRF) spectra were obtained at APS stations 10BM-B and 5BM-D using a Vortex four element silicon drift diode detector (SDD). Spectra were collected at 26.014 keV (above the Ag K edge energy, 25.514 keV) to determine the Ag-to-Au atomic ratio from the areas under the Au L alpha and Ag K alpha fluorescence lines. Elemental XRF cross sections,[46] detector

efficiency, and attenuation due to solvent media were taken into account in determining the Ag/Au ratio.

4.3.7 X-ray absorption spectroscopy

X-ray absorption fine-structure (XAFS) spectra at the Au L_3 edge and Ag K edge (11.919 keV and 25.514 keV, respectively) were collected at MR-CAT station 10BM-B located at the APS. Energy scans were taken over a range from -150 eV to 600 eV with respect to the Au or Ag absorption edge using a Si(111) monochromator. XAFS spectra of the samples were collected in XRF-mode using a four-element Vortex SDD, and calibrated with an Au or Ag metal foil standard in transmission-mode. Samples were concentrated via centrifugation to micromolar concentrations of Au/Ag atoms and placed in 3 mm inner diameter quartz capillary tubes.

XAFS data was processed using ATHENA and ARTEMIS software, part of the IFEFFIT package[116]. EXAFS spectra were modeled according to the EXAFS equation:[50-51, 52, 47]

$$\chi(k) = \sum_{\Gamma}[\frac{N_{\Gamma}S_0^2F_{\Gamma}(k)}{2kR_{\Gamma}^2}e^{-2k^2\sigma_{\Gamma}^2}e^{-2R_{\Gamma}/\lambda(k)} \times \sin\big(2kR_{\Gamma} + \phi_{\Gamma}(k)\big)] \quad (4.1)$$

Where Γ is the summation over the individual scattering pathways included in the model, k is the photoelectron wavevector magnitude, $F_{\Gamma}(k)$ is the scattering amplitude, $\lambda(k)$ is the mean free path of inelastically-scattered photoelectrons and $\Phi(k)$ is the phase shift, which is calculated as a function of the absorbing and scattering atom. S_0^2, the amplitude reduction factor, was set to the value extracted from fitting a bulk Au or Ag foil as applicable. This enables a more accurate determination of the coordination number.[52] Degeneracy (N_{Γ}), inter-atomic distance (R_{Γ}), energy shift parameter (E_0), and mean-squared disorder (σ_{Γ}^2), which includes contributions from structural and thermal disorder (Debye-Waller factor),[50] were adjusted to determine the best fit model. These parameters were extracted for the first Ag or Au coordination shell.

4.4 Results

STEM images collected at various timepoints throughout the 120 minute nanorod synthesis reaction are shown in Figure 4.2. Most notably, from the spherical seed particles, anisotropy is induced early in the reaction (between 6 and 8 minutes). This anisotropy event is also observed from UV-vis spectra (Figure 4.3b), which show the emergence of a longitudinal band around 800 nm and transverse bad around 550 nm during this same 6-8 minute time frame, which is characteristic of a nanorod morphology.[35] These results agree with a previous HRTEM study of symmetry breaking of Au seeds, which only occurred after the seeds reached a critical size (> 5 minutes)[19]. By 8 minutes into the reaction, the seeds evolve into anisotropic rods with an aspect ratio of 1.5. Over the next 4 minutes, the nanorods exhibit a rapid elongation, reaching their final aspect ratio of ~4. This aspect ratio is maintained for the remainder of the reaction as the nanorods continue to grow until the two hour reaction is complete.

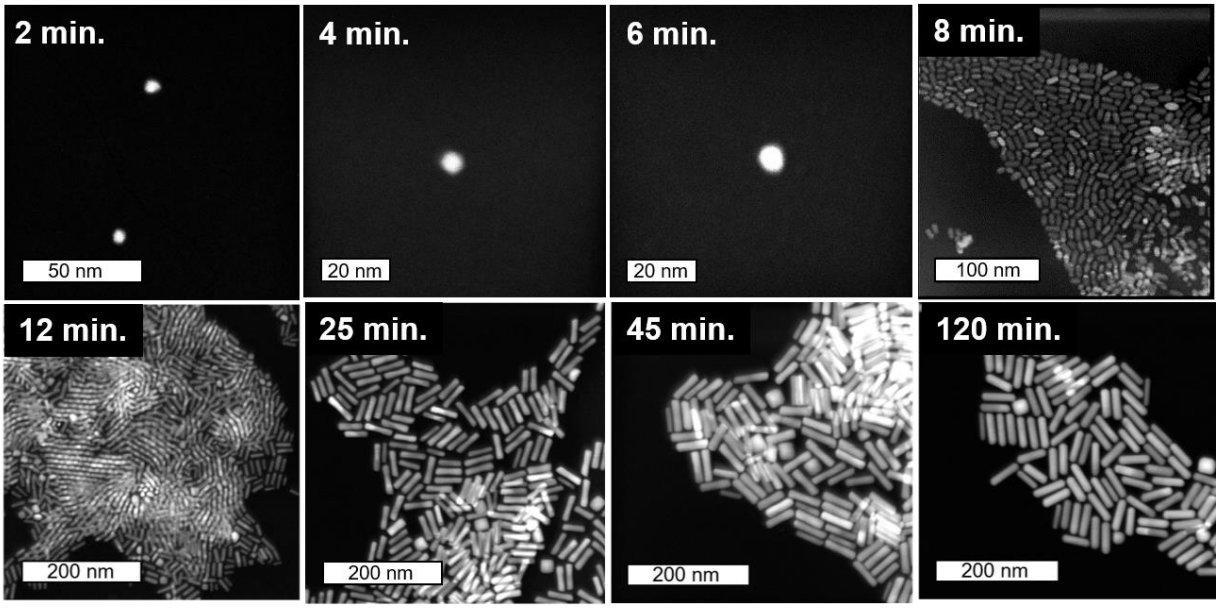

Figure 4.2 Timecourse STEM images. Starting from 2 nm Au seeds, STEM images taken from colloidally synthesized Au nanorods quenched with BSPP at timepoints from 2 minutes into growth (top-left) to final product nanorods (bottom-right). The first three images are cryo-STEM of unconcentrated particles. (See appendix A4 for details.)

Statistics from STEM-determined particle dimensions were used to track the length and diameter growth rates of the nanorods as a function of reaction time (Figure 4.3a).While the diameter growth rate appears relatively constant throughout the reaction, the length growth rate exceeds the diameter growth rate during the time frame from 8 – 30 minutes. After 30 minutes, the length and width growth rates match each other and minimal particle growth is observed from 45 to 120 minutes. These results reveal that the anisotropic growth steps leading to nanorod formation occur early in the reaction, while the late reaction stages do not contribute to particle anisotropy.

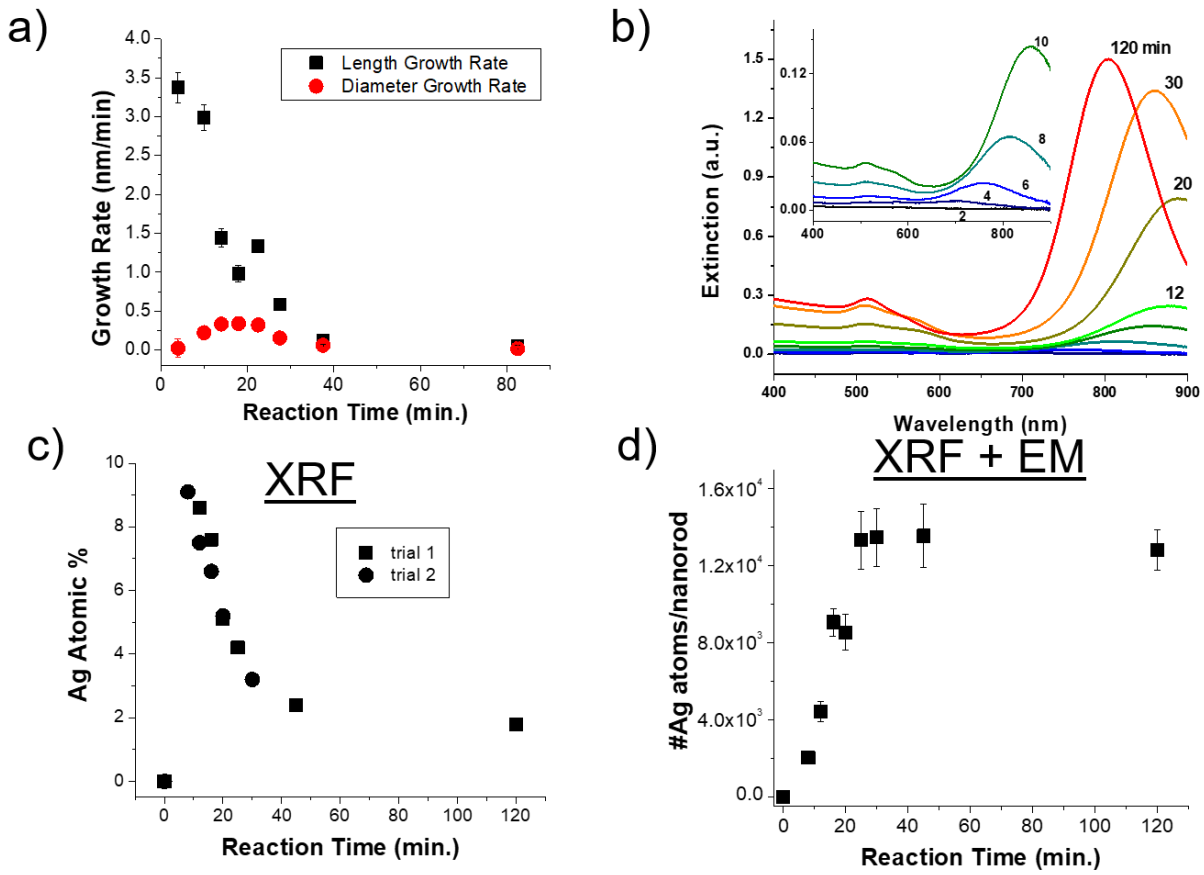

Figure 4.3 Nanoparticle growth and composition. a) EM determined length and diameter growth rates as a function of reaction time, b) UV-vis spectra as a function of reaction time, c) XRF-determined nanoparticle composition and d) XRF and EM determined number of Ag atoms per nanorod.

XRF data (Figure 4.3c) shows that the Ag incorporates early in the Au nanorods and the Ag atomic % decreases with reaction time. This finding was shown to be repeatable through multiple trials. Yet additional analysis that combines the XRF with STEM results (Figure 4.3d) shows that the absolute number of Ag atoms per nanorod increases in the first 45 min. This suggests that the

decrease in the atomic % Ag as a function of reaction time is not explained by Galvanic exchange, which would have shown a decrease in the number of Ag atoms per particle over reaction time.

XANES results show that throughout the course of the reaction, Ag is in the metallic Ag^0 state. In Figure 4.4, the XANES spectrum for the final product nanorods is compared to relevant Ag^+ standards, which include AgBr (a species previously proposed to cap the nanorod {110} surface facets)[152] and Ag_2O, as well as Ag^0 standards, which include an Ag metal foil and the as-synthesized Au nanorods overgrown with an Au shell, which should encapsulate any surface Ag.[132] In comparing the fingerprint signatures of the Ag^+ and Ag^0 standards, we see that for the Ag^0 species, there is a defined dip in the near-edge region at ~25.535 keV that is absent in the Ag^+ spectra, where there is a slight peak. Also, there is a defined peak at ~25.545 keV that is also absent in the Ag^+ spectra. These spectral changes are due to differences in the Ag^0 and Ag^+ 3d unoccupied densities of states. The Au nanorod spectrum near edge features mimic those of the Ag^0 standards (Figure 4.4, right). In particular, the spectrum appears the same for the Ag in the final-product nanorods (green) as when they are overgrowth with an Au shell (blue), when all Ag should be Ag^0 due to encapsulation of any surface species into the FCC interior. However, when the Au nanorods are not isolated from solution (magenta), the signature is primarily Ag^+ due to excess $AgNO_3$ in solution. This confirms that a majority of the Ag present in solution does not incorporate into the nanorods.[149] We not only observe these comparisons for the final product nanorods, but for the nanorods throughout each step of the timecourse reaction, even early on when Ag is the dominant surface species (Figure A4.7). Ag therefore incorporates into the nanorod as Ag^0.

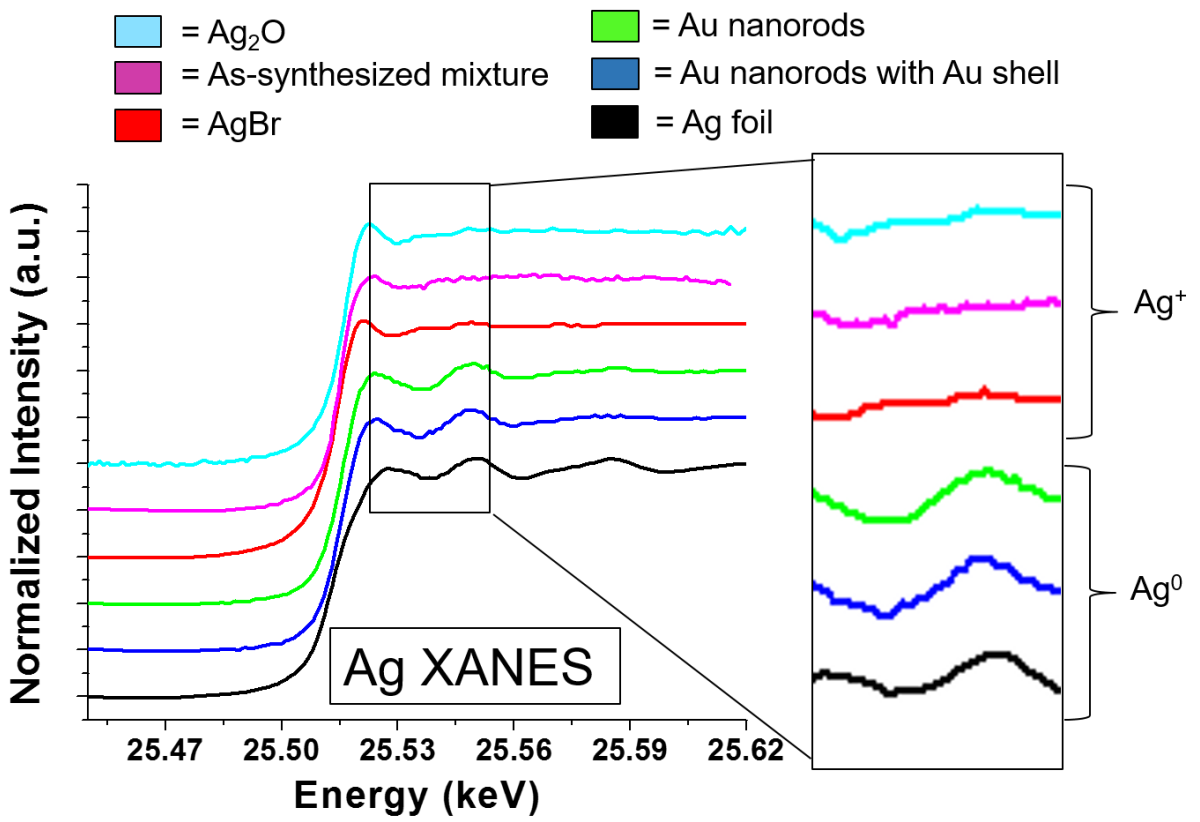

Figure 4.4 Ag K-edge XANES data from 120 min final product nanorods (middle, green) compared to standards with Ag^+ (top 3) and Ag^0 (bottom 2). A blowup of the near edge region is shown on the right-hand-side for each spectrum.

Coordination numbers (CNs) obtained through EXAFS modeling analysis are shown in Figure 4.5a. Since a bulk coordination number for an FCC metal is 12, a coordination number less than 12 indicates a significant fraction of surface-coordinated atoms. Thus EXAFS gives insight into whether atoms are predominantly at the surface or in the bulk of the nanoparticle. While the Au CN throughout the reaction is 12, the Ag CN increases from < 8 at 8 minutes into the reaction,

to a full shell of 12 by 40 min. This suggests that Ag starts on the nanoparticle surface and incorporates into the bulk as the reaction progresses.

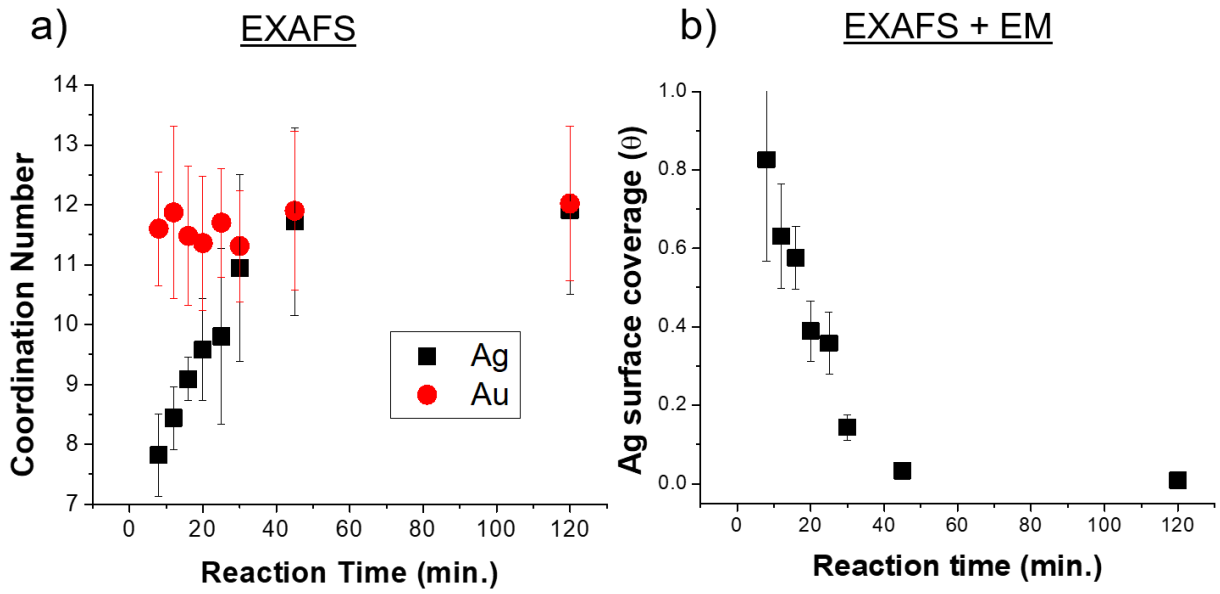

Figure 4.5 EXAFS results. a) Coordination numbers extracted from Ag K and Au L3 edge XAFS spectra. b) Ag surface coverage, extracted from a combination of XAFS-extracted coordination numbers, EM-determined dimensions and the assumption that Ag on the surface has a CN of 7.

The Ag CN (Figure 4.5a) is used to determine the fraction of nanorod Ag atoms on the surface, assuming a surface CN of 7 and a bulk CN of 12. (See Appendix A4 for details.) This is then combined with our previous Fig. 3 results for overall Ag atomic % and nanoparticle dimensions to determine the composition of the nanorod surface. As shown in Figure 4.5b the nanorod surface composition is at 84 at% Ag at 8 minutes and reduces to a few percent after 45 minutes into the reaction. (Note that this analysis shows that the decrease in coordination number is not only due to the reduction in surface area to volume ratio during nanorod growth.) To our knowledge,

nanorod surface coverage has not been previously measured, but has been hypothesized[36, 38, 142] to strongly influence the deposition rate of the Au and Ag atoms during nanorod evolution.

Now that the evolution of the overall nanorod surface coverage is determined, the next logical step is to explore the composition of particular nanorod faces, since an inequivalence in Ag surface composition has been hypothesized to lead to an inequivalence in nanorod growth rates along different directions.[142] XPS spectra were collected from a collection of nanorods preferentially oriented on their sides or their ends. This strategy, requiring uniformly oriented domains, only worked for larger nanorods and could therefore not be used for early reaction time points. Oriented XPS studies of the final product nanorods showed no preference of Ag for the ends vs. sides of the nanorods (Figure A4.6). However, EDX mapping (Figure 4.6) was effective for studying the Au and Ag distribution in a nanorod 12 minutes into the reaction. Here in can be seen that Ag is present on the sides of the nanorods as illustrated in Figure 4.6 (bottom, center). The resolution of the measurement is not sufficient to tell whether the Ag is also on the ends of the nanorods. Yet the possibility that the Ag is only on the tips of the nanorods is eliminated as illustrated in Figure 4.6, (bottom, right). At 12 minutes into the reaction, the majority of surface atoms in the nanoparticle are Ag (Figure 4.5), making the Ag distribution found at this timepoint relevant to Ag deposition conditions. The Ag distribution within early timepoint nanorods and its implication on anisotropic growth will be further discussed in the following paragraphs.

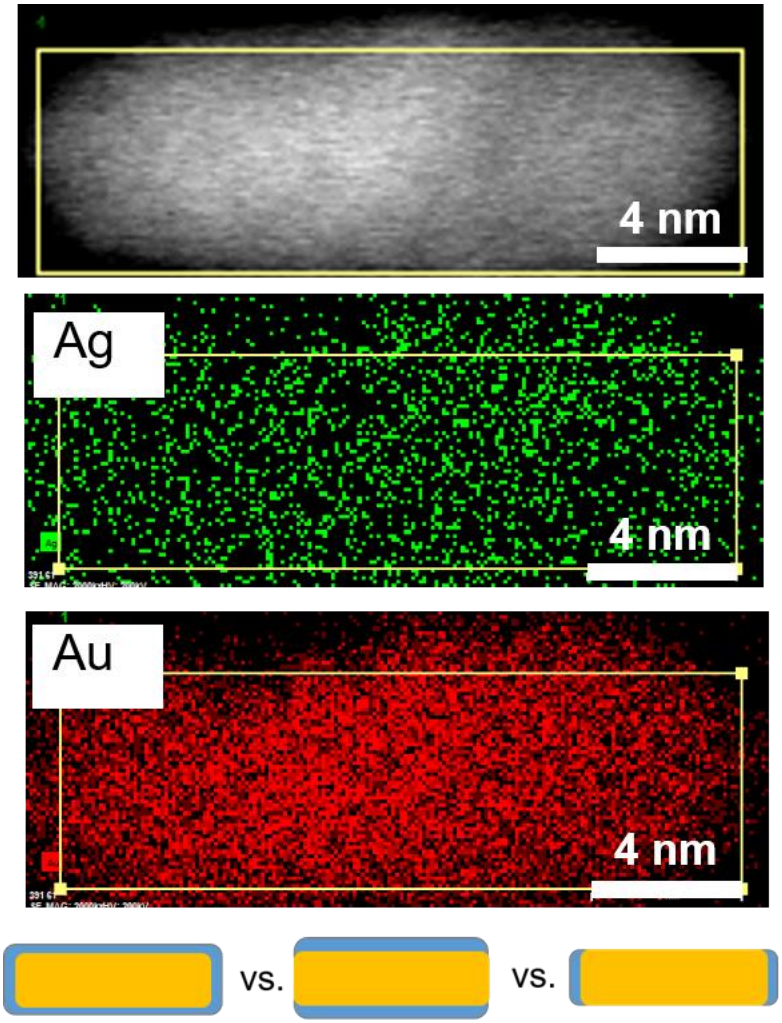

Figure 4.6 SEM (top), and EDX maps of Ag and Au at 12 minutes into the reaction where Ag is predominantly at the surface (Figure 4.5). The bottom schematic shows the three types of Ag (blue) surface distributions considered. EDX eliminates the case for Ag only on the ends of the nanorods (bottom right).

4.5 Discussion

The above structural characterization results can be used to determine whether or not the reaction pathway for the synthesis of Au nanorods well-aligns with those that have been previously

proposed. To this end, Figure 4.7 outlines a series of questions that lead to a logical determination of the appropriate anisotropic growth hypothesis. It is first important to consider whether or not Ag incorporates into the particles at the time that symmetry is broken. From STEM images and UV-Vis spectra, we find that anisotropy is induced between 6 and 8 minutes into the reaction. By 8 minutes into the reaction Ag has already deposited onto the nanorod surface such that the rods are ~10 % Ag, and 84 % of the Ag in the nanorod is on the surface. This proves that Ag is incorporated early on in the reaction, which is also when we observe that anisotropy is induced. This observation agrees with previous studies that suggest that Ag stabilizes {110} facets prior to 8 minutes in the reaction,[19] leading to anisotropic growth at early reaction stages.

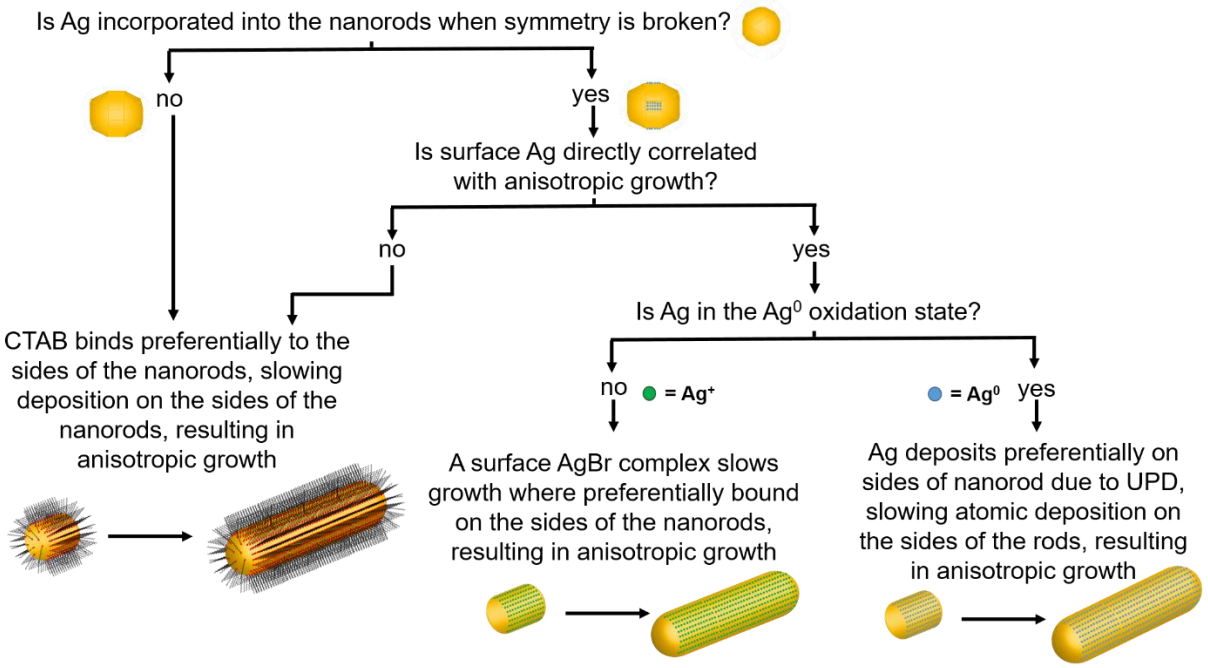

Figure 4.7 Flow chart connecting anisotropic growth hypotheses. The flow chart relates nanorod structural attributes to the appropriate hypothesis for nanorod anisotropic growth. This study provides answers to the questions posed, leading to identification of the UPD hypothesis as the most in line with the reason behind nanorod anisotropic growth.

To determine whether this surface incorporated Ag plays a role in nanorod anisotropic growth, XRF, EXAFS and STEM results are combined to derive the nanorod length and diameter growth rates in Figure 4.8 as a function of Ag surface coverage. Interestingly, the length growth rate of the nanorods is directly correlated with the amount of surface Ag, whereas the diameter growth rate shows no correlation. This indicates that towards the beginning of the reaction when the majority of the surface is Ag, the length growth rate exceeds the diameter growth rate, resulting in an anisotropic nanoparticle. As the reaction progresses and Ag becomes increasingly incorporated into the bulk of the nanorod and its surface coverage drops, the length growth rate slows until for

the rest of the reaction. The length and width growth rates are essentially equivalent when the majority of surface atoms are Au.

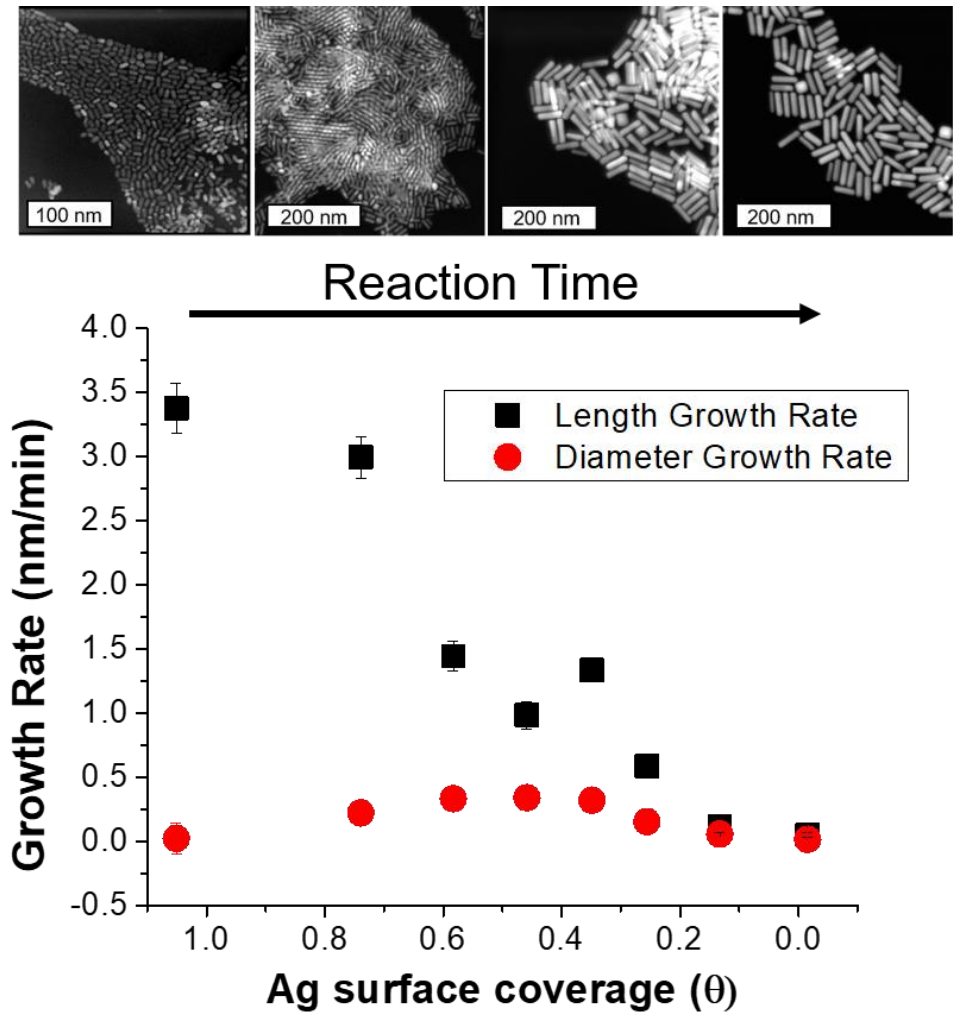

Figure 4.8 Nanorod growth rates vs. Ag surface coverage. Combining the results of XRF, EXAFS and STEM, the diameter growth rate is shown to be unaffected by surface Ag, while the length growth rate is directly correlated.

The results show that surface Ag is directly correlated with nanorod anisotropic growth. Yet to provide an explanation for how surface Ag may contribute to anisotropic growth, results must

be evaluated to see if the previously proposed UPD hypothesis, or if a different or new hypothesis better explains the observed phenomenon. In bulk UPD, Ag deposits as Ag^0 rather than as an Ag^+ adsorbate complex.[143-144] From XANES, in the nanorod case, Ag also deposits as Ag^0. The spectrum features match those of Ag^0 standards and not other proposed species including AgBr and AgO_2.[13]

The UPD hypothesis also relies on the deposition of Ag^0 onto higher surface energy (i.e., lower coordination number) facets of the nanorod preferentially compared to other facets.[38, 142] EXAFS-derived coordination numbers give insight into which surface Ag is deposited on, as atoms incorporated into different surface facets have a different associated coordination number. A coordination number of CN = 12 corresponds to bulk, while for unreconstructed fcc surfaces CN = 9 for {111}, 8 for {100} and 7 for {110}. The EXAFS measured coordination number at the 8 minute timepoint (7.8 ± 0.8) indicates that the Ag likely deposits on the {110} facets, since the measured CN should not be lower than the facet to which the Ag is coordinated due to atoms in the bulk that have a full coordination shell of 12. This agrees with the previous hypothesis that Ag is on the {110} facets. [142, 145] If we assume that the Ag is indeed on the {110} facets at the 8 minute timepoint, then the 84% Ag on the surface is on {110} facets with the remaining 16% in the bulk (i.e., 0.84•7 + 0.16•12 = 7.8). EDX mapping provides further evidence that Ag deposits onto the {110} facets (sides of the nanorods). Clearly the low CN eliminates the possibility of deposition onto lower energy {111} facets, which directly supports the UPD hypothesis that Ag has preference for higher surface energy facets on the nanorod.

In summary, the structural characterization results herein are in line with what would be expected for Ag UPD. Timecourse local and global structural details lead to the proposal of a plausible pathway for the anisotropic growth of Ag nanorods. In particular, quantitative details

about the Ag content and distribution within the nanorods as a function of reaction time are provided. Figure 4.9 outlines pictorially the following stages in the proposed reaction pathway: 1) From quasi-spherical ~2 nm Au seeds, Ag deposits as Ag^0 between 6-8 minutes into the reaction as a result of UPD, stabilizing {110} facets of the nanorods, and inducing anisotropic growth. 2) By 8 minutes into the reaction, the rods are anisotropic with an aspect ratio of ~1.6, with an Ag surface coverage of 0.8. 3) By 12 minutes into the reaction, the final nanorod aspect ratio of ~3.6 is reached, while a majority of surface atoms are still Ag. 4) As the reaction progresses, the rate of Ag deposition slows, such that the Ag surface coverage reduces and the length growth rate of the nanorod decreases. The length growth rate of the nanorods is directly proportional to the amount of surface Ag, whereas the diameter growth rate is not correlated. The most plausible explanation for why surface Ag inhibits Au deposition in comparison to surfaces that are Au rich is the higher bond-strength of Au-Au vs. Au-Ag, resulting in preferential Au deposition onto surfaces where Ag is not present. It is also the case that reduction potential is lowered for a metal onto a more noble metal (Au) than a less noble metal (Ag).[144] 5) Ag diffuses into the layers below the nanorod surface, as additional Au atoms are deposited, such that the Ag coverage is reduced. Thus the length growth rate slows, such that the ~3.6 aspect ratio is maintained during growth. 6) By 45 minutes into the reaction, Ag surface coverage approaches zero, and the length and diameter growth rates are essentially equivalent until 120 minutes, when the final product nanorods cease growing.

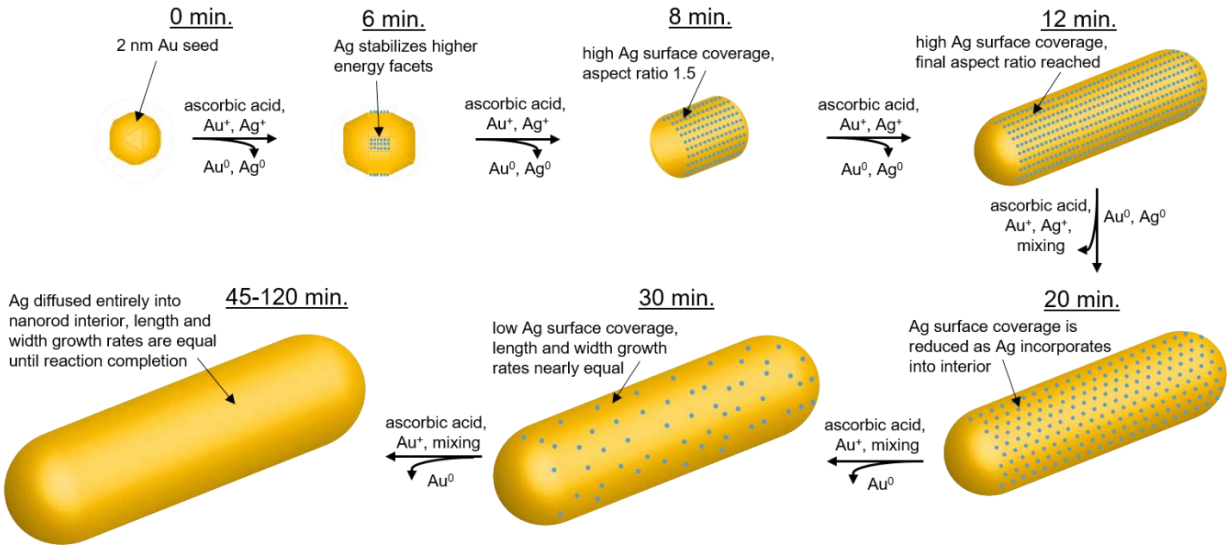

Figure 4.9 Proposed reaction pathway for Au nanorod growth. Starting with ~ 2 nm Au seeds (0 minutes), Ag deposits between 6-8 minutes in the reaction, stabilizing {110} facets and inducing anisotropic growth. By 8 minutes into the reaction, the nanorods are anisotropic with an aspect ratio of 1.5. The final aspect ratio of 3.6 is reached by 12 minutes into the reaction. Over time, Ag deposition slows and incorporated Ag diffuses into the nanorod interior. By 45 minutes into the reaction, Ag surface coverage approaches zero, and the length and diameter nanorod growth rates remain equivalent until reaction completion (120 minutes, final product).

4.6 Conclusion

Through use of EM, EDX mapping, UV-vis, XAFS, and XPS applied in a timecourse strategy, the Ag distribution within Au nanorods is revealed. This bridges the gap between the morphological evolution that results in the formation of the Au nanorods from Au seeds and the role that Ag plays in this process. Structural characterization results reveal the key insight that surface Ag directs anisotropic facet growth rates of the nanorods and enable the proposal of a plausible reaction pathway based on the Ag distribution in the nanorods over time. Nanorod length

growth rate is directly proportional to the nanorod Ag surface coverage, whereas Ag incorporation is not correlated with nanorod diameter growth rate. Ag deposits as Ag^0 preferentially onto higher surface energy {110} facets early in the reaction, a pattern which supports the UPD hypothesis previously proposed.[142] The nanorods reach their final aspect ratio of ~3.6 by 12 minutes into the reaction, indicating that anisotropic growth dominates early in the reaction, when a majority of {110} surface atoms are Ag. As the reaction progresses, Ag incorporates into the bulk of the nanorod, and by 45 minutes into the reaction, Ag surface coverage approaches zero, leading to equivalence in length and diameter growth rates until reaction completion. These results are not just important for the nanorod synthesis, but may be applicable to the many Au anisotropic nanoparticle synthesis reactions which make use of trace Ag[36, 38]and the many other nanoparticle synthesis reactions involving trace external species.

4.7 Proposed future work

4.7.1 Exploring the role of trace Ag in the synthesis of anisotropic nanoparticles

In this study, the role of trace Ag in the synthesis of Au nanorods was investigated. Given that an approach has already been established, it is an obvious extension to also study the role of trace Ag in the synthesis of the large number of Au anisotropic nanoparticles that make use of the UPD approach.[36, 38] While in Au nanorods, it is found that surface Ag is directly correlated with anisotropic growth, it would be useful to investigate whether or not this is the general trend for all anisotropic shapes. In addition, this would help inform why the amount of Ag introduced into solution affects the resulting nanoparticle morphology. If additional synthetic systems were investigated, the overall role of trace Ag in the synthesis of anisotropic Au nanoparticles could be determined.

4.7.2 The role of trace I^- in the synthesis of Au nanoprisms

Similar to the case of Ag^+ in the synthesis of Au nanorods, trace solution I^- is suspected to play a role in the synthesis of Au nanoprisms.[40] This role is also poorly understood, however is hypothesized to be a controlling factor in the resulting nanoparticle morphology. Using the same combination of techniques used in the nanorod study, the role of trace I^- in the synthesis of Au nanoprisms could be explored. To this end, the I K x-ray absorption edge was probed in a preliminary experiment at station 20 IDB of the APS. Unfortunately, the concentration of iodine in the nanoparticle samples was sufficiently low that no signal could be observed. This means that either the amount of iodine in the particles is extremely low, and the particles would need to be further concentrated in order to observe a fluorescence signal, or the iodine previously observed from XPS experiments[40] was actually a byproduct of the drying process. Further investigation is necessary in order to clarify this issue.

Chapter 5: Investigating the Structure of CTAB on the Surfaces of Au NPs

5.1 Abstract

CTAB is widely utilized as a surfactant and stabilizing agent in the synthesis of monodisperse Au nanoparticles. Despite the important role that CTAB has been proposed to play in directing the synthesis of anisotropic nanoparticles, evidence behind the function of CTAB in nanoparticle synthetic pathways has been inherently limited due to the lack of knowledge about the nature of the nanoparticle-CTAB interface. To date, it has remained controversial whether or not the bromide counterion coordinates with the Au surface. To investigate the structure of CTAB on Au nanoparticle surfaces, XAFS was used as a probe with element-specificity. XAFS, a bulk technique, is employed as a surface-sensitive technique by using sufficiently small (~2 nm) Au nanoparticles that are composed of a majority of surface atoms. Through this approach, specific detail about the CTAB-Au NP interface is resolved; namely, Br- and the CTA^+ headgroup both adhere to the Au surface. This enables the formation of a stable CTAB bilayer around the nanoparticle surface while maintaining an Au surface that is relatively charge neutral. The results of this study not only provide insight into how CTAB binds to Au nanoparticle surfaces, but also establish an effective methodology for investigating nanoparticle surface structure *in situ.*

5.2 Introduction

Nanoparticle colloidal synthesis relies on the introduction of a surfactant or stabilizing agent into solution to bind to the nanoparticle surface. Without a surface-binding species, nanoparticles irreversibly aggregate due to their high surface energy, making such species a necessary reaction component. One commonly used stabilizing agent in Au nanoparticle systems is cetyl-trimethyl ammonium bromide (CTAB) (molecular structure shown in Figure 5.1, bottom), which has been

used to synthesize Au nanoparticles across a range of sizes and morphologies.[35, 153-155] In particular, CTAB has been attributed to directing nanoparticle anisotropic growth in the synthesis of Au nanorods,[13, 140-141] as discussed in more detail in chapter 3 of this thesis. Despite its advantageous capabilities as a surfactant, however, CTAB also presents a series of challenges to nanoparticle systems. For example, CTAB has proven difficult to effectively remove during ligand exchange processes necessary for coating nanoparticles with functional molecules, requiring complex strategies to be employed.[132, 156-157] CTAB removal is especially problematic when considering these particles for use in biomedical applications, as CTAB has been shown to be mildly cytotoxic.[158]

Understanding the role of CTAB in nanoparticle synthesis in addition to its preferred removal requires a thorough knowledge of the CTAB-nanoparticle interface structure. Yet due to controversy concerning the nature of CTAB surface binding, these issues remain unresolved. The controversy results from the lack of atomic scale information about how CTAB adheres to the Au surface.[13] Specifically, it has yet to be confirmed whether or not the Br^- counterions coordinate with Au surface atoms. While some studies rely on the assumption that Br^- is the primary binding species (Figure5.1b),[13, 143-144, 152] others claim that is only the CTA^+ head group that adheres to the Au surface (Figure 5.1a).[13] It is also possible that both the CTA^+ headgroup and Br^- counterion both adhere to the nanoparticle surface (Figure 5.1c). In fact, the only experimentally confirmed aspect of the CTAB structure is the formation of a bilayer around the nanoparticle, rather than a single layer.[159] On the atomic scale, the CTAB-Au interface structure remains experimentally unconfirmed.

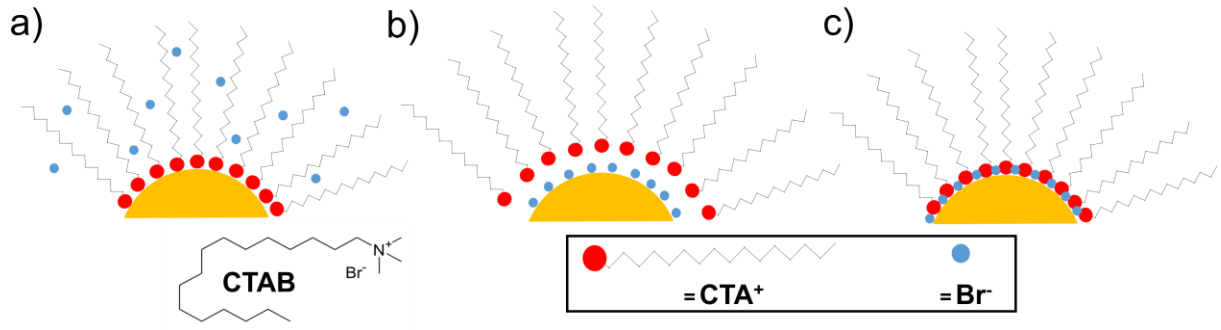

Figure 5.1 Possible nanoparticle-CTAB interface structure configurations. a) The CTA^+ headgroup binds to the nanoparticle surface, b) The Br^- counterion binds to the nanoparticle surface and c) Both the CTA^+ headgroup and Br^- counterion adhere to the nanoparticle surface.

In order to elucidate how CTAB adheres to an Au nanoparticle surface, it is necessary to employ a technique which provides atomic scale information that is also element-specific. To this end, XAFS at the Au L_3 edge is employed. From the near edge (XANES) region of the spectrum, the oxidation state of surface Au can be determined. From the extended (EXAFS) region, the species bound to the Au surface atoms, as well as inter-atomic spacings and coordination numbers, can be extracted. It is possible by this method to differentiate between Au neighboring elements as long as their atomic numbers (Z) are $\Delta Z \geq 5$. This element sensitivity in the EXAFS signal relies on differences in atomic scattering of the Au emitted photoelectrons. XAFS, in theory, proves a viable method to differentiate whether or not Br^-, CTA^+, or both adhere to surface Au atoms in the nanoparticle.

Although XAFS is a bulk technique, which probes the environment of an element of interest in the structure on average, surface structure can be realized when nanoparticles are sufficiently small. Previous XANES work proves that nanoparticle surface-specific effects are dominant in sub

2-nm nanoparticles, for which the majority of atoms are at the surface.[24] By the same principle, EXAFS can be used in tandem with XANES results in order to glean quantitative and element specific binding information of atoms attached to the nanoparticle surface.

We make use of this unique XAFS strategy to investigate the structure of CTAB on the surface of sub-2 nm Au nanoparticles. As a model system, seed particles typically used to make anisotropic Au nanostructures were used.[35] A global CTAB concentration of 50 mM was chosen, as it is within the range of concentrations typically employed in common nanoparticle synthesis reactions.[35, 153-155] This enables the extension of the results of this study to multiple synthetic systems that make use of similar nanostructures. The key result from this study is that both CTA^+ and Br^- from CTAB are found to adhere to the Au NP surface (Figure 5.1c), enabling a vesicle-like structure to form around the particles in solution. This finding has important implications not only for nanoparticle surface charge, but also for the inherent stability of the CTAB attachment to the particle surface. Knowledge from this study should enable a better understanding of the role that CTAB plays in the synthesis of Au nanoparticles, and aid in the development of strategies to effectively remove CTAB to preferentially functionalize the Au surface with alternative ligands.

5.3 Methods

5.3.1 Nanoparticle synthesis

~2 nm Au capped nanospheres were synthesized via the procedure established by El-Sayed and co-workers.[35] Briefly, 0.6 mL of 0.01 M ice cold $NaBH_4$ (Sigma Aldrich) was added to a stirring solution of 5 mL 0.2 M CTAB (Sigma Aldrich), 0.25 mL 0.01 M HAuCl4 (Sigma Aldrich) and 4.75 mL NANOpure™ H2O in a 20 mL glass vial at room temperature. This resulted within a matter of seconds in the synthesis of ~2 nm Au nanoparticles capped with CTAB, with a global

CTAB concentration of 94 mM. The particles were then diluted with NANOpure™ to a global CTAB concentration of 50 mM.

5.3.2 XAFS data collection and analysis

XAFS spectra at the Au L_3 edge (11919 eV) were collected at the Dupont Northwestern Dow (DND)-CAT sector 5BMD of the Advanced Photon Source at Argonne National Laboratory. Data was obtained using a Si (111) monochromator and collected over a range from 11.8 to 12.3 keV. XAFS spectra were collected in fluorescence mode using a four-element SDD fluorescence detector, with the Au L3 edge energy calibrated with an Au metal foil standard. CTAB-capped Au nanoparticles (50 mM CTAB) were suspended in 0.5 mL polypropylene tubes for measurement. To improve statistics, twenty half-hour scans at 4 spectra/scan were averaged. Self-absorption was not a concern in the measurement, because the Au atomic concentration was in the dilute limit (~1 μM).

XAFS data was processed using ATHENA and ARTEMIS software, part of the IFEFFIT package.[116] Crystal structures from theory were imported using ATOMS.[160] The absorption edge energy was determined from the maximum of the first derivative in the absorption data and the background was subtracted using the AUTOBK algorithm.[161] The EXAFS region (greater than 100 eV above the absorption edge)[50] was normalized and a k-weight of 1 was chosen in order to provide an even spectrum throughout the region of interest (2 – 10 $Å^{-1}$), as a result of domination of low-k scatterers from low-Z surface elements.[49] EXAFS spectra were modeled according to the EXAFS equation:[47, 50-52]

$$\chi(k) = \sum_{\Gamma}\left[\frac{N_\Gamma S_0^2 F_\Gamma(k)}{2kR_\Gamma^2} e^{-2k^2\sigma_\Gamma^2} e^{-2R_\Gamma/\lambda(k)} \times \sin(2kR_\Gamma + \phi_\Gamma(k))\right] \quad (5.1)$$

Where Γ is the summation over the individual scattering pathways included in the model, k is the photoelectron wavevector, $F_\Gamma(k)$ is the scattering amplitude, $\lambda(k)$ is the mean free path for inelastic scattering of the photoelectron and $\Phi(k)$ is the phase shift, which is calculated as a function of the absorbing and scattering atom using the ARTEMIS software. S_0^2, the amplitude reduction factor, was set to 0.74 during fitting (the value extracted from fitting the Au foil). This enables a more accurate determination of the coordination number.[52] Degeneracy (or number of neighbors in a given shell of the same type) (N_Γ), interatomic distance (R_Γ), energy shift parameter (E_0), and mean-squared disorder (σ_Γ^2), which includes contributions from structural and thermal disorder to the Debye-Waller factor,[50] were adjusted to determine the best fit model.

Goodness of fit parameters for the models were evaluated using minimization of the R-factor parameter and error bars for individual parameters were estimated to one sigma through altering the value of the parameter until the value of chi-square for the overall fit was increased by one. Spectra were fit first in k-space, then evaluated in R-space and q-space, in order to ensure that the best fit to the raw data in k-space was translatable to the other fitting spaces.

5.4 Results

5.4.1 Determination of nanoparticle size

Due to the tendency of ~2 nm Au nanoparticles to fuse together when deposited onto a surface,[19] it is necessary to use an *in-situ* measurement to determine the particle size. X-ray scattering was also not a possibility, due to the high solution scattering from CTAB in solution, making it not possible to discern any signal from the nanoparticles themselves (Figure A5.1). EXAFS, however, has been previously used to determine the size of spherical FCC nanoparticles from the reduction in average atomic coordination number in comparison to their bulk counterparts according to the following expression derived by Calvin et. al:[118]

$$n_{nano} = \left[1 - \frac{3}{4}\left(\frac{r}{R}\right) + \frac{1}{16}\left(\frac{r}{R}\right)^3\right] n_{bulk} \quad (5.2)$$

Where n_{nano} is the EXAFS-determined Au coordination number for the nanoparticles, n_{bulk} is the Au bulk coordination number (12), r is the distance between nearest neighbor atoms and R is the nanoparticle radius. From this relation, we find the nanoparticle diameter for our system to be 1.7 nm. From this quantity, using spherical cluster approximation[162], we find that ~ 65 % of the atoms within the nanoparticle are on the nanoparticle surface. Large mean-squared disorder values compared to bulk (~ 51 % larger) are also observed, giving support to the concept that a large number of Au atoms are located on the surface, resulting in greater average disorder due to the high concentration of surface defects.[163-164] Furthermore, this shows that the average Au atom within the particles should be exposed to the solution environment. In theory, this means that the EXAFS-derived coordination environment should show contribution from solution and surface species.

5.4.2 Demonstrated XAFS sensitivity to nanoparticle surface structure

The XANES (Figure 5.2a) and EXAFS (Figure 5.2b) regions of the Au L_3 edge absorption spectrum both show a significant sensitivity to surface structure. This is seen by the comparison of spectrum from the CTAB coated ~2 nm Au nanoparticles to that of an Au foil. Reduction in Au coordination number alone due to the small nanoparticle size would reduce the amplitude of the EXAFS oscillations without changing their phase or k-dependence, and should not change the XANES signature. Rather, both the XANES and EXAFS regions are drastically different from those of the Au foil. From Figure 5.2b, the EXAFS oscillations differ from those of the Au foil in amplitude, phase and k-dependence. This reveals that the spectrum cannot be modeled using Au-

Au contributions from the nanoparticle core alone and requires extraction of nanoparticle-solution interface structure.

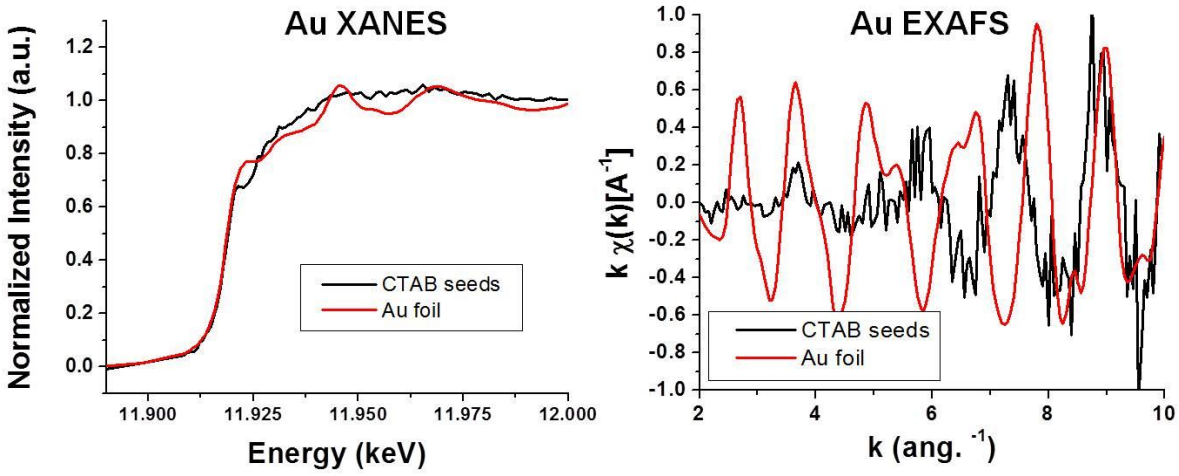

Figure 5.2 Au L_3 edge XAFS spectra of CTAB-capped Au nanoparticles compared with Au foil. Both XANES (left) and EXAFS (right) regions of a bulk Au foil (red) in comparison to 1.7 nm CTAB-capped Au nanoparticles (black) show that the XAFS spectrum is sensitive to nanoparticle interface structure.

5.4.3 XANES

From XANES results (see Figure 5.2a), we find, that CTAB induces a very slight negative charge on the nanoparticle surface. This is deduced from the intensity of the white line peak, which is inversely proportional to the occupancy of Au 5d states.[24, 28, 165] Therefore a decrease in the intensity of the white line peak in comparison to the Au foil denotes that the Au atoms on the nanoparticle surface have a slight net negative charge. While this is in line with the hypothesis that the CTA^+ molecule coordinates with the Au surface, which would create Au^- surface atoms, a viable oxidation state for Au, the only slight net negative charge suggests that either there must be

either a low surface coverage or weak coordination of CTA^+ or charge screening from another solution entity. In contrast, if the primary mode of Au-CTAB surface coordination is the formation of an AuBr complex as has been previously speculated in literature,[27] the formation of Au^+ would be expected rather than the slight negative charge observed. Thus, if Au does bond to the Br counterion, then it must be the case that there is significant charge screening from surrounding positive ions. In either case, it is clear that the Au surface is not positively charged.

5.4.4 EXAFS

EXAFS modeling parameters are shown in Table 5.1. It should be noted that while Au-Br, Au-Au and Au coordination to C or N can be differentiated, Au-C and Au-N contributions cannot be distinguished from each other since ΔZ is not sufficient.[28] This is demonstrated in Fig. A5.1, which shows simulations of EXAFS spectra from possible surface-coordinated species at the same bonding distances. For this system, however, since C and N are both species in the CTA^+ part of the molecule, this does not limit the determination of whether CTA^+ or the Br^- counterion is coordinated with the Au surface atoms.

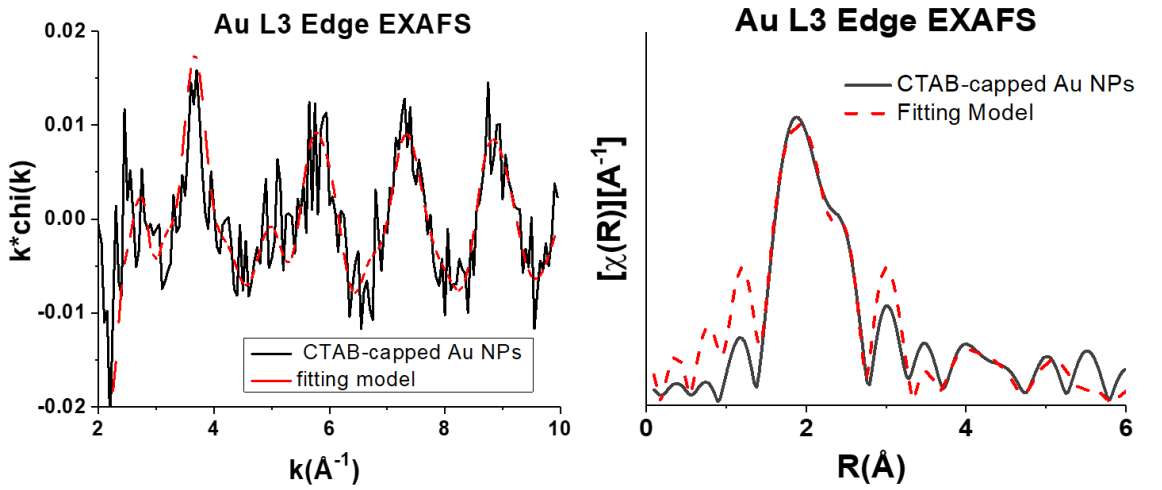

Figure 5.3 EXAFS k-space spectrum of CTAB-capped Au nanoparticles (black) and fitting model (red). The model matches the data in both low k and high k regions (left) and in R-space (right). Parameters listed in the table below were extracted from this model.

Table 5.1 EXAFS modeling parameters summary based on Eq. 5.1.

Pathway	**Coordination Number**	**Interatomic spacing (Å)**	**Mean-squared disorder ($Å^2$ x 10^{-3})**
Au - Br	2.1 ± 0.5	2.39 ± 0.01	3 ± 2
Au - N/C	1.7 ± 0.4	2.40 ± 0.03	3 ± 2
Au - Au	8.9 ± 2	2.83 ± 0.03	16 ± 7

The above table summarizes the parameters (coordination number (CN), interatomic spacing (R), and mean-squared disorder (σ^2)) obtained for the ligand species closest to the Au surface. Additional contributions and parameters are included in the appendix. Parameters shown represent average radial structure for an Au atom within the given sample.

Local structure parameters were derived from EXAFS modeling (Figure 5.3). The most notable result is that Au-Br pathways were required to achieve a reasonable model. Without the inclusion of Au-Br, a good statistical fit to the EXAFS spectrum could not be achieved (See Figure A5.2). EXAFS-derived coordination numbers (Table 5.1) reveal that the ratio of Au-Br to Au-N/C is approximately 1:1. Thus this suggests that although we find the Br^- counterion close to the Au surface which would suggest the induction of a positive charge on Au surface atoms, nearby CTA^+ also coordinated with the Au surface, such that the Au surface does not retain a positive charge, but rather a slightly negative charge. Low mean-squared disorder values reveal that both the Au-Br and Au-N/C contributions ($\sigma^2 = 0.0025 \pm 0.0015$ and 0.0025 ± 0.0021 Å^2, respectively) are well ordered[28] and are likely ionically coordinated with the Au surface. The determined Au-Br and Au-N/C bond-lengths for these species (~2.4 Å) are comparable to those previously observed in Au clusters from x-ray crystallography[166] and from computational modeling.[167]

5.5 Discussion

The differences observed between the CTAB-capped Au NP XAFS spectrum and the bulk FCC Au spectrum confirm that the Au NPs cannot be approximated using Au FCC pathways alone. At the small nanoparticle size (1.7 nm), we find that ~65 % of the Au atoms are on the surface. Likely, this high surface area/volume ratio, in addition to the higher ligand packing that occurs for particles with a higher degree of curvature, makes it necessary to include pathways from surface-coordinated atoms. By this method, we demonstrate that it is possible to extract structural details concerning particular interface-coordinated species. It should be noted that this method may not be suitable for larger nanoparticles, or for particles that have a smaller radius of curvature, affecting molecular packing capability.[25]

Concerning the question of whether or not Br coordinates with the Au surface, EXAFS analysis determines that Br is coordinated to the Au surface, at a close bonding distance of 2.39 Å. This distance is comparable to those observed for Br^- coordinated with Au clusters from x-ray crystallography and computational modeling.[166] XANES, results, however, confirm that it cannot be only Br^- that coordinates to the Au NP surface. If this were the case, then the surface Au oxidation state would be Au^+ rather than the surface atoms having a slight negative charge, which instead is observed. This is in agreement with work which suggests that the CTA^+ molecule adheres to the Au surface, assisting in the formation of a CTAB bilayer around the particles. We also observe coordination to CTA^+ from XAFS pathways at a comparable interatomic spacing to that observed for Au-Br. These bond lengths are also reasonable when compared to those for Au-N and Au-C from species coordinated to Au clusters.[166-167] Although a high N/Br ratio was previously suspected from EDX results,[168] this is not observed. Rather, we observe a N/Br ratio of ~1:1.

The coordination of both CTA^+ and Br^- to the Au surface in comparable amounts would result in an Au surface that is relatively charge neutral. This explains why from XANES, only a slight negative deviation from the Au foil white line is observed. The positive and negative ions close to the Au surface then enable a stable CTAB bilayer to form around the Au nanoparticle. This implies that in addition to removing both the CTA^+ molecule and Br^- counterions from the Au NP surface during ligand replacement, the CTAB bilayer must also be sufficiently disturbed, which is inherently stable as proven by CTAB's capability of forming vesicles in solution.[169] This multi-component coordination in a stable bilayer structure likely contributes to the stability of CTAB as a surfactant and the difficulty in using ionically-bound ligands to replace it.

5.6 Conclusion

Prior to this study, minimal information had been concretely obtained concerning the NP-solution interface interactions between Au nanoparticles and CTAB surfactant. To probe this interface at the atomic scale, we introduced the use of XAFS as a method to obtain surface-sensitive atomic coordination environment information. This is achieved through the use of sufficiently small Au NPs such that a majority of the atoms within the particle are on the surface. The key contribution of this work is to the best of our knowledge, the first experimental proof that the Br^- counterion from CTAB coordinates to the Au surface rather than the CTA^+ molecule alone, which has been a subject of debate in prior hypotheses of CTAB-capped NP surface structure. The coordination of Au-Br and Au-CTA^+ in a near 1:1 ratio results in screening of the Au surface such that only a slightly negative charge on the Au surface atoms remains. The surface structure of Au-CTAB NPs is considered essential to understanding the growth and preferential functionalization of nanostructures which employ the use of CTAB as a surfactant. Thus the results of this study have important implications on the validity of such hypothesis and understanding of these processes.

5.7 Proposed future work

5.7.1 Computational verification of CTAB structure

Given the difficulty of experimentally verifying the aforementioned EXAFS-derived nanoparticle surface ligand structure at the atomic scale in-situ, computational investigation of the most energetically stable structure for CTAB on NP surfaces provides a reasonable alternative. In providing information about system energetics, this may also aid in providing an explanation for not only the structure, but also for why it is preferred.

Computational methods have been used to consider the most energetically favorable states for surface bound species on nanoparticles.[167] One particular approach involves the use of density functional theory (DFT) to first determine binding modes to the NP surface, followed by a molecular dynamics (MD) relaxation of the molecular structure of the surface species. This approach was attempted for this study by Daniel Hannah (Schatz group). Unfortunately, he determined after some preliminary work that due to the size of the CTAB molecule, there would be too many atoms in the simulation to make the investigation feasible with respect to computation time and cost. It is possible, however, that with further development of computational approaches, that the structure could be investigated in this method and compared with the XAFS-determined CTAB structure.

5.7.2 Study of CTAB structure on planar surfaces

This study focused on how CTAB binds to nanoparticle surfaces with high curvature. As particle size increases, surface curvature decreases and approaches that of a bulk surface. It is therefore interesting to consider how ligand binding to a nanoparticle surface compares with binding to a planar surface. While it is expected that ligand packing density will differ due to steric hindrance, it may be that the interface coordination differs as well.

To this end, XAFS experiments could still be performed using surface XAFS (SEXAFS) in glancing angle geometry, such that the measurement is surface-sensitive due to the low penetration depth as a result of the low measurement angle. A schematic of this measurement setup is shown in Figure 5.4. This approach has been used previously to study material surface structure, proving that this would be an appropriate method for studying molecules adhered to planar surfaces if the surface is sufficiently smooth.[170]

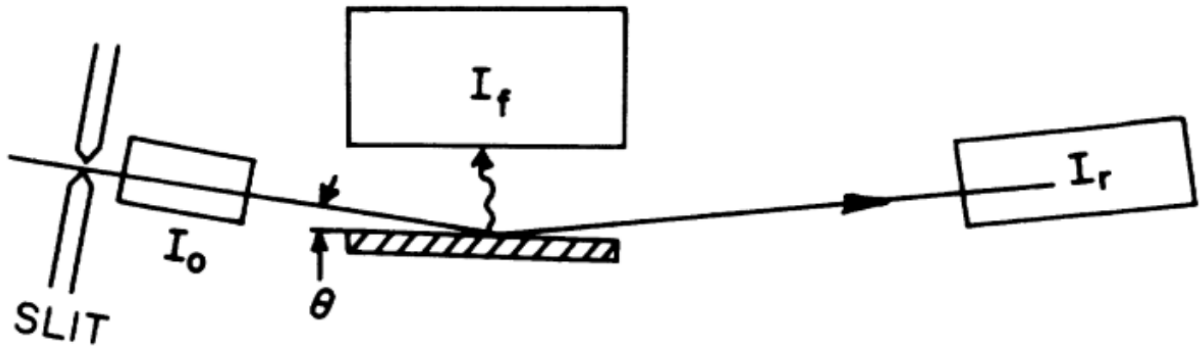

Figure 5.4 Measurement setup for SEXAFS, adapted from Heald et. al.[171] Using a glancing angle (θ), and placing a fluorescence detector at 90° (I_f), surface sensitivity can be obtained for a planar sample. If an additional detector is placed after the sample (I_r), X-ray reflectivity measurements can also be obtained to investigate sample roughness and electron density.

Another advantage to studying the structure of CTAB on a planar surface is the potential to use X-ray standing wave (XSW) to study the distance between the Br^- counterion and the Au surface. This method has previously proven successful in determining the distance of adsorbed Br atoms from a Si surface.[172] One challenge that can be anticipated in applying this approach is its reliance on the Br^- ions to be at a fixed distance from the Au surface. This would require complete removal of Br^- ions not adhered to the Au surface from solution, which remains a challenge.

5.7.3 Study of CTAB structure on faceted nanoparticle surfaces

As mentioned in the previous section, SEXAFS and XSW can be used to study surfaces in planar structures. The same methods could be employed for nanoparticles if the particles are faceted and monodisperse, and deposited onto an atomically smooth surface. The structure of CTAB on nanorod surfaces has been of particular interest due to the role that CTAB is thought to

play in the synthesis of these particles.[13] It was shown in chapter 3 of this thesis that nanorods can be deposited in a single layer onto a substrate. The challenges to such a study would be ensuring that there was sufficient surface coverage of Au particles, in addition to those mentioned in the previous section. Investigation of the CTAB structure on Au nanorod surfaces, and those of other anisotropic nanoparticles would be an important contribution, especially in light of the investigation from chapter 4. As speculated, it is possible that CTAB binding to surface Ag may explain our result since surface Ag is directly correlated to nanorod anisotropic growth.

Chapter 6: Towards understanding CTAB replacement on Au NP surfaces

6.1 Abstract

Removal of CTAB from Au nanoparticle surfaces is commonly required for surface functionalization with alternative ligands and due to its cytotoxicity. Determining quantitative exchange behavior and the overall surface structure upon ligand exchange, however, remains relatively unexplored. Herein, we study the replacement of CTAB with phosphine and thiol ligands (BSPP and PEG-thiol) in equal concentration. XAFS is used as a method to study the Au-solution interface using sub 2 nm core templates. This enables atomic-scale structural information to be combined with molecular-scale information obtained from conventional UV-vis and zeta-potential measurements. In particular, even when all three ligands are together in solution at equal concentration, we find that a significant amount of CTAB remains on the nanoparticle surface. Also, while BSPP and PEG-thiol are both capable of replacing a fraction of surface CTAB, the CTAB-bilayer structure is perturbed in different ways depending on the replacing species.

6.2 Introduction

Control over nanoparticle surface structure has become a subject of increased interest due to the intimate connections between the nanoparticle surface chemistry and resulting novel properties. As the advantages of nanoparticles over their bulk counterparts are a result of their high surface area to volume ratio, a thorough elucidation of their surface environment is critically important in determining their functionality. For example, in the creation of nanocomposites and metamaterials which involve the use of nanoparticles, it has been found that it is the organic species on the nanoparticle surfaces, rather than the core material, which affect their distribution within the

surrounding matrix material, causing the nanoparticles to distribute in a way that mimics the free polymer species.[173] Surface species also affect the optical properties and dielectric behavior of nanoparticle constructs.[174-175] As surfaces are used for catalysis, nanoparticles present an ideal construct, yet the surface chemistry and degree of access to preferential surface sites are highly affected by nanoparticle surface chemistry.[153, 165] Nanoparticle surfaces can also be modified with species such as DNA or peptides, which proves useful in biomedical applications and programmable assembly methods.[9, 176] Thus nanoparticle surfaces are essential in dictating their functionality, yet in order to control and optimize nanoparticle surface species, it becomes necessary to employ and understand nanoparticle ligand exchange chemistry.

One particular surface species that has been of interest for ligand exchange is CTAB, a ligand whose structure is discussed in detail in chapter 5 of this thesis. CTAB is an important component in the synthesis of anisotropic Au nanostructures.[35, 154-155] However, due to its cytotoxicity, CTAB removal is often desired to make use of these particles in biological applications.[158] To this end, a variety of sophisticated procedures have been developed to replace CTAB.[132, 156-157] There are, however, no reliable ways to determine whether a majority of CTAB has been removed, due to lack of atomic scale information concerning the surface species, in addition to the difficulty of removing excess CTAB from solution. In this study, atomic scale information from XAFS is combined with molecular scale information obtained from UV-vis absorption spectroscopy and zeta-potential measurements to investigate the exchange of CTAB with (BSPP (bis(p-sulfanatophenyl)phenyl-phosphine) and PEG (polyethylene glycol)-thiol). For the purpose of studying which ligand is the preferred surface species, ligands were brought to the same global concentration in solution (50 mM or 10 mM). A schematic of the nanoparticle samples and ligand molecular structures is shown in Figure 6.1.

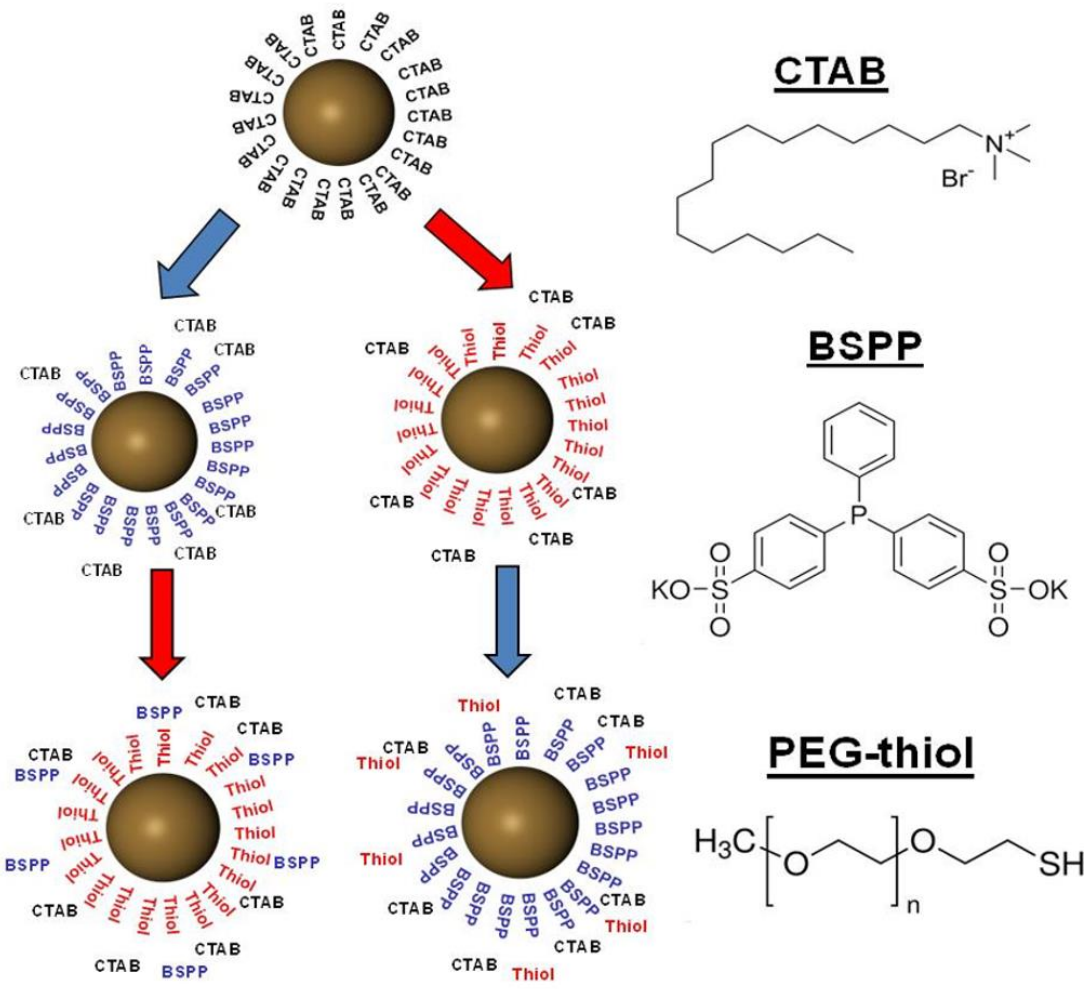

Figure 6.1 Schematic of nanoparticle samples (left) and ligand molecular structures (right). Starting with CTAB-capped Au nanoparticles (top), nanoparticle solutions were brought to equal concentrations of either BSPP (blue) or PEG-thiol (red, n = 4) (middle). Structures where the third ligand was added (bottom) were also investigated, to study which ligand (BSPP or thiol) has a greater affinity to the Au surface.

In literature, it is hypothesized that thiolated species would have the greatest affinity for the Au surface, and should effectively replace CTAB except in the case of surface-facet specific

processes.[140] The key results of this study show, in contrast, that at a 1:1 concentration of CTAB and replacement ligands, a significant amount of CTAB still remains on the nanoparticle surface. Also, while BSPP and PEG-thiol are both capable of displacing a fraction of the CTAB from the nanoparticle surface, they disrupt the CTAB bilayer in different ways. As a result, when all three ligands are present in solution, the same overall surface composition results, whether BSPP or PEG-thiol is the first exchange species introduced. In addition, through combining atomic scale information derived from XAFS with molecular scale information from UV-vis spectroscopy and Zeta-potential measurements, a method is introduced to better understand ligand structure and exchange. This method can be extended to create a library of surface species binding information to better inform nanoparticle synthesis and exchange methods that make use of preferential surface species.

6.3 Methods

6.3.1 Synthesis of CTAB-capped particles

CTAB-capped Au ~2 nm nanospheres were synthesized via the procedure established by El-Sayed and co-workers.[35] Briefly, 0.6 mL of 0.01 M ice cold $NaBH_4$ (Sigma Aldrich) was added to a stirring solution of 5 mL 0.2 M CTAB (Sigma Aldrich), 0.25 mL 0.01 M $HAuCl_4$ (Sigma Aldrich) and 4.75 mL NANOpure^{TM} H_2O in a 20 mL glass vial at room temperature. Within a matter of seconds the reaction produces ~2 nm Au nanoparticles capped with CTAB, with a global CTAB concentration of 94 mM.

To synthesize CTAB-capped Au 15 nm nanospheres, the as-synthesized ~2 nm Au nanoparticles were overgrown with additional Au according to the procedure developed by Fenger

et al.[153] Briefly, 80 mL of 0.1M CTAB and 10 mL 0.01M $HAuCl_4$ were added to 400 mL NANOpure™ water. 2 mL 0.1 M ascorbic acid (Sigma Aldrich) was then added, reducing Au^{3+} to Au^{+}, turning the solution from goldenrod to clear. 5 mL of the as-synthesized 2 nm Au nanoparticles were added to this solution, resulting in the solution turning ruby-red over several minutes. This resulted in the formation of ~15 nm CTAB-capped Au nanoparticles used in UV-vis spectroscopy and zeta potential measurements.

6.3.2 Functionalization of CTAB-capped particles with BSPP and PEG-thiol

BSPP (Strem Chemicals) or PEG-thiol (Sigma Aldrich) was added to the CTAB-capped Au nanospheres as synthesized above, such that the final concentrations of both ligands was equivalent (50 mM or 10 mM). In the three mixed-ligand case, PEG-thiol or BSPP were added to solutions of 1:1 CTAB:BSPP or CTAB:PEG-thiol Au nanoparticles respectively, such that the final concentration of each of the three ligands in solution was 50 or 10 mM. After each ligand addition, the nanoparticle-ligand solutions were heated to a temperature of 50 °C for 30 minutes and allowed to cool down to room temperature in an attempt to drive the system towards its equilibrium Au NP-solution interface structure.

6.3.3 XAFS data collection and analysis

XAFS data collection and general analysis methods followed the same procedure described in Section 5.3.2 of this thesis. Additionally, it should be noted that in order to isolate the effects of the nanoparticle surface structure, the assumption was made in the modeling process that the Au-Au pathways from the nanoparticle core remained constant from sample to sample. Making this assumption and fixing the Au core pathways assumes that any change in the spectrum is a result of changes in the Au surface structure. From model to model, the process mimicked the exchange

behavior in that the ligand exchanged model began with the model from the previous structure and was altered accordingly until the best fit model was achieved.

6.3.4 UV-vis spectroscopy

UV-Vis Spectroscopy scans of samples in 1 ml NANOpure^{TM} water were taken using a Cary 5000 UV-vis spectrophotometer across the range of 200-800 nm using a 1 cm path length.

6.3.5 Zeta potential measurements

Zeta potential measurements were collected on a Malvern Zetasizer Nano instrument. 3 sets of 100 measurements were collected and averaged to achieve statistical significance.

6.3.6 Small angle X-ray scattering

Small angle X-ray scattering measurements were collected in the NU X-ray diffraction facility using a Rigaku SMAX3000 instrument with a Bruker Vantec 2000 2-D detector system and Cu anode. For measurement, as-synthesized CTAB-capped Au nanoparticles were concentrated via centrifugation and placed in a 1.5 mm inner diameter quartz capillary (Charles Supper). Measurements were collected over a duration of 30 minutes. Sample-to-detector distance was calibrated using a silver behenate standard. Data was processed (including angle integrated) using Nika[177] and fit to a spherical form factor using Igor Pro.

6.4 Results

6.4.1 Determination of nanoparticle size

Since CTAB-capped Au 2 nm nanoparticles came from the same batch as those used in Chapter 5 of this thesis, NP size was determined via the same method established by Calvin et. al[118] and determined to be 1.7 nm in diameter (refer to Section 5.4.1).

For the larger CTAB-capped Au nanoparticles, nanoparticle size was determined from SAXS fitting to a spherical form factor (Figure 6.2). From the best fit model, the particle size was determined to be 14.7 nm in diameter, with a polydispersity of 13 %. The larger nanoparticle size from the overgrowth was therefore sufficient to support localized surface plasmon resonance (LSPR) to compare ligand optical properties and appropriate for light scattering measurements to determine the nanoparticle zeta potential.

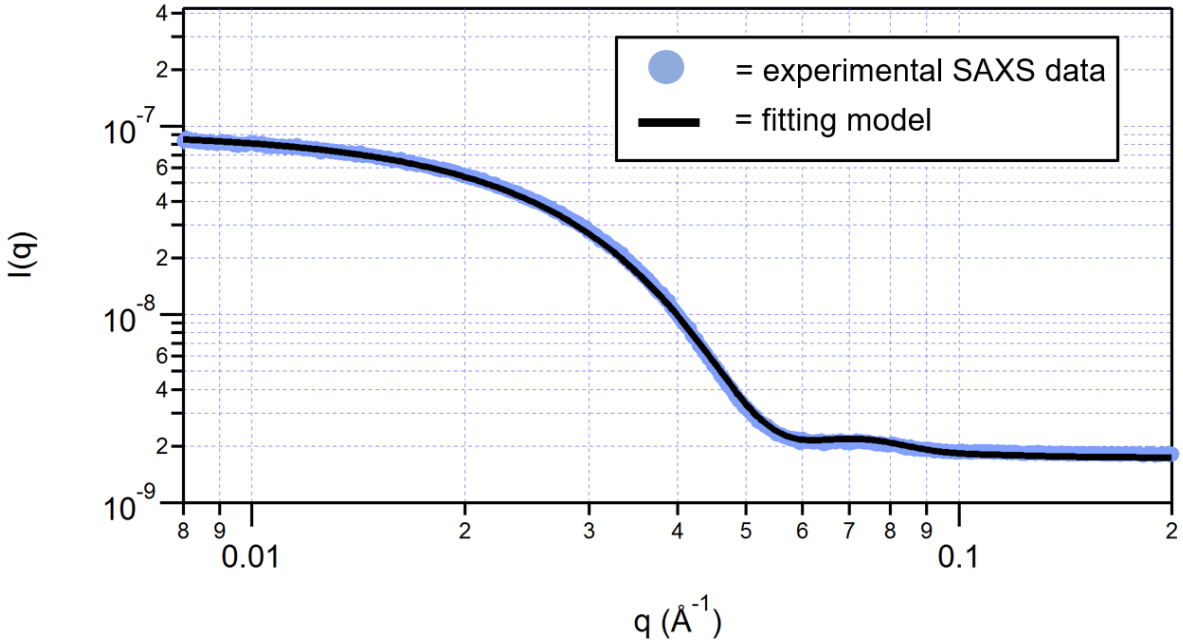

Figure 6.2 SAXS pattern of CTAB-capped Au NPs. ~2 nm Au nanoparticles subsequent to overgrowth with additional Au were determined to be 14.7 nm in diameter based on SAXS modeling (black line) using a spherical form factor compared to the Au nanoparticle SAXS data (purple circle).

6.4.2 UV-vis spectroscopy

Due to the sensitivity of nanoparticle optical properties to their surrounding environment, UV-vis spectroscopy has traditionally been used to monitor ligand replacement by observing a shift in the nanoparticle LSPR peak.[175] Using 14.7 nm Au NPs and global ligand concentrations of 10 mM, LSPR positions (Table 6.1) determined from UV-vis spectra (Figure 6.3) were tracked as a function of ligand replacement. It should be noted that 0.1 mM PEG-thiol concentrations rather than 10 mM were used for the case of these larger nanoparticles, since the particles were not stable under the higher thiol concentrations. Interestingly, however, the particles were stable with 10 mM PEG-thiol when 10 mM BSPP was first added to the solution. In addition, particles were stable with even higher PEG-thiol concentrations (50 mM) for the 1.7 nm Au cores. Regardless, to confirm that using the lower PEG-thiol concentration would not affect the overall nanoparticle surface structure, UV-vis spectra of 14.7 nm CTAB-capped Au NPs exchanged with 10 mM BSPP, followed by 10 mM or 0.1 mM PEG-thiol were collected (Figure A6.1) and show that the LSPR peak position is the same for both spectra within the 1 nm measurement resolution. This makes it appropriate for us to use 0.1 mM PEG-thiol to compare to the samples with 10 mM BSPP and CTAB.

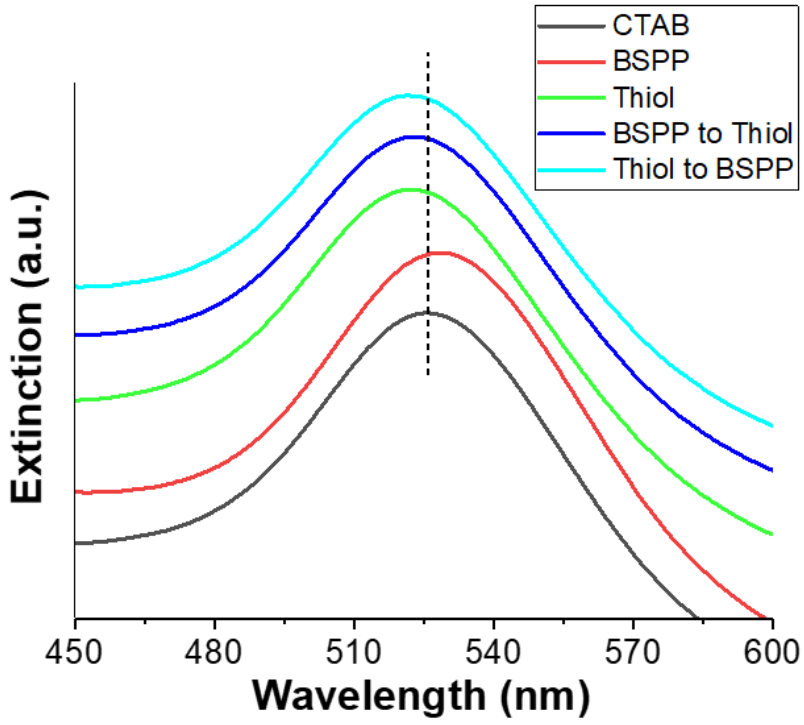

Figure 6.3 UV-vis spectra of 14.7 nm Au nanoparticles with varying surface structure. From UV-vis spectra, it is observed that from the initial CTAB-capped NPs (black), a red-shift is observed when BSPP is introduced into solution (red) and a blue-shift when PEG-thiol is introduced (green). In the case where both BSPP and PEG-thiol are added into solution, a blue-shift characteristic of PEG-thiol is also observed. All ligand concentrations are at 10 mM with exception of PEG-thiol, which is 10 mM in the case that BSPP has been added first (blue) and 0.1 mM otherwise (turquoise, green).

Table 6.1 LSPR peak positions

NP ligand solution species	LSPR peak position (nm)
CTAB	525
CTAB to BSPP	528
CTAB to PEG-thiol	522
CTAB to BSPP to PEG-thiol	523
CTAB to PEG-thiol to BSPP	522

The LSPR peak position does indeed change as expected when different ligand species are introduced into solution. The LSPR peak for the starting CTAB-capped Au NPs is observed at 525 nm. A red-shift to 528 nm is observed when BSPP is introduced into solution. This shift in the LSPR peak suggests that BSPP does indeed displace a significant fraction of CTAB and itself binds to the NP surface. A shift is also observed when PEG-thiol is introduced into solution, this time a blue-shift to 522 nm. Due to the different wavelength shifts induced by BSPP vs. PEG-thiol, the direction of the shift for the case that both BSPP and PEG-thiol are introduced into solution should provide insight into whether BSPP or PEG-thiol is the preferred surface species. Since the 522 nm LSPR position for these samples, regardless of whether PEG-thiol or BSPP is introduced first, matches that when PEG-thiol alone is introduced, this suggests that PEG-thiol is the preferred surface species among the three ligands.

6.4.3 Zeta-potential of Au NPs with varying solution ligands

Zeta potential measurements were collected as a function of introduced surface ligand species and are listed in Table 6.2. As has previously been observed,[168] a positive zeta potential is observed for CTAB-capped Au NPs. Note that zeta potential measures not the Au surface charge, but rather the charge due to the overall particle + surface species. This would be expected due to the formation of a bilayer of CTA^+ with Br^- as a counterion.

Table 6.2 Zeta potential

NP ligand solution species	Zeta potential (mV)
CTAB	66
CTAB to BSPP	-20
CTAB to PEG-thiol	45
CTAB to BSPP to PEG-thiol	-20
CTAB to PEG-thiol to BSPP	-22

When BSPP is added to the CTAB-capped Au NPs, the zeta potential becomes negative. This is in agreement with the UV-vis results which suggest that BSPP displaces a significant amount of CTAB from the Au NP surface. If the phosphorus atom binds to the Au NP surface, these results are reasonable, given that the BSPP molecule itself is negative, having two sulfonate groups with in this case 2 K^+ counterions (See Figure 6.1). When PEG-thiol is added to solution, the zeta potential remains positive. This is interesting, since the PEG-thiol itself is uncharged. This means that some, but not all, of the CTAB has been replaced with PEG-thiol. The residual positive charge is a result of CTAB still present on the NP surface.

For the cases where all three ligands (CTAB, BSPP and PEG-Thiol) are present in solution, the zeta potential is negative, which is the same result as observed for the case where BSPP is the only replacing ligand present. This is interesting since the UV-vis results suggested that it is PEG-thiol that is the dominant surface species for this sample. Thus our results appear to be in contrast with each other, since if this were the case, we would expect the zeta potential to be neutral or slightly positive if residual CTAB remains. Since these techniques do not provide conclusive evidence for either case, XAFS is required to provide more atomic scale information to discern between them.

6.4.4 XANES

By using 1.7 nm Au NPs, XAFS analysis becomes sensitive to nanoparticle surface structure, as demonstrated in chapter 5 of this thesis. From XANES results (see Figure 6.4a), we can determine the surface charge of the Au NPs in comparison to an Au foil (Au^0). In chapter 5, we determined that for the case of CTAB-capped Au NPs the white line peak shows a decrease in intensity, indicating a slight negative charge on the Au surface. In comparison, the XANES signatures for the case that BSPP or PEG-thiol are introduced into solution, an increase in the intensity of the white line peak is observed, as is typically observed for a positively-charged Au surface. Note that the intensity is greater for BSPP than PEG-thiol, meaning that BSPP induces a greater charge on the Au surface when added to CTAB in a 1:1 concentration ratio. When both BSPP and PEG-thiol are added into solution, the white line peak increases more substantially. This suggests that more CTAB is removed and additional replacement ligands are bound when both are introduced into solution, regardless of replacement order.

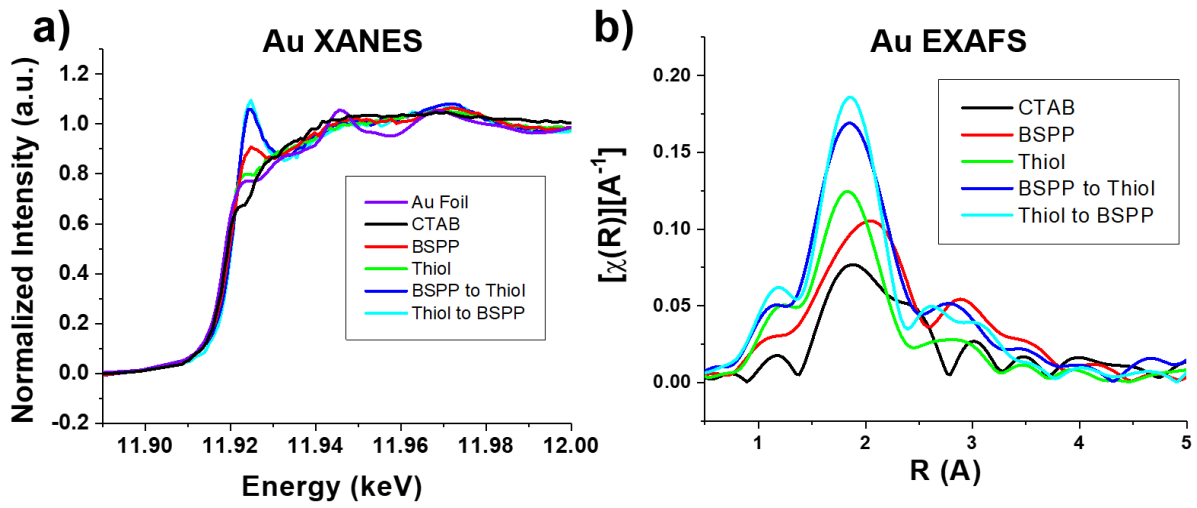

Figure 6.4 XAFS spectra at the Au L_3 edge of nanoparticle samples as a function of ligand species. a) XANES results show drastic differences in the intensity of the white line peak, which is inversely proportional to the occupancy of Au 5d states. b) EXAFS spectra show unique features related to the Au surface coordination when different ligand species are present in solution. Data was collected at a global ligand concentration of 50 mM for all ligand species present in solution. From Figures A6.2 and A6.3, it is observed that the XANES and EXAFS spectra are nearly identical for the case where 10 mM is used instead of 50 mM.

6.4.5 EXAFS

Qualitatively, from the EXAFS data (Figure 6.4b), the spectra differ when BSPP and/or PEG-thiol are introduced into solution, indicating a change in the coordination environment of Au surface atoms compared to a CTAB-capped Au NP surface (black). Also interestingly, we observe that for the cases that all three ligands are present in solution, the spectra appear to be a combination of the case where only BSPP or PEG-thiol are added rather than one or the other. This means that likely both BSPP and PEG-thiol are present on the NP surface in significant amounts.

Table 6.3 EXAFS-derived parameters

NP ligand solution species	Pathway	Coordination Number (N)	Interatomic Distance (R)	Mean-squared Disorder (σ^2)
CTAB	Au - Br	2.1 ± 0.5	2.39 ± 0.01	3 ± 2
	Au - N/C	1.7 ± 0.4	2.40 ± 0.03	3 ± 2
CTAB to BSPP	Au - P	1.0 ± 0.3	2.24 ± 0.03	3 ± 2
	Au - Br	0.7 ± 0.4	2.41 ± 0.03	3 ± 4
	Au - N/C	0.8 ± 0.4	2.28 ± 0.09	5 ± 3
CTAB to PEG-thiol	Au - S	1.0 ± 0.3	2.26 ± 0.02	4 ± 3
	Au - Br	1.0 ± 0.5	2.43 ± 0.04	4 ± 2
	Au - N/C	1.5 ± 0.4	2.44 ± 0.01	3 ± 3
CTAB to BSPP to PEG-thiol	Au - P/S	2.0 ± 0.6	2.26 ± 0.04	3 ± 2
	Au - Br	0.4 ± 0.3	2.41 ± 0.04	3 ± 6
	Au - N/C	0.4 ± 0.3	2.3 ± 0.1	5 ± 6
CTAB to PEG-thiol to BSPP	Au - P/S	2.5 ± 0.4	2.28 ± 0.04	4 ± 2
	Au - Br	0.5 ± 0.4	2.43 ± 0.04	3 ± 5
	Au - N/C	1.2 ± 0.3	2.52 ± 0.03	3 ± 5

Parameters derived from EXAFS modeling (Figure A6.4) are presented in Table 6.3. Pathways marked N/C and P/S are noted in this way due to the inability to distinguish pathways that are within atomic number Z ± 5 due to insufficient difference in atomic scattering.[28] Most notably, we observe that a significant amount of Au-Br pathways (unique to CTAB coordination) remain when a second ligand is introduced into solution. This is information that cannot be obtained from either of the aforementioned methods (UV-vis or zeta potential measurements) alone. While ~40 % of the Au-Br coordination is retained for the case of one additional ligand added, still ~25 % remains when both BSPP and PEG-thiol are introduced into solution. In a 1:1 ratio or even introducing additional replacing ligand, still a notable amount of CTAB is retained. When both BSPP and PEG-thiol are added, we also find that the resulting structure is the same within error, regardless of which ligand was added to the CTAB-capped Au NPs first.

6.5 Discussion

From UV-vis spectroscopy and zeta-potential measurements, it is unclear which species (CTAB, BSPP or PEG-thiol) has a greater affinity for the Au NP surface. The LSPR peak position in the case that all three ligands are together in solution matches that observed for the case that only PEG-thiol is introduced into the CTAB-capped Au NP solution. This would suggest that PEG-thiol is the preferred surface species. In direct contrast, zeta-potential measurements for the combined three-ligand system match that observed for the case that only BSPP is introduced into the CTAB-capped Au NP solution. Thus, were only one of these techniques used to characterize ligand exchange behavior, an accurate result would not be obtained.

It is only when combining the aforementioned molecular-scale results with atomic scale EXAFS coordination that we are able to draw the conclusion that both BSPP and PEG-thiol are present on the nanoparticles in significant amounts in these samples, which explains why strong signatures from either one is observed in the molecular-scale measurements. This shows the importance of atomic-scale characterization of nanoparticle surface structure in gleaning an accurate picture of which ligands are present on the nanoparticle surface. We are also able to maintain from only the combined information that CTAB is still present to a significant extent both in the case that one additional ligand is introduced into solution (~ 40 % CTAB remaining based on Au-Br coordination) and both BSPP and PEG-thiol are introduced into solution (~ 25 % CTAB remaining). This is particularly significant in considering the cytotoxicity of CTAB. Without the atomic-scale coordination information, it would not be possible to conclude that CTAB remains on the nanoparticle surface, which would possibly lead to unintentional yet unwanted effects when considering their use for biomedical applications.[141, 158]

It is also of interest to discuss the result that although XANES results show that both BSPP and PEG-thiol induce a positive charge on the Au NP surface, BSPP induces a greater charge than PEG-thiol. This is interesting, considering that the reduction in Au-Br pathways (indicative of CTAB binding) is comparable for both ligand replacement cases. This can be explained if we consider that BSPP and PEG-thiol may disturb the CTAB bilayer differently. Note that for CTAB, both CTA^+ and Br^- adhere to the Au NP surface, as discussed in Chapter 5. If the replacing ligand were to replace in the sites Br^- is adhered to the Au surface, it is possible that more Br^- would be replaced than CTA^+, leading to an overall less-positive Au surface due to screening from CTA^+. Results would suggest that this is the mode by which PEG-thiol replaces CTAB, whereas BSPP displaces both CTA^+ and Br^- groups equally. This speculation is supported not only by XANES results, but also by zeta-potential results, that still show a positive zeta potential for the case where PEG-thiol is added to solution. Also, we note from coordination numbers that a greater amount of Au-N/C (indicative of CTA^+) is retained for the case of PEG-thiol than BSPP. The increased charge-transfer and P/S coordination observed when all three ligands are present in solution, along with the difference in BSPP and PEG-thiol replacement modes, indicates that a mixed-ligand strategy towards functionalization of CTAB with preferred ligands may prove useful.

6.6 Conclusion

In this study, we present three main achievements: 1) We present a methodology to study ligand replacement at the atomic scale using XAFS. It is only when molecular scale measurements were combined with atomic scale-derived structure that the significant CTAB remaining on the nanoparticle surface was detected and preferred binding species identified. 2) We find that a significant amount of CTAB remains on the nanoparticle surface when a 1:1 ratio of BSPP or PEG-thiol are introduced into solution (~40 %) and even when a 1:1:1 ratio of CTAB, BSPP and PEG-

thiol are all three present in solution (~25 %). 3) While both BSPP and PEG-thiol are capable of displacing a fraction of CTAB from the nanoparticle surface, their replacement modes are unique. Results suggest that while BSPP replaces CTA^+ and Br^- adhered to the particle equally, PEG-thiol replaces the Br^- preferentially. Thus when all three ligands are present in solution, the greatest amount of CTAB is replaces, and an equilibriums structure is attained regardless of whether BSPP or PEG-thiol is the first replacement species. An incomplete picture of the nanoparticle surface composition is achieved if only molecular-scale measurements are used to evaluate replacement. This should be considered when using such methods to prove that ligand replacement has occurred.

6.7 Proposed future work

6.7.1 Computational study of ligand structure on nanoparticle surfaces

As discussed for the case of the structure of CTAB on Au NP surfaces (see Section 5.7.1), it may be useful to also attempt to determine the most energetically stable state where multiple ligands are introduced into solution. This may also be attempted via a combined DFT and MD simulation approach. It is likely that this would prove quite difficult due to an even increased number of atoms required in the simulation due to the presence of multiple surface species present in solution. Perhaps to this end a course-grain model would prove useful. To develop a potential approach, additional conversation and a collaboration with computational experts would be required.

6.7.2 Determination of ligand binding constant via in-situ XAFS with ligand titration

In this investigation 1:1 ratios of surface species were introduced into solution. While advantageous for exploring ligand competition, results may differ for cases where a deficit or

excess of replacement ligands are introduced. This is particularly relevant since for ligand exchange applications, often an excess of secondary ligand is added.

In particular, if our methodology for exploring ligand structure and exchange behavior is extended to multiple concentration ratios, a binding constant for the particular surface species may be derived.[178] A proposed approach to achieve this would be to start with a fixed concentration of CTAB, and titrate in a second ligand (BSPP or PEG-thiol) slowly while collecting *in-situ* measurements. As each of the methods used in this study (UV-vis spectroscopy, zeta-potential measurements and XAFS) are collected in the original solution environment, the methodology is particularly suitable for an *in-situ* titration study. One anticipated difficulty of pursuing this study would be the low particle concentrations resulting in long XAFS measurement time associated (~ 1 day for the case of 10 mM ligand concentration samples). The particles could not be concentrated further since they are too small to isolate via centrifugation and the tendency of CTAB to stick to the walls of spin filters, making CTAB concentration inaccurate. If a method to concentrate the particles were effectively developed, this may prove a useful contribution to understanding ligand binding chemistry.

6.7.3 A multi-ligand strategy to maximize DNA loading on CTAB-capped Au NPs

CTAB-capped Au NPs have been notoriously difficult to functionalize with dense DNA required for their preferentially assembly[132] and use in biomedical applications.[179-180] Considering that BSPP and PEG-thiol (a common attaching group for DNA onto Au-NP surfaces) have been found from the study outlined in this chapter to differ in the way that they displace CTAB from the Au NP surface, it may prove useful to employ them both in a strategy to maximize thiolated DNA attachment to the Au NP surface, and a more complete removal of CTAB.

For a preliminary study, we hypothesize that DNA loading may be improved if CTAB is first partially exchanged by adding a 1:1 ratio of BSPP into solution before functionalizing with DNA. This approach was considered with the knowledge that BSPP can partially remove CTAB from the Au-NP surface, yet PEG-thiol can also bind to the Au NP surface after BSPP exchange. To this end, 14.7 nm CTAB-capped Au NPs were functionalized with DNA based on a previously established strategy[181] for the case that CTAB alone is present in solution and the case that BSPP has been introduced in a 1:1 ratio.

Thiolated DNA (5'-AACAATTATACTCAGCAA-$(Sp18)_3$-C_3SH-3') was added in the amount of 1 OD per mL of Au NPs to the CTAB and CTAB with added BSPP samples and NaCl added to a final concentration of 0.5 M to enable attachment of the thiolated DNA to the Au NP surface. Particles were then washed 4x with 0.01 % sodium dodecyl sulfate (SDS) to remove excess DNA from solution. Zeta potential measurements were then collected. For the CTAB-capped Au NPs post-DNA functionalization, a zeta potential of -22 mV was collected, and -21 mV for CTAB-capped Au NPs when BSPP was introduced before functionalization. This shows that the CTAB-capped particles have indeed been functionalized with negatively charged DNA, since the CTAB-capped particles before functionalization had a positive zeta potential. For the case the BSPP has been introduced, however, this result is inconclusive, since the zeta potential for the pre-functionalized particles in this case, is also negative (-20 mV).

To compare DNA loading on CTAB-capped Au NPs compared to the case that BSPP was introduced in a 1:1 ratio, a fluorescence assay was performed. DNA strands were released by dissolving the Au NPs in 20 mM KCN at 50 °C before quantification through the OliGreen assay. A Quant-iT OliGreen (Invitrogen) assay was compared against a standard curve by measuring OliGreen fluorescence (λ_{ex} = 480 nm). The number of thiolated strands per particle was then

calculated by dividing the DNA concentration in the supernatant by the AuNP concentration, determined by UV-vis spectroscopy. From this method, the number of DNA strands/particle was determined to be 187 ± 20 for CTAB alone and 23 ± 5 when BSPP is also introduced.

In contradiction with our hypothesis, the loading of DNA was actually worse for the case that BSPP was also introduced into the solution. This deviation from behavior expected as a result of the study outlined in this chapter is perhaps expected, since DNA is a much larger and highly negatively charged molecule, in comparison to PEG-thiol alone, which may affect replacement behavior. Still, the NPs remained stable in the presence of BSPP, enabling some loading of DNA onto the particles. It is possible that with further optimization of a secondary ligand species by controlling the charge and size of the CTAB-removal species, that a multi-ligand strategy may prove advantageous. This trial approach, however, despite low DNA loading, may also prove useful in applications where CTAB removal is essential, since although loading is not improved, BSPP has been shown to remove a fraction of the CTAB from the nanoparticle surface. Further investigation is required in order to validate these hypotheses and may be worth exploring.

Chapter 7: Summary and Outlook

In summary, this thesis proposed and demonstrated an approach towards understanding nanoparticle-solution interface processes through a combined approach involving characterization of elemental and morphological changes observed at both the atomic and nanoscale. This was achieved by pairing atomic-scale *in-situ* X-ray characterization approaches with conventional methods, enabling resolution of nanoparticle structure in previously unachieved detail. Using this approach, important questions within the area of nanoparticle synthesis and transformation were addressed. These included the pathway behind the transformation from Ag nanospheres to AgAu nanocages, which was described in Chapter 3, and the role of trace Ag in the synthesis of Au nanorods, which was discussed in Chapter 4.

Chapters 5 and 6 demonstrated the effective use of XAFS, a bulk technique, to study the binding of molecular moieties to Au nanoparticle surfaces for the case that sufficiently small nanoparticles are used due to the majority surface atoms in these particles. When paired with conventional molecular methods, the atomic-scale parameters also provide insight into ligand replacement behavior.

While future work has been proposed to continue this work at the end of each respective chapter, it is also my expectation that this thesis will serve as a foundation and establish a methodology towards a more complete understanding of nanoparticle synthesis, transformation and surface ligand exchange processes. It has provided a first step in the direction of addressing the elusive nanoparticle-solution interface and addresses this identified important and necessary thrust area within in the field. Already, through this work, it has been established that through thorough atomic-scale characterization, previously elusive and even controversial claims have

been addressed and evaluated. If continued, perhaps true “bottom-up” fabrication with atomic-scale control will become a reality after all, since, according to the principles of materials science and engineering, knowledge of structure at the atomic-scale will provide the possibility for control over processing, properties and ultimately performance of devices from the atomic scale upwards.

APPENDIX

Appendix A: Supporting information for chapters 3-6

A.3 Supporting information for chapter 3

Extended Methods

Nanoparticle Synthesis

$HAuCl_4$ salt (Sigma-Aldrich) was dissolved in NANOpure^{TM} water to prepare a 0.1 mM solution. This Au solution was then titrated into a vial of ~3 pM (determined from XRF) citrate capped silver spheres (nominal diameter 20 nm, Ted Pella) using a syringe pump at a rate of 20 ml/hr at room temperature. Different volumes of Au solution were added to each sample of Ag particles in order to halt the reaction at different stages of transformation. After titration, samples were stirred for several minutes in order to ensure reaction completion. Transformed particles were isolated via centrifugation (21130 g for 20 mins) and the supernatant was removed to eliminate free ions from solution. Particle pellets were resuspended in 2 mL of NANOpure^{TM} water and centrifugation was repeated to remove excess Au^{3+} ions. After UV-vis measurements to probe the optical absorption spectra and localized surface plasmon resonance peak position, samples were isolated via centrifugation a final time and resuspended in 100 μL NANOpure^{TM} water. UV-vis spectra taken before and after this centrifugation step show that the particles maintain their nanocage structure and are not destroyed during the high-speed centrifugation (Figure A3.1). 20 μL of both a 1% (w/w) SDS and a 0.1% (w/w) Tween (Sigma-Aldrich) were added to samples to act as surfactant and to ensure longevity of particles.

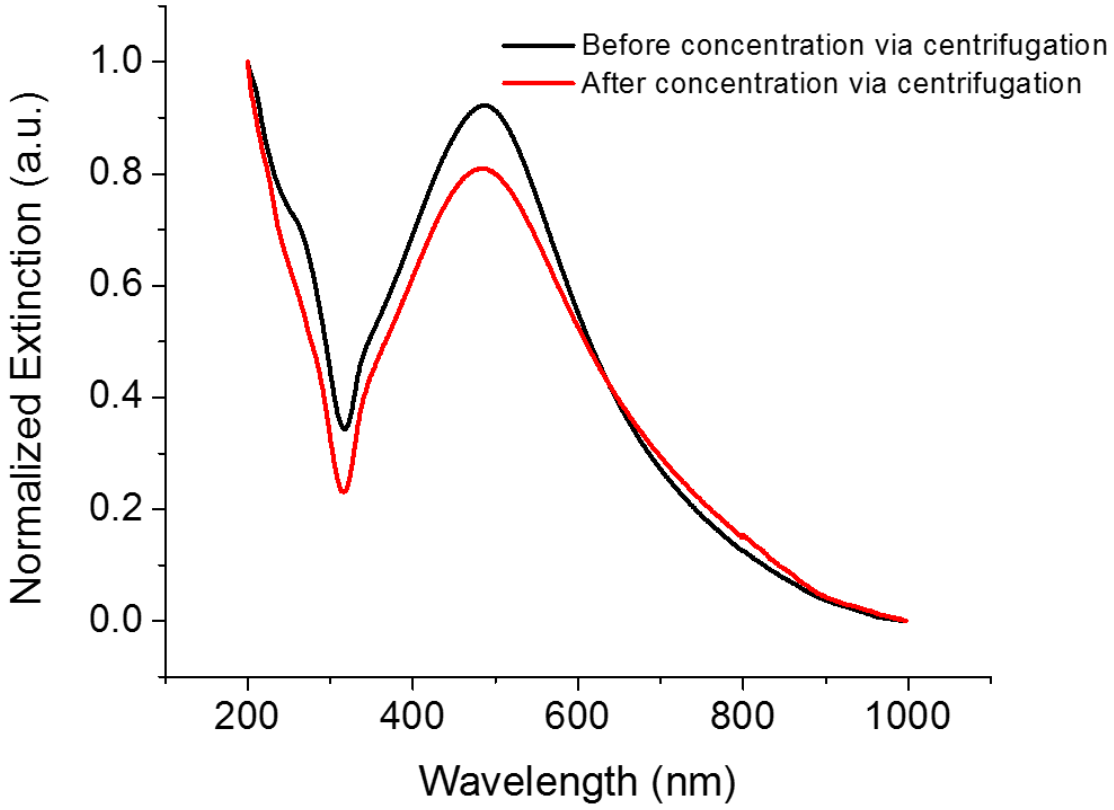

Figure A3.1 Partially transformed AgAu nanocage sample before and after concentration for x-ray measurements. Normalized UV-vis spectra of ~25 % Au nanocages before and after undergoing concentration via centrifugation for x-ray measurements show that the LSPR peak position and overall spectral features are maintained. This suggests that the particles do not collapse during the high-speed centrifugation step.

TEM Size Analysis

Nanoparticle size was determined by a statistical analysis of TEM images using the ImageJ particle counter software. The average number of particles used in the analysis was 113, with a minimum of 50 particles and a maximum of 250 particles at the extremes. Results of this analysis, along with particle size as determined from SAXS, are shown in Figure A3.10.

X-Ray Fluorescence

X-ray fluorescence (XRF) data from the Ag Kα and Au L fluorescence lines were collected along with XAFS data at sector 10BM-B at the Argonne National Laboratory Advanced Photon Source (APS). The corrected fluorescence intensities of the Ag Kα and Au Lα lines were used to determine the relative Au and Ag atomic percentages present in the isolated nanoparticle samples, with varying solution concentrations of $HAuCl_4$ added. Samples were contained in 3 mm (nominal, Charles Supper) inner diameter cylindrical quartz capillaries placed such that the capillary long axis was at a 45° angle with the detector normal and the incident x-ray beam. The XRF photons were collected in the horizontal plane with the detector at ~ 90° relative to the incident beam direction to minimize the intensity due to elastically scattered X-rays. XRF data was collected at an incident energy of 26.014 keV using a four-element Vortex ME-4 silicon drift diode detector. A schematic of the measurement setup is shown in Figure A3.2.

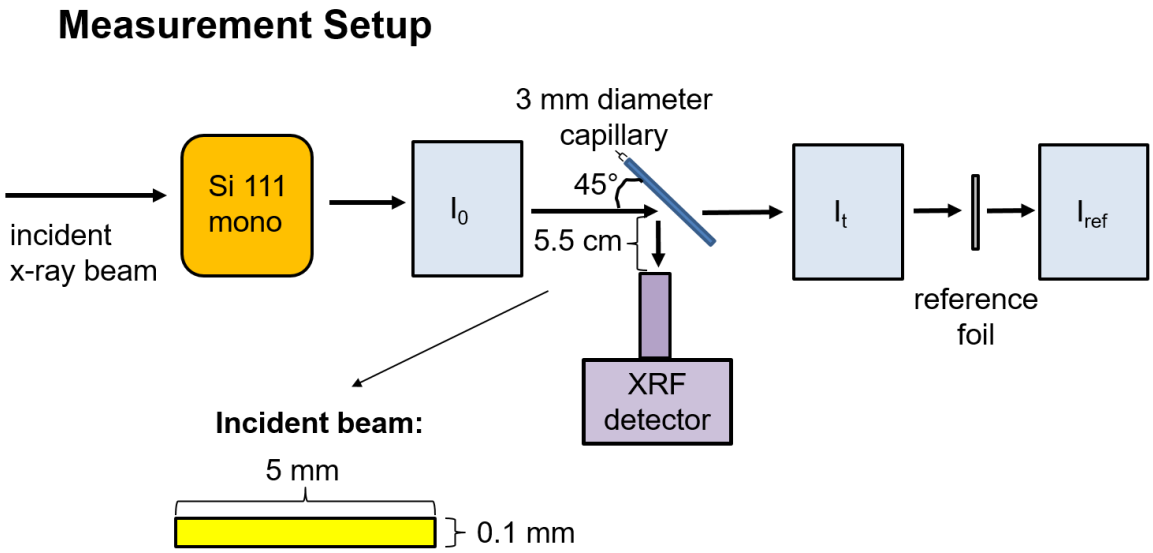

Figure A3.2. XRF and XAFS measurement setup. I_0 measures the incident and I_t the transmitted x-ray intensity. I_{ref} is used to measure the reference XAFS spectrum. The reference foil is either Ag or Au depending on the edge being scanned.

In order to determine the starting nanoparticle concentration, absolute number of Ag atoms in the starting nanoparticle solution as well as isolated supernatant were determined using XRF data collected at APS sector 5BM-D of DND-CAT at an incident energy of 26.014 keV. This was accomplished through including an internal Yb standard of known concentration (Sigma Aldrich) in the nanoparticle solution. Ag nanoparticles were contained in 2 mm quartz capillaries and placed at a 45° angle from two four-element Vortex ME-4 silicon drift diode detectors placed on either side of the sample.

Qualitatively, we observe (Figure A3.3) that with increasing $HAuCl_4$ incorporated into solution, the Au Lα fluorescence intensity increases while the higher energy Ag Kα fluorescence intensity decreases as would be expected. Quantitative analysis of the Au and Ag relative atomic

percentages were conducted using areas under the Ag Kα (22.163 keV) and Au Lα (9.705 keV) fluorescence lines, with peaks fit to a Gaussian function after background subtraction. Elemental XRF cross sections,[46] detector efficiency, and attenuation due to solvent media were taken into account in determining the Ag/Au ratio. (Note that self-absorption by the metal NPs could be neglected due to their low μM atomic concentrations in the solvent.) The beam size was 0.1 mm (vertical) x 5 mm (horizontal). Therefore, for attenuation correction for Ag Kα and Au Lα X-rays coming from the 2 or 3 mm diameter cylinder of water, we neglected the vertical beam size. The path lengths and attenuation corrections for fluorescence X-rays were calculated by dividing the horizontal illuminated 10 - 15 mm^2 area into 121 differential emission elements arranged on a 2D lattice. The corrected intensities yielded the same atomic fraction for Au when Au Lα, Au Lβ or Au Lγ fluorescence lines were used, validating this correction procedure.

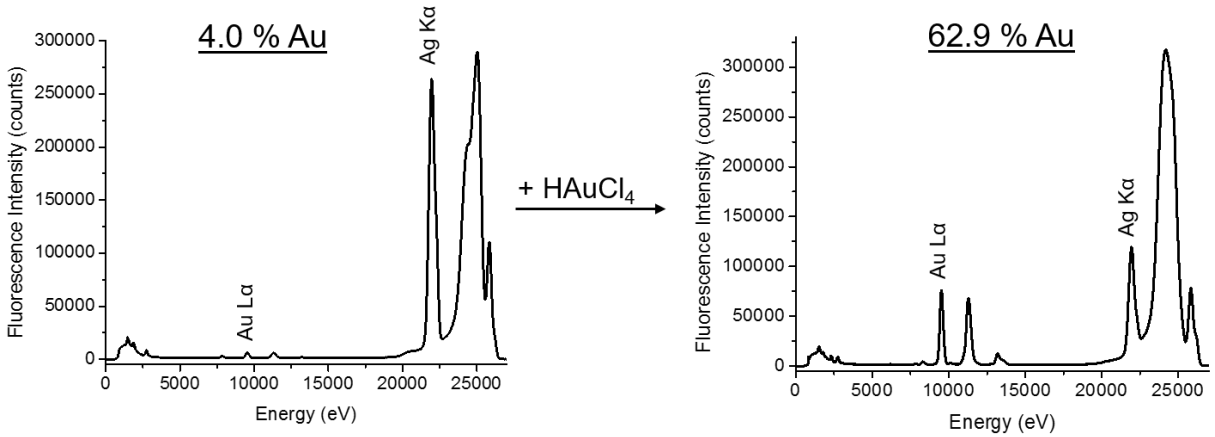

Figure A3.3. X-Ray fluorescence spectra. Qualitatively, it can be observed that both Au and Ag fluorescence lines are present in the raw XRF spectra. From low amounts to higher amounts of $HAuCl_4$ added (left to right), the Au L fluorescence lines increase in intensity, while the Ag Kα intensity decreases. From quantitative analysis, the relative atomic percentages were determined

to be 4.0 % Au (left) to 62.9 % Au (right). This is reasonable considering the amount of $HAuCl_4$ introduced into solution.

X-ray Scattering

X-ray scattering measurements were performed using 10.00 keV X-rays at beamline 5ID-D of the Advanced Photon Source (APS) at the Argonne National Laboratory. The aqueous nanoparticle dispersions were placed in a quartz capillary tube (inner diameter ~ 1.5 mm), which was embedded in a flow cell. To avoid radiation damage, the aqueous solutions were continuously flowed (unidirectional flow) at a rate of 2 mm/s during data collection. Furthermore, a fast shutter was used such that the samples were exposed to X-rays only for the data collection periods. The X-ray spot size at the sample position was ~ 0.25 mm (H) × 0.25 mm (V). The incident flux was ~ 10^{12} photons/s. The scattered intensity was collected using a Rayonix CCD area detectors, which was placed at 7502.0 mm (range: q = 0.015 – 0.9 nm^{-1}) from the sample. The flight path between the sample flow cell and the detector was evacuated.

For each nanoparticle sample, five measurements were performed with an exposure time of 0.5 s each. To estimate background scattering, prior to measurements on every nanoparticle sample, five sets of data for empty capillary and capillary filled with water were collected with an exposure time of 10 s each. To account for fluctuations in the incident beam intensity and changes in the absorption of X-rays for different samples, the incident and the transmitted beam intensities were monitored using an ion chamber just before the sample and a pin diode embedded in the beam stop just in front of the SAXS detector. Transmission, detector solid angle and X-ray polarization corrections were applied to measured intensities before performing the azimuthal integration for extracting the 1D intensity profiles. The data shown (Figure A3.6) is the intensity above the background scattering from capillary and pure water, and is an average of five measurements.

X-ray Scattering Data Analysis

The measured intensity profile $I(q)$ could be reasonably described by assuming a spherical core-shell model for the form factor $[F(q)]$ of the Ag and Ag/Au alloy nanoparticles.[114] Specifically,

$$F(q) = \frac{4\pi}{q^3}[(\rho_c - \rho_s)\{\sin[qR_c] - qR_c\cos[qR_c]\} + (\rho_s - \rho_{sol})\{\sin[q(R_c + T_s)] - q(R_c + T_s)\cos[q(R_c + T_s)]\}] \quad \text{(A3.1)}$$

Here, R_c is the radius of the hollowed-out core for the Ag/Au alloy nanoparticles. For unalloyed pure Ag nanoparticles, R_c = 0. The electron density ρ_c for the hollowed out core is assumed to be the same as that for water solvent ($\rho_c = \rho_{sol}$ = 334 e^-/nm^3). T_s is the thickness of the metallic shell, and ρ_s is the electron density for the shell. And

$$I(q) = \frac{N}{V} r_e^2 \langle [F(q)]^2 \rangle + bkg \quad \text{(A3.2)}$$

To take into account the polydispersity (PD) of nanoparticles, the scattered intensity from an isolated nanoparticle $[F(q)]^2$ is averaged over a Schulz distribution[115] for particle sizes to yield $\langle [F(q)]^2 \rangle$. Here, the ratio of core radius and the shell thickness $[R_c/T_s]$ is assumed to be a constant for all the Ag/Au alloy particles in a given solution. In Eq. A3.2, r_e is the classical electron radius and $^N/_V$ is the number density of nanoparticles in the solution. The constant *bkg* represents any additional background scattering apart from those from the quartz capillary and water. For example, scattering from excess solution reagents, such as sodium citrate surfactant and $HAuCl_4$ salt. Overall, six parameters were used to fit the measured $I(q)$ for Ag/Au alloy nanoparticles. These were R_c, $[R_c/T_s]$, ρ_s, Z, $^N/_V$ *and bkg.* Z is the Schulz distribution parameter, which defines polydispersity: $\%PD = \frac{100}{\sqrt{Z+1}}$.

The Ag/Au alloy nanoparticles are not perfect spheres. TEM micrographs show nanoparticles with corrugated surfaces. Therefore, the spherical core-shell model is a simplified representation

of these nanoparticles. As can be seen in Figures A3.6.1-15 the core-shell model fits to the experimental $I(q)$ profiles are nearly perfect over a region $0.01 < q < 0.09$ Å^{-1} that includes the form factor minimum and the maximum. Therefore it is reasonable to accept the fits from this method and the structural parameters derived thereof despite small deviations, which are accounted for within the subsequent error analysis.

X-Ray Absorption Fine Structure

XAFS spectra at the Au L_3 edge and Ag K edge (11.919 keV and 25.514 keV) were collected at MR-CAT sector 10BM-B of the APS. Energy scans were taken over a range from -150 eV to 600 eV with respect to the absorption edge using a Si(111) monochromator. XAFS spectra were collected in fluorescence mode using a four-element Vortex ME-4 Silicon drift diode fluorescence detector, calibrated with an Au or Ag metal foil standard. Ag or Au foil spectra were simultaneously collected along with the nanoparticle samples, as shown in Figure A3.2, in order to ensure calibration and compare absorption edge positions. Samples were concentrated via centrifugation to μM concentrations of Au/Ag atoms and placed in 3 mm inner diameter quartz capillary tubes, positioned 45 degrees with respect to both the incident x-ray beam and the fluorescence detector. To improve statistics, a minimum of five half-hour scans at 4 spectra/scan were averaged. Self-absorption was not a concern in the measurement, because of the low concentration of the element of interest (Au or Ag).

XAFS data was processed using ATHENA and ARTEMIS software, part of the IFEFFIT package.[116] Theoretical crystals structures were imported and converted to scattering pathways using ATOMS.[160] Absorption edge energy was determined from the maximum of the first derivative in the absorption data and the background was subtracted using the AUTOBK

algorithm.[161] The EXAFS region (greater than 100 eV above the absorption edge)[50] was normalized and a k-weight of 2 was chosen in order to provide an even spectrum throughout the region of interest (2 – 12 $Å^{-1}$). EXAFS spectra were modeled according to the EXAFS equation, a simplified version of which is:[50-51, 52, 47]

$$\chi(k) = \sum_{\Gamma}[\frac{N_{\Gamma}S_0^2F_{\Gamma}(k)}{2kR_{\Gamma}^2}e^{-2k^2\sigma_{\Gamma}^2}e^{-2R_{\Gamma}/\lambda(k)} \times \sin\big(2kR_{\Gamma} + \phi_{\Gamma}(k)\big)] \qquad \text{(A3.3)}$$

Where Γ is the summation over the individual scattering pathways included in the model, *k* is the photoelectron wavevector, $F_{\Gamma}(k)$ is the scattering amplitude, $\lambda(k)$ is the mean free path of inelastically-scattered photoelectrons and $\Phi(k)$ is the phase shift, which is calculated as a function of the absorbing and scattering atom using the ARTEMIS software. S_0^2, the amplitude reduction factor, was set to the value extracted from fitting a bulk Au or Ag foil as applicable. This enables a more accurate determination of the coordination number.[52] Degeneracy (N_{Γ}), half-path length (R_{Γ}), energy shift parameter (E_0), and mean-squared disorder (σ_{Γ}^2), which includes contributions from structural and thermal disorder (Debye-Waller factor),[50] were adjusted to determine the best fit model. Fits with values for these variables outside the realm of physical reasonability (i.e. negative mean-squared disorder) were restricted. ΔE_0 was fixed to a single variable for all pathways with the same absorbing and scattering element in order to limit the number of variables, as ΔE_0 values should be nearly equal for similar bonds within the structure.[182]

Goodness of fit parameters for the models were evaluated using minimization of the statistical R-factor parameter and error bars for individual parameters were estimated to one sigma (~ 68% confidence level) from the R-space spectrum. Spectra were fit first in k-space, then evaluated in R-space and q-space, in order to ensure that the best fit to the raw data in k-space was translatable

to the other fitting spaces. Individual fitting models and a summary of both fitting and goodness of fit parameters are included in Figure A3.16.

Supplementary Results

Energy Dispersive X-Ray Spectroscopy

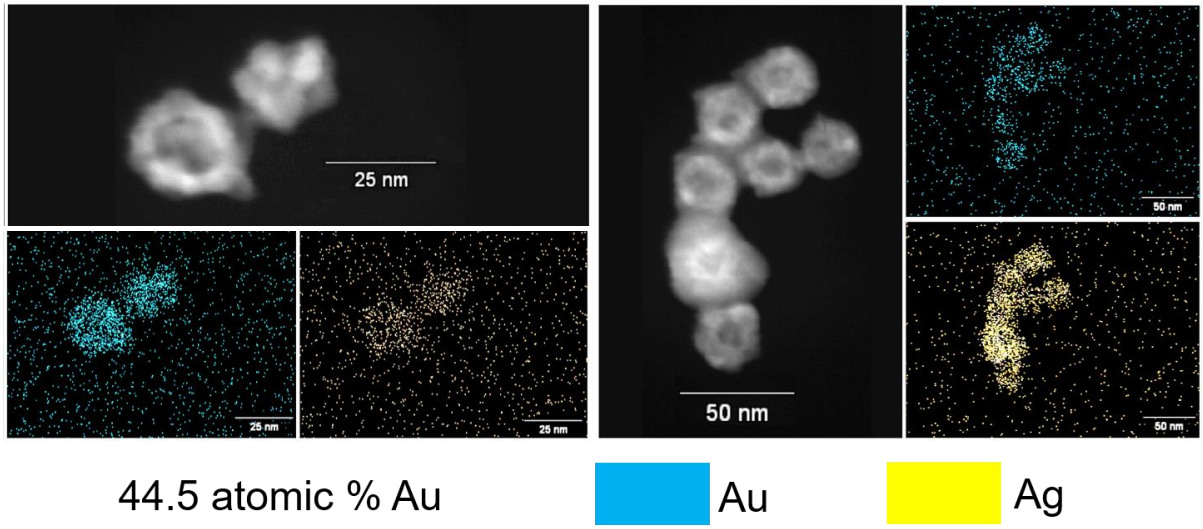

Figure A3.4. EDX mapping of Au and Ag spatial distribution. EDX mapping of nanoparticles that have been partially titrated with $HAuCl_4$ shows that both the Ag signal (yellow) and Au signal (blue) are distributed evenly throughout the nanoparticles. Given the resolution of EDX is ~ 2 nm and we observe local clustering from XAFS coordination numbers, this suggests that the local Au and Ag clusters within the particles are < 2 nm. The particles are atomically segregated, but alloyed at the nanoscale.

XAFS-derived Ag and Au cluster size in AgAu nanoparticles

The size of Ag and Au domains in the AgAu nanoparticles were estimated using the procedure established by Calvin et. al, which makes use of first-shell XAFS-derived coordination numbers to estimate particle size (Eq. A3.4), where N_{nano} is the XAFS-derived coordination number for Au-Au or Ag-Ag within the particles, $N_{bulk} = 12$, r is the nearest-neighbor distance (2.884 Å) and R is the radius of the Au or Ag cluster size.[118]

$$N_{nano} = [1 - \frac{3}{4}\left(\frac{r}{R}\right) + \frac{1}{16}\left(\frac{r}{R}\right)^3]N_{bulk} \qquad \text{(A3.4)}$$

As the presence of Ag and Au clustering as been observed from the deviation of CNs from the case of alloy homogeneity (Figure 3.5), this approach can be used to estimate cluster size. The results of this analysis are shown in Figure A3.5 and show that the local clustering of Ag and Au is solely at the atomic scale (< 1 nm).

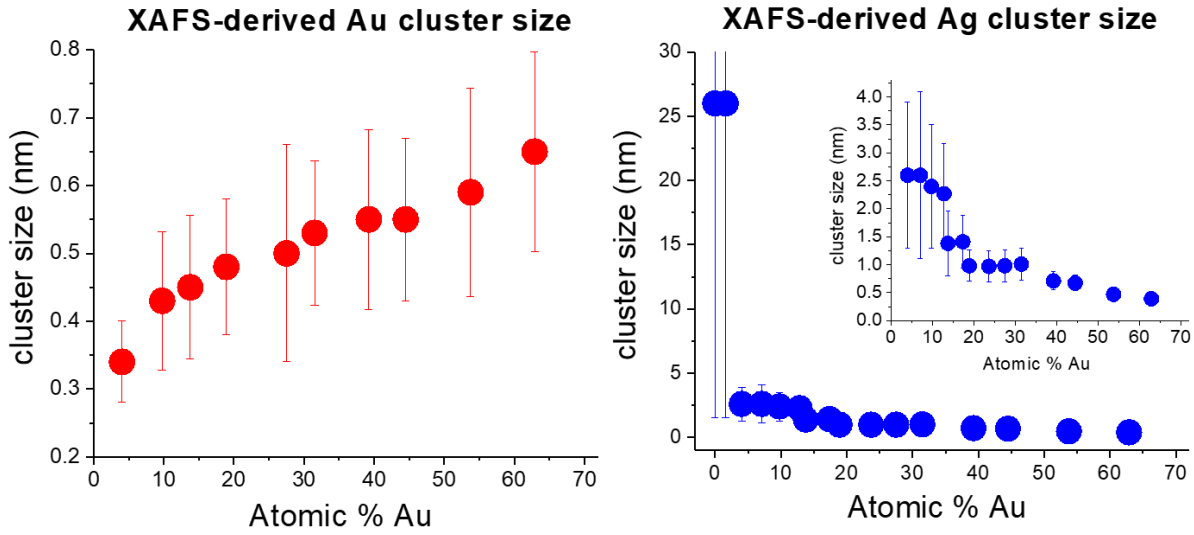

Figure A3.5. Ag and Au cluster size in AgAu nanoparticles. Au (left, red) and Ag (right, blue) sizes of Ag and Au regions within the atomically-segregated particles were estimated from XAFS first-shell coordination numbers. Throughout, the Au cluster radius is < 1 nm and after the initial transformation stages, the Ag cluster radius is also < 1nm, which agrees with EDX data (Figure A3.4) which shows that the AgAu nanocages are alloys on the nanoscale. Ag and Au regions are limited to the local atomic scale.

Quantitative Investigation of Ag:Au Exchange Ratio

The Ag:Au exchange ratio was calculated by comparing the ratio of the number of Ag atoms lost from the total number of Ag atoms originally in the nanoparticles (determined by XRF) to the number of Au atoms incorporated into the nanoparticle (number of Au atoms added minus the percentage unreacted in the supernatant (determined from ICP-MS)):

$$\frac{\text{number of Ag atoms lost from particles}}{\text{number of Au atoms incorporated into particles}}$$

Au atomic %	Ag:Au Replacement Ratio
1.6	0.5 ± 0.1
4.0	2.1 ± 0.4
7.1	3.2 ± 0.5
9.8	3.0 ± 0.4
12.8	2.9 ± 0.4
13.8	2.4 ± 0.3
17.4	2.1 ± 0.3
18.9	1.5 ± 0.2
23.7	2.0 ± 0.3
27.5	2.0 ± 0.2
31.5	1.6 ± 0.2
39.3	1.6 ± 0.2
44.5	1.6 ± 0.2
53.8	1.7 ± 0.1

62.9	1.7 ± 0.2

Table A3.1. Ag:Au replacement ratio as a function of $HAuCl_4$ addition. This table reveals the result that the exchange of Ag with Au atoms deviates from the expected 3:1 ratio from the Galvanic reaction alone. Rather, initially the Ag:Au replacement ratio is 1/2, indicating the addition of 2 Au atoms onto the nanoparticle surface for every Ag atom removed. The replacement ratio then increases to mimic the 3:1 ratio and again decreases as the reaction progresses until the nanoparticles begin to deteriorate.

Single-Shell SAXS Spectra + Fits

SAXS Error Reporting

The error bars on the measured data (Figures A3.6 and A3.8, green) are smaller than the marker sizes. Positive and negative error values for parameters shown in the tables below were calculated based on $\Delta\chi^2 = 1$ maps and represent 68 % confidence intervals. The average polydispersity in the total nanoparticle size was 21 % with a std. dev. of 6 % between samples from different batches. The confidence intervals on the electron density are estimated in a different manner as described next. To fit the data, we multiplied by an overall scale factor, which ideally represents the product of the sample concentration multiplied by the square of the classical electron radius. The value of the scale factor over the whole series of samples showed a variation of ± 50 %. In our specific case of core-shell particles with the same electron density in the core as the surrounding bulk

$$I \propto scale\ factor * (\rho - \rho_w)^2 \qquad \text{(A3.5)}$$

Assuming that the concentration of particles was constant throughout the measurements, the error in scale factor corresponds to a maximum of 25 % error in the electron density of the shell.

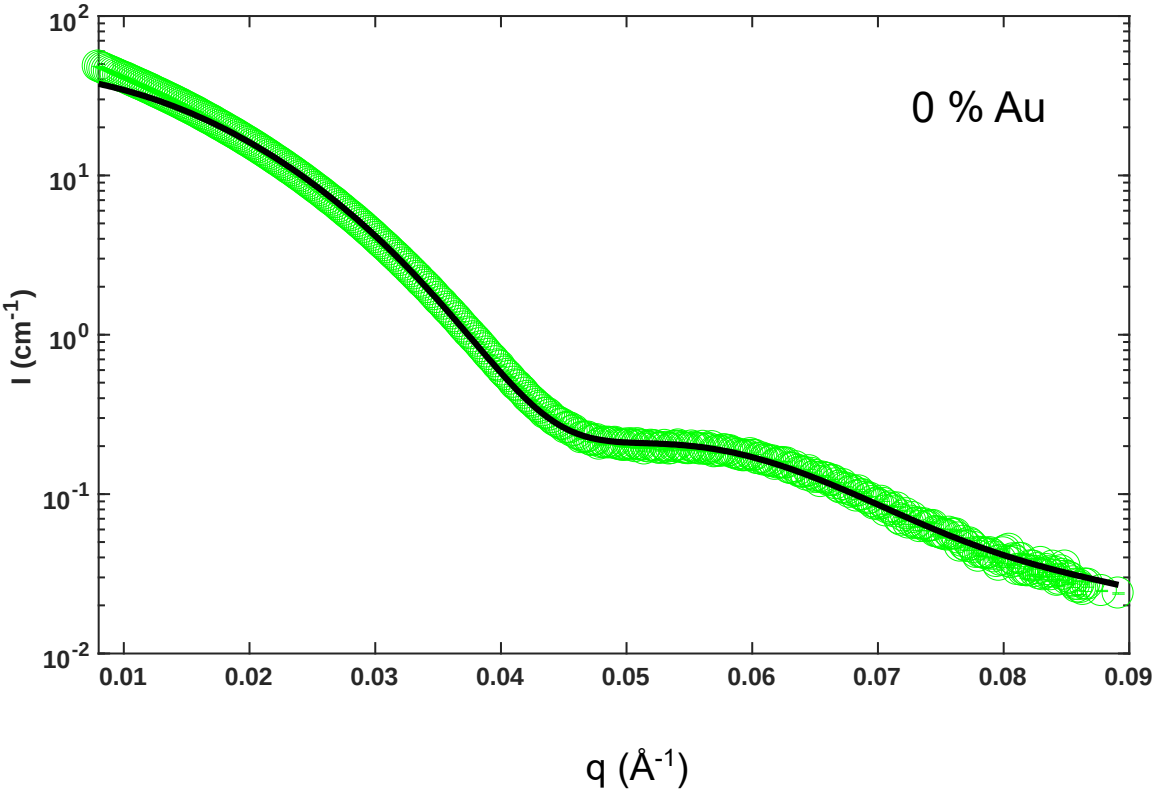

Total Particle Radius (nm)	Core Radius:Shell Thickness	Shell Electron Density (e^-/nm^3)
$9.3^{+0.25}_{-0.20}$	0	2900

Figure A3.6.1. 0 % Au nanoparticle sample SAXS spectrum and fitting model. SAXS data was collected and the form factor fit in order to determine relevant morphological parameters, which are included in the table below the plot. In this case the electron density of the particle was fixed to that of bulk Ag.

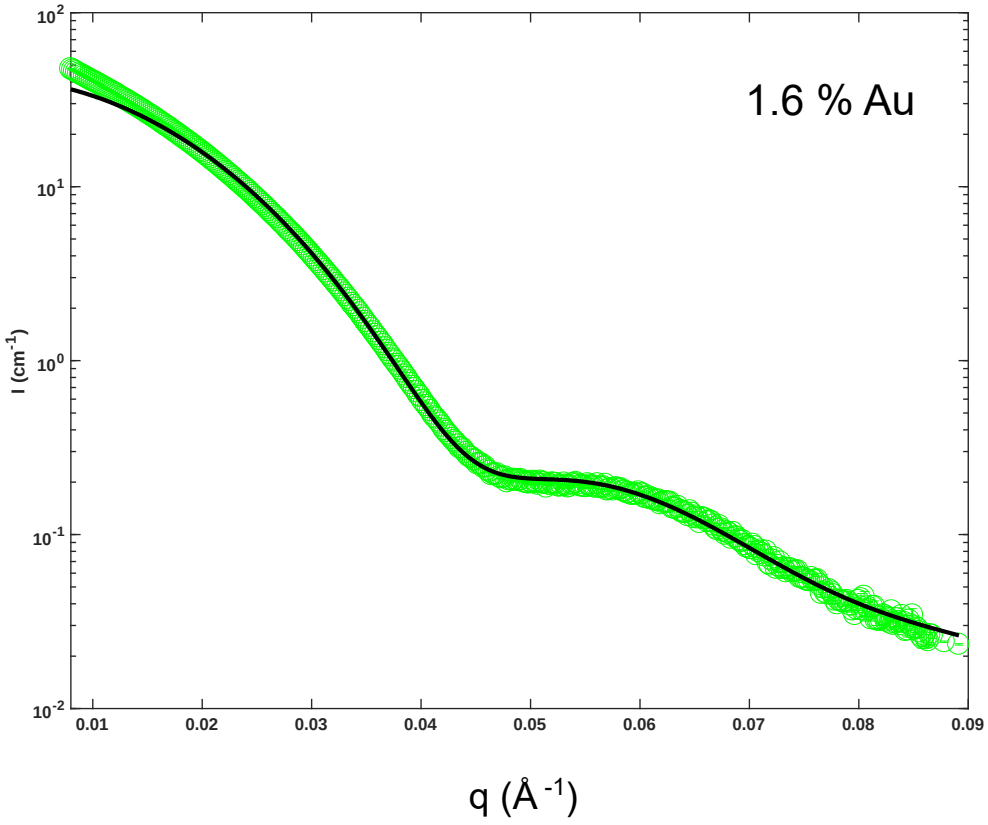

Total Particle Radius (nm)	Core Radius:Shell Thickness	Shell Electron Density (e^-/nm^3)
$9.3^{+0.6}_{-0.1}$	$0.150^{+0.004}_{-0.004}$	2921

Figure A3.6.2. 1.6 % Au nanoparticle sample SAXS spectrum and fitting model. SAXS data was collected and the form factor fit in order to determine relevant morphological parameters, which are included in the table below the plot.

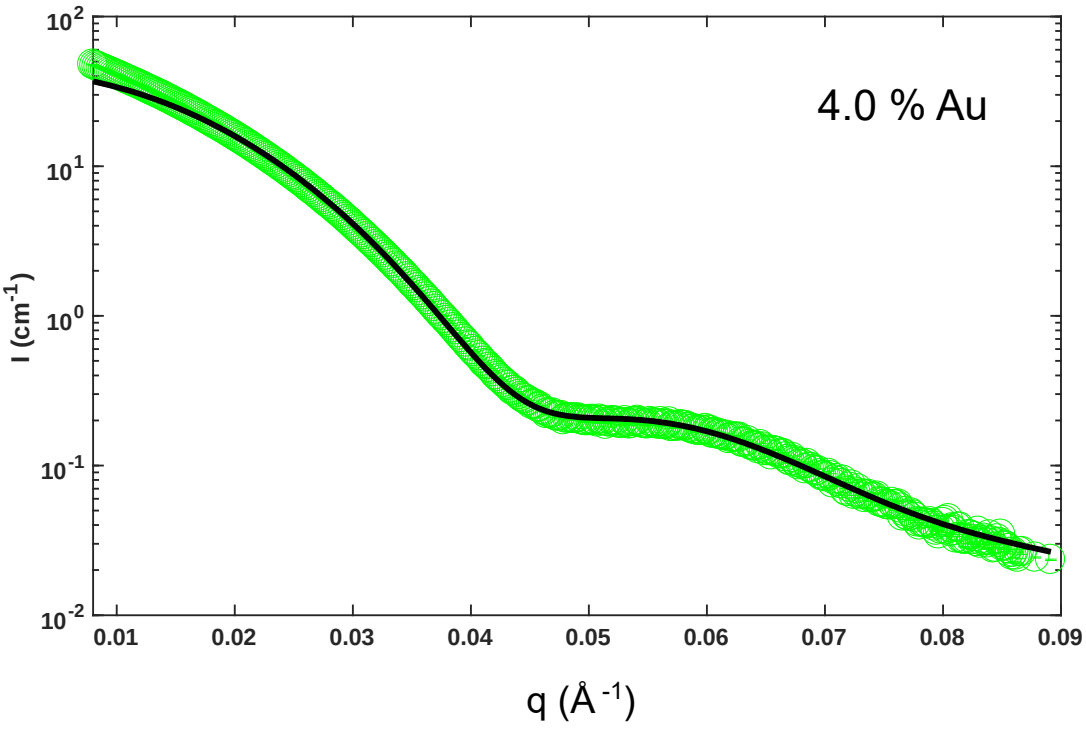

Total Particle Radius (nm)	Core Radius:Shell Thickness	Shell Electron Density (e^-/nm^3)
$9.3^{+0.7}_{-0.1}$	$0.150^{+0.003}_{-0.003}$	2920

Figure A3.6.3. 4.0 % Au nanoparticle sample SAXS spectrum and fitting model. SAXS data was collected and the form factor fit in order to determine relevant morphological parameters, which are included in the table below the plot.

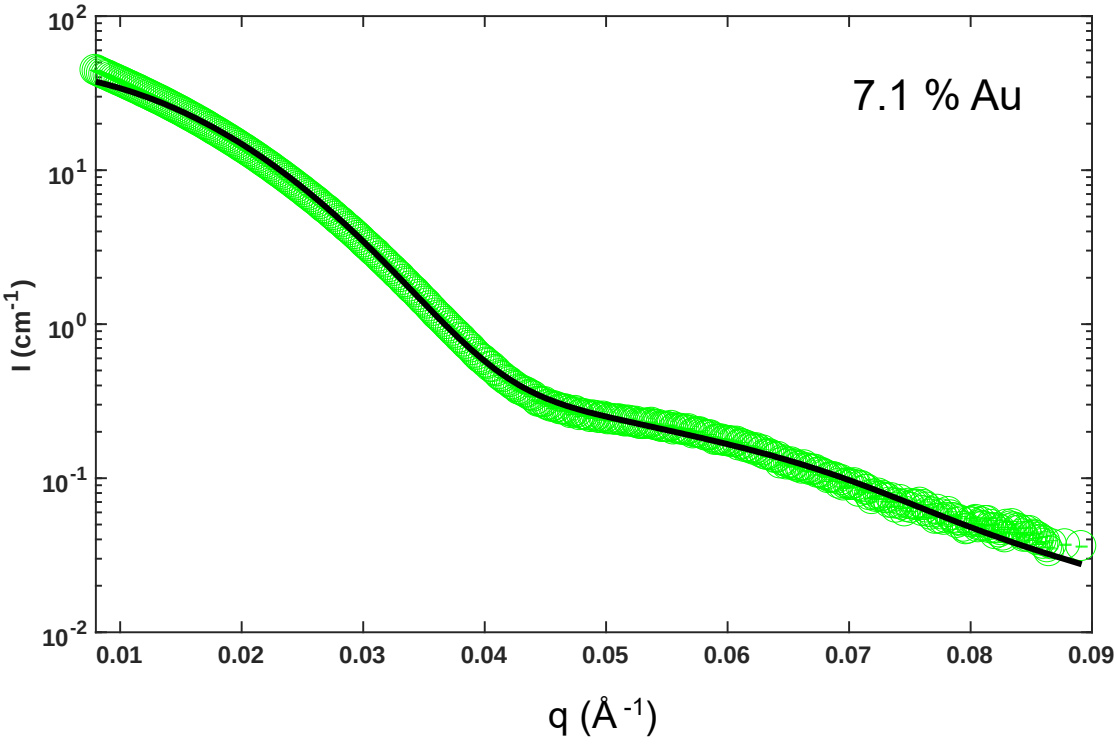

Total Particle Radius (nm)	Core Radius:Shell Thickness	Shell Electron Density (e^-/nm^3)
$9.4^{+0.3}_{-0.1}$	$0.191^{+0.005}_{-0.005}$	2919

Figure A3.6.4. 7.1 % Au nanoparticle sample SAXS spectrum and fitting model. SAXS data was collected and the form factor fit in order to determine relevant morphological parameters, which are included in the table below the plot.

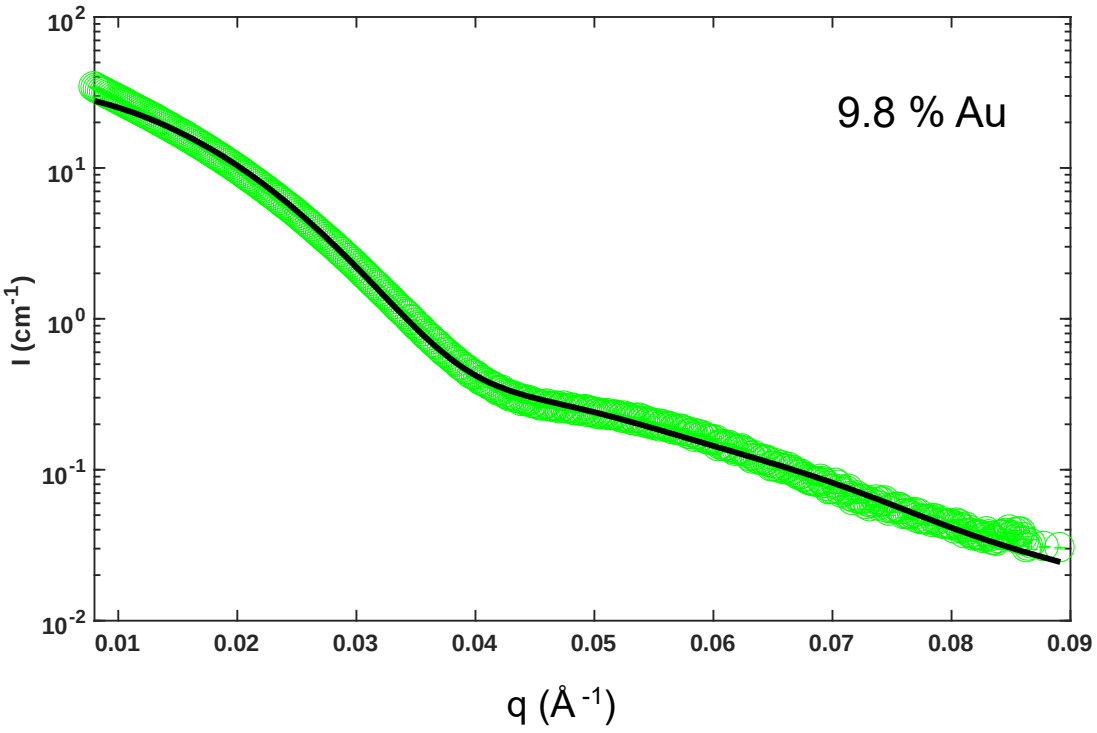

Total Particle Radius (nm)	Core Radius:Shell Thickness	Shell Electron Density (e^-/nm^3)
$9.5^{+0.3}_{-0.3}$	$0.346^{+0.008}_{-0.008}$	2905

Figure A3.6.5. 9.8 % Au nanoparticle sample SAXS spectrum and fitting model. SAXS data was collected and the form factor fit in order to determine relevant morphological parameters, which are included in the table below the plot.

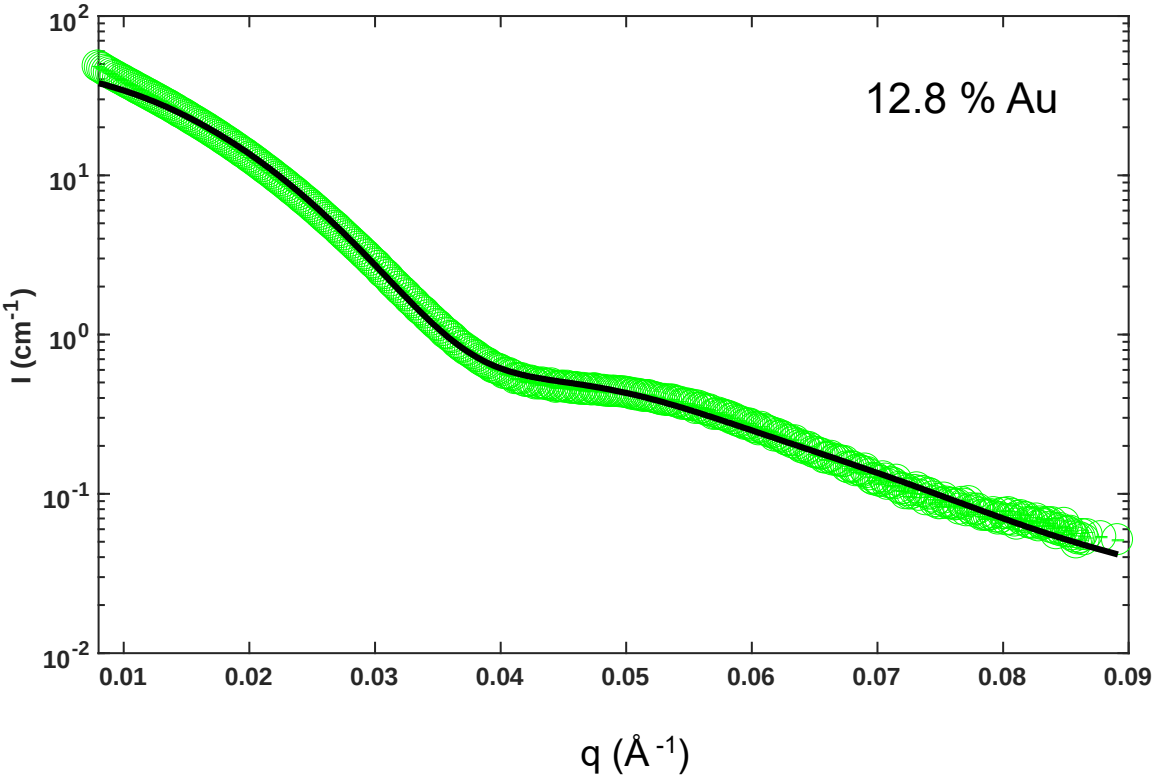

Total Particle Radius (nm)	Core Radius:Shell Thickness	Shell Electron Density (e^-/nm^3)
$9.5^{+0.3}_{-0.3}$	$0.49^{+0.01}_{-0.04}$	2921

Figure A3.6.6. 12.8 % Au nanoparticle sample SAXS spectrum and fitting model. SAXS data was collected and the form factor fit in order to determine relevant morphological parameters, which are included in the table below the plot.

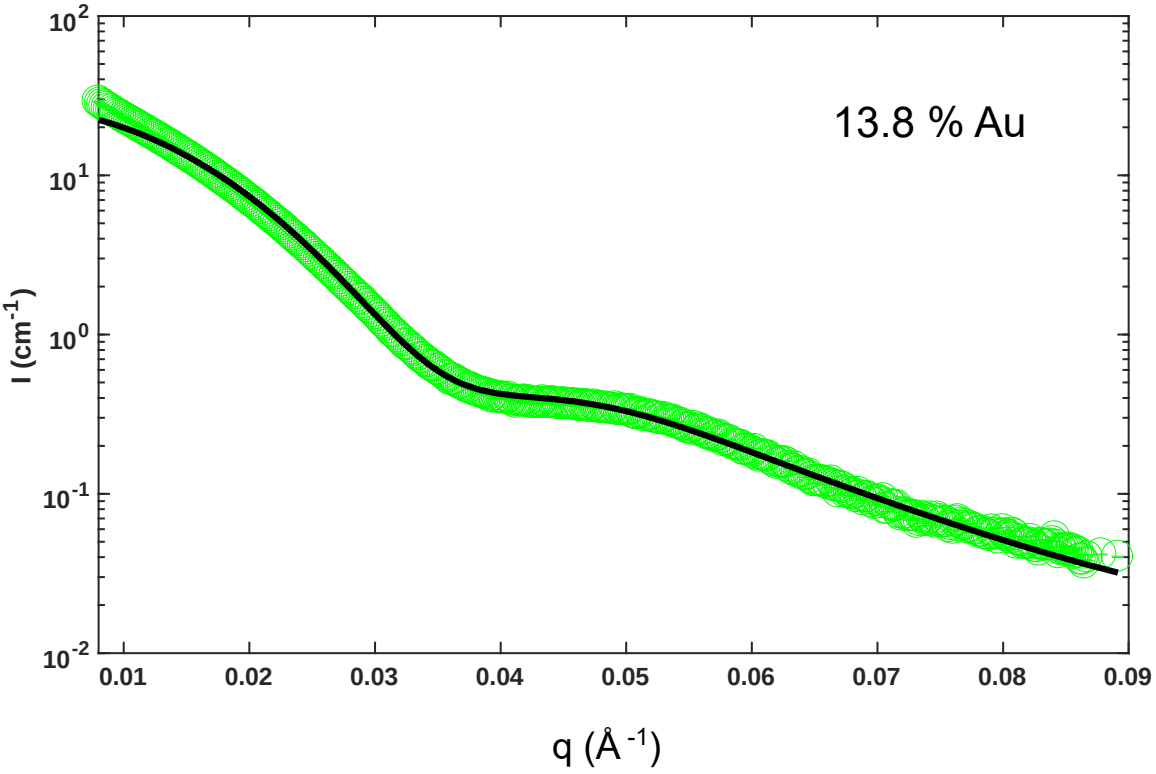

Total Particle Radius (nm)	Core Radius:Shell Thickness	Shell Electron Density (e^-/nm^3)
$9.6^{+0.4}_{-0.3}$	$0.67^{+0.02}_{-0.02}$	2902

Figure A3.6.7. 13.8 % Au nanoparticle sample SAXS spectrum and fitting model. SAXS data was collected and the form factor fit in order to determine relevant morphological parameters, which are included in the table below the plot.

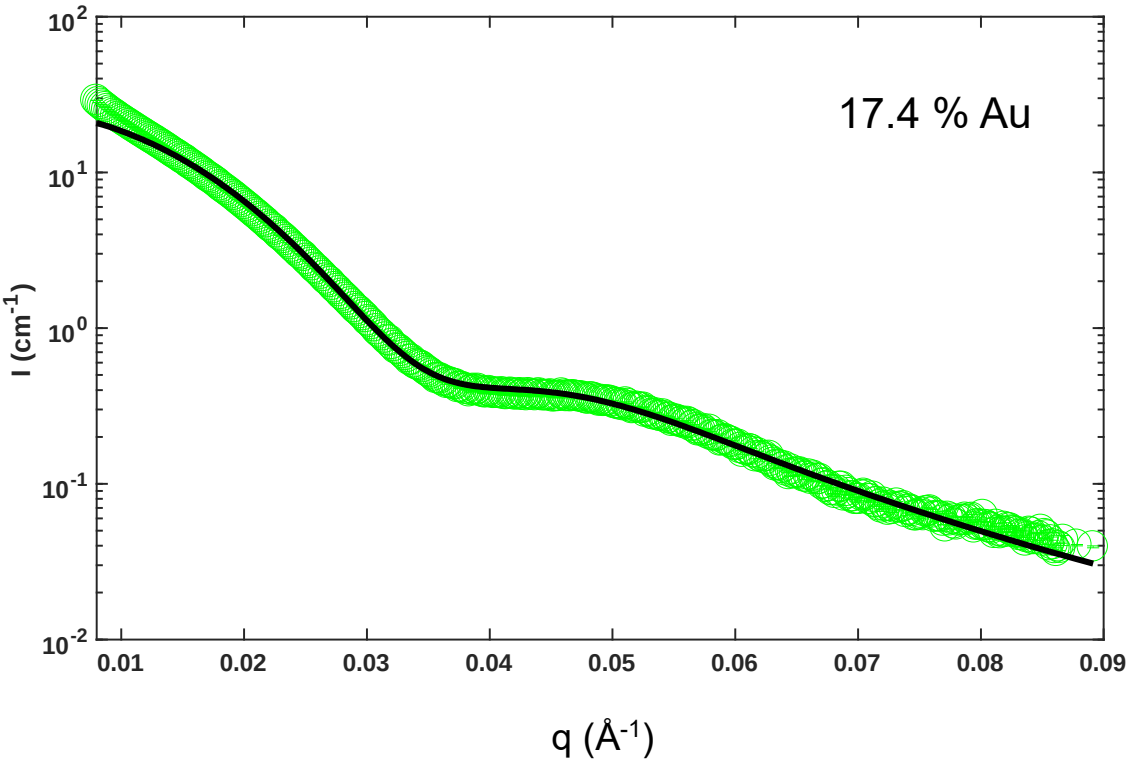

Total Particle Radius (nm)	Core Radius:Shell Thickness	Shell Electron Density (e^-/nm^3)
$9.9^{+0.4}_{-0.4}$	$0.73^{+0.02}_{-0.02}$	2904

Figure A3.6.8. 17.4 % Au nanoparticle sample SAXS spectrum and fitting model. SAXS data was collected and the form factor fit in order to determine relevant morphological parameters, which are included in the table below the plot.

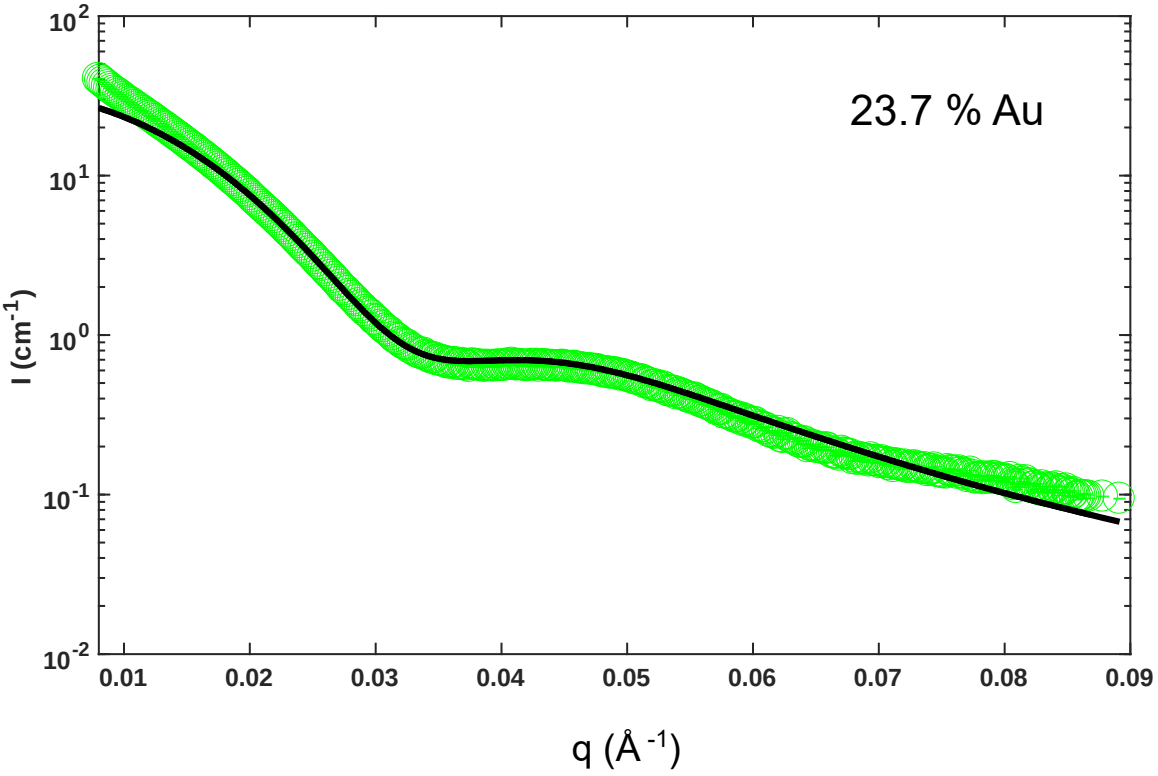

Total Particle Radius (nm)	Core Radius:Shell Thickness	Shell Electron Density (e^-/nm^3)
$10.2^{+0.5}_{-0.5}$	$0.83^{+0.08}_{-0.02}$	2919

Figure A3.6.9. 23.7 % Au nanoparticle sample SAXS spectrum and fitting model. SAXS data was collected and the form factor fit in order to determine relevant morphological parameters, which are included in the table below the plot.

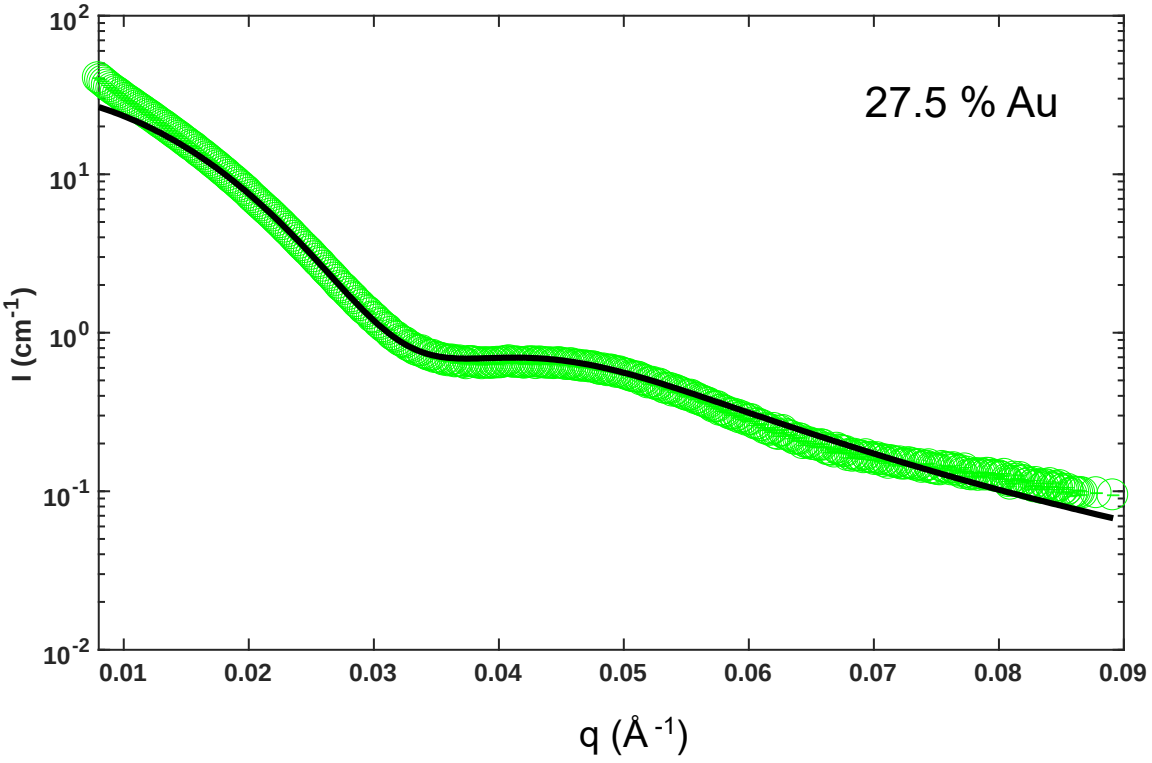

Total Particle Radius (nm)	Core Radius:Shell Thickness	Shell Electron Density (e^-/nm^3)
$10.4^{+0.5}_{-0.5}$	$0.89^{+0.02}_{-0.02}$	2916

Figure A3.6.10. 27.5 % Au nanoparticle sample SAXS spectrum and fitting model. SAXS data was collected and the form factor fit in order to determine relevant morphological parameters, which are included in the table below the plot.

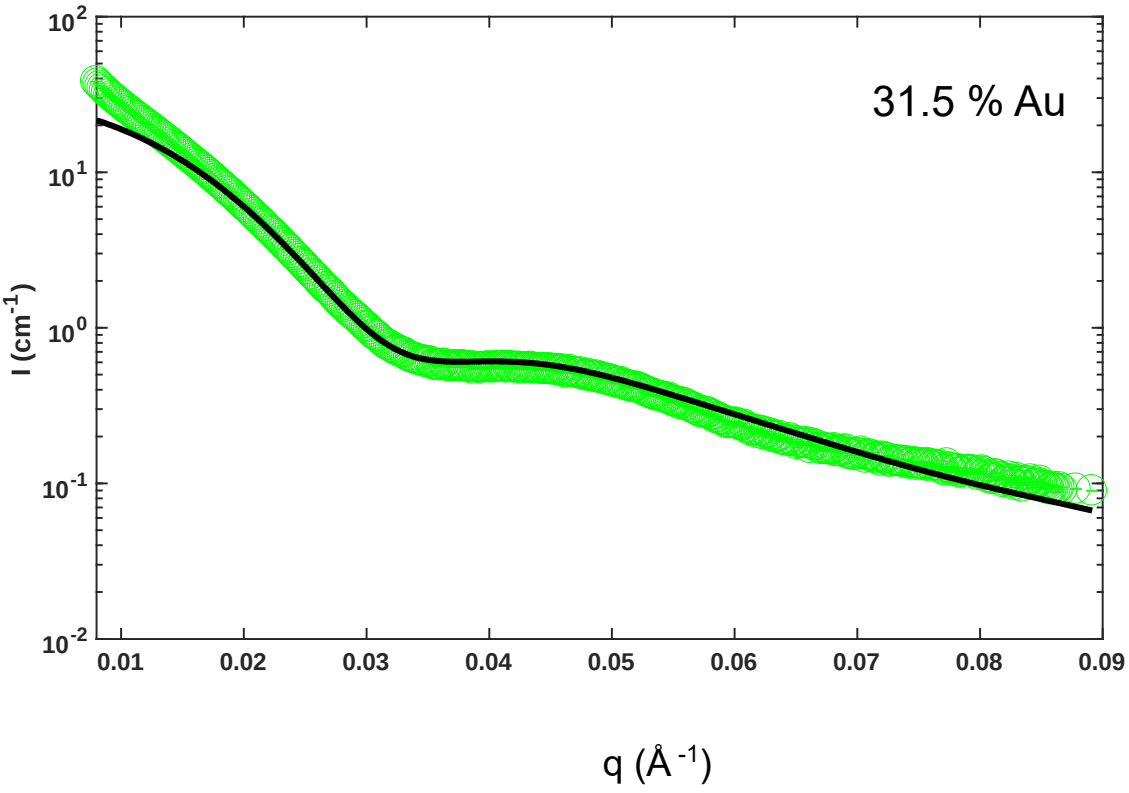

Total Particle Radius (nm)	Core Radius:Shell Thickness	Shell Electron Density (e^-/nm^3)
$10.5^{+0.6}_{-0.4}$	$0.90^{+0.09}_{-0.02}$	2945

Figure A3.6.11. 31.5 % Au nanoparticle sample SAXS spectrum and fitting model. SAXS data was collected and the form factor fit in order to determine relevant morphological parameters, which are included in the table below the plot.

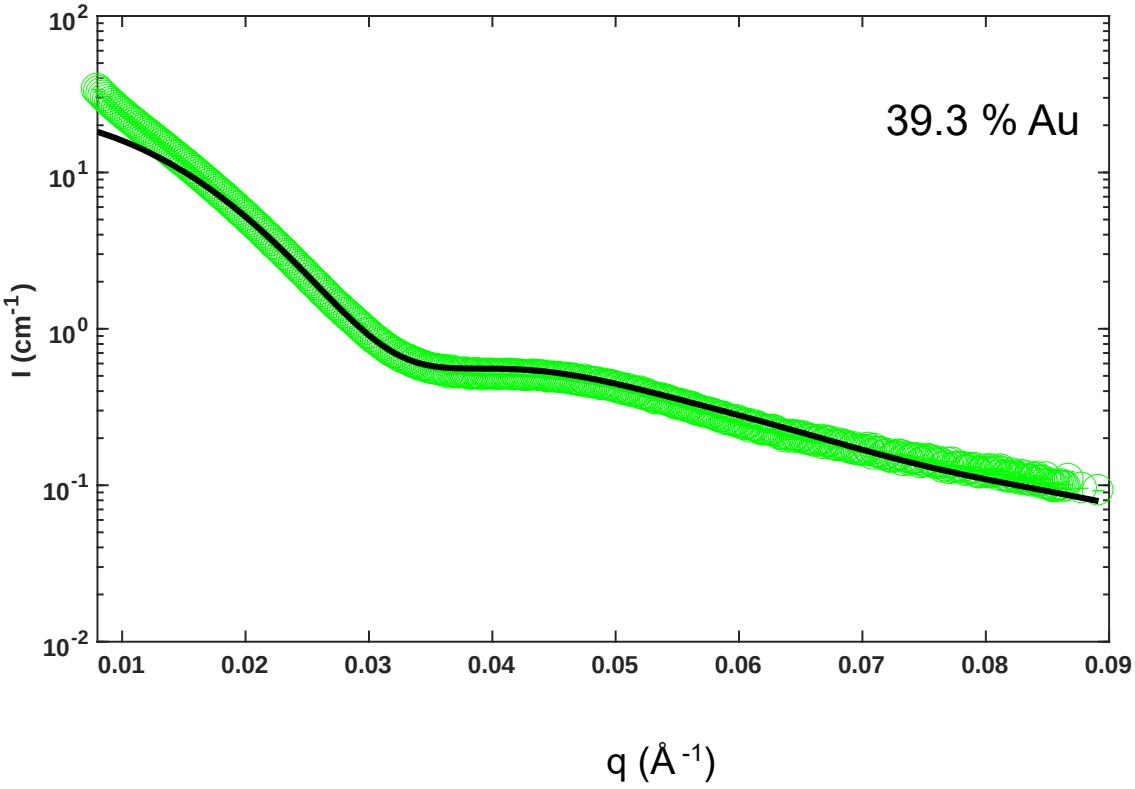

Total Particle Radius (nm)	Core Radius:Shell Thickness	Shell Electron Density (e^-/nm^3)
$10.3^{+0.5}_{-0.4}$	$0.97^{+0.02}_{-0.02}$	2899

Figure A3.6.12. 39.3 % Au nanoparticle sample SAXS spectrum and fitting model. SAXS data was collected and the form factor fit in order to determine relevant morphological parameters, which are included in the table below the plot.

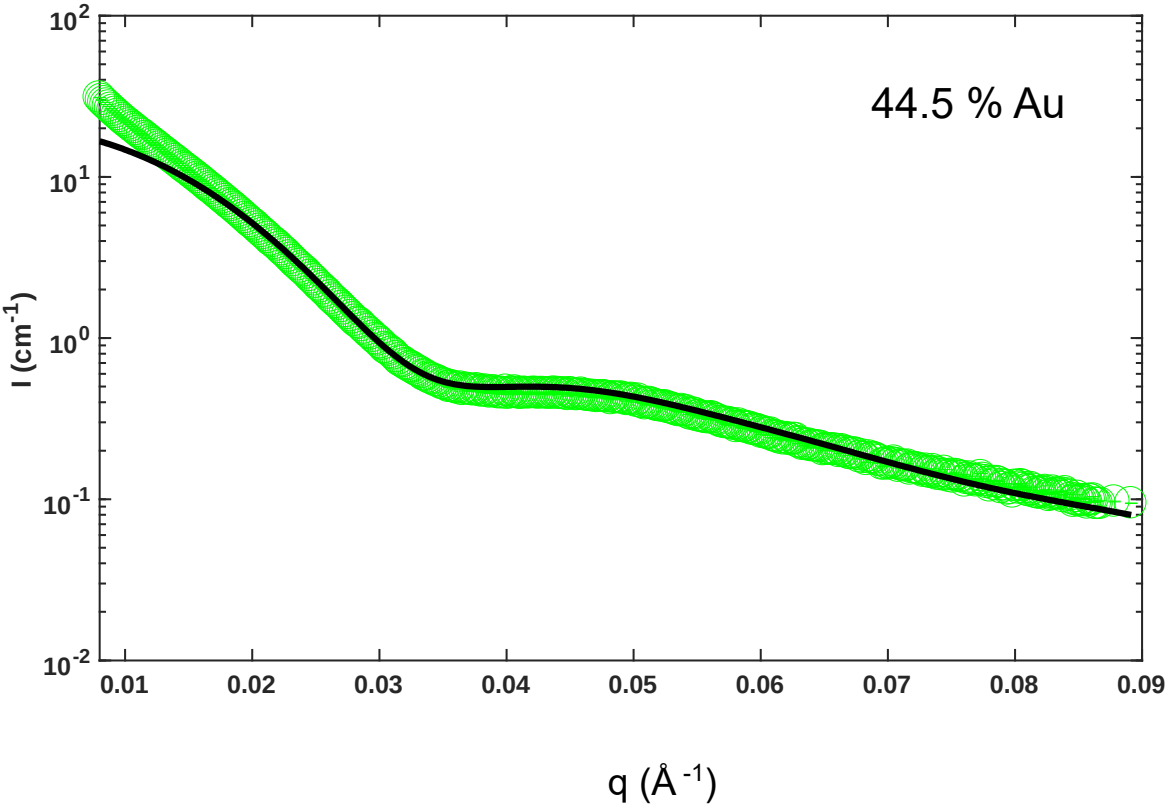

Total Particle Radius (nm)	Core Radius:Shell Thickness	Shell Electron Density (e^-/nm^3)
$10.0^{+0.4}_{-0.4}$	$0.99^{+0.03}_{-0.03}$	2896

Figure A3.6.13. 44.5 % Au nanoparticle sample SAXS spectrum and fitting model. SAXS data was collected and the form factor fit in order to determine relevant morphological parameters, which are included in the table below the plot.

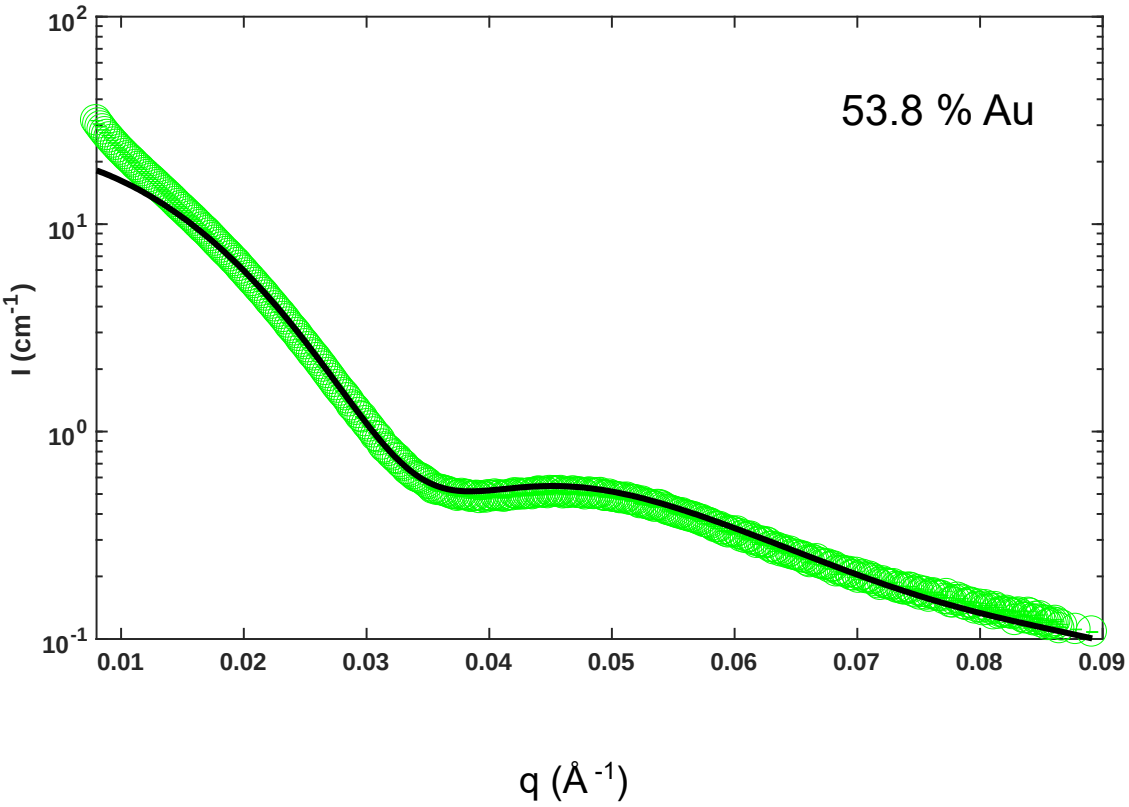

Total Particle Radius (nm)	Core Radius:Shell Thickness	Shell Electron Density (e^-/nm^3)
$9.8^{+0.3}_{-0.4}$	$1.09^{+0.02}_{-0.03}$	2882

Figure A3.6.14. 53.8 % Au nanoparticle sample SAXS spectrum and fitting model. SAXS data was collected and the form factor fit in order to determine relevant morphological parameters, which are included in the table below the plot.

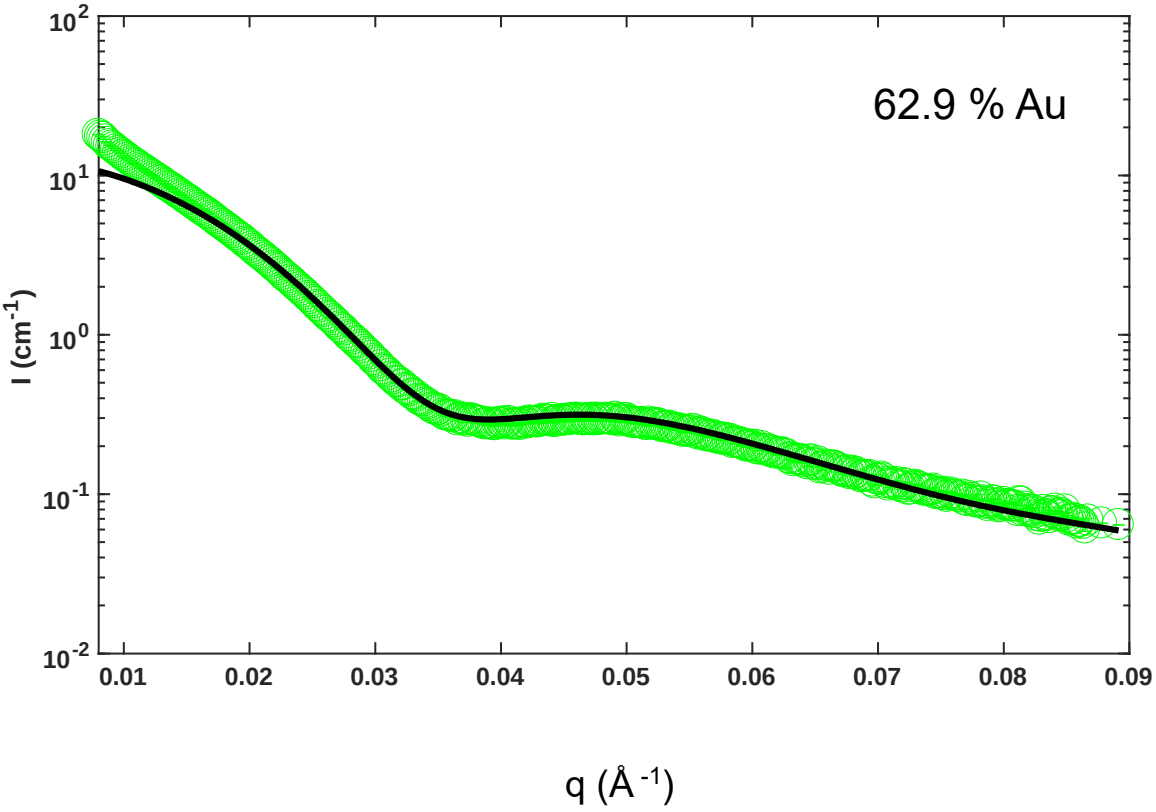

Total Particle Radius (nm)	Core Radius:Shell Thickness	Shell Electron Density (e^-/nm^3)
$9.6^{+0.4}_{-0.4}$	$1.10^{+0.02}_{-0.03}$	2931

Figure A3.6.15. 62.9 % Au nanoparticle sample SAXS spectrum and fitting model. SAXS data was collected and the form factor fit in order to determine relevant morphological parameters, which are included in the table below the plot.

Multi-Shell SAXS Data + Fits

The measured intensity profile $I(q)$ could be reasonably described by assuming a spherical core-shell model. Due to irregularity in shape and deviation from the used single-shell model, another analytical model was used to attempt to minimize the error in using the core-shell model. The transformed nanoparticles, as seen in the electron micrographs (Figure 3.3), can be thought of has having a diffuse outer layer created by protrusions that extend beyond the average outer shell radius. By appending a third layer to the core-shell model we have attempted to contain the additional, small but excess, electron density with a low density shell that was allowed to freely range in size during the fitting process. Results from this model were similar to the original single-shell model with an extended average total size. This model also tracked the electron density of both the primary and secondary shells and showed that consistently the inner shell contained the majority of the electron density of the particle, despite allowing the outer shell to extend to a maximum of 30 nm during fitting. This leads to the conclusion that the outer shell is extremely diffuse and contains very little actual mass using this model. The comparison between the results of the single-shell and multi-shell model fits are negligible and the confidence intervals on the individual tracked parameters are narrower in the single-shell model presented in the main text.

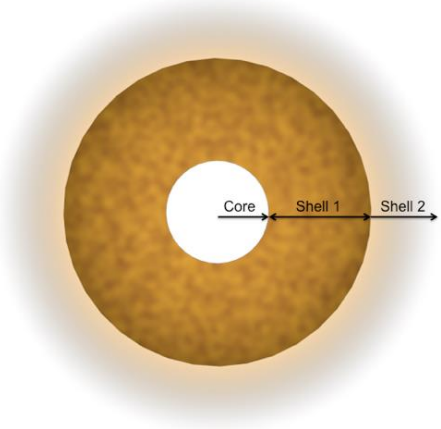

Figure A3.7. Pictorial schematic of multi-shell SAXS model. A better low-q fit was obtained for the SAXS data through use of a more complex model. This model involves an additional diffuse shell outside of the first dense shell. This may be due to the rough surface layers of the nanoparticle subsequent to exchange, resulting in a quasi-spherical particle.

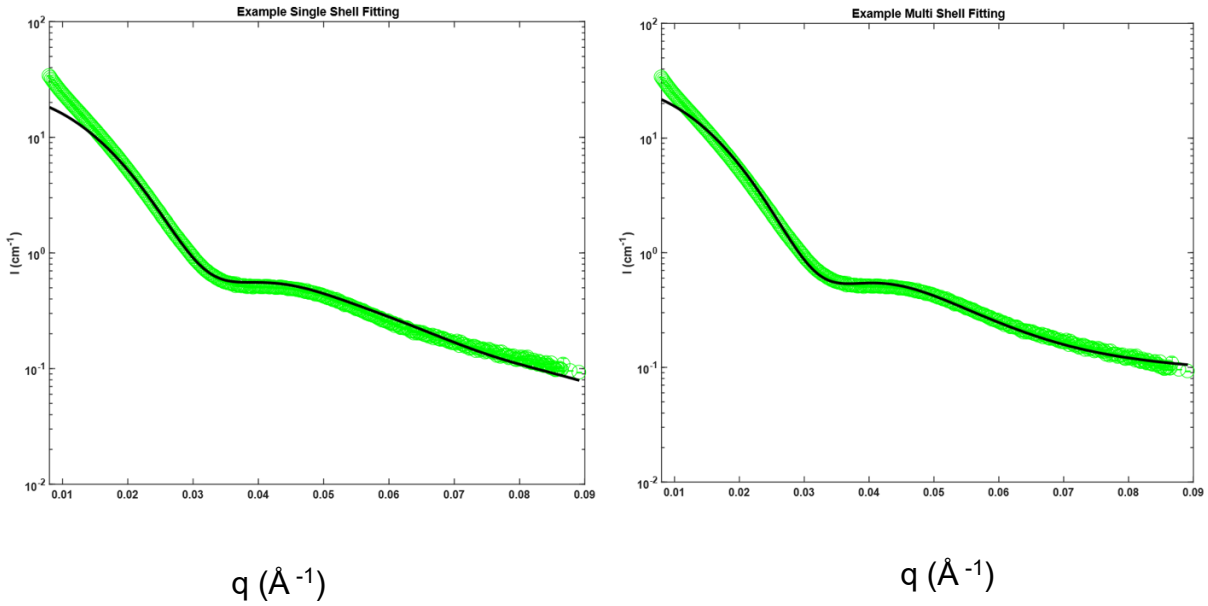

Figure A3.8. Example of single vs. multi-shell SAXS models. The same SAXS data (39.3 % Au) fit with two different models (single-shell, left, and multi-shell, right), shows good agreement for both models. Yet the multi-shell model shows an improvement in the goodness-of-fit in the low-q region.

Figure A3.8 (above) shows the fits (red) of the same X-Ray Scattering spectrum (black, 39.3 % Au). The multi-shell fit (right) provides a better fit for the spectra at low values of q. This is likely only due to the fact that the model includes more parameters within the fit and is mathematically more flexible. The parameters tracked include: total mean radius, core to shell thickness ratio, second shell thickness, shell 1 and shell 2 density and polydispersity.

However, introduction of additional parameters increases the error associated with the individual parameter. The multi-shell model contains 6 independent parameters, while the single-shell model only includes 4, thus introducing unneeded error into the relevant parameters for examining the

relevant mechanism. Comparison of these features between the two models reveals a similar trend of approximately the same values with exaggerated error in the multi-shell model (Figure A3.9 below).

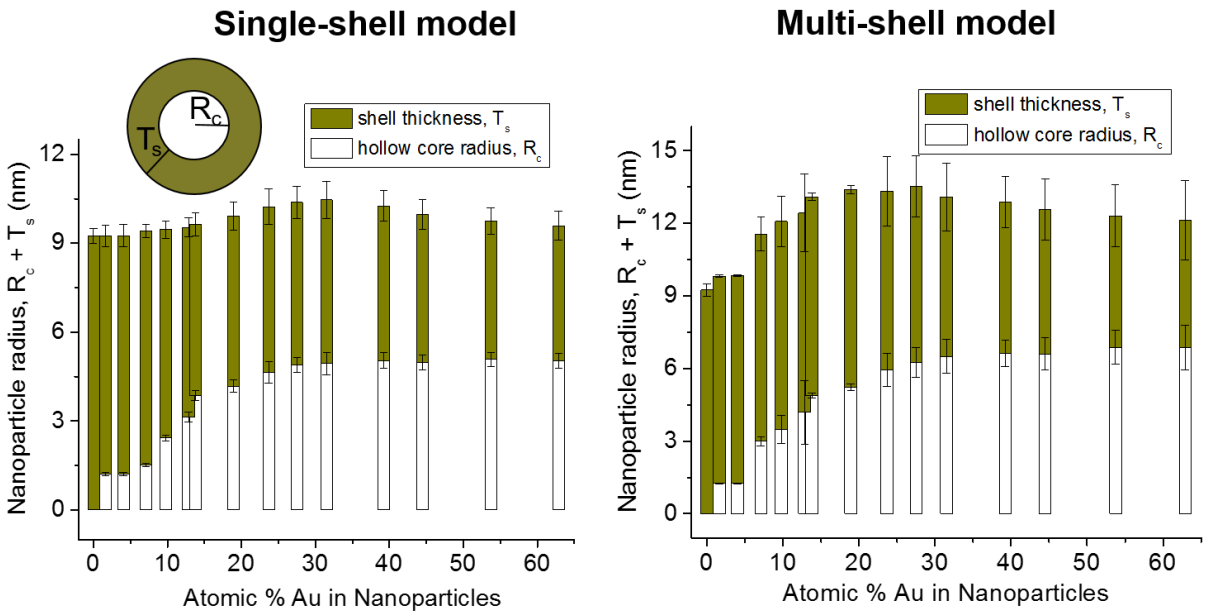

Figure A3.9. Parameter comparison between single and multi-shell SAXS models. While overall nanoparticle radius is slightly larger in the multi-shell case due to the inclusion of a secondary diffuse shell, parameter trends of hollow core growth along with decreasing shell thickness are consistent between the two separate models, demonstrating the repeatability of these trends.

Nanoparticle Size Determination

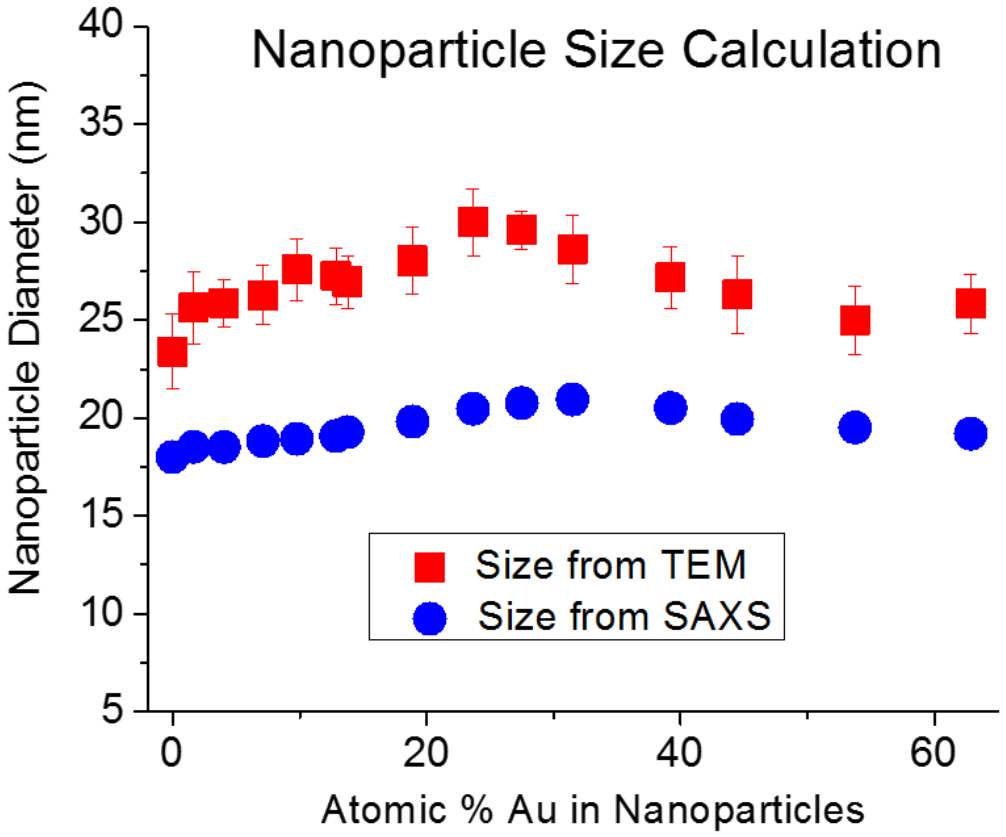

Figure A3.10. Nanoparticle Size Determination. Nanoparticle size as a function of Au atomic % within the nanoparticles is plotted as determined from TEM size analysis and SAXS form factor modeling. While slightly smaller nanoparticle sizes were determined from SAXS modeling, the trend persists that the nanoparticle size is not highly variant throughout the Galvanic replacement reaction.

XANES Results

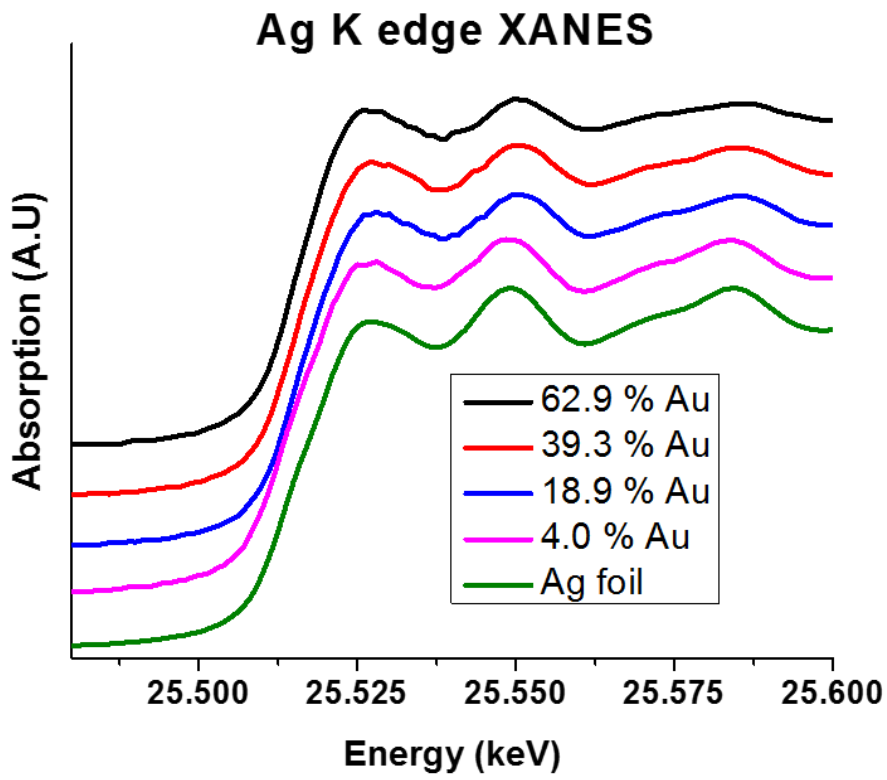

Figure A3.11. Ag K edge XANES spectra. Ag XANES spectra of each of the nanoparticle samples, regardless of transformation stage or Au content, resemble that of an Ag foil (green). This shows that Ag is in the Ag^0 state.

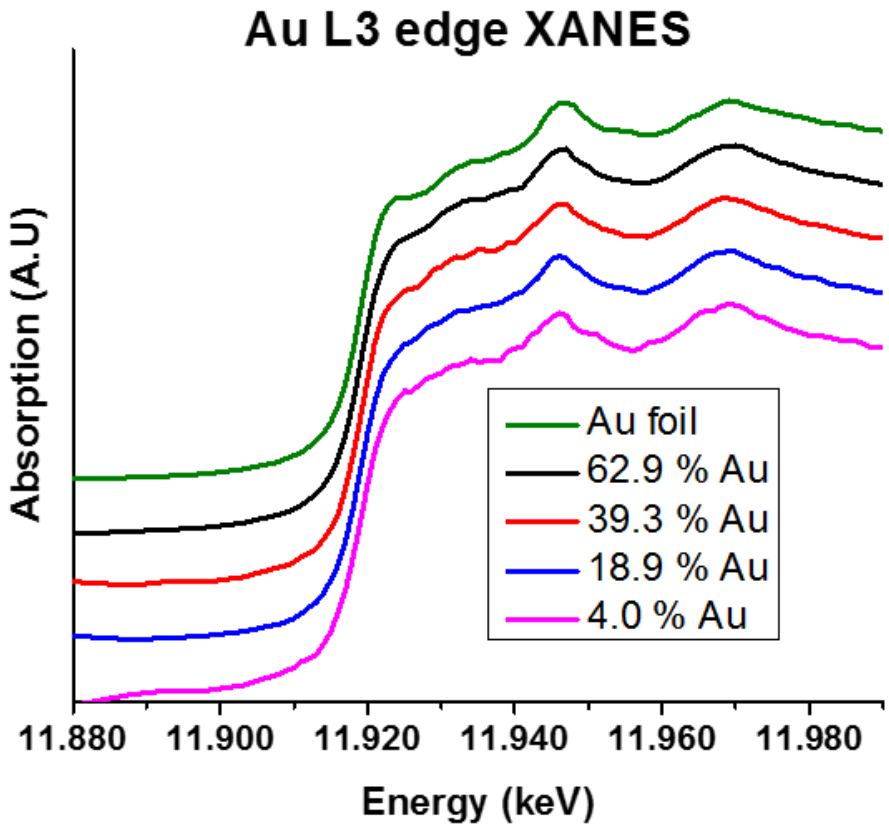

Figure A3.12. Au L3 edge XANES spectra. Au XANES spectra of each of the nanoparticle samples resemble the Au foil pattern (green) in both the edge and near-edge regions. This suggests that Au is in a similar reduced state (Au^0).

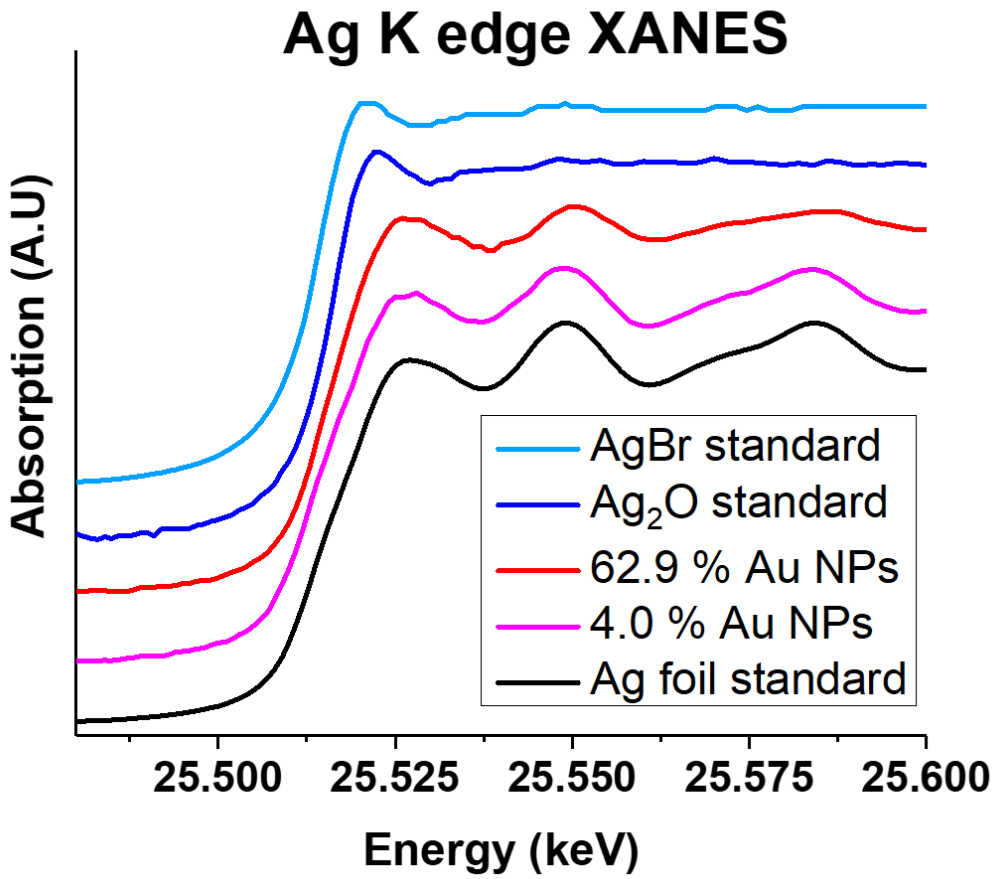

Figure A3.13. Comparison of Ag K edge XANES spectra. We compare nanoparticle spectra from low (magenta) and high (red) Au atomic % stages in the transformation from Ag nanospheres to AgAu nanocages to Ag^0 and Ag^+ standards. In order to investigate the possible presence of An Ag^+ species from Cl^- or O^{2-} etching, we compare the NP spectra to AgO_2 and AgBr (which should have a similar density of states to AgCl) standards, and find that both NP spectra more closely resemble the Ag foil standard (Ag^0). This reveals that the Ag within the particles is Ag^0.

XAFS Spectra and Fitting Models

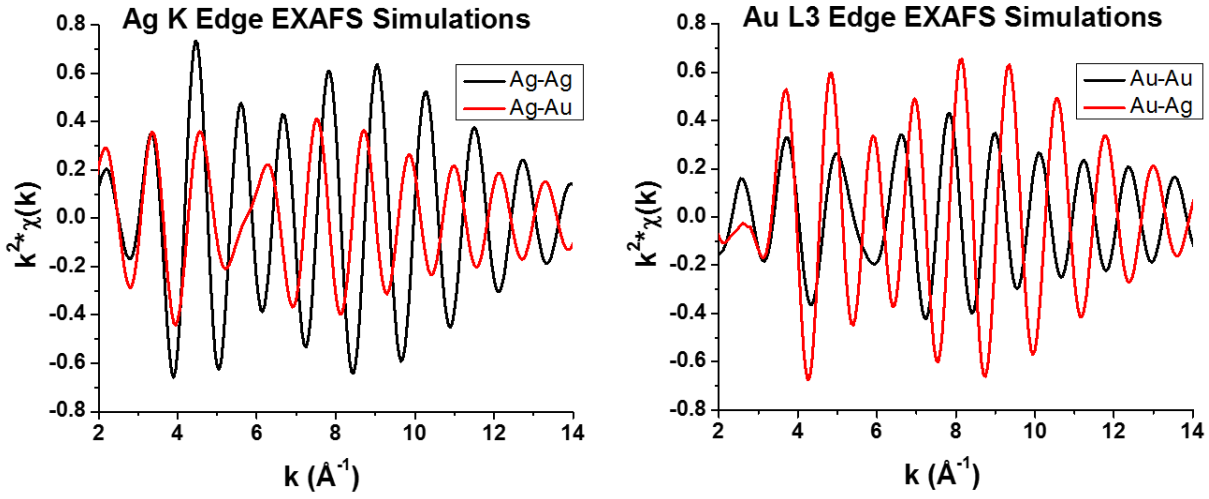

Figure A3.14. Ag K edge and Au L3 edge simulations show we can distinguish Ag-Ag and Ag-Au as well as Au-Au and Au-Ag pathways. Ag K edge simulations (left) and Au L3 edge simulations (right) of first shell pathways set at 2.884 Å with all identical parameters (coordination number, σ^2, etc.) are shown. Changes in phase shift result in an offset in the phase of the scattering pathways. There is also a notable difference in the scattering amplitude as a function of k. These drastic spectral differences enable quantitative analysis of the amounts of Ag-Ag, Ag-Au and Au-Au present within the nanoparticles as a function of their transformation.

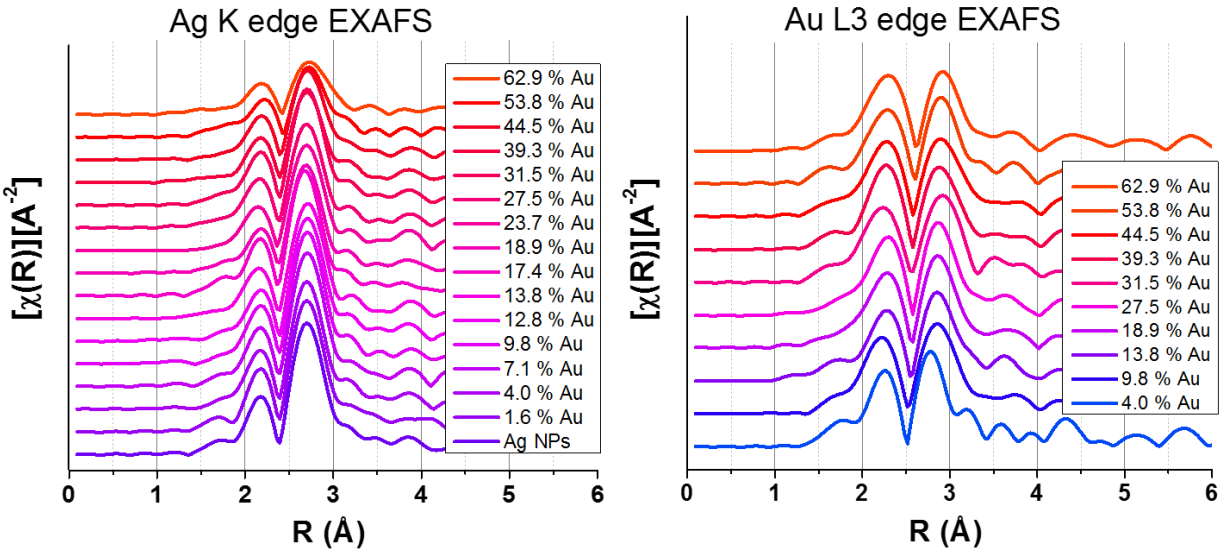

Figure A3.15. Ag K edge and Au L3 edge EXAFS data as a function of nanoparticle transformation. Ag K edge EXAFS spectra (left) and Au L3 edge EXAFS spectra (right) are plotted with vertical offsets in a gradient from low-Au content (blue) to high-Au content (red). The spectral features remain relatively constant throughout due to the high concentration of Ag-Ag and Au-Au bonds as a result of local phase segregation.

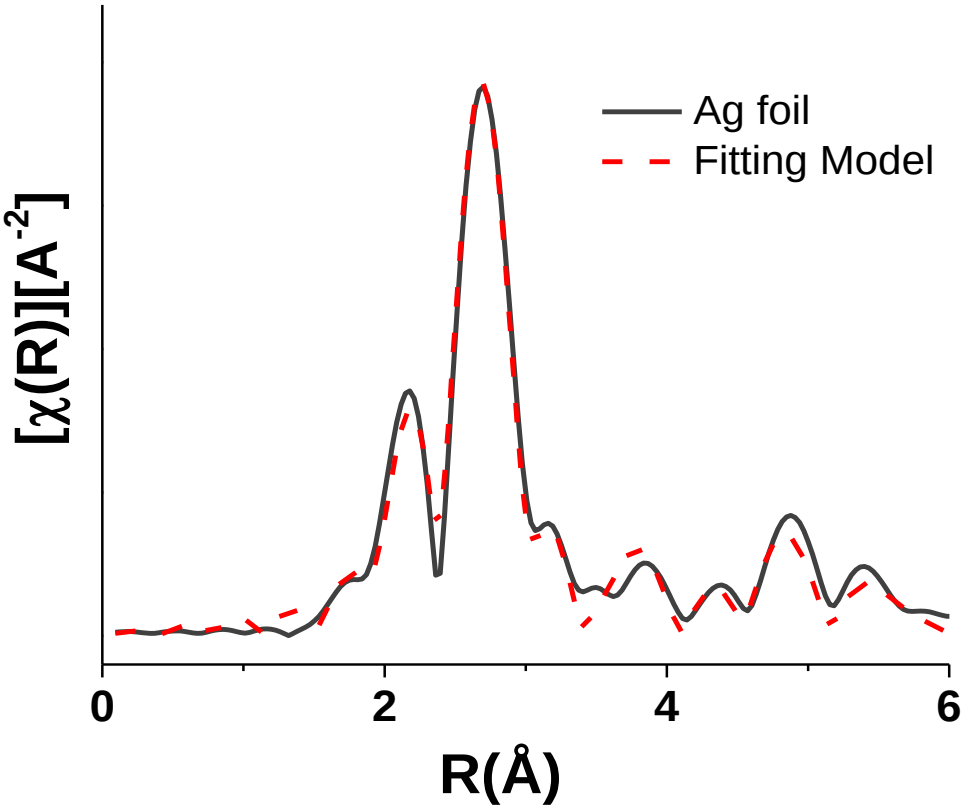

Pathway	N_{theory}	S_0^2	R (Å)	E_0 (eV)	σ^2 (Å^2) x 10^{-3}
Ag–Ag (shell 1)	12	0.74	2.866	2.35	8.03
Ag–Ag (shell 2)	6	0.74	4.062	2.35	9.85
Ag–Ag (shell 3)	24	0.74	5.009	2.35	12.1

Figure A3.16.1. Ag foil EXAFS standard and fitting model. Ag foil data was collected and modeled in order to determine the amplitude reduction factor (S_0^2), since the coordination number is a fixed known. A fitting range from 1.5 to 5 Å and a k-range from 2 to 12 Å^{-1} was used. The R-factor parameter associated with the goodness of fit for this model was 0.034.

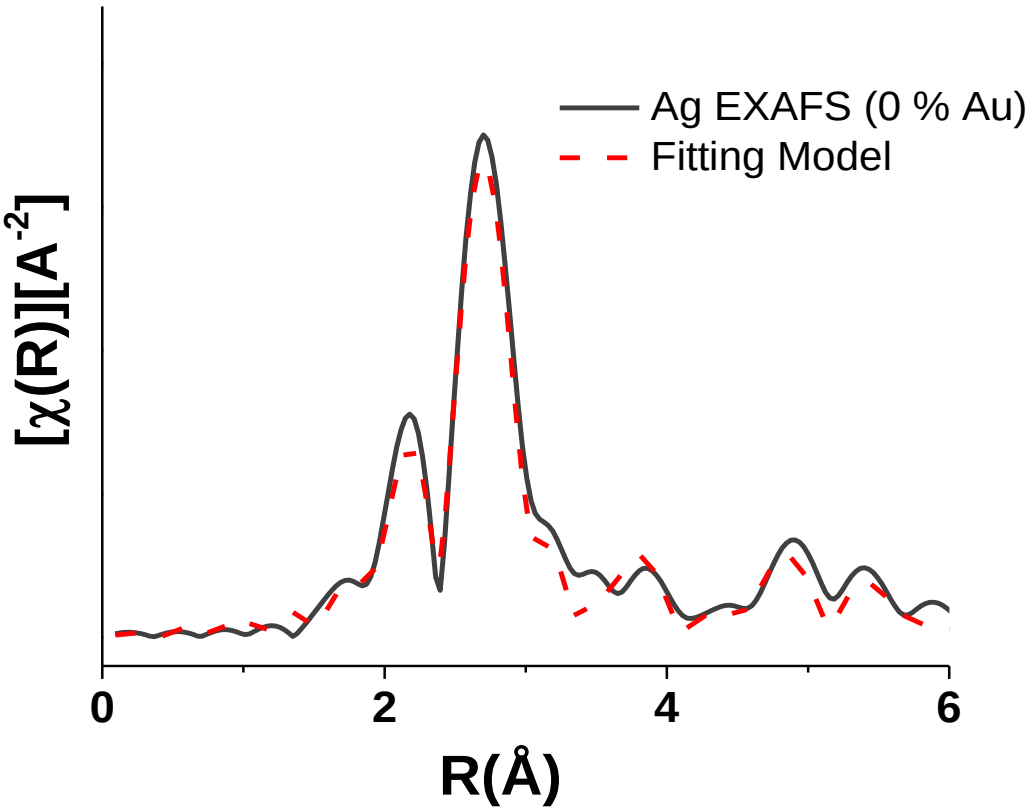

Pathway	N	R (Å)	E_0 (eV)	σ^2 (Å^2) x 10^{-3}
Ag–Ag (shell 1)	11.9 ± 0.8	2.862 ± 0.004	3.4 ± 0.3	9.3 ± 0.5

Figure A3.16.2. Starting template Ag nanoparticle EXAFS spectrum and fitting model. The Ag K-edge nanoparticle spectrum was fit using first coordination-shell Ag atomic pathways. A fitting range from 1.5 to 3.5 Å and a k-range from 2 to 12 Å^{-1} was used. The R-factor parameter associated with the goodness of fit for this model was 0.023.

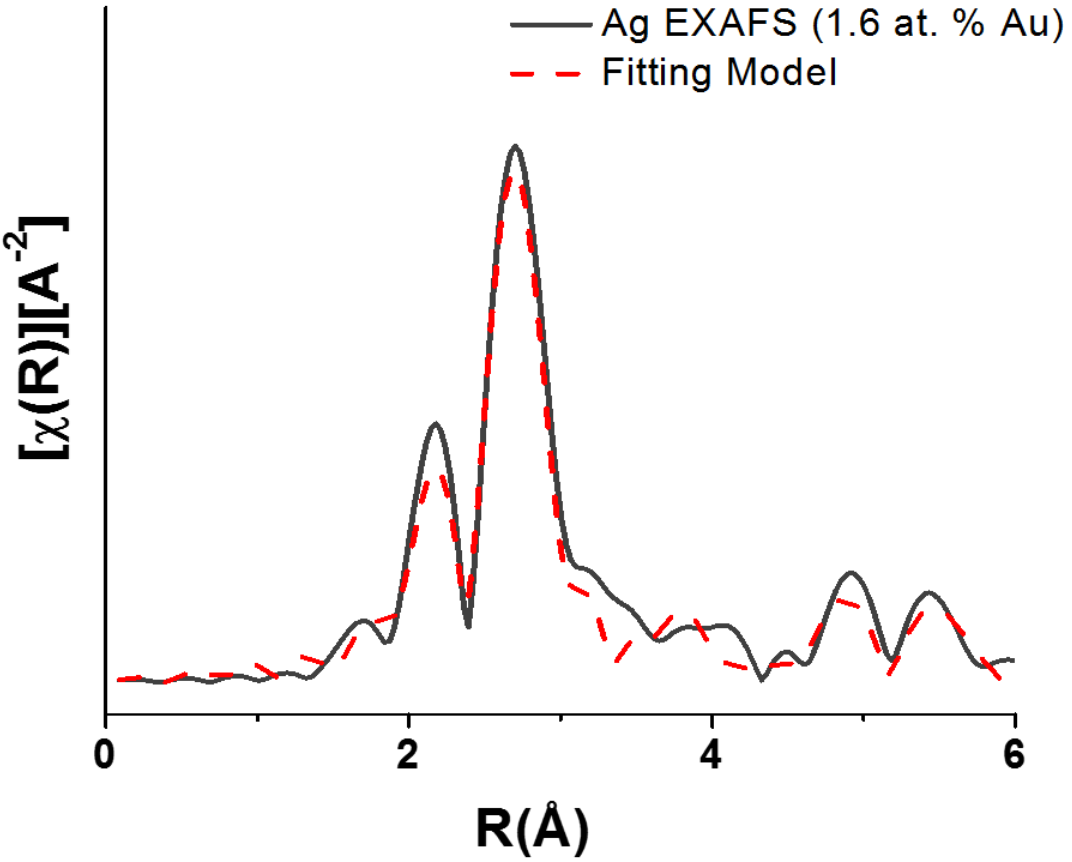

Pathway	N	R (Å)	E_0 (eV)	σ^2 (Å^2) x 10^{-3}
Ag–Ag (shell 1)	11.9 ± 1.6	2.861 ± 0.008	3.3 ± 1.2	9.0 ± 0.9
Ag–Au (shell 1)	0.5 ± 0.5	2.89 ± 0.09	2.4 ± 3.2	7.9 ± 6.3

Figure A3.16.3. Ag K edge EXAFS spectrum and fitting model for 1.6 at. % Au nanoparticle sample. The Ag K-edge nanoparticle spectrum was fit using first coordination-shell atomic pathways. A fitting range from 1.5 to 3.5 Å and a k-range from 2 to 12 Å^{-1} was used. The R-factor parameter associated with the goodness of fit for this model was 0.026.

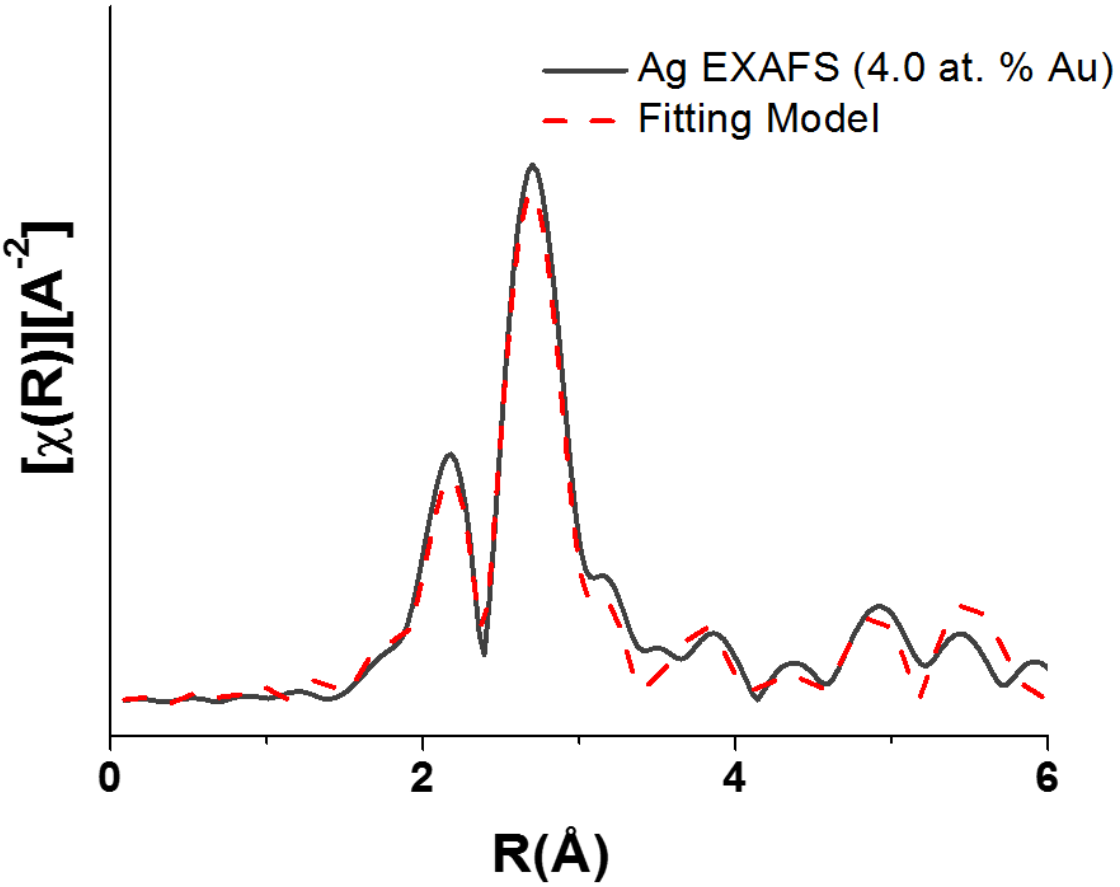

Pathway	N	R (Å)	E_0 (eV)	σ^2 (Å^2) x 10^{-3}
Ag–Ag (shell 1)	11.0 ± 1.0	2.860 ± 0.006	2.6 ± 0.7	8.8 ± 0.7
Ag–Au (shell 1)	1.1 ± 1.0	2.857	1.2 ± 3.5	8.5

Figure A3.16.4. Ag K edge EXAFS spectrum and fitting model for 4.0 at. % Au nanoparticle sample. The Ag K-edge nanoparticle spectrum was fit using first coordination-shell atomic pathways. Parameters without error bars were fixed based on results from the corresponding Au L3 Edge EXAFS model. A fitting range from 1.5 to 3.5 Å and a k-range from 2 to 12 Å^{-1} was used. The R-factor parameter associated with the goodness of fit for this model was 0.017.

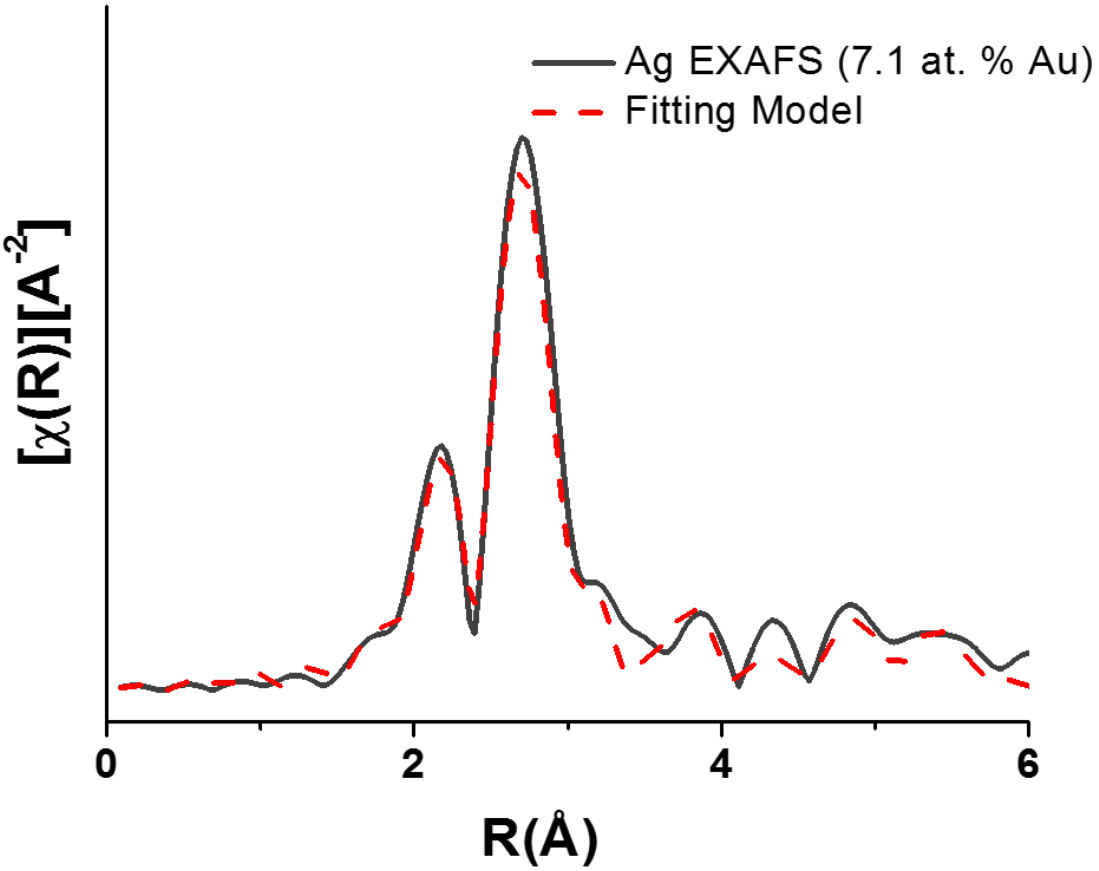

Pathway	N	R (Å)	E_0 (eV)	σ^2 (Å^2) x 10^{-3}
Ag–Ag (shell 1)	11.0 ± 1.3	2.859 ± 0.009	2.8 ± 0.8	8.6 ± 1.2
Ag–Au (shell 1)	1.3 ± 1.1	2.84 ± 0.04	1.3 ± 9.2	7.9 ± 6.5

Figure A3.16.5. Ag K edge EXAFS spectrum and fitting model for 7.1 at. % Au nanoparticle sample. The Ag K-edge nanoparticle spectrum was fit using first coordination-shell atomic pathways. A fitting range from 1.5 to 3.5 Å and a k-range from 2 to 12 Å^{-1} was used. The R-factor parameter associated with the goodness of fit for this model was 0.020.

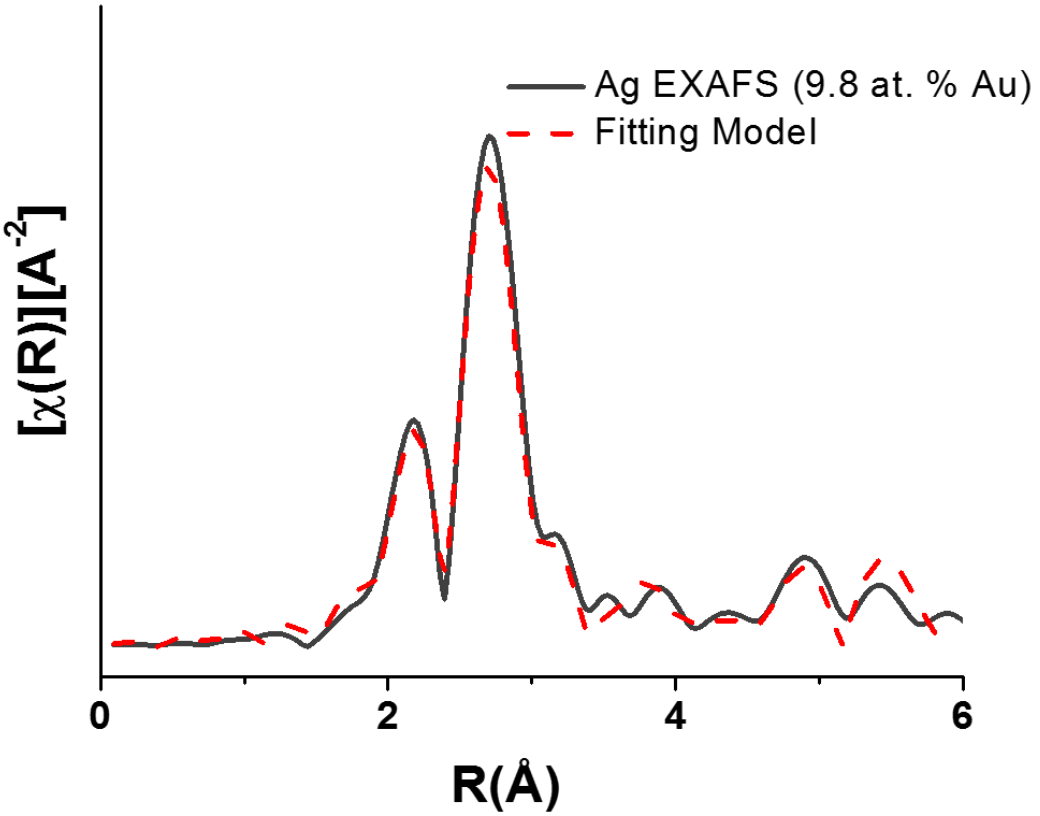

Pathway	N	R (Å)	E_0 (eV)	σ^2 (Å^2) x 10^{-3}
Ag–Ag (shell 1)	10.9 ± 0.9	2.858 ± 0.006	3.1 ± 0.6	8.6 ± 0.6
Ag–Au (shell 1)	1.4 ± 0.9	2.844	1.2 ± 3.7	8.6

Figure A3.16.6. Ag K edge EXAFS spectrum and fitting model for 9.8 at. % Au nanoparticle sample. The Ag K-edge nanoparticle spectrum was fit using first coordination-shell atomic pathways. Parameters without error bars were fixed based on results from the corresponding Au L3 Edge EXAFS model. A fitting range from 1.5 to 3.5 Å and a k-range from 2 to 12 Å^{-1} was used. The R-factor parameter associated with the goodness of fit for this model was 0.014.

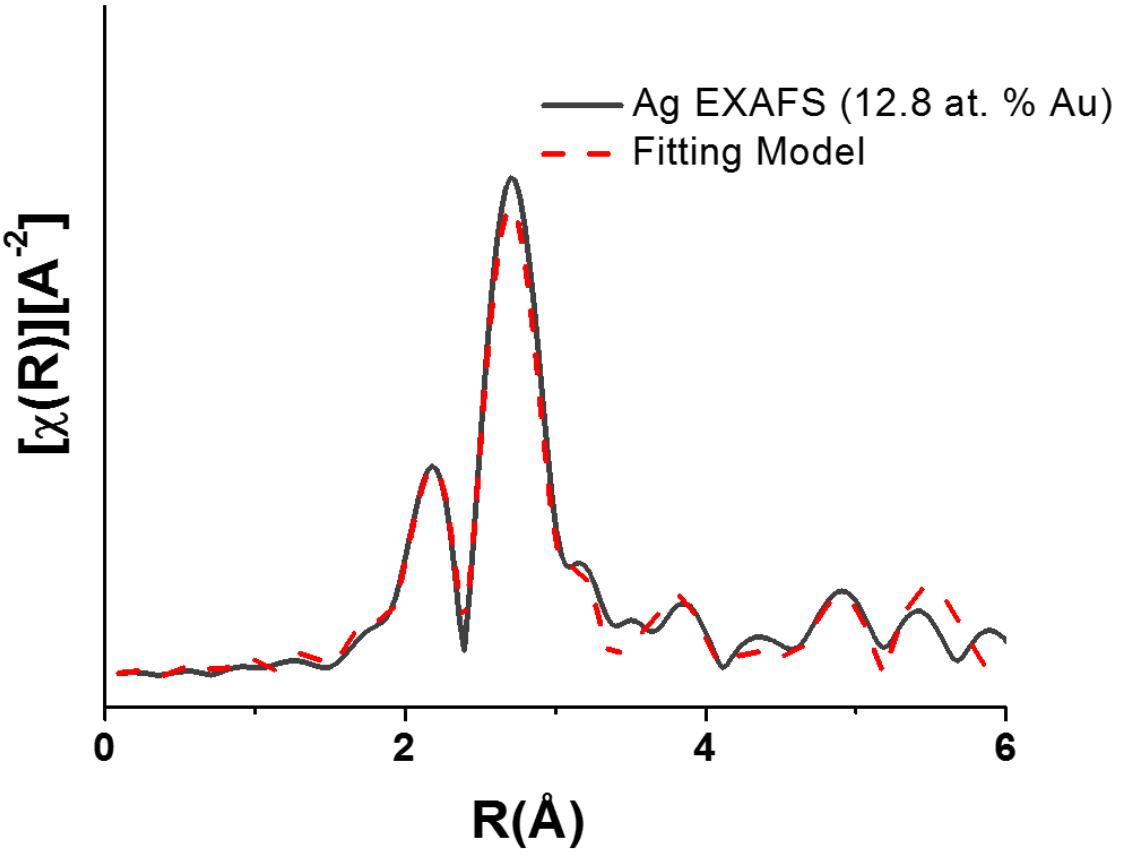

Pathway	N	R (Å)	E_0 (eV)	σ^2 (Å^2) x 10^{-3}
Ag–Ag (shell 1)	10.9 ± 0.8	2.865 ± 0.004	3.2 ± 0.5	8.9 ± 0.5
Ag–Au (shell 1)	1.5 ± 0.6	2.85 ± 0.05	2.7 ± 2.0	9.5 ± 4.0

Figure A3.16.7. Ag K edge EXAFS spectrum and fitting model for 12.8 at. % Au nanoparticle sample. The Ag K-edge nanoparticle spectrum was fit using first coordination-shell atomic pathways. A fitting range from 1.5 to 3.5 Å and a k-range from 2 to 12 Å^{-1} was used. The R-factor parameter associated with the goodness of fit for this model was 0.014.

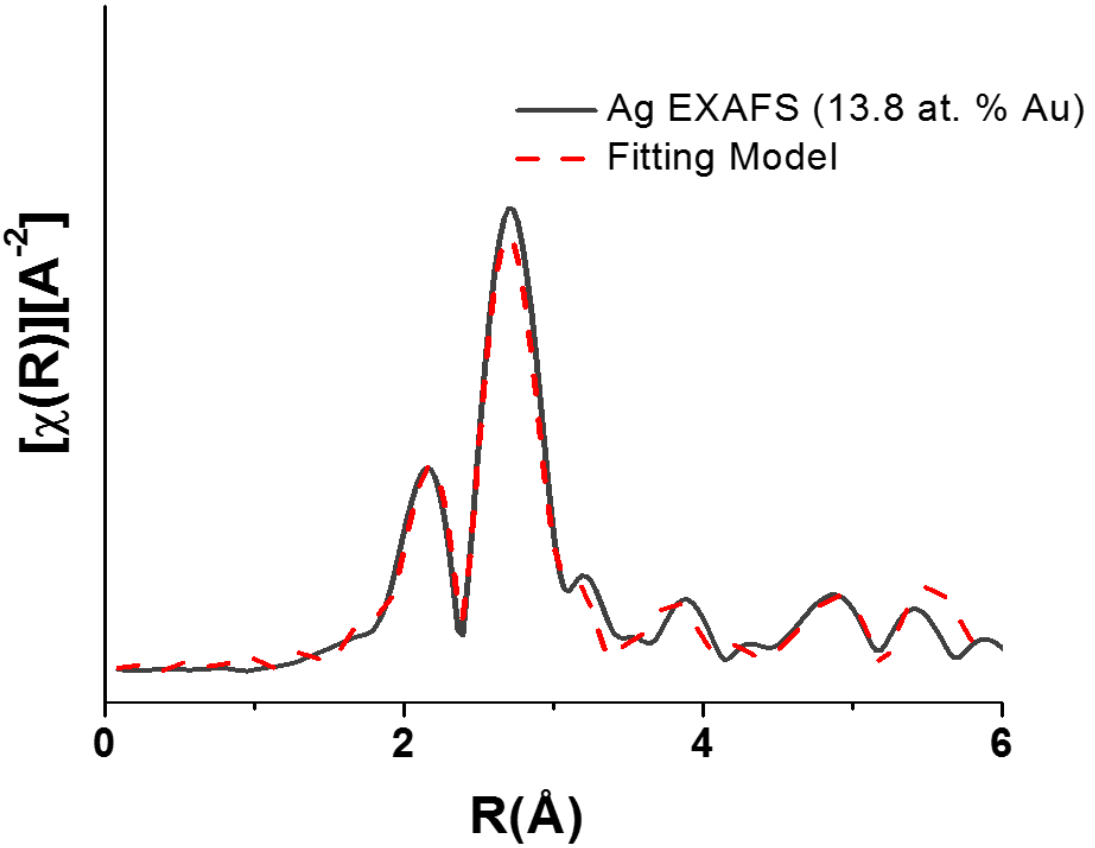

Pathway	N	R (Å)	E_0 (eV)	σ^2 (Å^2) x 10^{-3}
Ag–Ag (shell 1)	10.1 ± 1.3	2.860 ± 0.009	2.1 ± 0.9	9.0 ± 0.9
Ag–Au (shell 1)	2.1 ± 1.3	2.863	1.6 ± 5.5	9.2

Figure A3.16.8. Ag K edge EXAFS spectrum and fitting model for 13.8 at. % Au nanoparticle sample. The Ag K-edge nanoparticle spectrum was fit using first coordination-shell atomic pathways. Parameters without error bars were fixed based on results from the corresponding Au L3 Edge EXAFS model. A fitting range from 1.5 to 3.5 Å and a k-range from 2 to 12 Å^{-1} was used. The R-factor parameter associated with the goodness of fit for this model was 0.020.

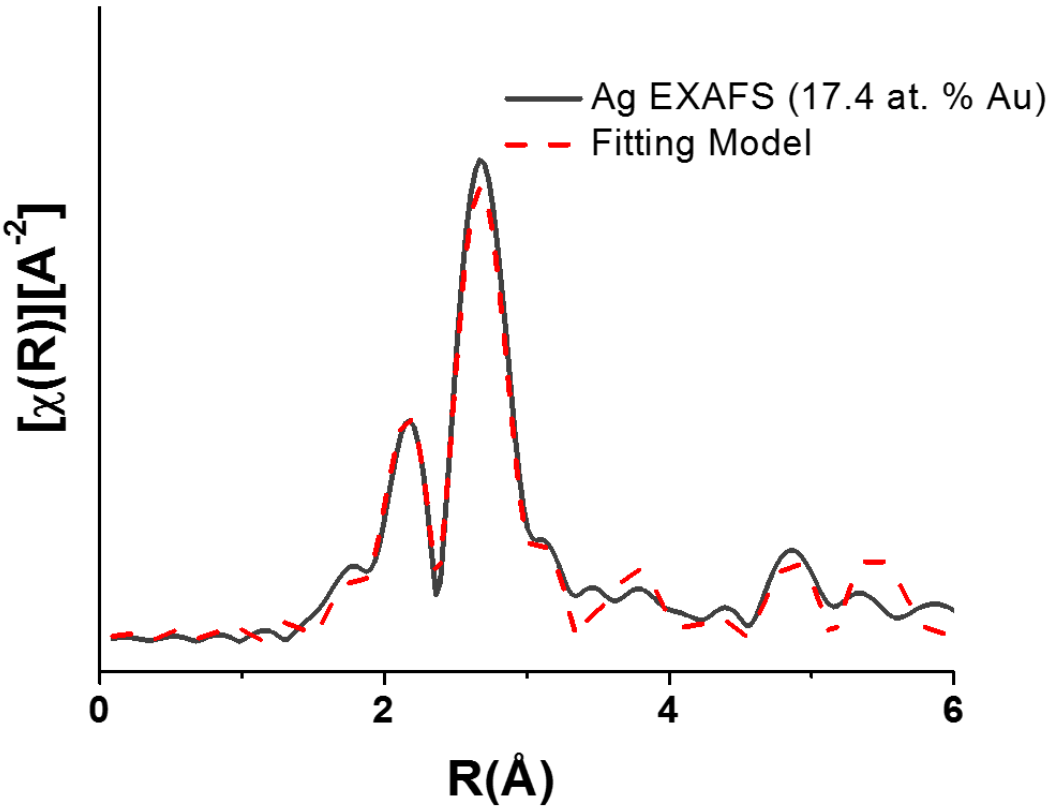

Pathway	N	R (Å)	E_0 (eV)	σ^2 (Å^2) x 10^{-3}
Ag–Ag (shell 1)	10.2 ± 0.9	2.859 ± 0.005	0.8 ± 0.7	7.9 ± 0.6
Ag–Au (shell 1)	2.3 ± 1.1	2.89 ± 0.06	0.5 ± 1.8	7.4 ± 5.0

Figure A3.16.9. Ag K edge EXAFS spectrum and fitting model for 17.4 at. % Au nanoparticle sample. The Ag K-edge nanoparticle spectrum was fit using first coordination-shell atomic pathways. A fitting range from 1.5 to 3.5 Å and a k-range from 2 to 12 Å^{-1} was used. The R-factor parameter associated with the goodness of fit for this model was 0.015.

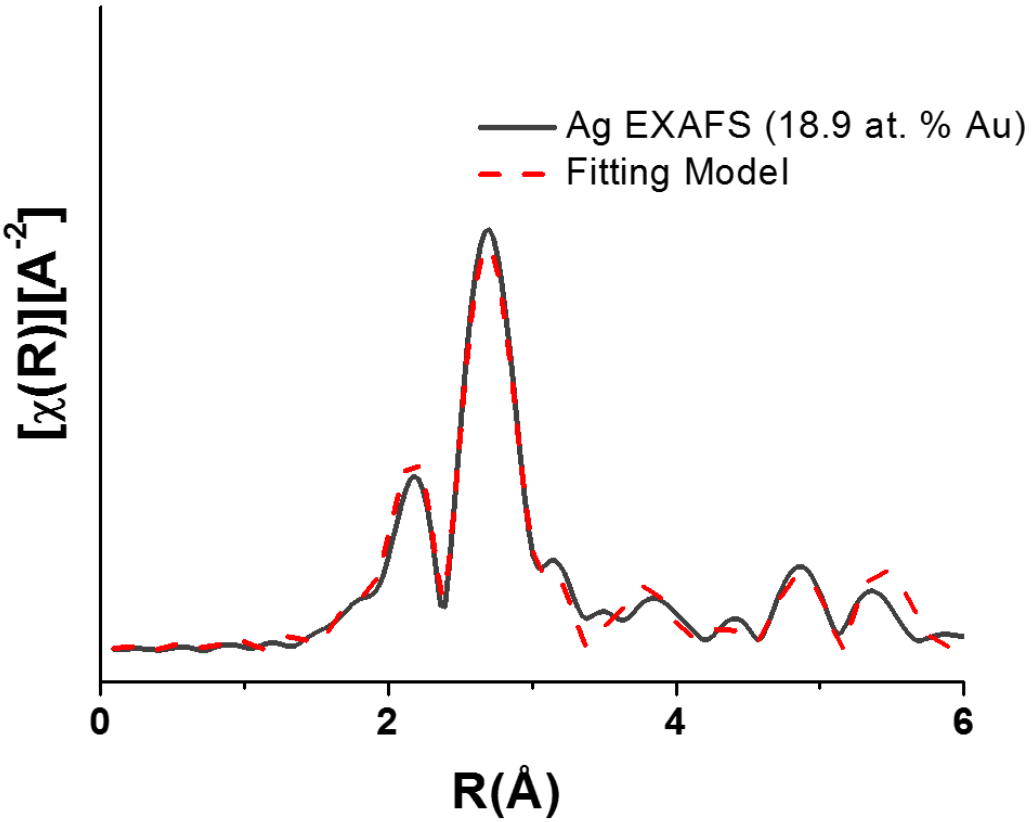

Pathway	N	R (Å)	E_0 (eV)	σ^2 (Å^2) x 10^{-3}
Ag–Ag (shell 1)	9.4 ± 1.0	2.859 ± 0.008	1.3 ± 0.8	8.7 ± 0.8
Ag–Au (shell 1)	1.9 ± 1.0	2.851	0.1 ± 3.8	8.3

Figure A3.16.10. Ag K edge EXAFS spectrum and fitting model for 18.9 at. % Au nanoparticle sample. The Ag K-edge nanoparticle spectrum was fit using first coordination-shell atomic pathways. Parameters without error bars were fixed based on results from the corresponding Au L3 Edge EXAFS model. A fitting range from 1.5 to 3.5 Å and a k-range from 2 to 12 Å^{-1} was used. The R-factor parameter associated with the goodness of fit for this model was 0.013.

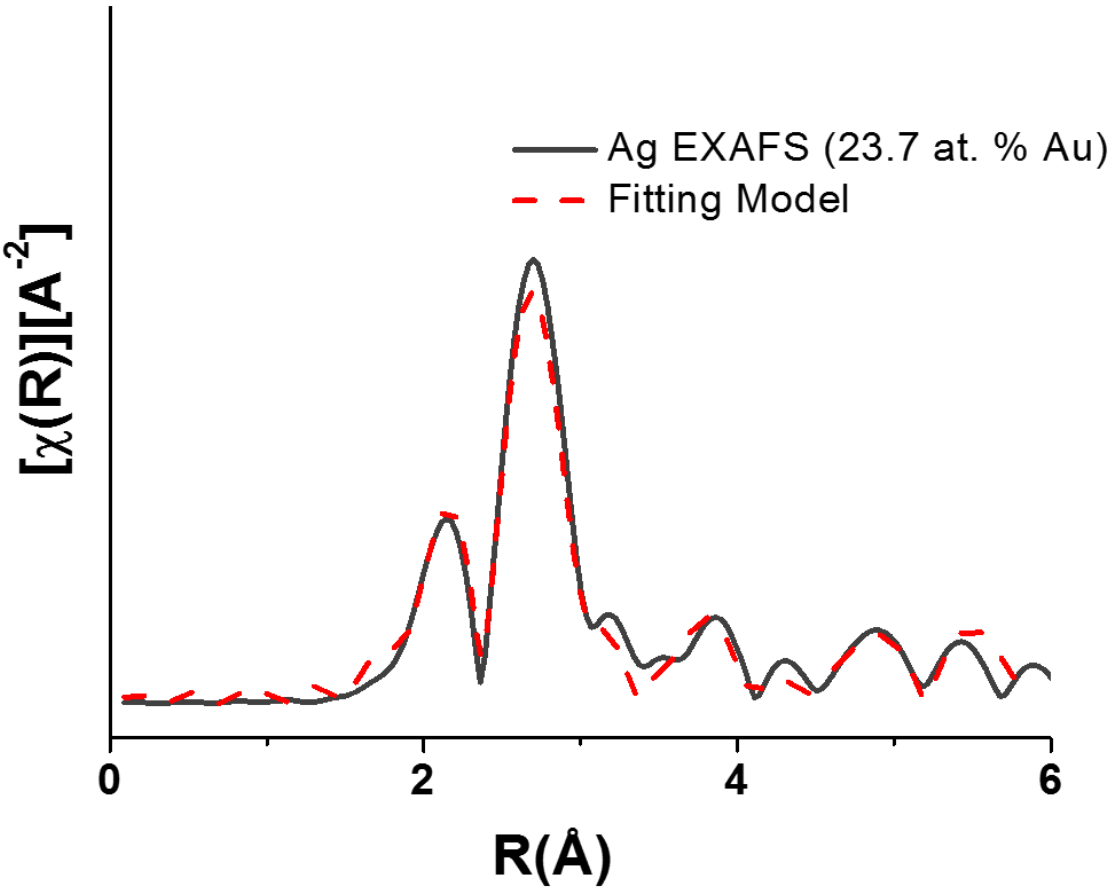

Pathway	N	R (Å)	E_0 (eV)	σ^2 (Å^2) x 10^{-3}
Ag–Ag (shell 1)	9.3 ± 1.1	2.857 ± 0.007	0.9 ± 0.6	9.2 ± 0.9
Ag–Au (shell 1)	2.0 ± 1.1	2.85 ± 0.07	0.2 ± 4.2	8.9 ± 5.0

Figure A3.16.11. Ag K edge EXAFS spectrum and fitting model for 23.7 at. % Au nanoparticle sample. The Ag K-edge nanoparticle spectrum was fit using first coordination-shell atomic pathways. A fitting range from 1.5 to 3.5 Å and a k-range from 2 to 12 Å^{-1} was used. The R-factor parameter associated with the goodness of fit for this model was 0.021.

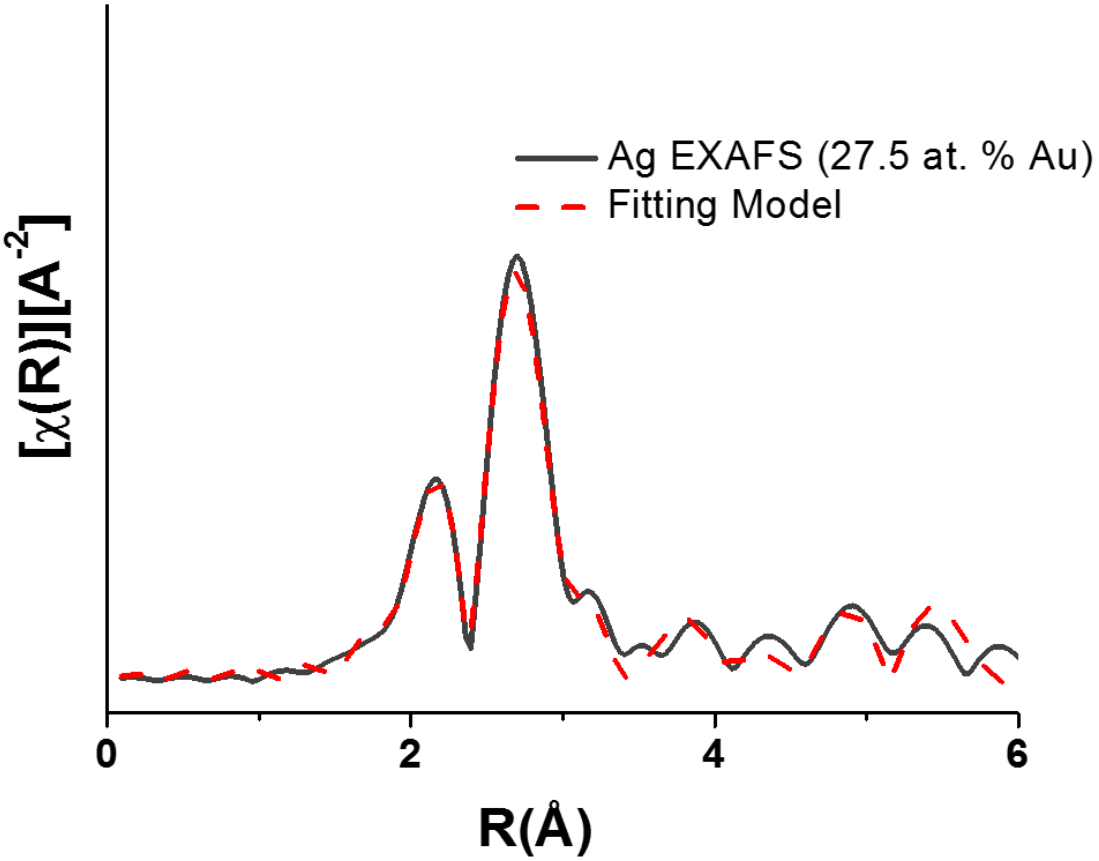

Pathway	N	R (Å)	E_0 (eV)	σ^2 (Å^2) x 10^{-3}
Ag–Ag (shell 1)	9.4 ± 1.1	2.860 ± 0.008	1.2 ± 0.9	8.9 ± 0.9
Ag–Au (shell 1)	2.1 ± 1.0	2.859	-0.1 ± 4.0	7.9

Figure A3.16.12. Ag K edge EXAFS spectrum and fitting model for 27.5 at. % Au nanoparticle sample. The Ag K-edge nanoparticle spectrum was fit using first coordination-shell atomic pathways. Parameters without error bars were fixed based on results from the corresponding Au L3 Edge EXAFS model. A fitting range from 1.5 to 3.5 Å and a k-range from 2 to 12 Å^{-1} was used. The R-factor parameter associated with the goodness of fit for this model was 0.013.

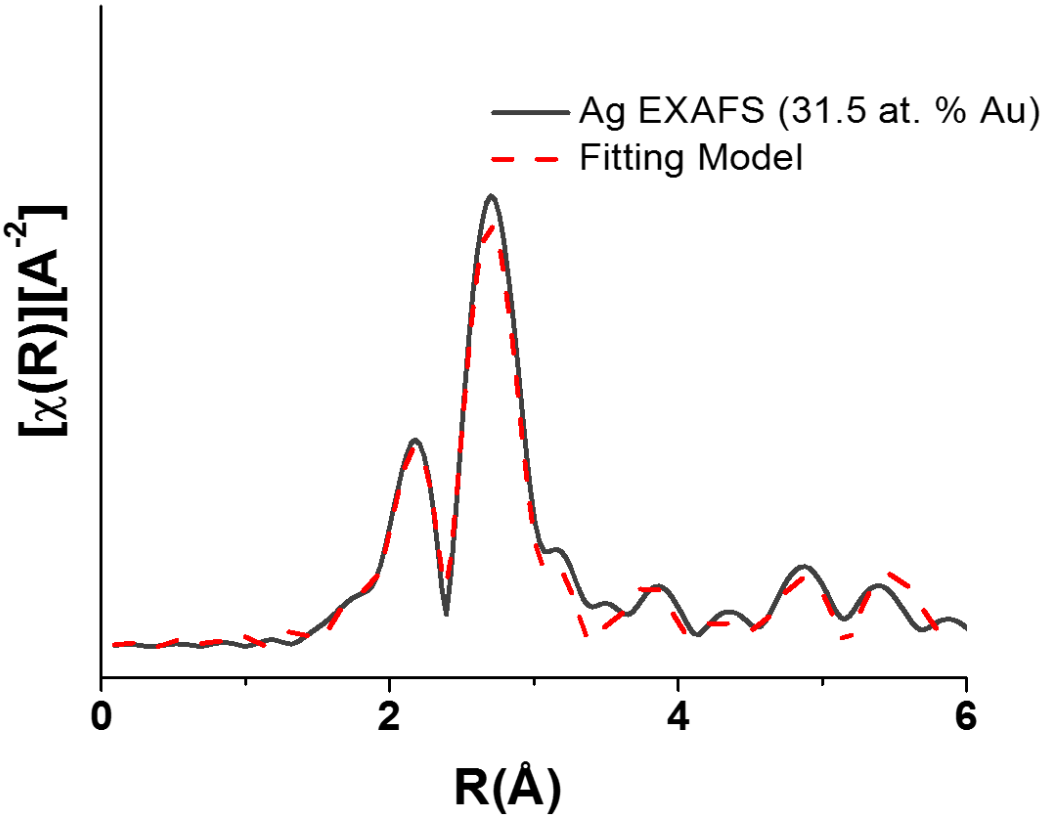

Pathway	N	R (Å)	E_0 (eV)	σ^2 (Å^2) x 10^{-3}
Ag–Ag (shell 1)	9.5 ± 1.0	2.857 ± 0.007	2.1 ± 0.7	8.6 ± 0.7
Ag–Au (shell 1)	2.1 ± 1.0	2.827	-0.3 ± 3.5	7.7

Figure A3.16.13. Ag K edge EXAFS spectrum and fitting model for 31.5 at. % Au nanoparticle sample. The Ag K-edge nanoparticle spectrum was fit using first coordination-shell atomic pathways. Parameters without error bars were fixed based on results from the corresponding Au L3 Edge EXAFS model. A fitting range from 1.5 to 3.5 Å and a k-range from 2 to 12 Å^{-1} was used. The R-factor parameter associated with the goodness of fit for this model was 0.018.

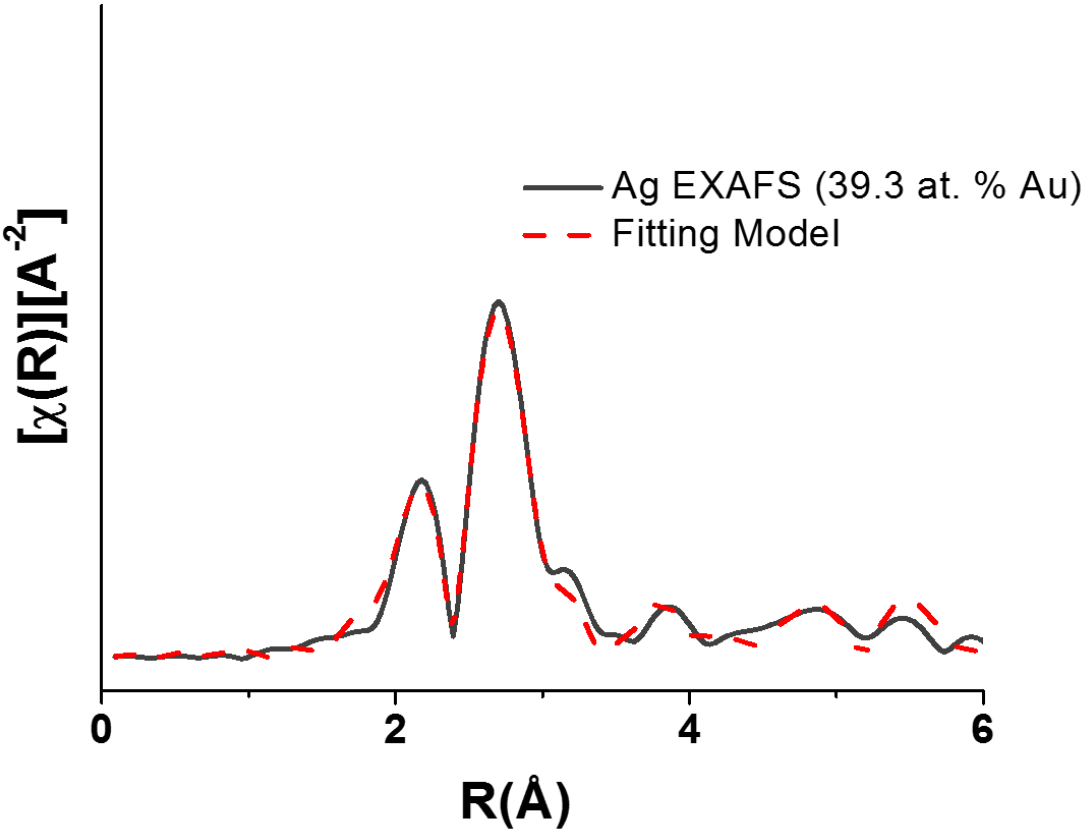

Pathway	N	R (Å)	E_0 (eV)	σ^2 (Å^2) x 10^{-3}
Ag–Ag (shell 1)	8.4 ± 1.1	2.859 ± 0.009	1.4 ± 1.0	9.2 ± 1.0
Ag–Au (shell 1)	2.2 ± 1.0	2.849	0.0 ± 3.6	7.6

Figure A3.16.14. Ag K edge EXAFS spectrum and fitting model for 39.3 at. % Au nanoparticle sample. The Ag K-edge nanoparticle spectrum was fit using first coordination-shell atomic pathways. Parameters without error bars were fixed based on results from the corresponding Au L3 Edge EXAFS model. A fitting range from 1.5 to 3.5 Å and a k-range from 2 to 12 Å^{-1} was used. The R-factor parameter associated with the goodness of fit for this model was 0.014.

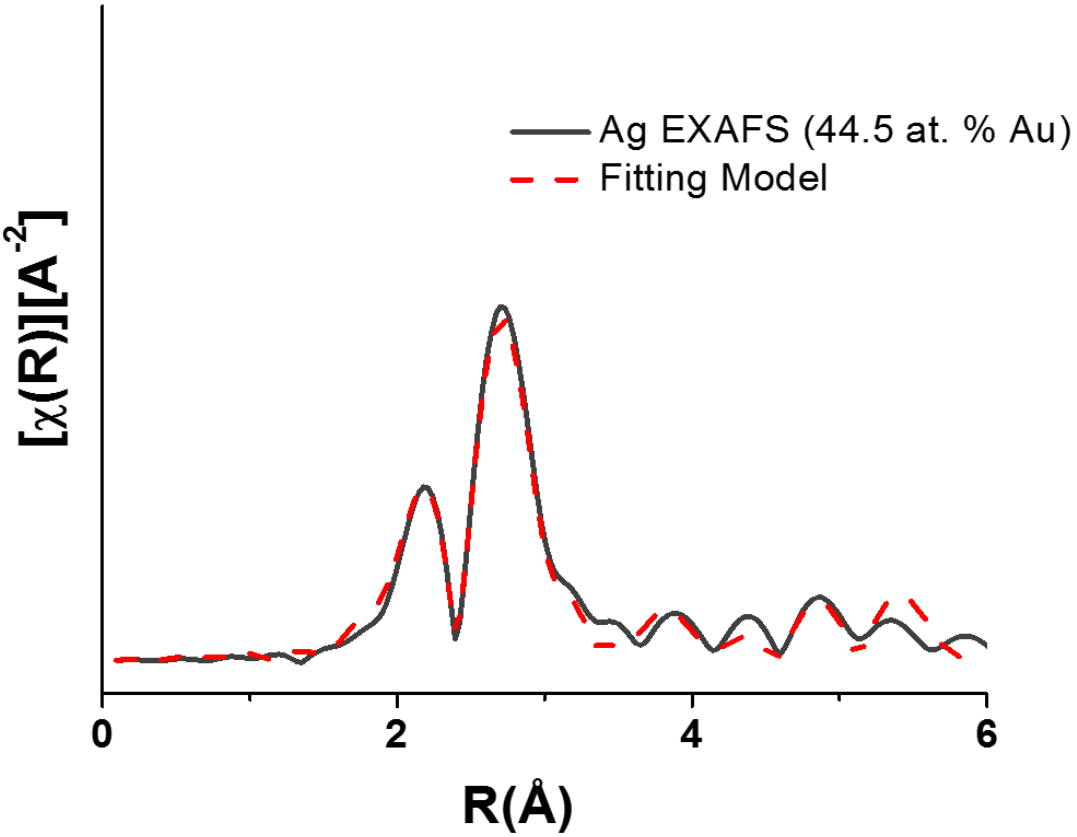

Pathway	N	R (Å)	E_0 (eV)	σ^2 (Å^2) x 10^{-3}
Ag–Ag (shell 1)	8.2 ± 1.0	2.860 ± 0.009	1.7 ± 0.9	9.3 ± 0.9
Ag–Au (shell 1)	2.6 ± 1.0	2.845	0.3 ± 3.1	7.9

Figure A3.16.15. Ag K edge EXAFS spectrum and fitting model for 44.5 at. % Au nanoparticle sample. The Ag K-edge nanoparticle spectrum was fit using first coordination-shell atomic pathways. Parameters without error bars were fixed based on results from the corresponding Au L3 Edge EXAFS model. A fitting range from 1.5 to 3.5 Å and a k-range from 2 to 12 Å^{-1} was used. The R-factor parameter associated with the goodness of fit for this model was 0.014.

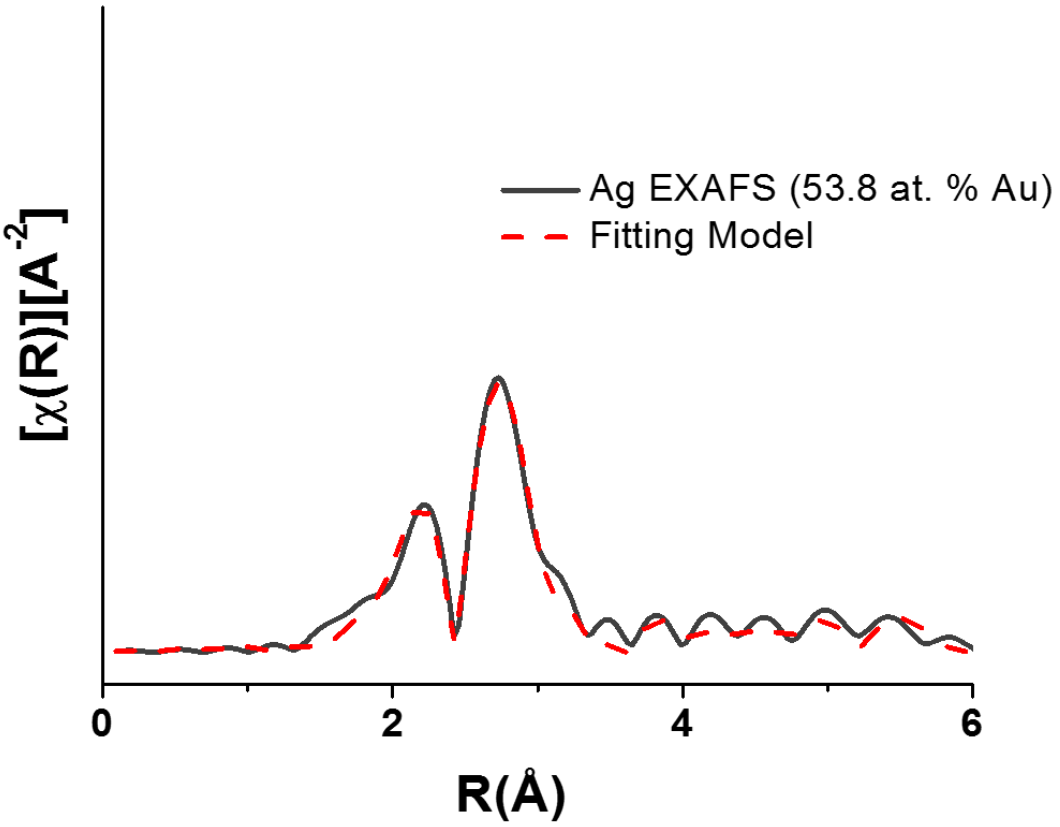

Pathway	N	R (Å)	E_0 (eV)	σ^2 (Å^2) x 10^{-3}
Ag–Ag (shell 1)	6.7 ± 1.1	2.86 ± 0.01	1.8 ± 1.4	9.9 ± 1.4
Ag–Au (shell 1)	3.1 ± 1.0	2.846	0.3 ± 2.6	8.3

Figure A3.16.16. Ag K edge EXAFS spectrum and fitting model for 53.8 at. % Au nanoparticle sample. The Ag K-edge nanoparticle spectrum was fit using first coordination-shell atomic pathways. Parameters without error bars were fixed based on results from the corresponding Au L3 Edge EXAFS model. A fitting range from 1.5 to 3.5 Å and a k-range from 2 to 12 Å^{-1} was used. The R-factor parameter associated with the goodness of fit for this model was 0.023.

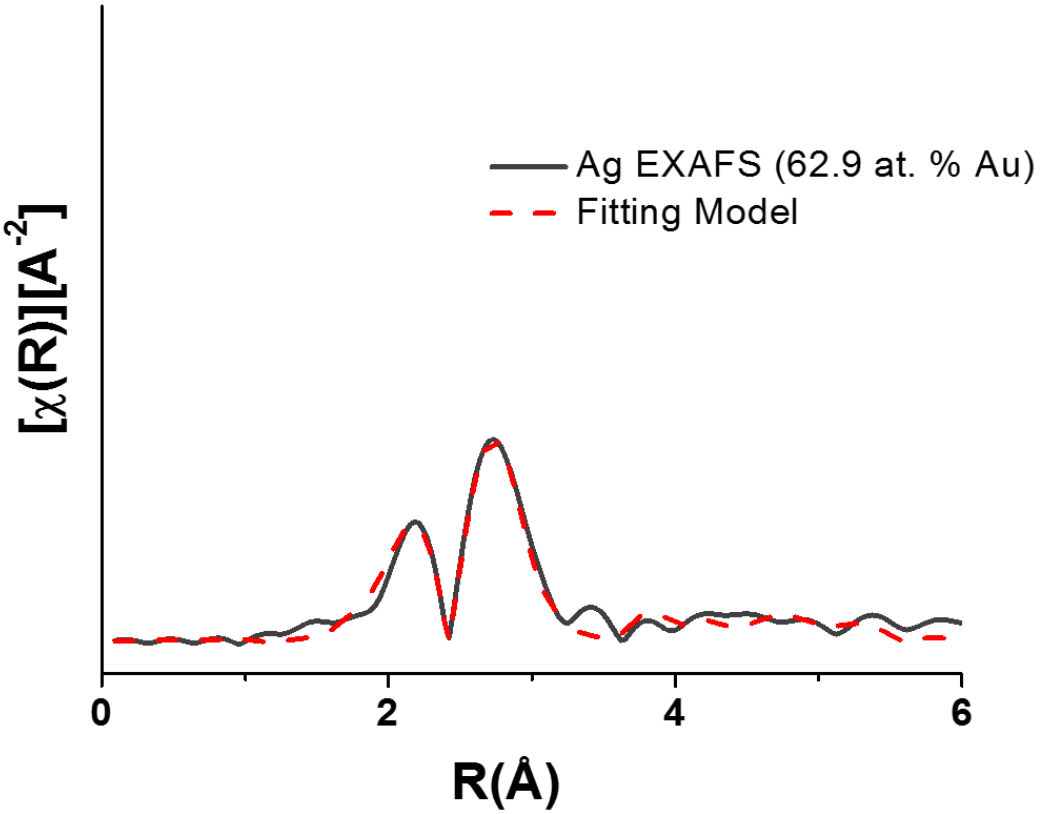

Pathway	N	R (Å)	E_0 (eV)	σ^2 (Å^2) x 10^{-3}
Ag–Ag (shell 1)	5.6 ± 1.0	2.86 ± 0.02	0.1 ± 1.5	10.7 ± 1.6
Ag–Au (shell 1)	3.2 ± 0.9	2.848	-0.2 ± 2.4	8.5

Figure A3.16.17. Ag K edge EXAFS spectrum and fitting model for 62.9 at. % Au nanoparticle sample. The Ag K-edge nanoparticle spectrum was fit using first coordination-shell atomic pathways. Parameters without error bars were fixed based on results from the corresponding Au L3 Edge EXAFS model. A fitting range from 1.5 to 3.5 Å and a k-range from 2 to 12 Å^{-1} was used. The R-factor parameter associated with the goodness of fit for this model was 0.024.

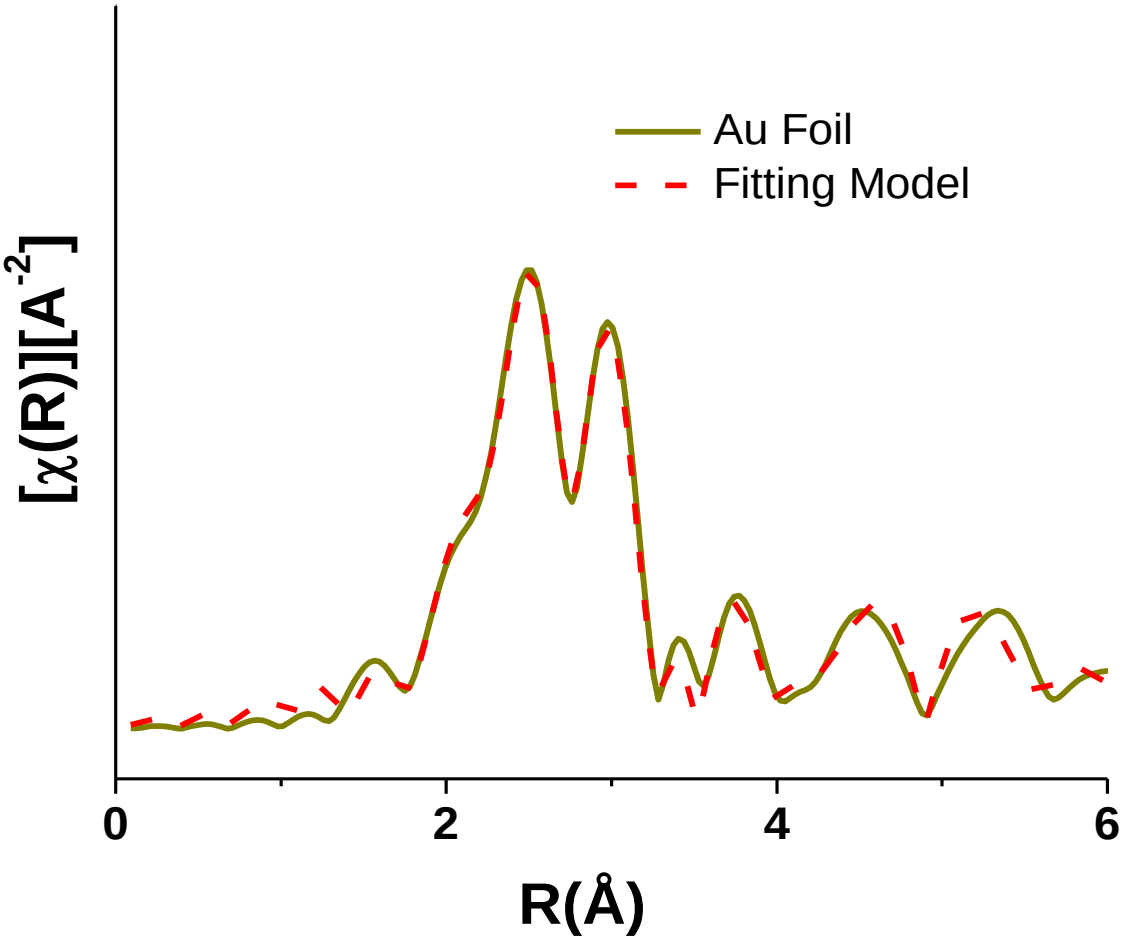

Pathway	N_{theory}	S_0^2	R (Å)	E_0 (eV)	σ^2 (Å^2) x 10^{-3}
Au–Au (shell 1)	12	0.75	2.861	5.11	7.71
Au–Au (shell 2)	6	0.75	4.051	5.11	10.8
Au–Au (shell 3)	24	0.75	4.986	5.11	12.0

Figure A3.16.18. Au L_3 edge Au foil EXAFS standard and fitting model. Au foil data was collected and modeled in order to determine the amplitude reduction factor (S_0^2), since the coordination number is a fixed known. A fitting range from 1.5 to 5 Å and a k-range from 2 to 12 Å^{-1} was used. The R-factor parameter associated with the goodness of fit for this model was 0.009.

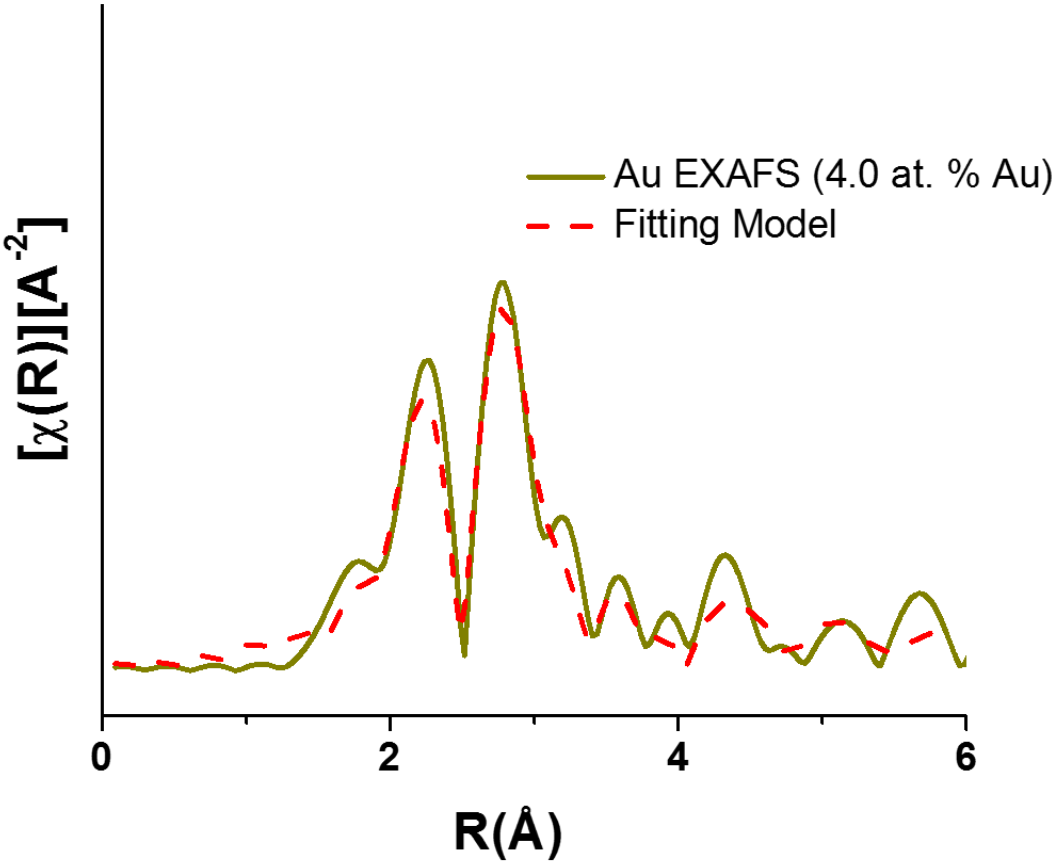

Pathway	N	R (Å)	E_0 (eV)	σ^2 (Å^2) x 10^{-3}
Au–Au (shell 1)	4.8 ± 1.3	2.88 ± 0.02	3.1 ± 0.9	10.2 ± 4.0
Au–Ag (shell 1)	6.4 ± 0.8	2.857 ± 0.009	5.0 ± 1.3	8.5 ± 1.1

Figure A3.16.19. Au L3 edge EXAFS spectrum and fitting model for 4.0 at. % Au nanoparticle sample. The Au L3-edge nanoparticle spectrum was fit using first coordination-shell atomic pathways. A fitting range from 1.5 to 3.5 Å and a k-range from 2 to 12 Å^{-1} was used. The R-factor parameter associated with the goodness of fit for this model was 0.052.

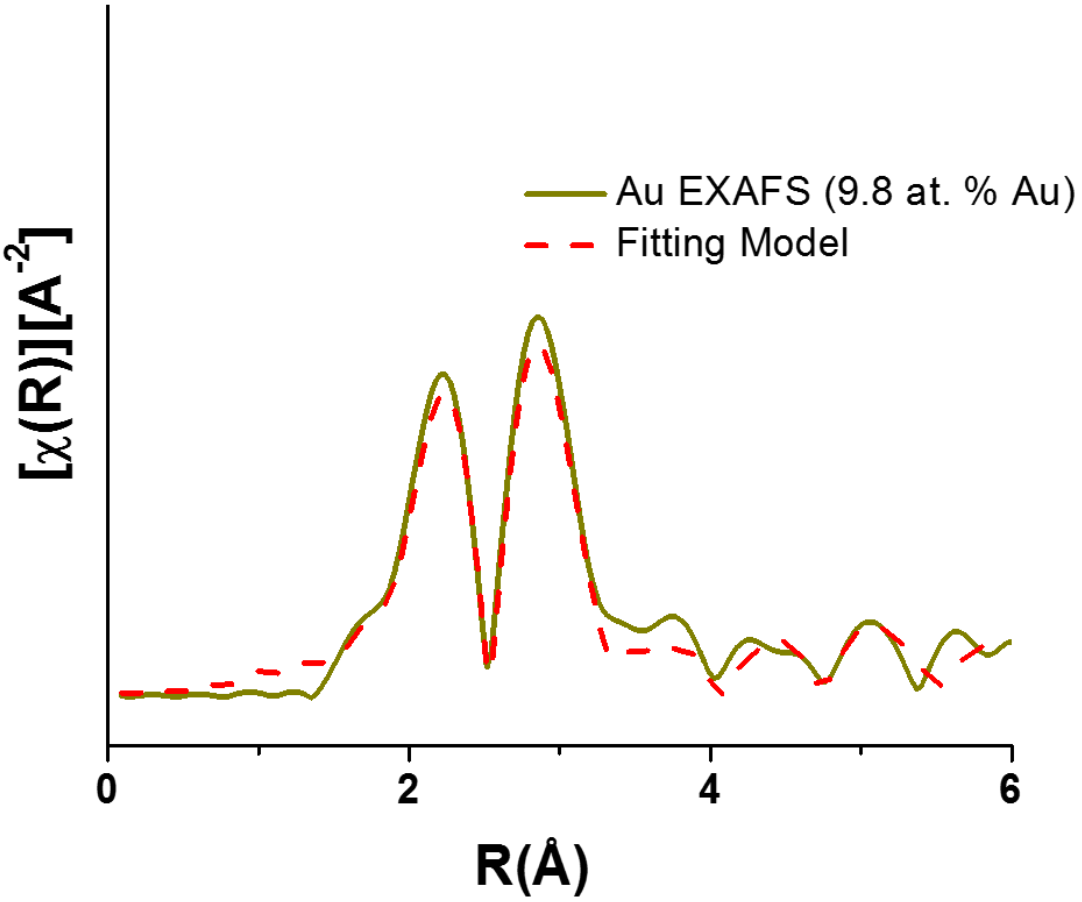

Pathway	N	R (Å)	E_0 (eV)	σ^2 (Å^2) x 10^{-3}
Au–Au (shell 1)	6.2 ± 1.6	2.86 ± 0.01	3.7 ± 1.1	7.9 ± 2.2
Au–Ag (shell 1)	5.8 ± 0.9	2.84 ± 0.01	3.9 ± 1.2	8.6 ± 1.4

Figure A3.16.20. Au L3 edge EXAFS spectrum and fitting model for 9.8 at. % Au nanoparticle sample. The Au L3-edge nanoparticle spectrum was fit using first coordination-shell atomic pathways. A fitting range from 1.5 to 3.5 Å and a k-range from 2 to 12 Å^{-1} was used. The R-factor parameter associated with the goodness of fit for this model was 0.022.

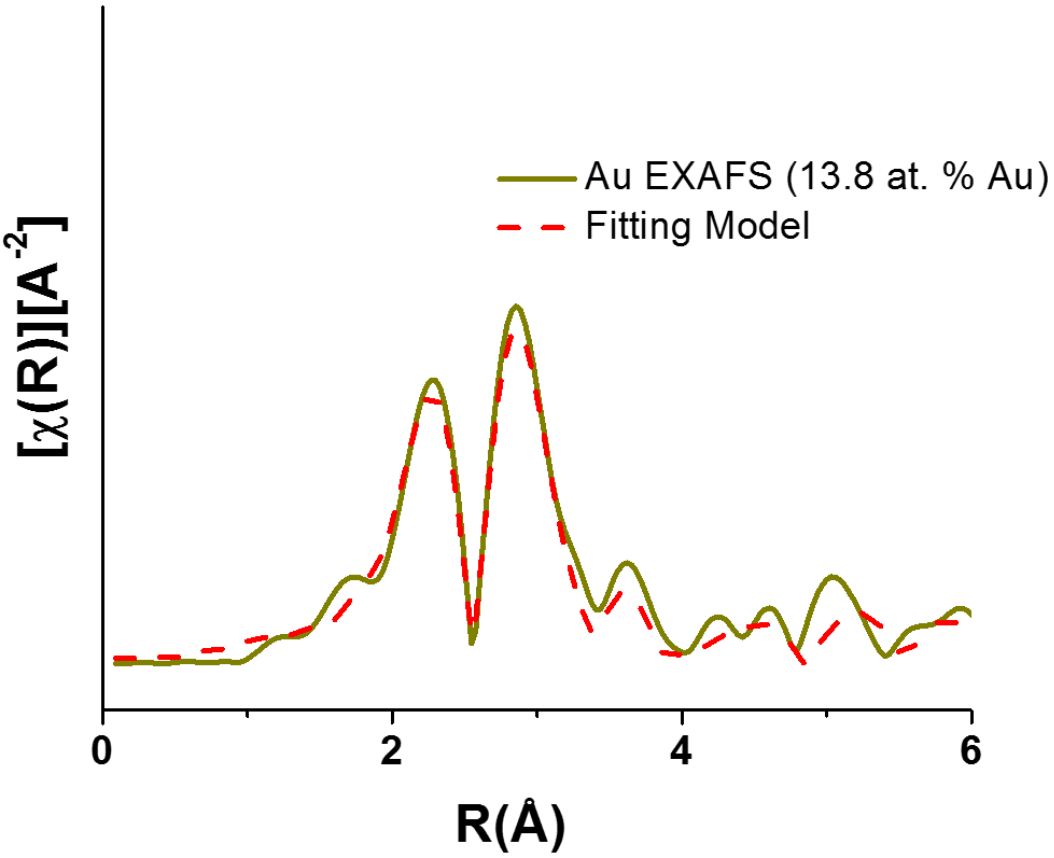

Pathway	N	R (Å)	E_0 (eV)	σ^2 (Å^2) x 10^{-3}
Au–Au (shell 1)	6.4 ± 1.5	2.86 ± 0.02	3.9 ± 0.9	9.5 ± 4.0
Au–Ag (shell 1)	5.5 ± 0.9	2.86 ± 0.01	4.7 ± 1.2	9.1 ± 1.2

Figure A3.16.21. Au L3 edge EXAFS spectrum and fitting model for 13.8 at. % Au nanoparticle sample. The Au L3-edge nanoparticle spectrum was fit using first coordination-shell atomic pathways. A fitting range from 1.5 to 3.5 Å and a k-range from 2 to 12 Å^{-1} was used. The R-factor parameter associated with the goodness of fit for this model was 0.022.

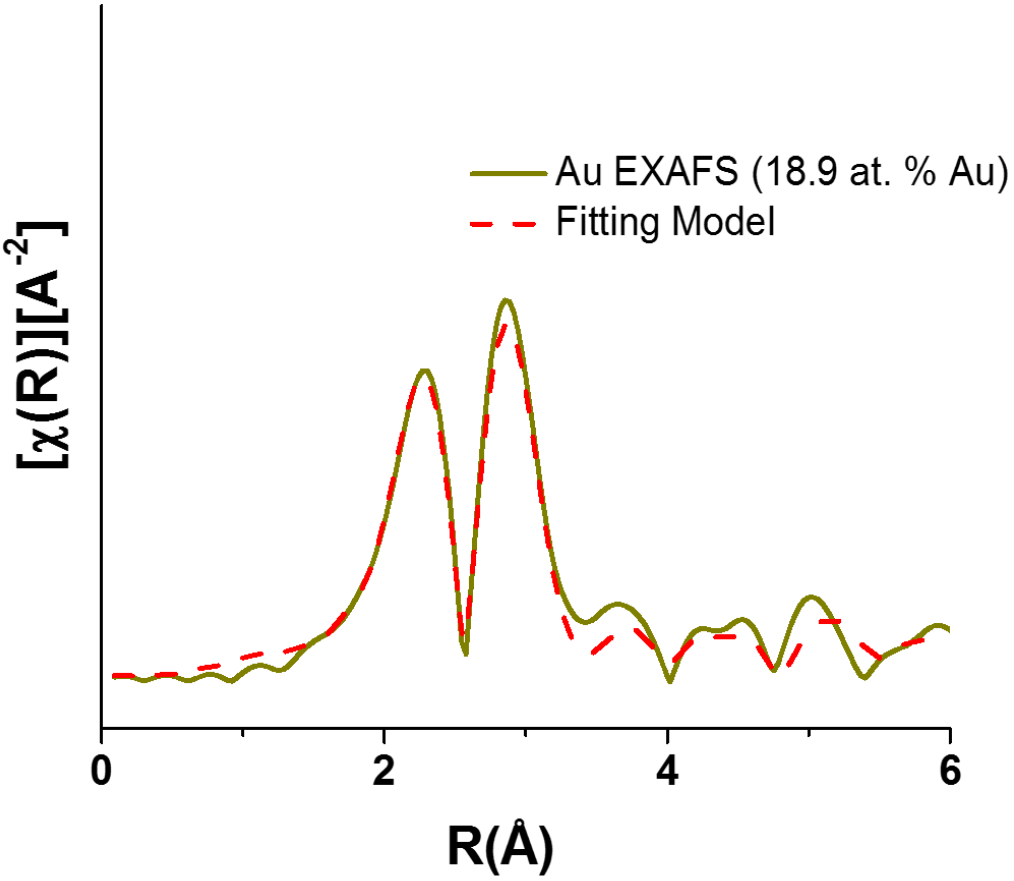

Pathway	N	R (Å)	E_0 (eV)	σ^2 (Å^2) x 10^{-3}
Au–Au (shell 1)	6.8 ± 1.3	2.847 ± 0.009	3.7 ± 0.7	8.1 ± 2.0
Au–Ag (shell 1)	5.0 ± 0.9	2.85 ± 0.01	4.4 ± 0.9	8.3 ± 1.0

Figure A3.16.22. Au L3 edge EXAFS spectrum and fitting model for 18.9 at. % Au nanoparticle sample. The Au L3-edge nanoparticle spectrum was fit using first coordination-shell atomic pathways. A fitting range from 1.5 to 3.5 Å and a k-range from 2 to 12 Å^{-1} was used. The R-factor parameter associated with the goodness of fit for this model was 0.011.

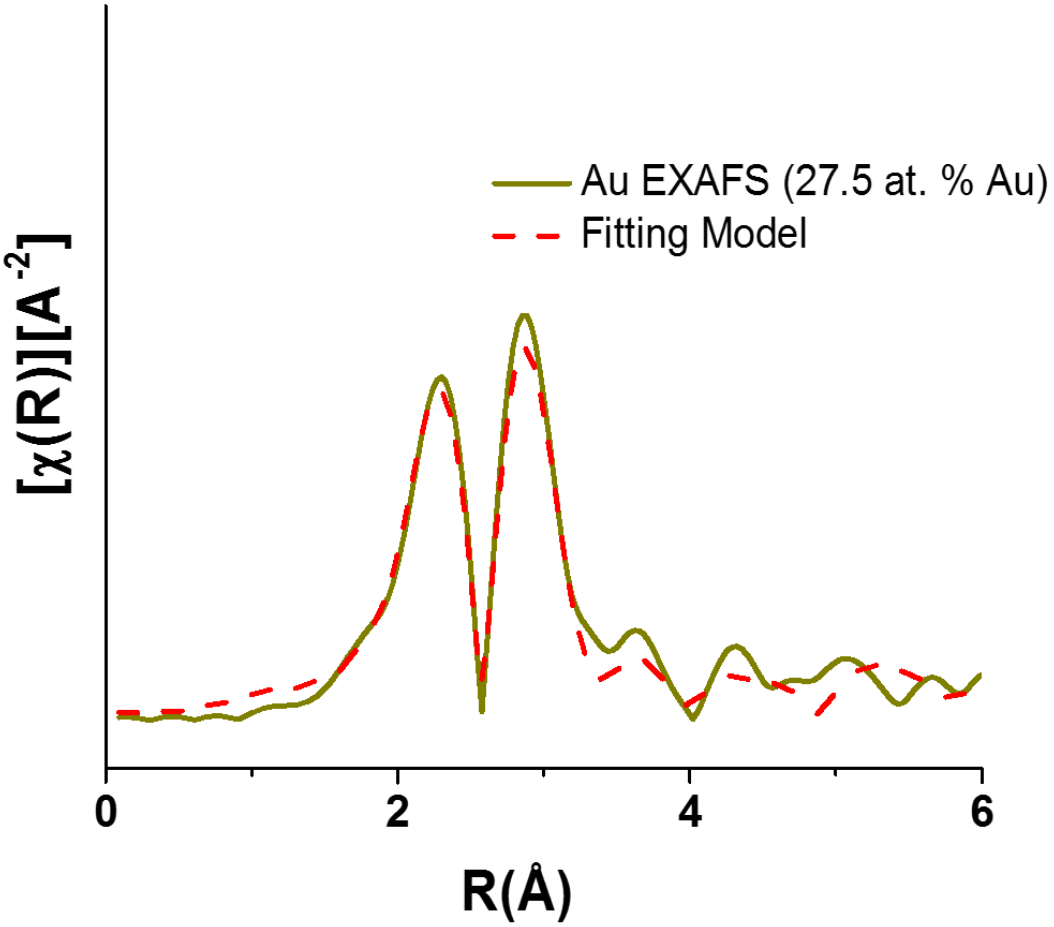

Pathway	N	R (Å)	E_0 (eV)	σ^2 (Å^2) x 10^{-3}
Au–Au (shell 1)	6.9 ± 2.1	2.85 ± 0.01	3.5 ± 0.8	8.1 ± 2.8
Au–Ag (shell 1)	4.8 ± 0.7	2.86 ± 0.01	5.3 ± 1.1	7.9 ± 1.1

Figure A3.16.23. Au L3 edge EXAFS spectrum and fitting model for 27.5 at. % Au nanoparticle sample. The Au L3-edge nanoparticle spectrum was fit using first coordination-shell atomic pathways. A fitting range from 1.5 to 3.5 Å and a k-range from 2 to 12 Å^{-1} was used. The R-factor parameter associated with the goodness of fit for this model was 0.017.

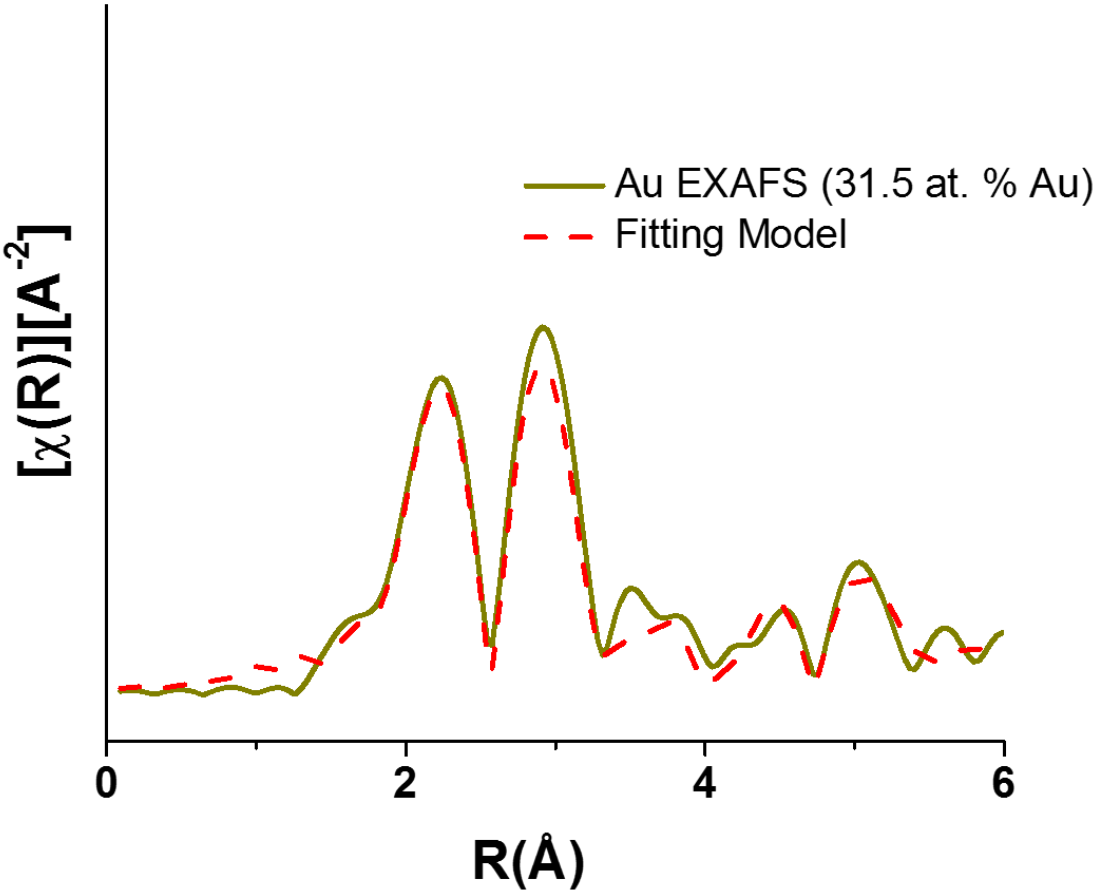

Pathway	N	R (Å)	E_0 (eV)	σ^2 (Å^2) x 10^{-3}
Au–Au (shell 1)	7.2 ± 1.1	2.847 ± 0.007	4.1 ± 0.8	7.2 ± 1.4
Au–Ag (shell 1)	4.5 ± 0.7	2.83 ± 0.01	3.6 ± 1.1	7.7 ± 1.3

Figure A3.16.24. Au L3 edge EXAFS spectrum and fitting model for 31.5 at. % Au nanoparticle sample. The Au L3-edge nanoparticle spectrum was fit using first coordination-shell atomic pathways. A fitting range from 1.5 to 3.5 Å and a k-range from 2 to 12 Å^{-1} was used. The R-factor parameter associated with the goodness of fit for this model was 0.018.

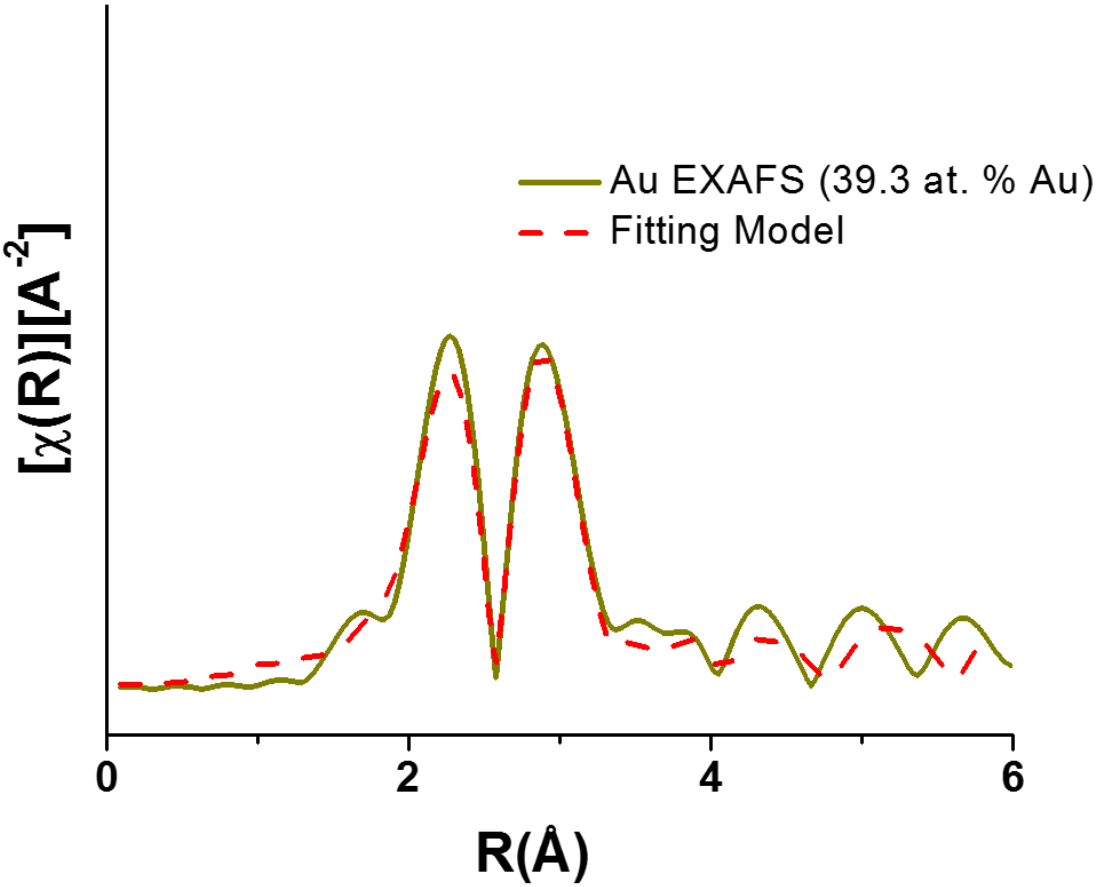

Pathway	N	R (Å)	E_0 (eV)	σ^2 (Å^2) x 10^{-3}
Au–Au (shell 1)	7.4 ± 1.3	2.854 ± 0.008	3.7 ± 0.9	7.9 ± 1.6
Au–Ag (shell 1)	4.5 ± 0.6	2.849 ± 0.009	4.3 ± 1.2	7.6 ± 1.1

Figure A3.16.25. Au L3 edge EXAFS spectrum and fitting model for 39.3 at. % Au nanoparticle sample. The Au L3-edge nanoparticle spectrum was fit using first coordination-shell atomic pathways. A fitting range from 1.5 to 3.5 Å and a k-range from 2 to 12 Å^{-1} was used. The R-factor parameter associated with the goodness of fit for this model was 0.013.

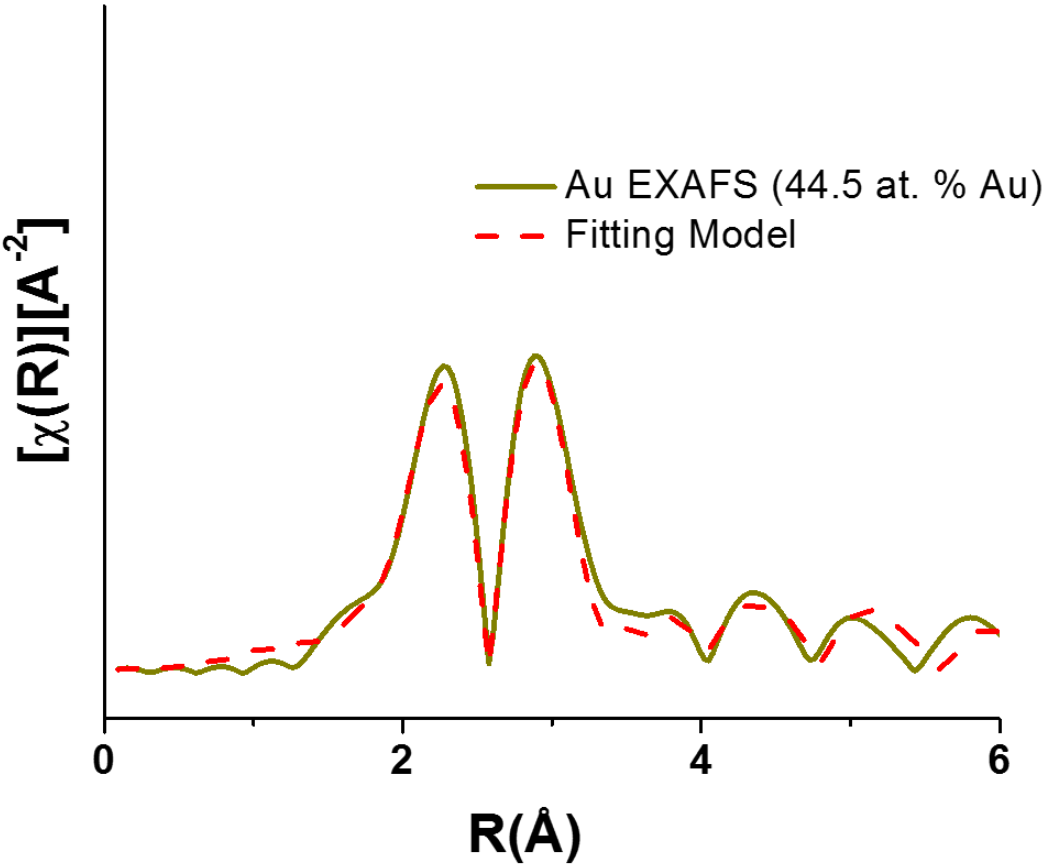

Pathway	N	R (Å)	E_0 (eV)	σ^2 (Å^2) x 10^{-3}
Au–Au (shell 1)	7.4 ± 1.2	2.854 ± 0.006	3.7 ± 0.6	8.2 ± 1.3
Au–Ag (shell 1)	4.3 ± 0.4	2.845 ± 0.008	3.8 ± 0.9	7.9 ± 0.9

Figure A3.16.26. Au L3 edge EXAFS spectrum and fitting model for 44.5 at. % Au nanoparticle sample. The Au L3-edge nanoparticle spectrum was fit using first coordination-shell atomic pathways. A fitting range from 1.5 to 3.5 Å and a k-range from 2 to 12 Å^{-1} was used. The R-factor parameter associated with the goodness of fit for this model was 0.017.

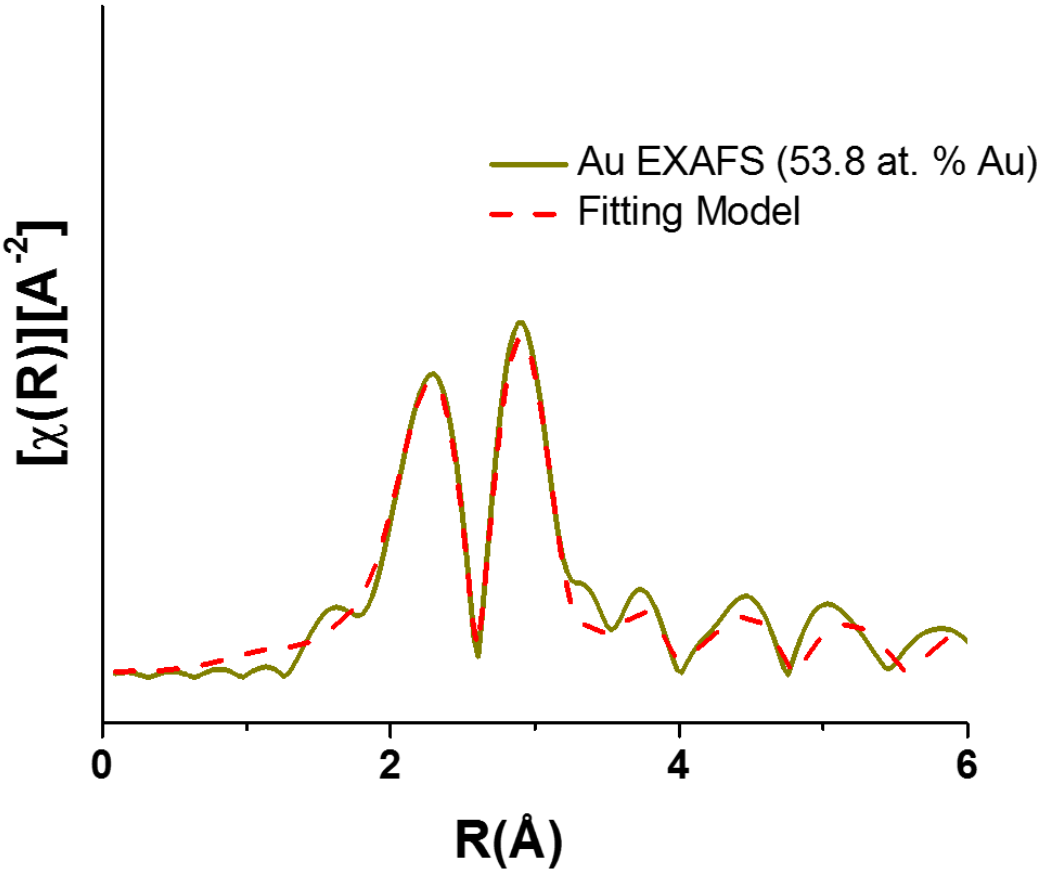

Pathway	N	R (Å)	E_0 (eV)	σ^2 (Å^2) x 10^{-3}
Au–Au (shell 1)	7.7 ± 1.4	2.84 ± 0.01	3.9 ± 1.0	8.0 ± 1.9
Au–Ag (shell 1)	4.2 ± 0.8	2.85 ± 0.02	4.5 ± 1.6	8.3 ± 1.8

Figure A3.16.27. Au L3 edge EXAFS spectrum and fitting model for 53.8 at. % Au nanoparticle sample. The Au L3-edge nanoparticle spectrum was fit using first coordination-shell atomic pathways. A fitting range from 1.5 to 3.5 Å and a k-range from 2 to 12 Å^{-1} was used. The R-factor parameter associated with the goodness of fit for this model was 0.011.

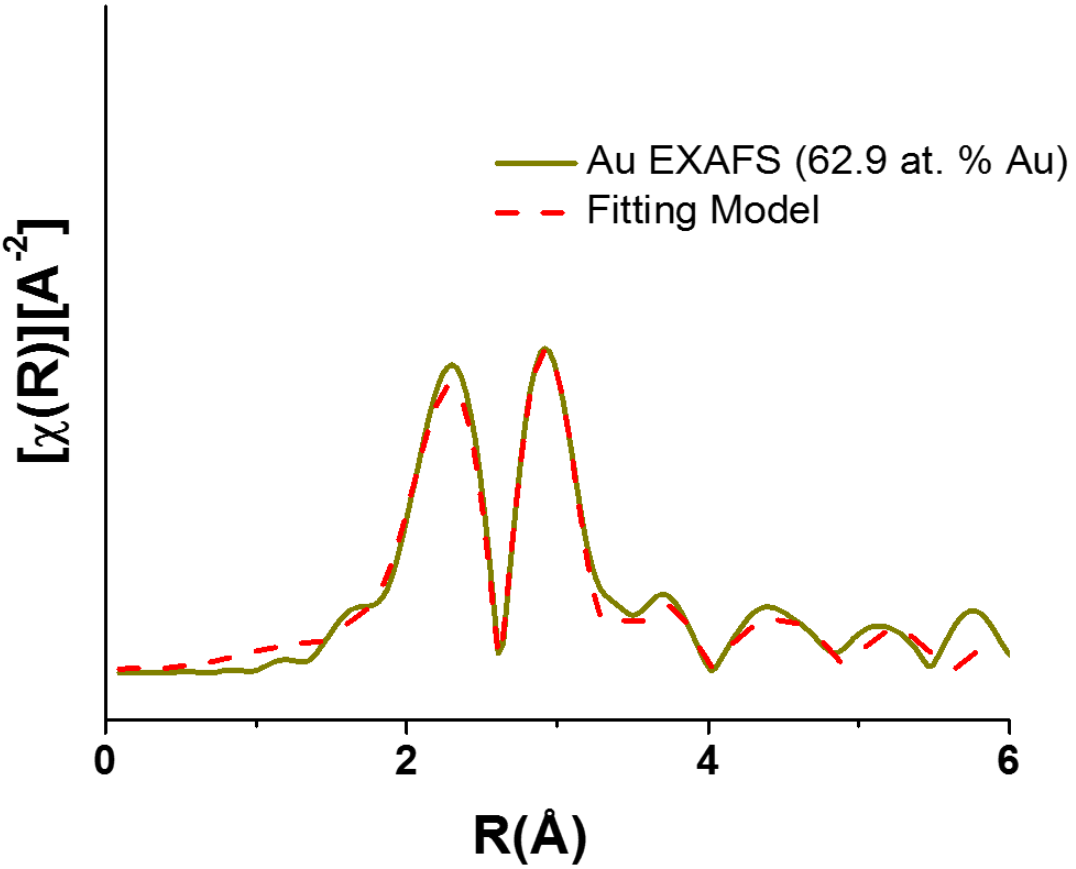

Pathway	N	R (Å)	E_0 (eV)	σ^2 (Å^2) x 10^{-3}
Au–Au (shell 1)	8.1 ± 1.1	2.851 ± 0.006	4.1 ± 0.6	8.2 ± 1.3
Au–Ag (shell 1)	4.0 ± 0.5	2.85 ± 0.01	4.5 ± 1.3	8.5 ± 1.3

Figure A3.16.28. Au L3 edge EXAFS spectrum and fitting model for 62.9 at. % Au nanoparticle sample. The Au L3-edge nanoparticle spectrum was fit using first coordination-shell atomic pathways. A fitting range from 1.5 to 3.5 Å and a k-range from 2 to 12 Å^{-1} was used. The R-factor parameter associated with the goodness of fit for this model was 0.011.

A.4 Supporting information for Chapter 4

Extended Methods

Nanorod Synthesis

According to the synthesis method established by El-Sayed and co-workers,[35] Au seed nanoparticles were synthesized by adding 0.6 mL of 0.01 M ice cold $NaBH_4$ (Sigma-Aldrich) to a stirring solution containing 5 mL 0.2 M CTAB (bioWORLD), 0.25 mL 0.01 M $HAuCl_4$ (Sigma-Aldrich) and 4.75 mL NANOpure^{TM} water (18.2 MΩ ionic purity). In a separate vial, 5 mL 0.2 M CTAB, 0.3 mL 0.004 M $AgNO_3$ (Sigma-Aldrich), 0.5 mL 0.01 M $HAuCl_4$ and 4.5 mL NANOpure^{TM} water were combined and 0.07 mL of 0.078 M ascorbic acid (Sigma-Aldrich) added to reduce Au^{3+} to Au^{+}. 0.012 mL of the as-synthesized seeds were added to this solution and reacted for 120 minutes to form the final nanorod product. It should be noted that in order to obtain sufficient sample with concentrations appropriate for XAFS measurements (micromolar concentrations of the element of interest within the nanoparticles), the aforementioned synthesis volumes were scaled up as appropriate to a final reaction solution volume of up to 1 L. In order to quench the reaction, halting growth at timepoints prior to reaction completion, 100 mM bis(*p*-sulfonatophenyl)phenylphosphine (BSPP, Sigma Aldrich) was added to the nanorod growth solution to a final concentration of 2 mM. For ex-situ STEM measurements, nanorod were concentrated via high-speed centrifugation (21130 g) to form a pellet and re-suspended in 100 µL NANOpure^{TM} water. For X-ray measurements, nanorods were concentrated to micromolar concentrations of Ag or Au atoms and washed several times with NANOpure^{TM} water to remove excess reactant from solution. This ensured that global average X-ray measurements were representative of the Ag and Au atoms within the nanoparticles rather than any excess which may remain in the growth solution.

X-Ray Photoelectron Spectroscopy

X-ray photoelectron spectra were obtained using a Thermo Scientific ESCALAB 250Xi XPS spectrometer with an Al anode at 20 kV emitting monochromated Al Kα (1486.5 eV) radiation. The hemispherical energy analyzer was operated at a pass energy of 50.0 eV and energy calibrated using the carbon emission line. Samples were measured 100 scans each (~2 hours). As-synthesized nanorods were isolated via centrifugation and the supernatant removed. The particles were then resuspended in 100 mM CPC, an alternative surfactant that does not crystallize at room temperature. For the nanorods to assemble in a side-normal fashion, 10 μL of the particle solution was dropcast onto a silicon wafer and dried quickly in a desiccator. For the nanorods to assemble in a tip-normal fashion, 100 μL of the particle solution was dropcast onto a silicon wafer and left to dry slowly in a high-humidity chamber. Overall, faster drying speed prefers rod films with a side-normal orientation whereas slower drying speeds promotes films with nanorods in a tip-normal orientation.

STEM Size Analysis

Nanoparticle size was determined by a statistical analysis of TEM images using the ImageJ particle counter software. At least 100 particles were analyzed per timepoint aliquot in order to ensure a statistically meaningful sample population.

X-Ray Fluorescence

X-ray fluorescence (XRF) data from the Ag Kα and Au L fluorescence lines were collected along with XAFS data at sectors 10BM-B and 5 BM-D at the Argonne National Laboratory

Advanced Photon Source (APS). The corrected fluorescence intensities of the Ag Kα and Au Lα lines were used to determine the relative Au and Ag atomic percentages present in the isolated nanoparticle samples quenched at various reaction timepoints. Samples were contained in 3 mm (nominal, Charles Supper) inner diameter cylindrical quartz capillaries placed such that the capillary long axis was at a 45° angle with the detector normal and the incident x-ray beam. The XRF photons were collected in the horizontal plane with the detector at ~ 90° relative to the incident beam direction to minimize the intensity due to elastically and inelastically scattered X-rays. XRF data was collected at an incident energy of 26.014 keV using a four-element Vortex ME-4 silicon drift diode detector.

Figure A4.1 shows a sample XRF spectrum from Quantitative analysis of the Au and Ag relative atomic percentages were conducted using areas under the Ag Kα (22.163 keV) and Au Lα (9.705 keV) fluorescence lines, with peaks fit to a Gaussian function after background subtraction. Elemental XRF cross sections,[46] detector efficiency, and attenuation due to solvent media were taken into account in determining the Ag/Au ratio. (Note that self-absorption by the metal NPs could be neglected due to their low μM atomic concentrations in the solvent.) The beam size was 0.4 mm (vertical) x 5 mm (horizontal). Therefore, for attenuation correction for Ag Kα and Au Lα X-rays coming from the 2 or 3 mm diameter cylinder of water, we neglected the vertical beam size. The path lengths and attenuation corrections for fluorescence X-rays were calculated by dividing the horizontal illuminated 10 - 15 mm^2 area into 121 differential emission elements arranged on a 2D lattice. The corrected intensities yielded the same atomic fraction for Au when Au Lα, Au Lβ or Au Lγ fluorescence lines were used, validating this correction procedure.

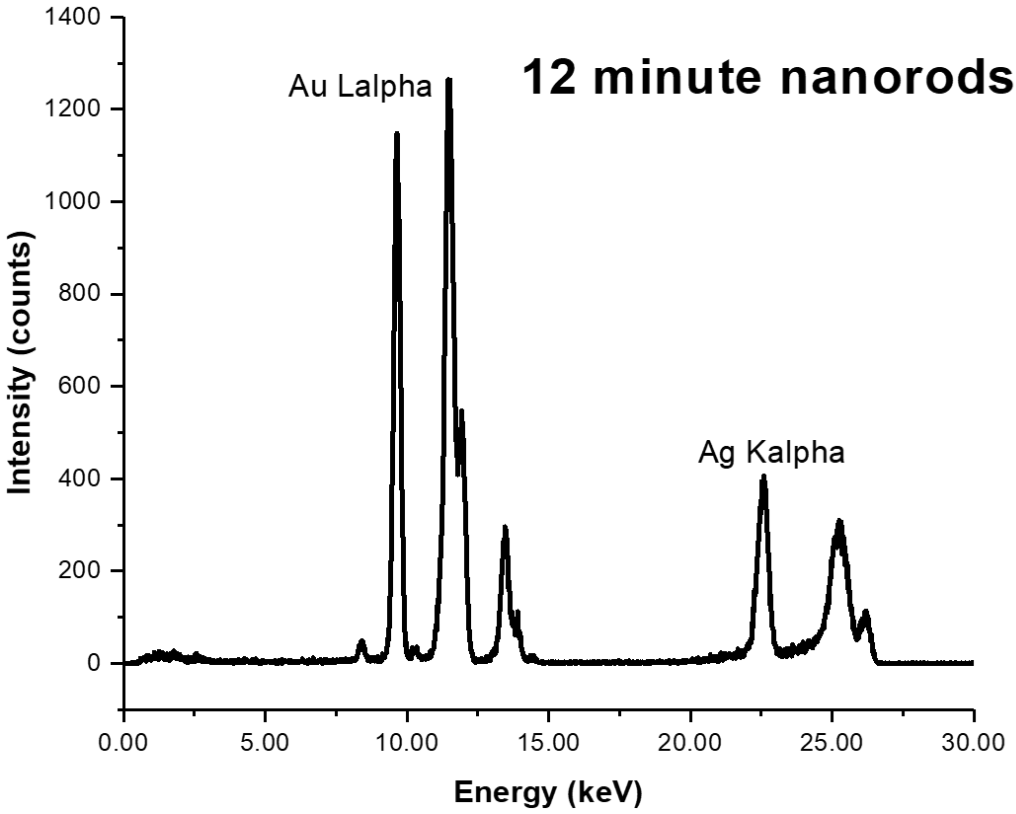

Figure A4.1. Sample X-Ray fluorescence spectrum. A sample XRF spectrum of the 12 minute nanorod aliquot is shown. The atomic % Ag and Au within the nanorods were determined from the corrected areas under the Au L alpha and Ag K alpha fluorescence lines (labeled). Lines other than the expected Au fluorescence lines between 10 and 15 keV are from Br present due to solution CTAB.

X-Ray Scattering

Small angle X-ray scattering (SAXS) measurements were performed using 10.00 keV X-rays at beamline 5ID-D of the Advanced Photon Source (APS) at the Argonne National Laboratory. The aqueous nanoparticle dispersions were placed in a quartz capillary tube (inner diameter ~ 1.5 mm). To avoid radiation damage, the sample was translated in the beam to 5 nonoverlapping

positions, from which the scattering patterns were averaged together. Furthermore, a fast shutter was used such that the samples were exposed to X-rays only for the data collection periods. The X-ray spot size at the sample position was ~ 0.25 mm (H) × 0.25 mm (V). The incident flux was ~ 10^{12} photons/s. The scattered intensity was collected using a Rayonix CCD area detector, which was placed at 7502.0 mm (range: q = 0.015 – 0.9 nm^{-1}) from the sample. The flight path between the sample and detector was under vacuum.

For each nanoparticle sample, five 0.5 sec SAXS patterns were collected at each of the five spots. To account for fluctuations in the incident beam intensity and changes in the absorption of X-rays for different samples, the incident and the transmitted beam intensities were monitored using an ion chamber just before the sample and a pin diode embedded in the beam stop just in front of the SAXS detector. Transmission, detector solid angle and X-ray polarization corrections were applied to measured intensities before performing the azimuthal integration for extracting the 1D intensity profiles (Figure A4.5).

X-Ray Absorption Fine Structure

XAFS spectra at the Au L_3 edge and Ag K edge (11.919 keV and 25.514 keV) were collected at MR-CAT sector 10BM-B of the APS. Energy scans were taken over a range from -150 eV to 600 eV with respect to the absorption edge using a Si(111) monochromator. XAFS spectra were collected in fluorescence mode using a four-element Vortex ME-4 Silicon drift diode fluorescence detector. The edge energies were calibrated with an Au or Ag metal foil standard. Ag or Au foil spectra were simultaneously collected along with the nanoparticle samples, as shown in Figure A4.12, in order to ensure calibration and compare absorption edge positions. Samples were concentrated via centrifugation to μM concentrations of Au/Ag atoms and placed in 3 mm inner

diameter quartz capillary tubes, positioned 45 degrees with respect to both the incident x-ray beam and the fluorescence detector. To improve statistics, a minimum of five half-hour scans at 4 spectra/scan were averaged. Self-absorption was not a concern in the measurement, because of the low concentration of the element of interest (Au or Ag).

XAFS data was processed using ATHENA and ARTEMIS software, part of the IFEFFIT package.[116] Theoretical crystals structures were imported and converted to scattering pathways using ATOMS.[160] Absorption edge energy was determined from the maximum of the first derivative in the absorption data and the background was subtracted using the AUTOBK algorithm.[161] The EXAFS region (greater than 100 eV above the absorption edge)[50] was normalized and a k-weight of 2 was chosen in order to provide an even spectrum throughout the region of interest (2 – 12 $Å^{-1}$). EXAFS spectra were modeled according to the EXAFS equation, a simplified version of which is:[50-51, 52, 47]

$$\chi(k) = \sum_{\Gamma}[\frac{N_{\Gamma}S_0^2F_{\Gamma}(k)}{2kR_{\Gamma}^2}e^{-2k^2\sigma_{\Gamma}^2}e^{-2R_{\Gamma}/\lambda(k)} \times \sin\big(2kR_{\Gamma} + \phi_{\Gamma}(k)\big)] \qquad \text{(A4.1)}$$

Where Γ is the summation over the individual scattering pathways included in the model, k is the photoelectron wavevector, $F_{\Gamma}(k)$ is the scattering amplitude, $\lambda(k)$ is the mean free path of inelastically-scattered photoelectrons and $\Phi(k)$ is the phase shift, which is calculated as a function of the absorbing and scattering atom using the ARTEMIS software. S_0^2, the amplitude reduction factor, was set to the value extracted from fitting a bulk Au or Ag foil as applicable. This enables a more accurate determination of the coordination number.[52] Degeneracy (N_{Γ}), half-path length (R_{Γ}), energy shift parameter (E_0), and mean-squared disorder (σ_{Γ}^2), which includes contributions from structural and thermal disorder (Debye-Waller factor),[50] were adjusted to determine the best fit model. Fits with values for these variables outside the realm of physical reasonability (i.e.

negative mean-squared disorder) were restricted. ΔE_0 was fixed to a single variable for all pathways with the same absorbing and scattering element in order to limit the number of variables, as ΔE_0 values should be nearly equal for similar bonds within the structure.[182]

Goodness of fit parameters for the models were evaluated using minimization of the statistical R-factor parameter and error bars for individual parameters were estimated to one sigma (~ 68% confidence level) from the R-space spectrum. Spectra were fit first in k-space, then evaluated in R-space and q-space, in order to ensure that the best fit to the raw data in k-space was translatable to the other fitting spaces. Individual fitting models and a summary of both fitting and goodness of fit parameters are included in Figure A4.12.

Sample Calculations

Calculation of Nanorod Growth Rates

Nanorod dimensions were determined from STEM analysis and are listed in Table A4.1. As dimensions were determined as a function of reaction time, this enabled calculation of length, diameter and volume growth rates according to the following equation, where d is dimension, t_1 is time 1 and t_2 is time 2 :

$$growth\ rate = \frac{d_{t_1} - d_{t_2}}{t_1 - t_2} \qquad \text{(A4.2)}$$

Growth rates were then plotted at time . For example, to determine the nanorod length growth rate plotted at 10 minutes,

$$Length\ growth\ rate = \frac{23.1\ nm - 9.6\ nm}{12\ min. - 8\ min.}$$

$$Length\ growth\ rate = 3.4\ \frac{nm}{min.}$$

Calculation of Total Number of Ag Atoms per Nanorod

The total number of Ag atoms per nanorod (N_{Ag}) was calculated using nanorod volume (V_{rod}) determined from STEM dimensions, unit cell volume for FCC Au ($V_{u.c.}$), the number of atoms per unit cell (4) and the atomic fraction of Ag (F_{Ag}) in the nanorod determined from XRF:

$$N_{Ag} = \frac{V_{rod}}{V_{u.c.}} * 4 * F_{Ag} \quad \text{(A4.3)}$$

For example, for the 8 minute nanorod aliquot:

$$N_{Ag} = \frac{378\ nm^3}{0.0678\ nm^3} * 4 * 0.091$$

$$N_{Ag} = 2027 \pm 328$$

Calculation of % Ag in Nanorods that is on the Nanorod Surface

Coordination numbers (CNs) extracted from EXAFS analysis were used to determine the fraction (x_{Ag}) of Ag atoms in the nanorods that are on the nanorods surfaces. $CN_{Ag} = 12$ would indicate all Ag are in the bulk of the nanorod, i.e. $x_{Ag} = 0$. Whereas $CN_{Ag} < 12$ indicates that $x_{Ag} > 0$. The at 8 mins we measured $CN_{Ag} = 7.8$, which indicates that surface Ag must be mostly on {110} surfaces since the 110 has the lowest CN of 7. Therefore if we assume that surface Ag have CN = 7 and nonsurface Ag have CN =12 then

$$x_{Ag} = \frac{12 - CN_{Ag}}{5} \qquad \text{(A4.4)}$$

For example, at 8 mins. when CN = 7.8, $x_{Ag} = 0.84 \pm 0.07$.

Note that Ag surface coverage x_{Ag} is the fraction of nanorod surface atoms that are Ag. Whereas, x_{Ag} is the fraction of Ag atoms in the nanorod that are on the nanorod surface.

Calculation of {110} Ag surface coverage

Ag {110} surface coverage (θ_{Ag}) was calculated from x_{Ag} the fraction of Ag in the nanorods that is on the surface (see above calculation), the total number of Ag atoms in the nanorods (N_{Ag}, see above calculation) and the total number of atoms (Ag and Au) on the nanorod {110} surfaces ($N_{total,\{110\}}$) assumed as number of atoms on surface area of the sides of the nanorods, since the sides of the rods have been found to be {110}).[142] $N_{total,\{110\}}$ was calculated from the surface area of the sides of the nanorods ($A_{\{110\}}$) and the planar density the {110} plane (σ_{110}). For FCC Au, which has a lattice parameter of 0.408 nm, $\sigma_{110} = 8.501\ nm^{-2}$

$$N_{total,\{110\}} = (A_{\{110\}} * \sigma_{110}) \quad \text{(A5.5)}$$

$$\theta_{Ag} = \frac{N_{Ag} * x_{Ag}}{N_{total,\{110\}}} \quad \text{(A5.6)}$$

For example, for the 8 min. nanorod sample,

$N_{total,\{110\}} = (A_{\{110\}} * \sigma_{110})$

$N_{total,\{110\}} = (241\ nm^2 * 8.501\ nm^{-2})$

$N_{total,\{110\}} = 2049 \pm 613$

$\theta_{Ag} = \frac{N_{Ag} * x_{Ag}}{N_{total,\{110\}}}$

$\theta_{Ag} = \frac{2027 * 0.84}{2049}$

$\theta_{Ag} = 0.83 \pm 0.26$

Supplementary Results

L and W Dimensions from STEM analysis. Assumed $V_{rod} = LW^2$ and $A_{110} = 4LW$

Time (minutes)	Length (nm)	Width (nm)	Aspect ratio
8	9.6 ± 2.5	6.3 ± 0.9	1.5 ± 0.5
12	23.1 ± 3.9	6.3 ± 0.7	3.6 ± 0.7
16	33.6 ± 3.5	8.0 ± 0.7	4.2 ± 0.6
20	34.7 ± 4.5	9.0 ± 1.0	3.8 ± 0.7
25	43.1 ± 4.8	11.2 ± 1.4	3.9 ± 0.6
30	48.0 ± 5.4	12.2 ± 1.5	3.9 ± 0.7
45	50.9 ± 5.3	13.7 ± 1.9	3.7 ± 0.6
120	54.4 ± 4.4	14.9 ± 1.4	3.7 ± 0.4

Table A4.1 Dimensions determined from STEM analysis. Length and width determined from statistical analysis of STEM images and the determined aspect ratio of the nanorods for aliquots taken as a function of reaction time from 8 to 120 minutes.

Nanorod Dimension Evolution

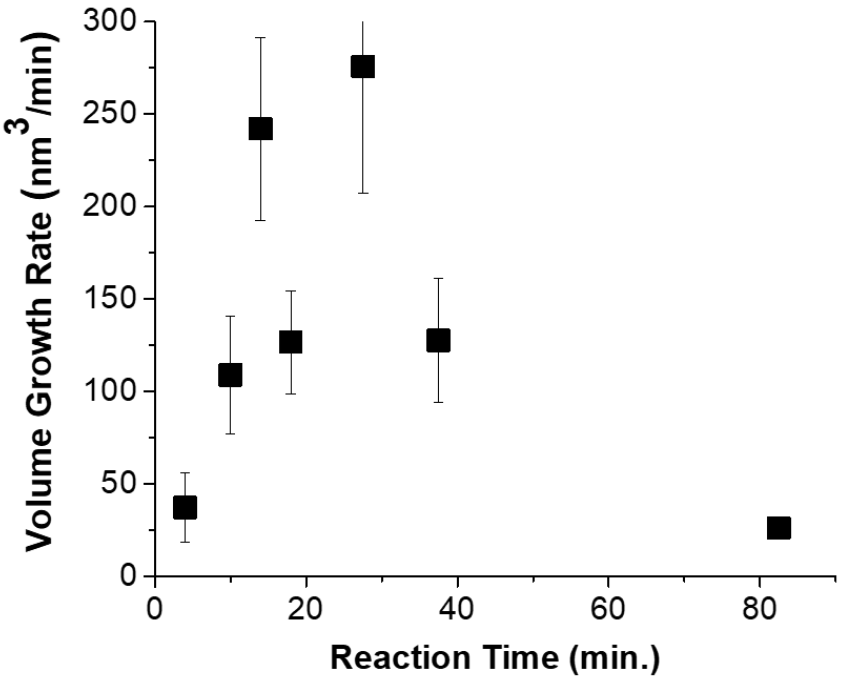

Figure A4.2. Nanorod volume growth rate. Volume growth rate as determined from STEM dimensions as a function of reaction time.

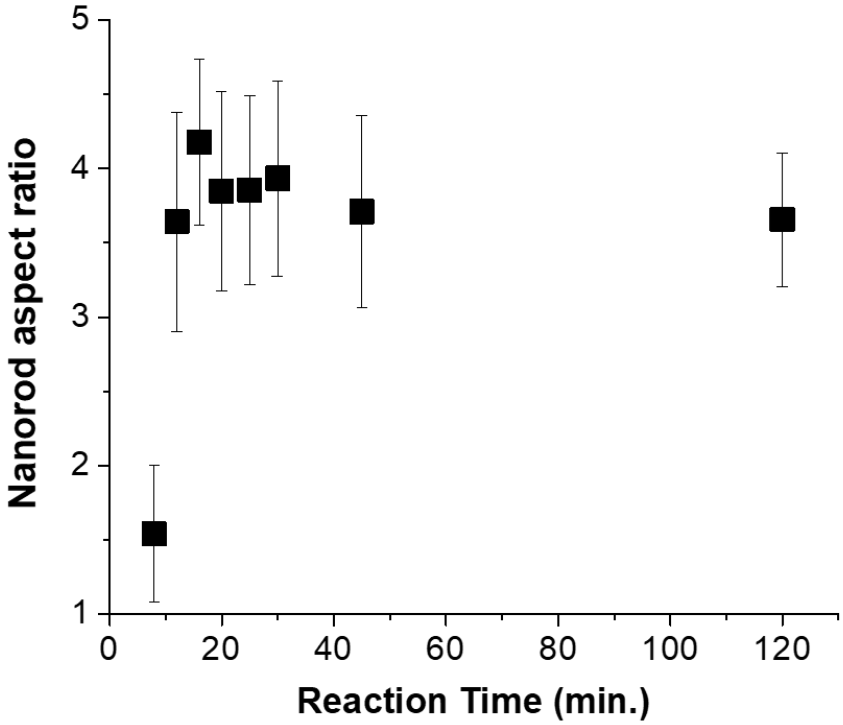

Figure A4.3. Nanorod aspect ratio. Nanorod aspect ratio as determined from STEM dimensions as a function of reaction time.

Evaluation of BSPP as an exchange ligand

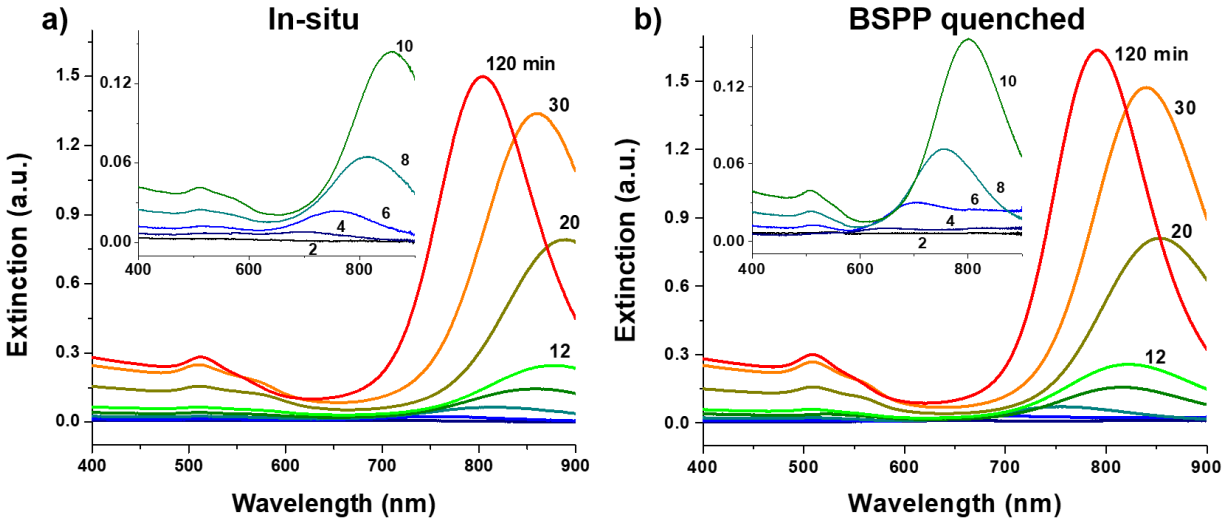

Figure A4.4 UV-vis spectra for nanorods synthesized in-situ and quenched with BSPP**.** To confirm that BSPP quenching does not affect the nanorod structure, UV-vis spectra were collected during the same synthesis reaction in-situ (left) and quenched with BSPP (right) at varying timepoints throughout the course of the synthesis reaction. It is observed that the spectral trends remain the same for the BSPP-quenched as for the in-situ samples, indicating that the nanorod morphology is unaffected by quenching with BSPP. The slight blue-shift observed for the BSPP-quenched samples compared to in-situ samples of the same timepoint is uniform throughout the reaction and expected due to the sensitivity of UV-vis signatures to the surrounding dielectric environment.[175]

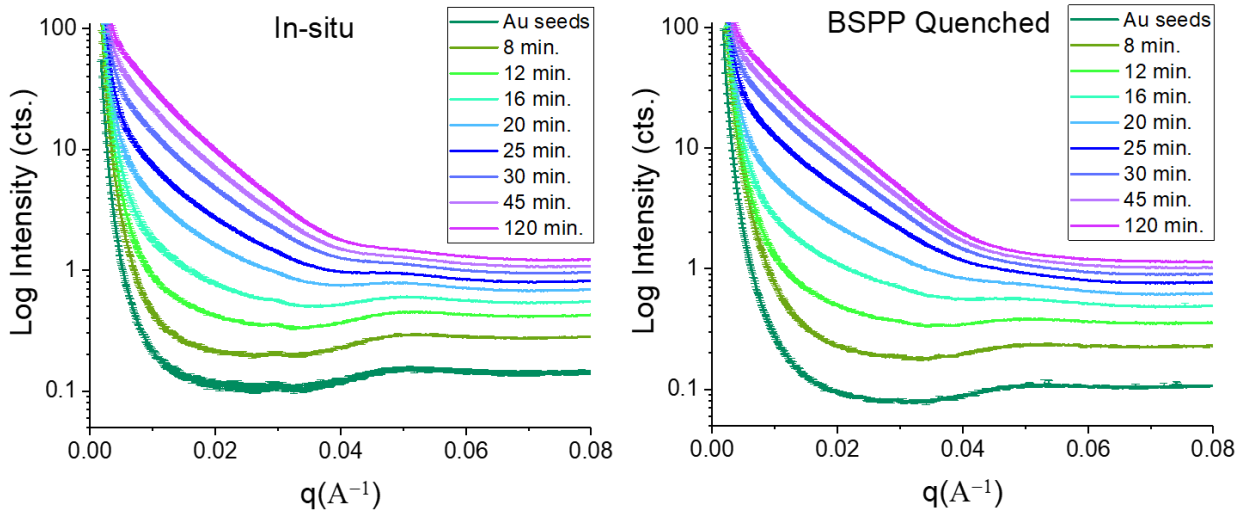

Figure A4.5 SAXS 1-D intensity profiles for nanorods synthesized in-situ and quenched with BSPP. SAXS patterns were collected during the same synthesis reaction in-situ (left) and quenched with BSPP (right) at varying timepoints throughout the course of the synthesis reaction. The observed trends are consistent between in-situ and ex-situ samples.

XPS Results

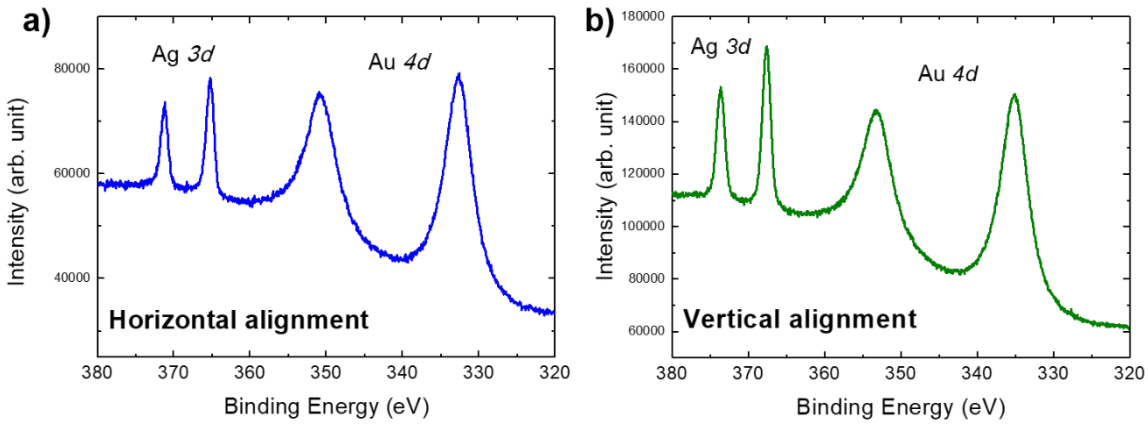

Figure A4.6. Nanorod XPS spectra. Nanorod XPS spectra of Ag 3d and Au 4d lines for horizontally (a) and vertically (b) aligned nanorods. Analysis of these spectra is outlined in the table below.

Point #	**Ag:Au ratio**	
	Horizontal alignment	**Vertical alignment**
1	0.135	0.27
2	0.16	0.25
3	0.17	0.225
4	0.11	
5		0.27
6		0.28
average	**0.14**	**0.26**

Table A4.2 Nanorod XPS determined Ag:Au ratios for final product nanorods. Ag:Au ratios were determined from the areas under the Ag 3d and Au 3d lines. For the final product nanorods, Ag is detected both in the horizontal and vertical alignment. Given that the inelastic mean free path (λ) ~ 1 nm (sampling depth = 3λ ~ 3 nm),[183] it is not possible to distinguish from these cases whether Ag is preferentially on the sides vs. tips of the nanorods as in the final nanorod product, XAFS data shows that Ag has diffused into the nanorod interior.

Tilt angle (degrees)	**Ag:Au ratio**
0	0.14
45	0.12

Table A4.3 XPS tilt series for horizontally-aligned nanorods. XPS becomes more surface sensitive as tilt angle is increased, decreasing the effective path length. If the Ag were on the nanorod surface, we would expect that the Ag:Au ratio would increase as the sample is tilted. We find, however, that the opposite is the case. This suggests that while Ag is present in layers near the surface (since a signal is obtained), the Ag is more prevalent in the nanorod bulk, in agreement with XAFS coordination results.

XANES Results

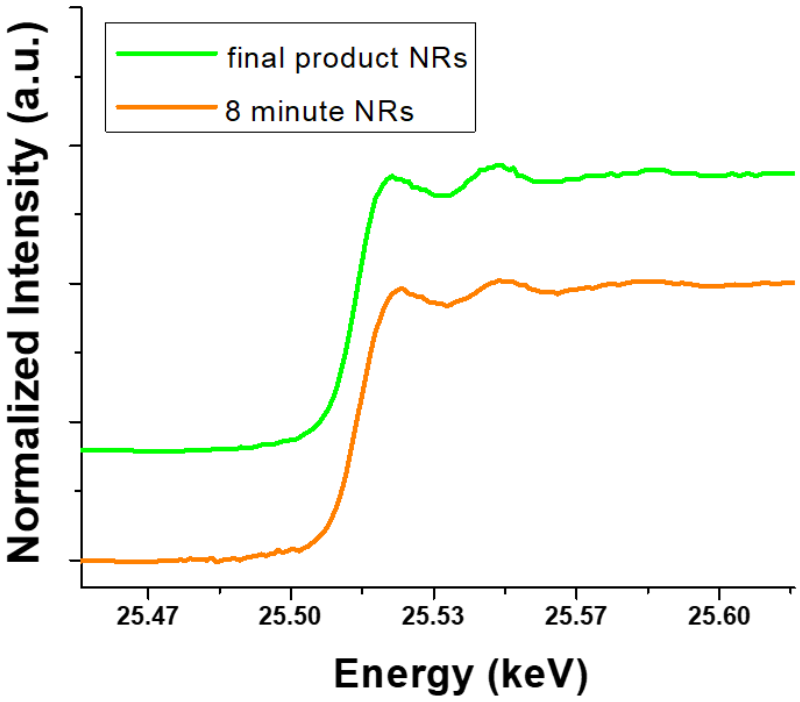

Figure A4.7 Nanorod XANES spectra. From the near edge region of the XAFS spectra, in comparison to Ag^{+} and Ag^{0} standards it was determined that the Ag in the final product nanorods (green) is Ag^{0}. The XANES spectrum of the 8 minute nanorods (orange), when most of the Ag is on the nanorod surface, is identical to that of the final product nanorods. This indicates that Ag is in the Ag^{0} state throughout the course of the reaction, even when Ag resides on the nanorod surface. This is in agreement with what is expected for Ag UPD.[142, 149]

XAFS-derived Results

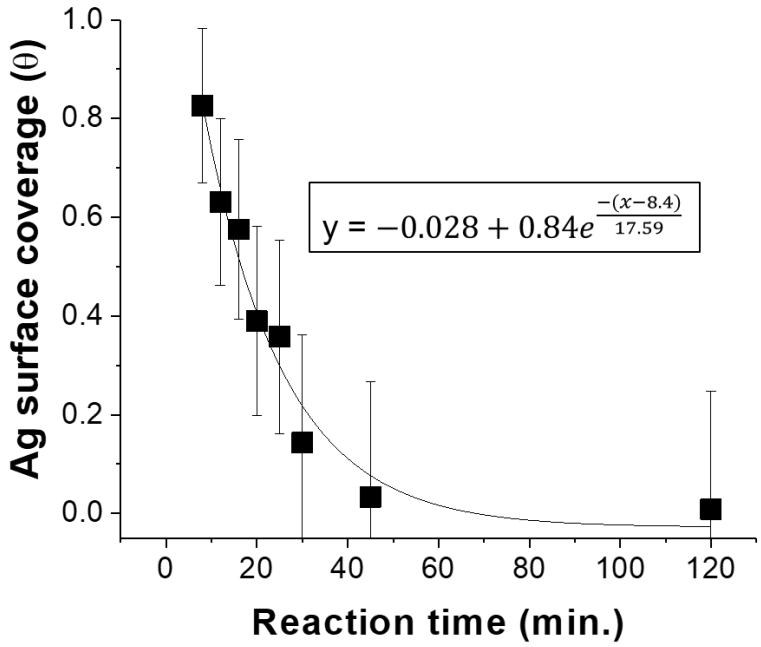

Figure A4.8. Equation fit to plot of Ag surface coverage vs. time. An exponential fit resulting in the equation plotted in the graph was used to extract Ag surface coverage at times between those collected (data points). The extracted values were used to obtain Ag surface coverage values at the mid-points corresponding with nanorod growth rate value determination, such that the Ag surface coverage and nanorod growth rates could be plotted together in Figure 4.8.

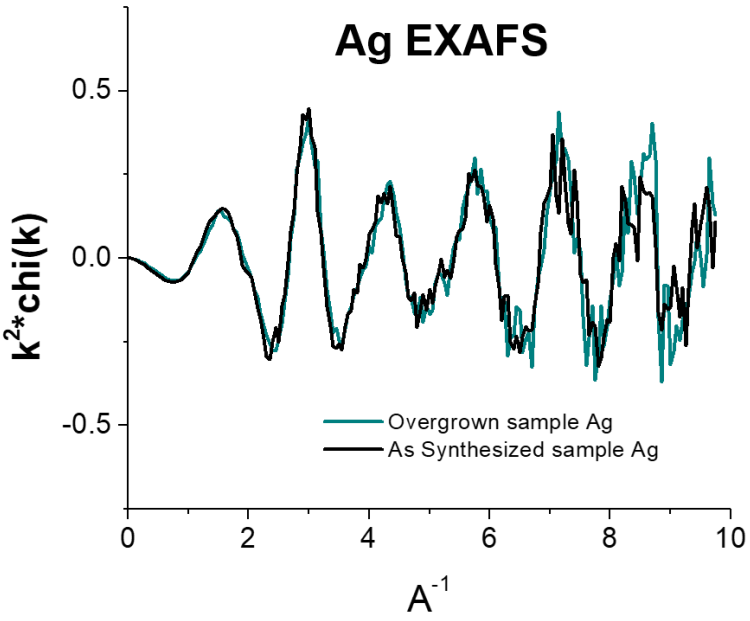

Figure A4.9. EXAFS k-space spectra of final product nanorods and final product nanorods overgrown with an Au shell. The k-space Ag K-edge EXAFS spectra of as-synthesized nanorods (black) and these same nanorods overgrown with an Au shell (teal) are identical. The overgrowth should encapsulate any surface Ag. If Ag were on the surface of the final product nanorods, differences between these two spectra should be apparent, due to differences in the coordination environment. If the Ag is already incorporated into the nanorod interior, however, the two spectra should be identical, which is the observed result.

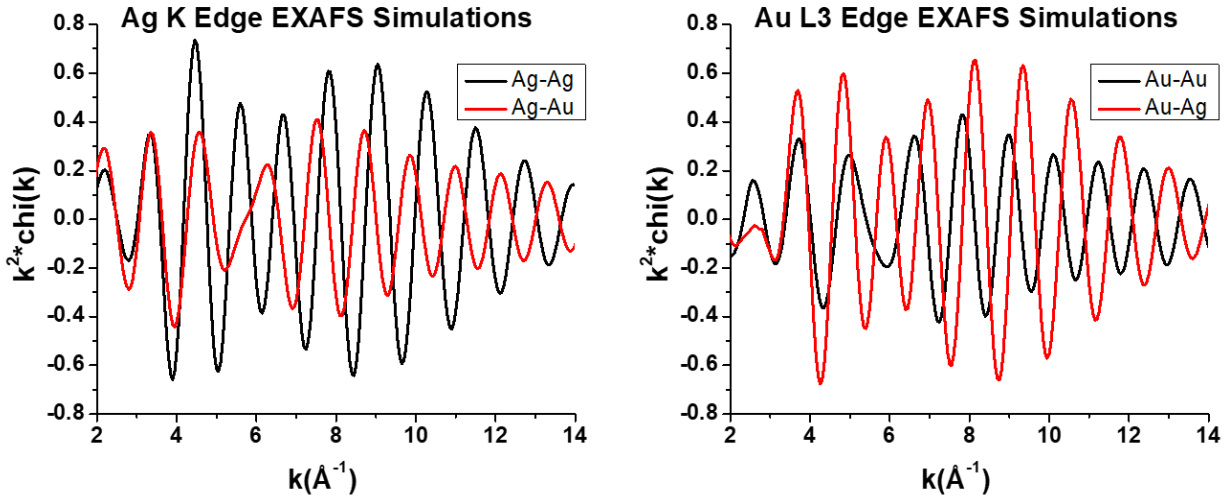

Figure A4.10 EXAFS Ag K edge and Au L3 edge simulations. Simulations of the Ag K-edge (left) and Au L3 edge (right) for different first-shell scattering atoms (Ag vs. Au) are shown. Major differences are observed in both the period of the oscillations as well as their amplitude as a function of k. Thus the contributions from the different scatterers can be extracted reliably through quantitative analysis

.

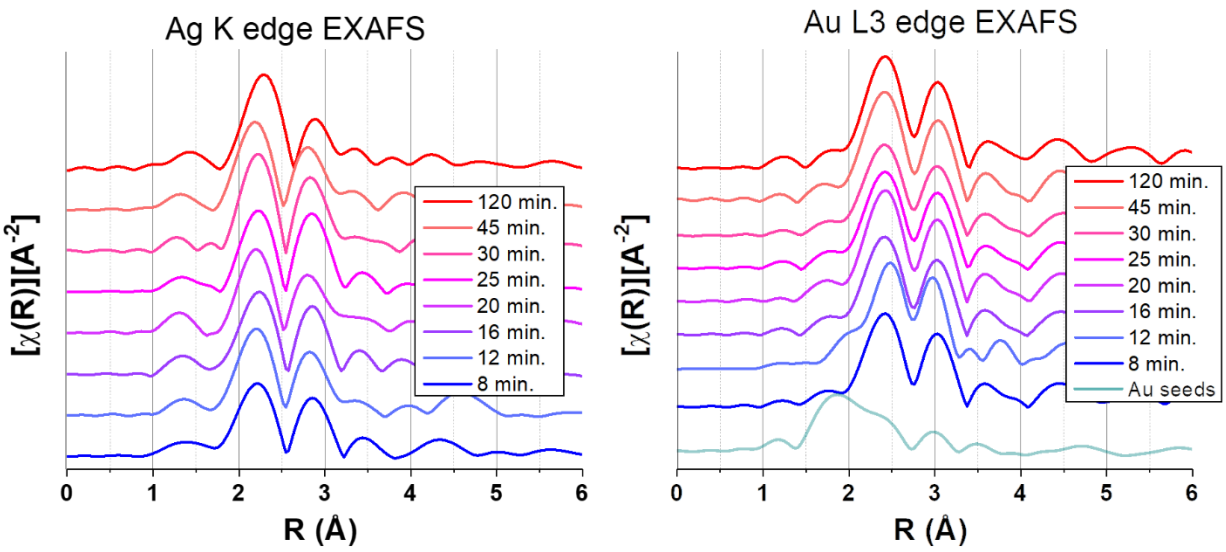

Figure A4.11 EXAFS Ag K edge and Au L3 edge data as a function of reaction time. Ag K edge EXAFS spectra (left) and Au L3 edge EXAFS spectra (right) are plotted with vertical offsets in a gradient from 8 minutes (blue) to final product nanorods (red).

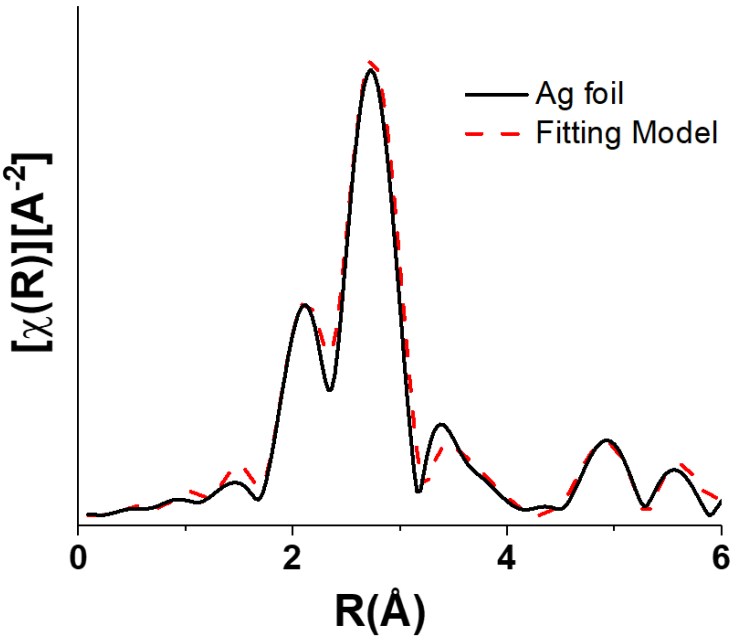

Pathway	N_{theory}	S_0^2	R (Å)	E_0 (eV)	σ^2 (Å^2) x 10^{-3}
Ag–Ag (shell 1)	12	0.74	2.866	2.35	8.03
Ag–Ag (shell 2)	6	0.74	4.062	2.35	9.85
Ag–Ag (shell 3)	24	0.74	5.009	2.35	12.1

Figure A4.12.1 Ag foil standard and fitting model. Ag foil data was collected and modeled in order to determine the amplitude reduction factor (S_0^2), since the coordination number is a fixed known. A fitting range from 1.5 to 5 Å and a k-range from 2 to 12 Å^{-1} was used. The R-factor parameter associated with the goodness of fit for this model was 0.034.

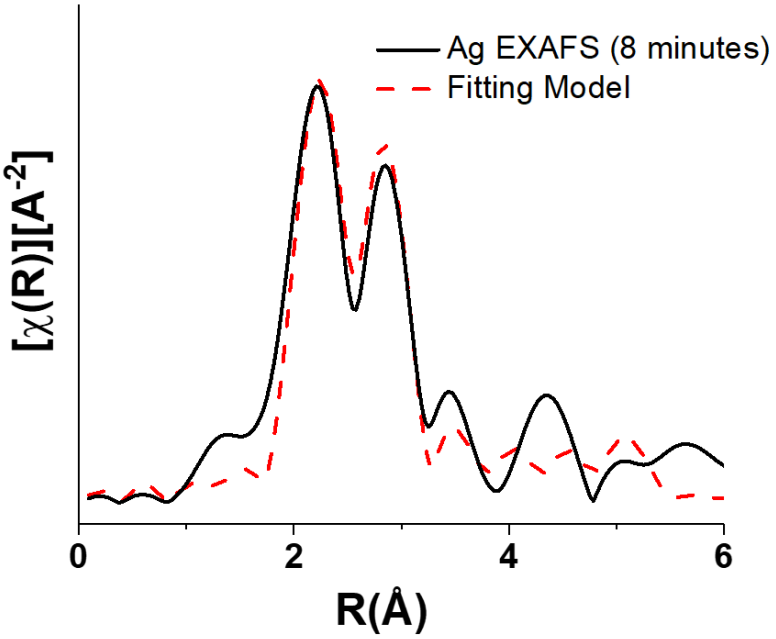

Pathway	N	R (Å)	E_0 (eV)	σ^2 (Å^2) x 10^{-3}
Ag–Ag (shell 1)	1.2 ± 0.2	2.83 ± 0.02	-8.1 ± 1.4	9.2 ± 2.1
Ag–Au (shell 1)	6.6 ± 0.6	2.865 ± 0.008	0.1 ± 0.4	12.5 ± 1.5

Figure A4.12.2 Ag K edge EXAFS spectrum and fitting model for 8 minute nanorod aliquot. The Ag K-edge nanoparticle spectrum was fit using first coordination-shell atomic pathways. A fitting range from 1.5 to 4 Å and a k-range from 2 to 10 Å^{-1} was used. The R-factor parameter associated with the goodness of fit for this model was 0.039.

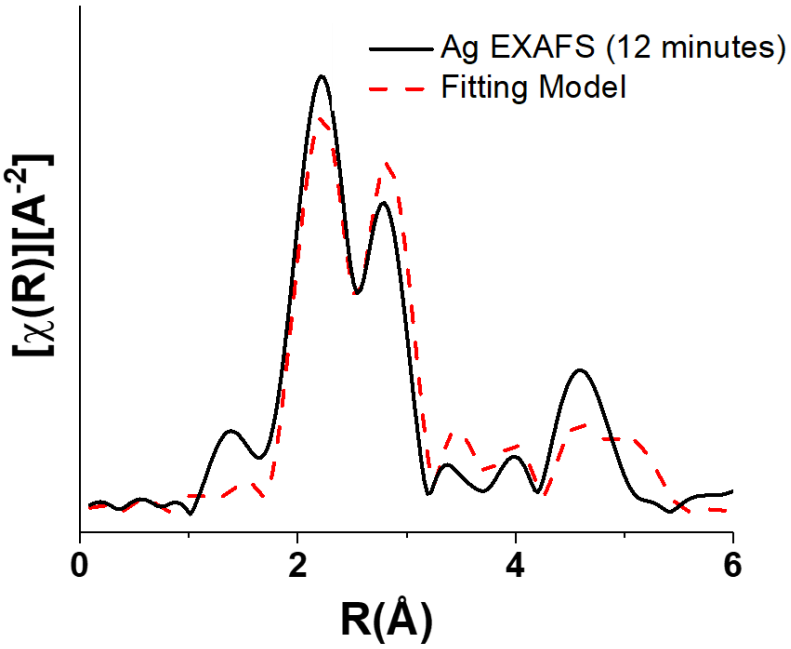

Pathway	N	R (Å)	E_0 (eV)	σ^2 (Å^2) x 10^{-3}
Ag–Ag (shell 1)	1.3 ± 0.2	2.83 ± 0.01	-7.9 ± 1.4	8.0 ± 1.2
Ag–Au (shell 1)	7.4 ± 0.5	2.865 ± 0.006	-0.2 ± 0.4	12.6 ± 0.8

Figure A4.12.3 Ag K edge EXAFS spectrum and fitting model for 12 minute nanorod aliquot. The Ag K-edge nanoparticle spectrum was fit using first coordination-shell atomic pathways. A fitting range from 1.5 to 4 Å and a k-range from 2 to 10 Å^{-1} was used. The R-factor parameter associated with the goodness of fit for this model was 0.035.

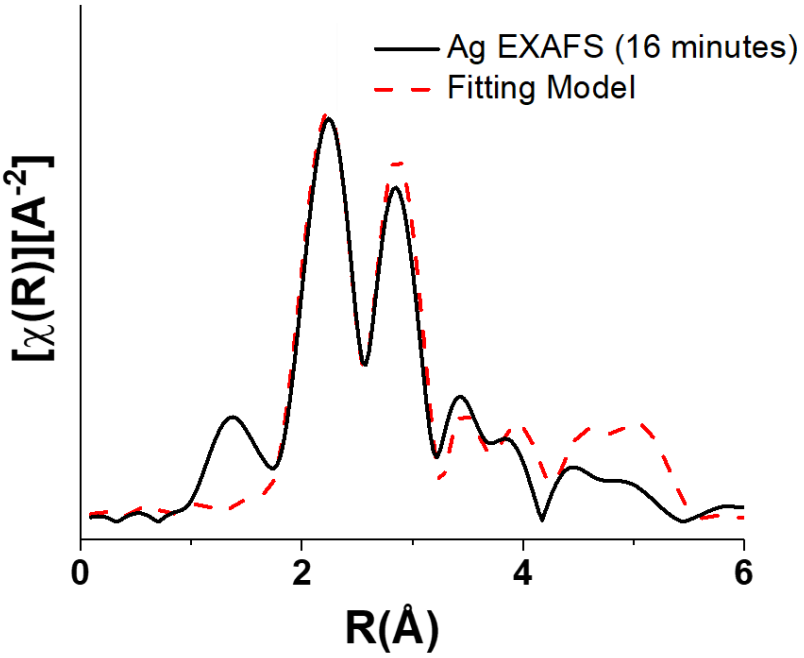

Pathway	N	R (Å)	E_0 (eV)	σ^2 (Å^2) x 10^{-3}
Ag–Ag (shell 1)	1.2 ± 0.1	2.83 ± 0.01	-4.8 ± 1.2	7.5 ± 1.3
Ag–Au (shell 1)	8.2 ± 0.3	2.863 ± 0.005	0.5 ± 0.3	12.4 ± 0.7

Figure A4.12.4 Ag K edge EXAFS spectrum and fitting model for 16 minute nanorod aliquot. The Ag K-edge nanoparticle spectrum was fit using first coordination-shell atomic pathways. A fitting range from 1.5 to 4 Å and a k-range from 2 to 10 Å^{-1} was used. The R-factor parameter associated with the goodness of fit for this model was 0.028.

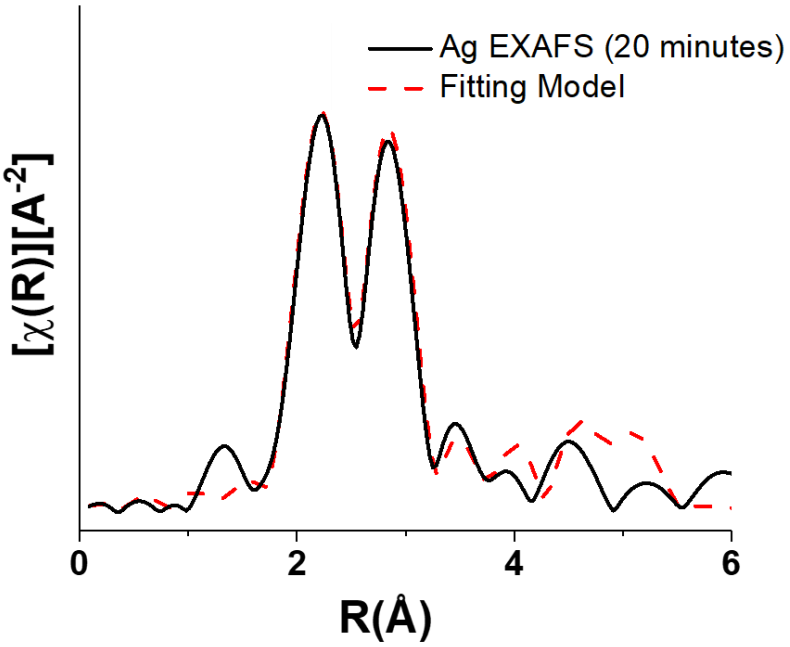

Pathway	N	R (Å)	E_0 (eV)	σ^2 (Å^2) x 10^{-3}
Ag–Ag (shell 1)	1.6 ± 0.4	2.829 ± 0.008	-6.8 ± 1.0	7.5 ± 2.4
Ag–Au (shell 1)	8.3 ± 0.8	2.865 ± 0.005	0.7 ± 0.3	12.5 ± 1.2

Figure A4.12.5 Ag K edge EXAFS spectrum and fitting model for 20 minute nanorod aliquot. The Ag K-edge nanoparticle spectrum was fit using first coordination-shell atomic pathways. A fitting range from 1.5 to 4 Å and a k-range from 2 to 10 Å^{-1} was used. The R-factor parameter associated with the goodness of fit for this model was 0.028.

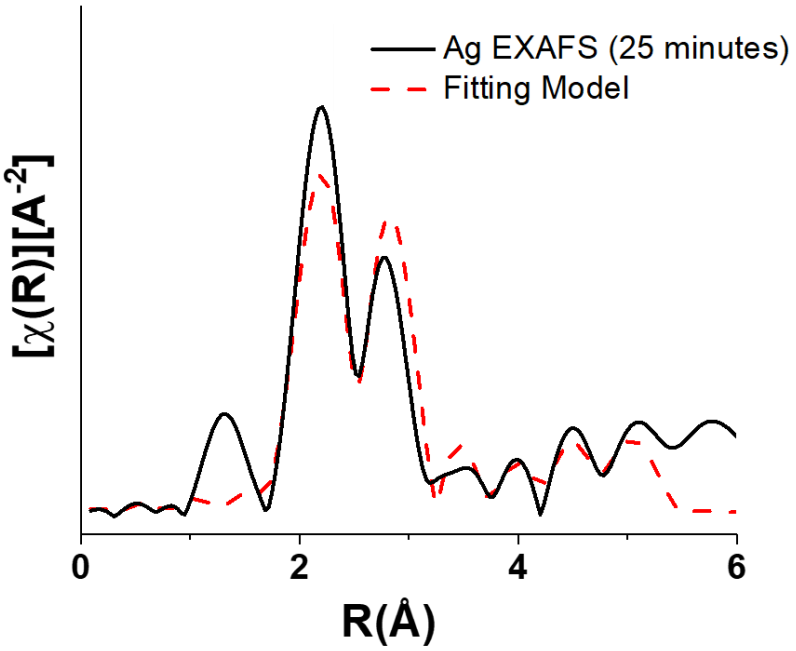

Pathway	N	R (Å)	E_0 (eV)	σ^2 (Å^2) x 10^{-3}
Ag–Ag (shell 1)	1.2 ± 0.3	2.82 ± 0.02	-8.7 ± 3.7	7.4 ± 3.6
Ag–Au (shell 1)	8.5 ± 1.4	2.87 ± 0.01	-0.4 ± 0.5	14.4 ± 2.6

Figure A4.12.6 Ag K edge EXAFS spectrum and fitting model for 25 minute nanorod aliquot. The Ag K-edge nanoparticle spectrum was fit using first coordination-shell atomic pathways. A fitting range from 1.5 to 4 Å and a k-range from 2 to 10 Å^{-1} was used. The R-factor parameter associated with the goodness of fit for this model was 0.038.

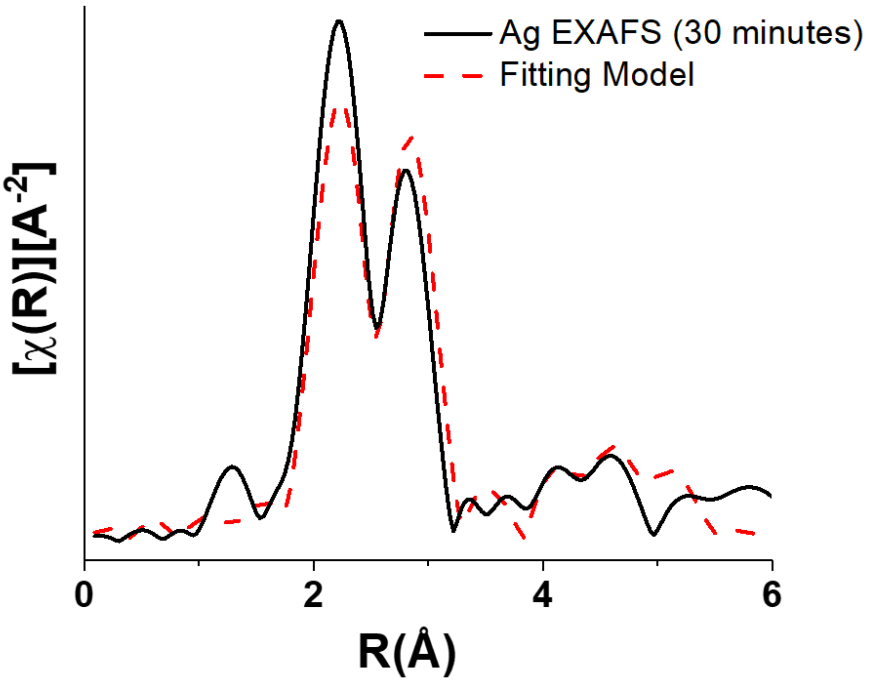

Pathway	N	R (Å)	E_0 (eV)	σ^2 (Å^2) x 10^{-3}
Ag–Ag (shell 1)	1.5 ± 0.3	2.85 ± 0.02	-6.4 ± 3.9	7.3 ± 2.9
Ag–Au (shell 1)	9.3 ± 1.6	2.87 ± 0.01	0.8 ± 0.7	14.0 ± 3.0

Figure A4.12.7 Ag K edge EXAFS spectrum and fitting model for 30 minute nanorod aliquot. The Ag K-edge nanoparticle spectrum was fit using first coordination-shell atomic pathways. A fitting range from 1.5 to 4 Å and a k-range from 2 to 10 Å^{-1} was used. The R-factor parameter associated with the goodness of fit for this model was 0.047.

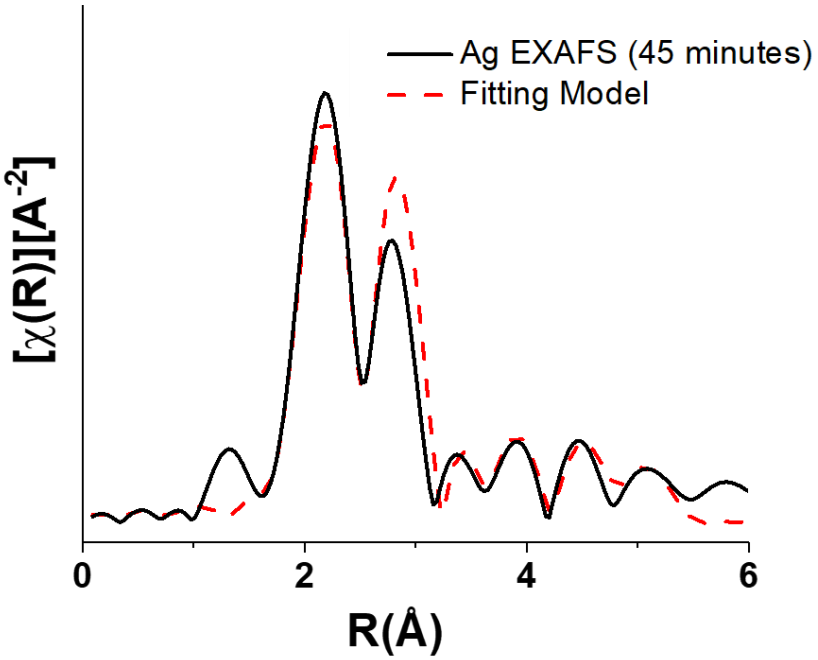

Pathway	N	R (Å)	E_0 (eV)	σ^2 (Å^2) x 10^{-3}
Ag–Ag (shell 1)	1.3 ± 0.3	2.82 ± 0.02	-8.9 ± 3.5	7.3 ± 1.6
Ag–Au (shell 1)	10.2 ± 1.5	2.87 ± 0.01	-1.3 ± 0.7	14.1 ± 2.8

Figure A4.12.8 Ag K edge EXAFS spectrum and fitting model for 45 minute nanorod aliquot. The Ag K-edge nanoparticle spectrum was fit using first coordination-shell atomic pathways. A fitting range from 1.5 to 4 Å and a k-range from 2 to 10 Å^{-1} was used. The R-factor parameter associated with the goodness of fit for this model was 0.048.

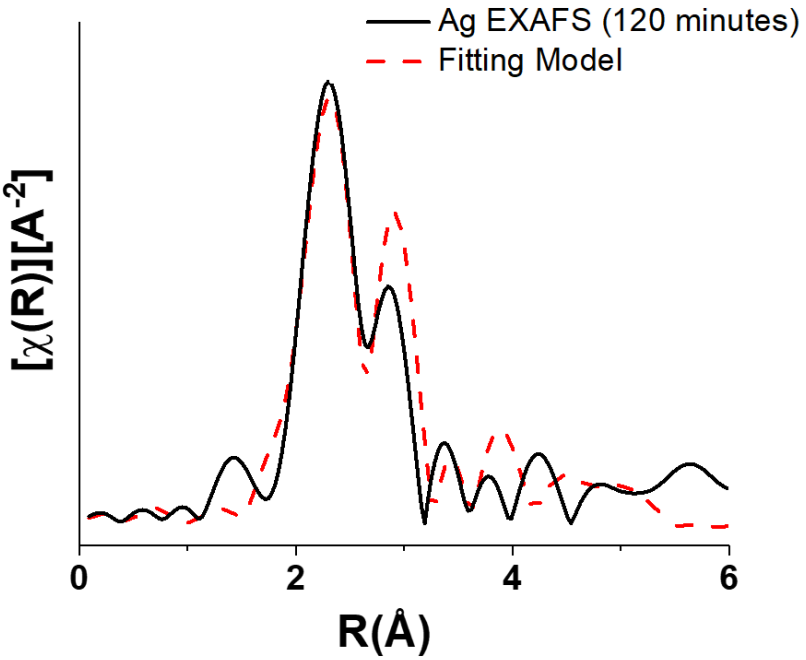

Pathway	N	R (Å)	E_0 (eV)	σ^2 (Å^2) x 10^{-3}
Ag–Ag (shell 1)	0.4 ± 0.4	2.83 ± 0.03	-3.0 ± 3	15.3 ± 5.2
Ag–Au (shell 1)	11.6 ± 1.4	2.89 ± 0.01	-1.2 ± 0.8	14.4 ± 1.9

Figure A4.12.9 Ag K edge EXAFS spectrum and fitting model for 120 minute final nanorod product. The Ag K-edge nanoparticle spectrum was fit using first coordination-shell atomic pathways. A fitting range from 1.5 to 4 Å and a k-range from 2 to 10 Å^{-1} was used. The R-factor parameter associated with the goodness of fit for this model was 0.1.

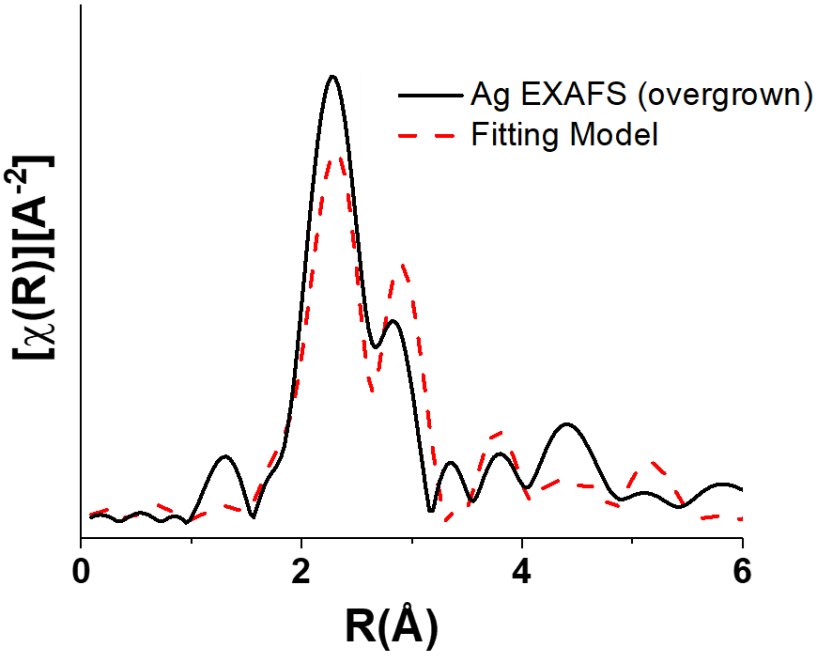

Pathway	N	R (Å)	E_0 (eV)	σ^2 (Å^2) x 10^{-3}
Ag–Ag (shell 1)	0.7 ± 1.3	2.81 ± 0.05	-4.1 ± 1.5	13.9 ± 4.2
Ag–Au (shell 1)	11.8 ± 1.7	2.88 ± 0.01	-1.1 ± 1.1	14.3 ± 2.4

Figure A4.12.10 Ag K edge EXAFS spectrum and fitting model for Au-overgrown nanorods. The Ag K-edge nanoparticle spectrum was fit using first coordination-shell atomic pathways. A fitting range from 1.5 to 4 Å and a k-range from 2 to 10 Å^{-1} was used. The R-factor parameter associated with the goodness of fit for this model was 0.15.

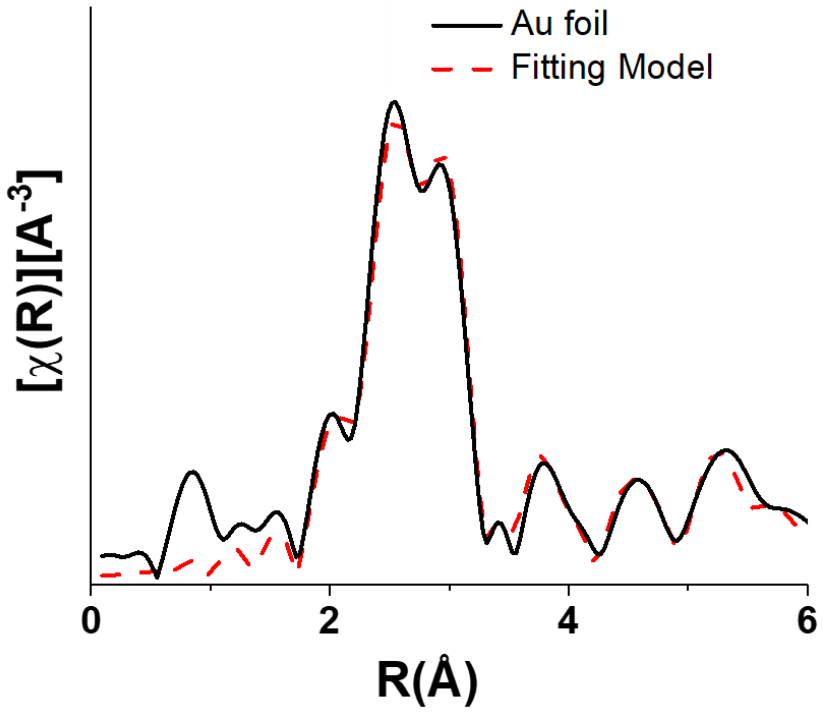

Pathway	N_{theory}	S_0^2	R (Å)	E_0 (eV)	σ^2 (Å^2) x 10^{-3}
Au–Au (shell 1)	12	0.75	2.861	5.11	7.71
Au–Au (shell 2)	6	0.75	4.051	5.11	10.8
Au–Au (shell 3)	24	0.75	4.986	5.11	12.0

Figure A4.12.11 Au foil standard and fitting model. Au foil data was collected and modeled in order to determine the amplitude reduction factor (S_0^2), since the coordination number is a fixed known. A fitting range from 1.5 to 5 Å and a k-range from 2 to 12 Å^{-1} was used. The R-factor parameter associated with the goodness of fit for this model was 0.034.

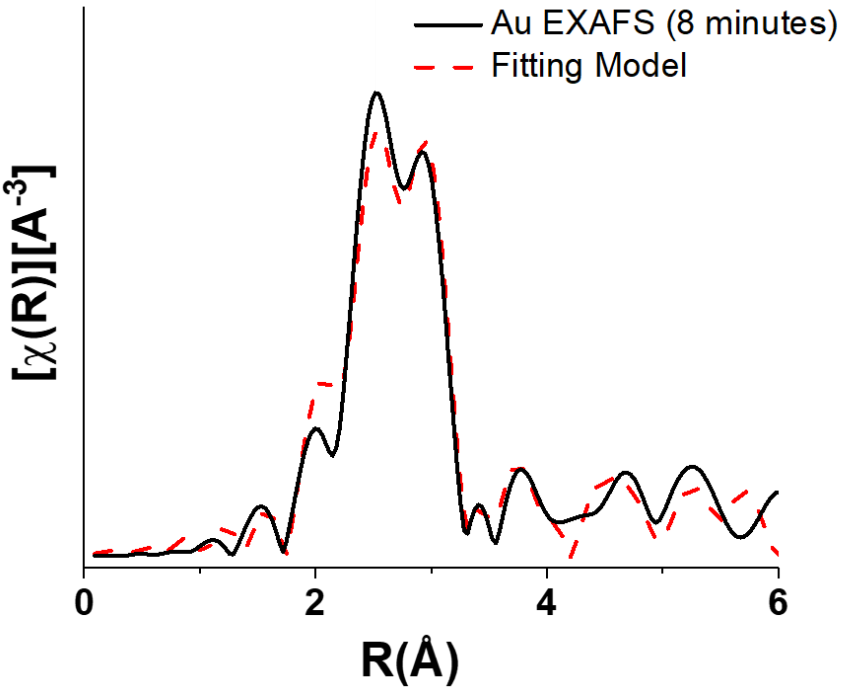

Pathway	N	R (Å)	E_0 (eV)	σ^2 (Å^2) x 10^{-3}
Au–Au (shell 1)	10.7 ± 0.9	2.858 ± 0.003	5.0 ± 0.4	7.3 ± 0.6
Au–Ag (shell 1)	1.3 ± 0.4	2.865	8.9 ± 4.4	12.5

Figure A4.12.12 Au K edge EXAFS spectrum and fitting model for 8 minute nanorod aliquot. The Au K-edge nanoparticle spectrum was fit using first coordination-shell atomic pathways. A fitting range from 1.5 to 4 Å and a k-range from 2 to 12 Å^{-1} was used. The R-factor parameter associated with the goodness of fit for this model was 0.02.

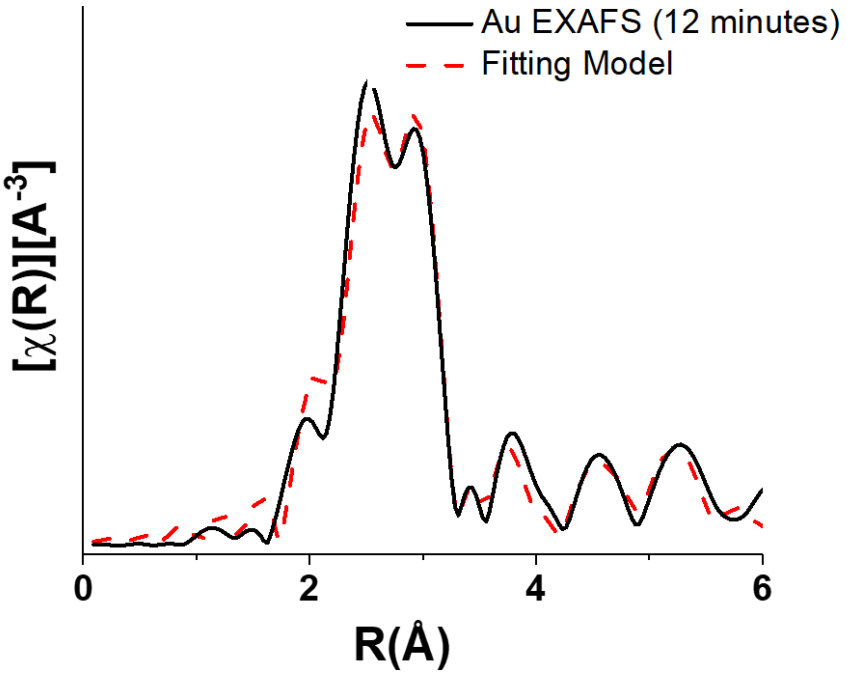

Pathway	N	R (Å)	E_0 (eV)	σ^2 (Å^2) x 10^{-3}
Au–Au (shell 1)	11.0 ± 1.3	2.859 ± 0.004	5.5 ± 0.5	10.7 ± 1.6
Au–Ag (shell 1)	1.0 ± 0.7	2.865	2.8 ± 10.6	12.6

Figure A4.12.13 Au L3 edge EXAFS spectrum and fitting model for 12 minute nanorod aliquot. The Au L3-edge nanoparticle spectrum was fit using first coordination-shell atomic pathways. A fitting range from 1.5 to 4 Å and a k-range from 2 to 12 Å^{-1} was used. The R-factor parameter associated with the goodness of fit for this model was 0.024.

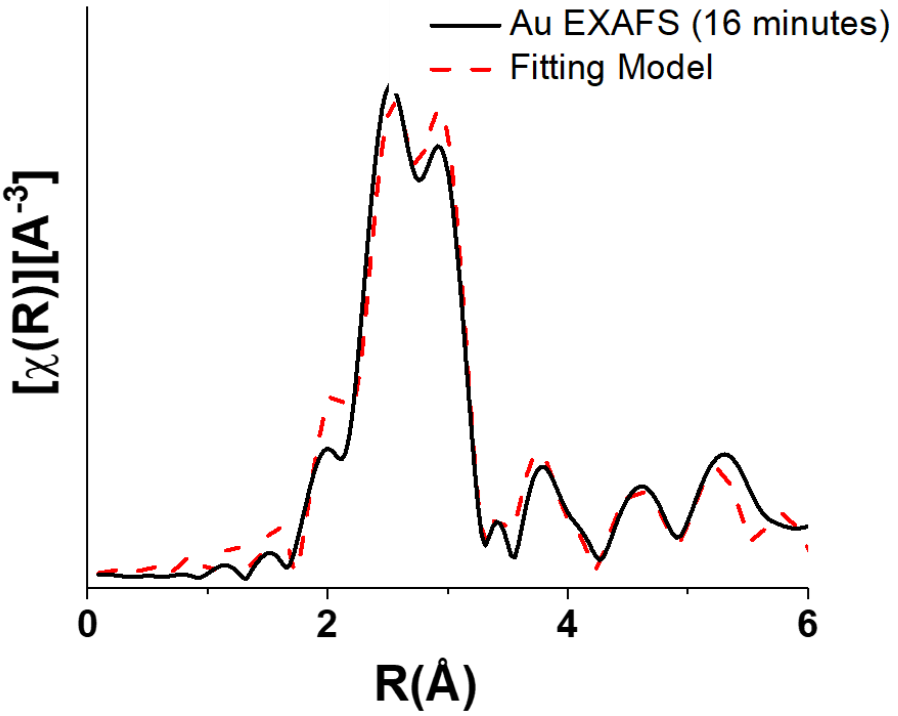

Pathway	N	R (Å)	E_0 (eV)	σ^2 (Å^2) x 10^{-3}
Au–Au (shell 1)	11.3 ± 1.1	2.859 ± 0.004	5.1 ± 0.4	7.4 ± 0.7
Au–Ag (shell 1)	0.7 ± 0.6	2.863	3.3 ± 8.9	12.4

Figure A4.12.14 Au K edge EXAFS spectrum and fitting model for 16 minute nanorod aliquot. The Au K-edge nanoparticle spectrum was fit using first coordination-shell atomic pathways. A fitting range from 1.5 to 4 Å and a k-range from 2 to 12 Å^{-1} was used. The R-factor parameter associated with the goodness of fit for this model was 0.018.

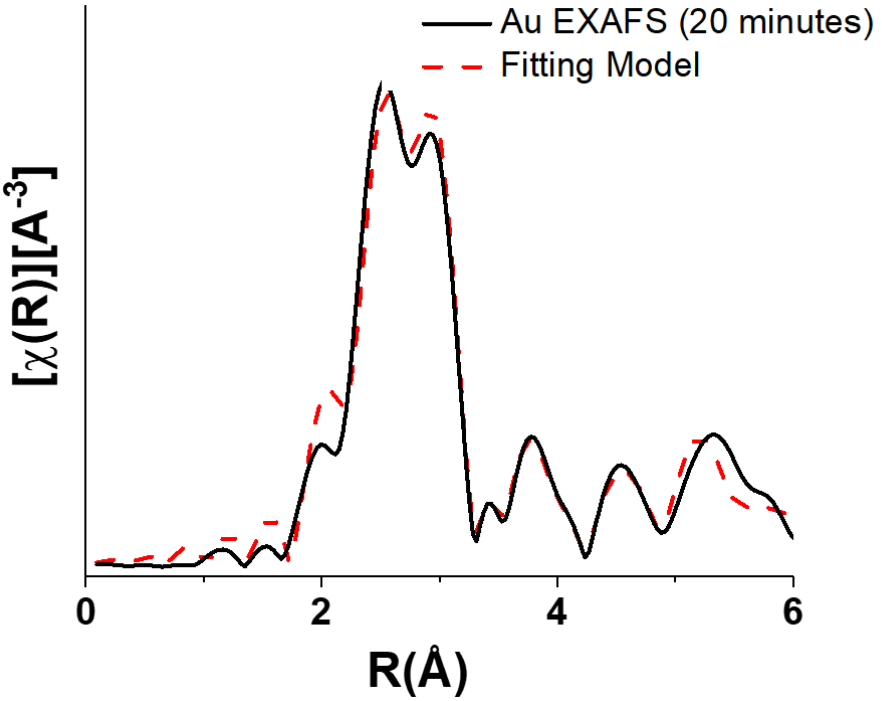

Pathway	N	R (Å)	E_0 (eV)	σ^2 (Å^2) x 10^{-3}
Au–Au (shell 1)	11.4 ± 1.0	2.859 ± 0.004	5.2 ± 0.4	7.4 ± 0.6
Au–Ag (shell 1)	0.5 ± 0.6	2.865	-0.3 ± 7.8	12.5

Figure A4.12.15 Au L3 edge EXAFS spectrum and fitting model for 20 minute nanorod aliquot. The Au L3-edge nanoparticle spectrum was fit using first coordination-shell atomic pathways. A fitting range from 1.5 to 4 Å and a k-range from 2 to 12 Å^{-1} was used. The R-factor parameter associated with the goodness of fit for this model was 0.015.

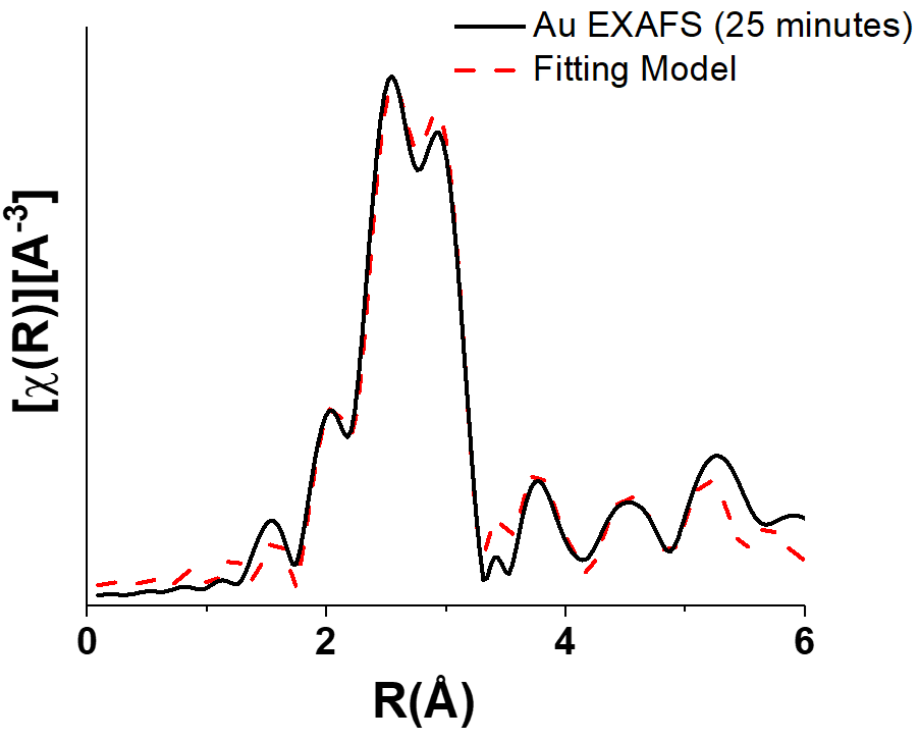

Pathway	N	R (Å)	E_0 (eV)	σ^2 (Å^2) x 10^{-3}
Au–Au (shell 1)	11.4 ± 0.8	2.860 ± 0.002	5.0 ± 0.3	7.1 ± 0.4
Au–Ag (shell 1)	0.2 ± 0.4	2.866	7.2 ± 6.2	14.4

Figure A4.12.16 Au L3 edge EXAFS spectrum and fitting model for 25 minute nanorod aliquot. The Au L3-edge nanoparticle spectrum was fit using first coordination-shell atomic pathways. A fitting range from 1.5 to 4 Å and a k-range from 2 to 12 Å^{-1} was used. The R-factor parameter associated with the goodness of fit for this model was 0.011.

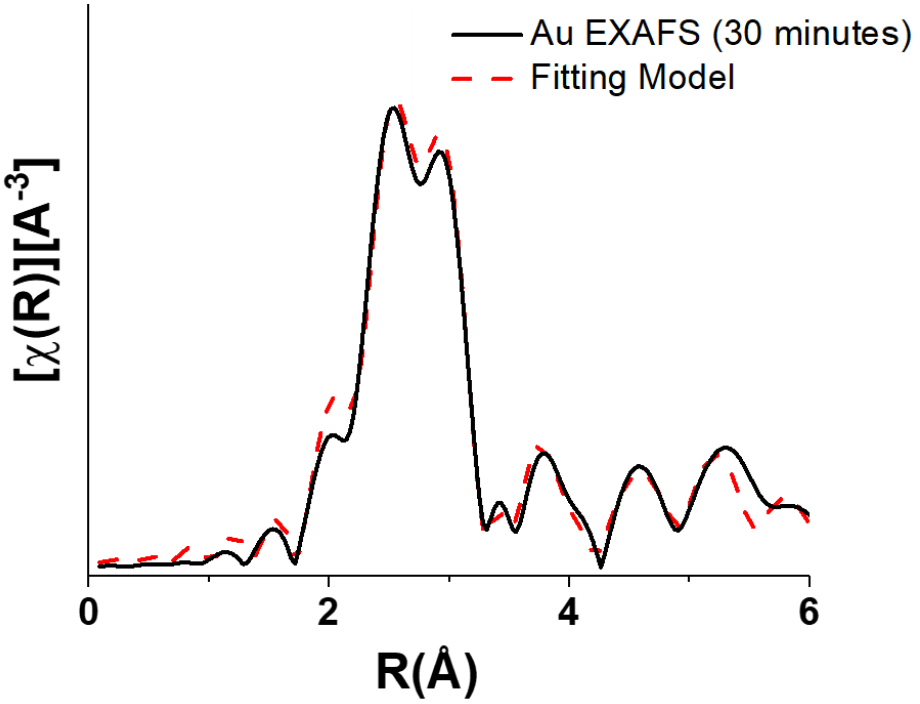

Pathway	N	R (Å)	E_0 (eV)	σ^2 (Å^2) x 10^{-3}
Au–Au (shell 1)	11.5 ± 0.8	2.858 ± 0.003	5.0 ± 0.3	7.9 ± 0.5
Au–Ag (shell 1)	0.3 ± 0.6	2.869	-9.7 ± 8.4	14.0

Figure A4.12.17 Au L3 edge EXAFS spectrum and fitting model for 30 minute nanorod aliquot. The Au L3-edge nanoparticle spectrum was fit using first coordination-shell atomic pathways. A fitting range from 1.5 to 4 Å and a k-range from 2 to 12 Å^{-1} was used. The R-factor parameter associated with the goodness of fit for this model was 0.009.

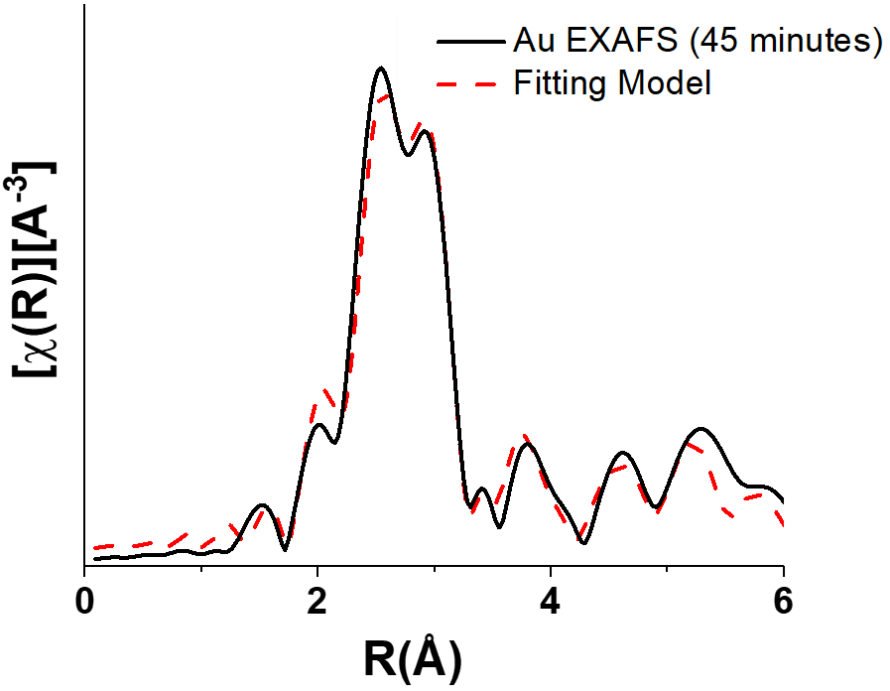

Pathway	N	R (Å)	E_0 (eV)	σ^2 (Å^2) x 10^{-3}
Au–Au (shell 1)	11.4 ± 1.0	2.859 ± 0.003	5.0 ± 0.4	7.0 ± 0.5
Au–Ag (shell 1)	0.1 ± 0.8	2.865	-8.7 ± 6.6	14.1

Figure A4.12.18 Au L3 edge EXAFS spectrum and fitting model for 45 minute nanorod aliquot. The Au L3-edge nanoparticle spectrum was fit using first coordination-shell atomic pathways. A fitting range from 1.5 to 4 Å and a k-range from 2 to 12 Å^{-1} was used. The R-factor parameter associated with the goodness of fit for this model was 0.014.

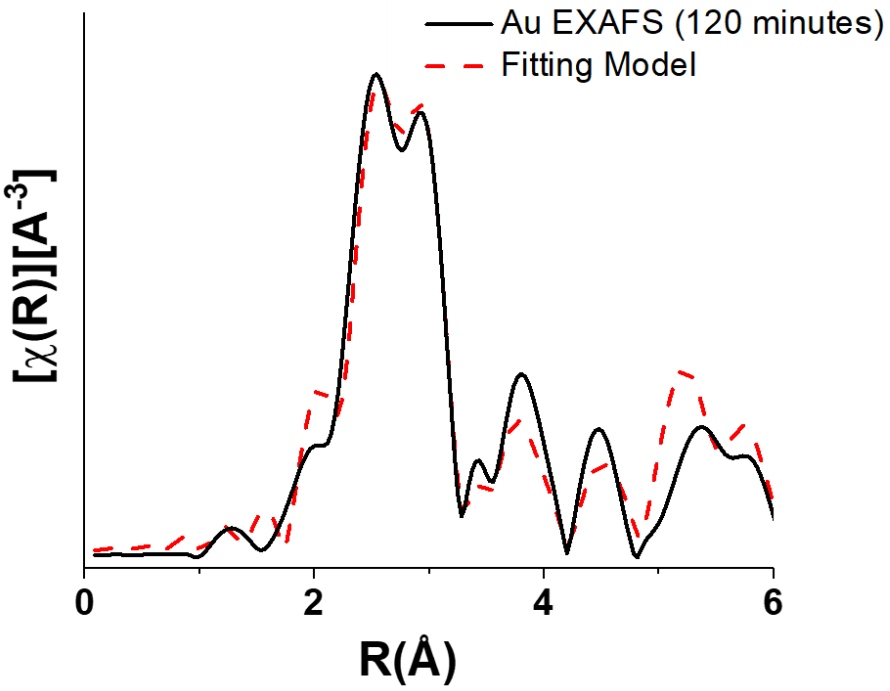

Pathway	N	R (Å)	E_0 (eV)	σ^2 (Å^2) x 10^{-3}
Au–Au (shell 1)	12.0 ± 1.3	2.857 ± 0.004	4.6 ± 0.5	6.8 ± 0.7

Figure A4.12.19 Au L3 edge EXAFS spectrum and fitting model for final product 120 minute nanorods. The Au L3-edge nanoparticle spectrum was fit using first coordination-shell atomic pathways. A fitting range from 1.5 to 4 Å and a k-range from 2 to 12 Å^{-1} was used. The R-factor parameter associated with the goodness of fit for this model was 0.027.

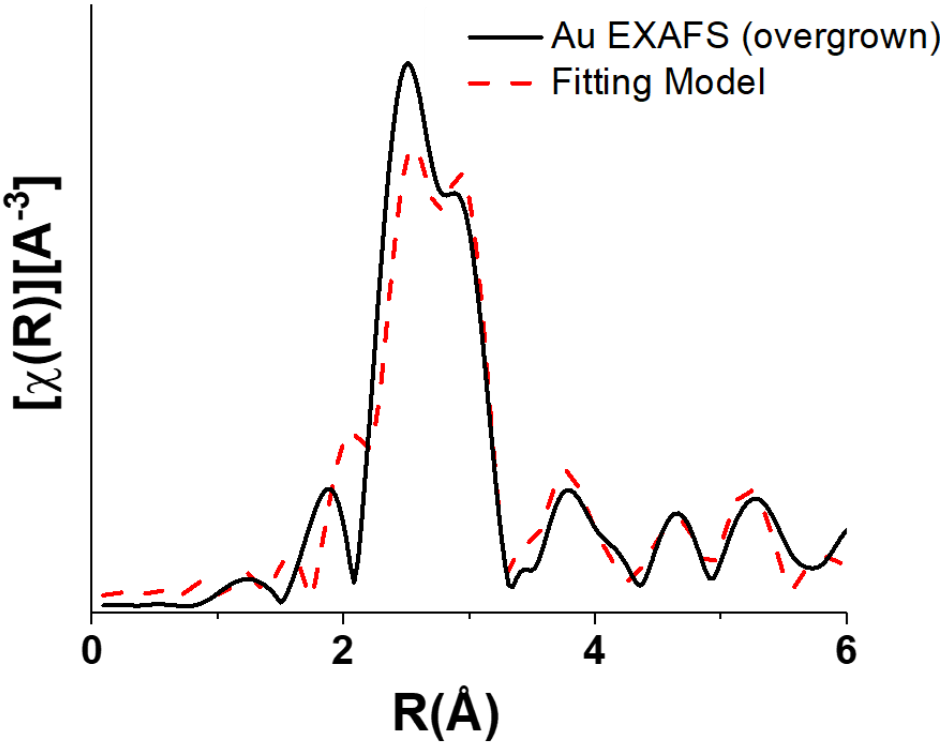

Pathway	N	R (Å)	E_0 (eV)	σ^2 (Å^2) x 10^{-3}
Au–Au (shell 1)	11.8 ± 2.4	2.861 ± 0.009	4.7 ± 1.1	7.6 ± 1.4

Figure A4.12.20 Au L3 edge EXAFS spectrum and fitting model for Au-overgrown nanorods. The Au L3-edge nanoparticle spectrum was fit using first coordination-shell atomic pathways. A fitting range from 1.5 to 4 Å and a k-range from 2 to 12 Å^{-1} was used. The R-factor parameter associated with the goodness of fit for this model was 0.091.

A.5 Supporting information for Chapter 5

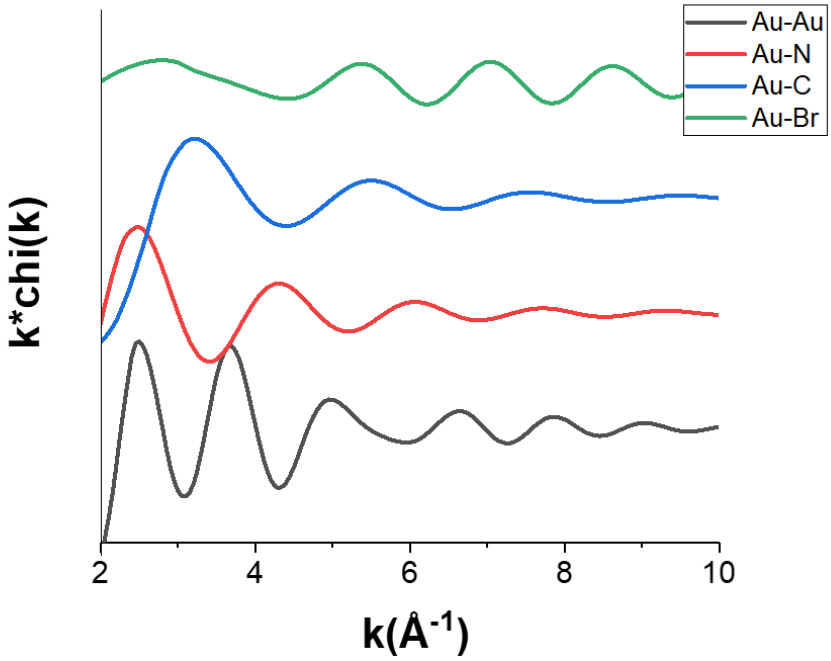

Figure A5.1 Simulations of XAFS spectra with varying scattering elements. Au-Au (using parameters from best fit model (Table 5.1)), and Au-N, Au-C and Au-Br using the same parameters (N = 1, R = 2.4 Å and σ^2 = 3 x 10^{-3} $Å^2$) first-shell simulations are shown. It can be observed that while Au-N and Au-C are not distinguishable, particularly as k increases, yet these are drastically different from Au-Au and Au-Br. This shows that in computational modeling, these pathways should be distinguishable.

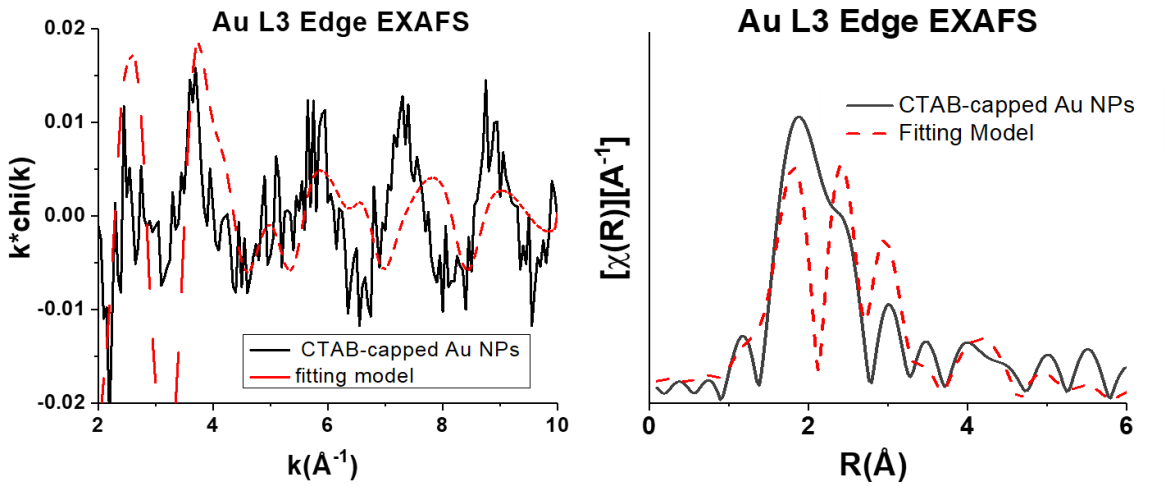

Figure A5.2 XAFS modeling excluding Au-Br pathways. Best-fit models (red) in k-space (left) and R-space (right) compared to the experimental data for CTAB-capped Au NPs (black) for the case that Au-Br pathways are excluded from the model. In particular, the higher-k regions do not fit well in phase or in amplitude. This makes sense when considering the k-dependence of scattering. From simulations of the different pathways (Figure A5.1) it is apparent that Au-Br, which scatters strongly from k = 6-10, is needed to achieve the experimental spectrum.

A.6 Supporting information for Chapter 6

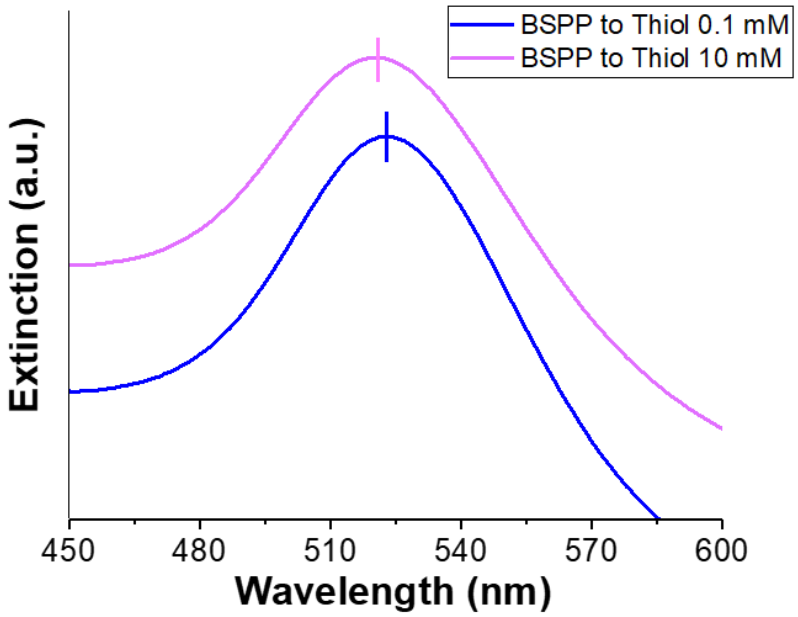

Figure A6.1 Comparison of UV-vis absorption spectra with different thiol concentration. The UV-vis spectra are nearly identical for the case where 0.1 mM and 10 mM are used. The LSPR peak position is the same within error (1 nm), and both show a blue-shift compared to the CTAB-capped Au NP spectrum (522 and 521 nm vs. 525 nm).

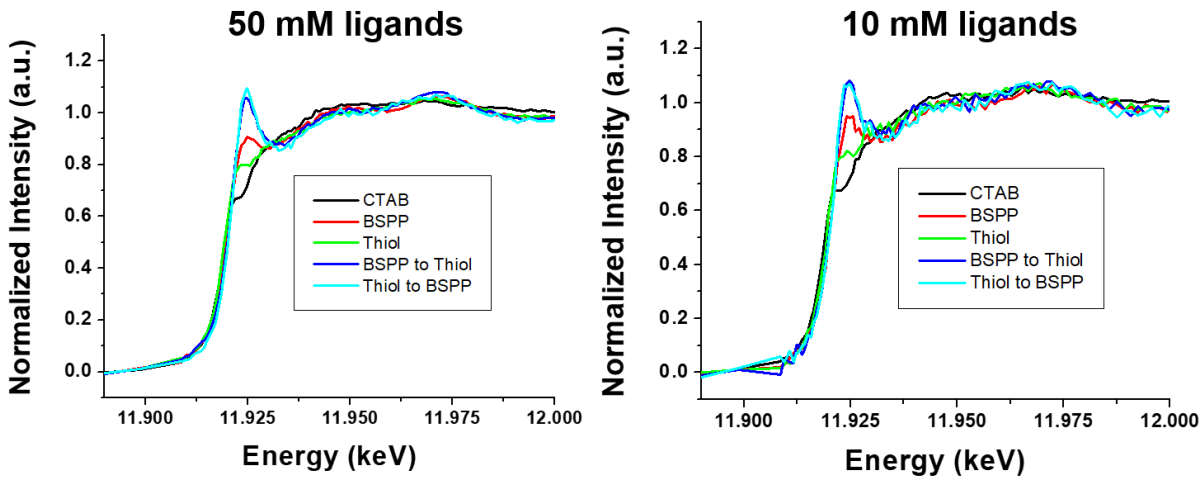

Figure A6.2 XANES data for 50 mM and 10 mM global ligand concentrations. In comparing the XANES signatures for the case where 50 mM (left) vs. 10 mM (right) global ligand concentrations are used, the exact same trends are observed from sample to sample.

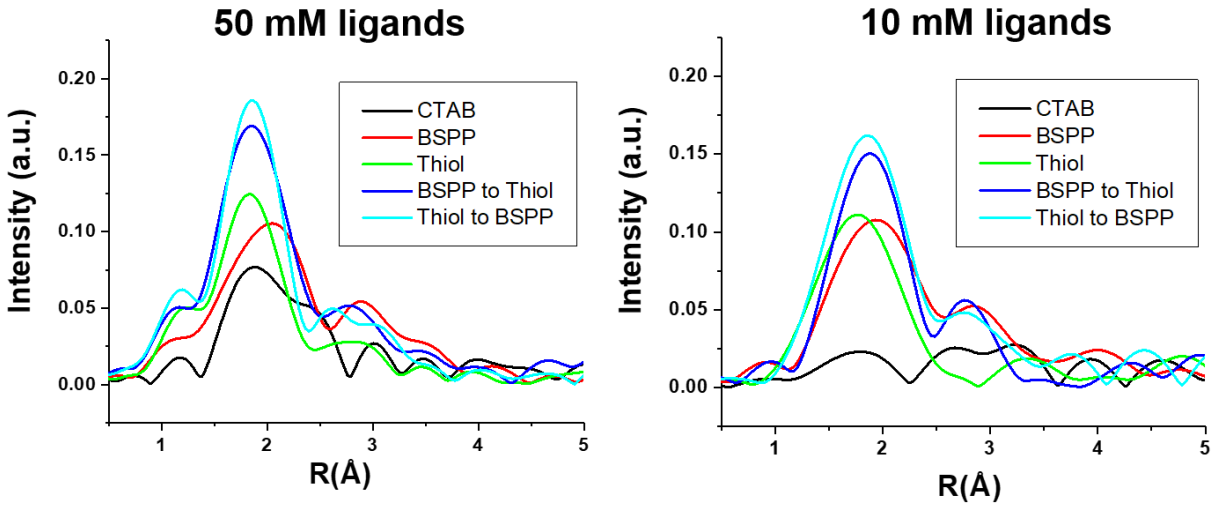

Figure A6.3 EXAFS data for 50 mM and 10 mM global ligand concentrations. In comparing the EXAFS data for the case where 50 mM (left) vs. 10 mM (right) global ligand concentrations are used, the exact same trends are observed from sample to sample. Differences observed in the

spectra between the two concentrations are due to the different k-ranges used (2 - 10 $Å^{-1}$ for the 50 mM case vs. 2 - 8 $Å^{-1}$ for the 10 mM case).

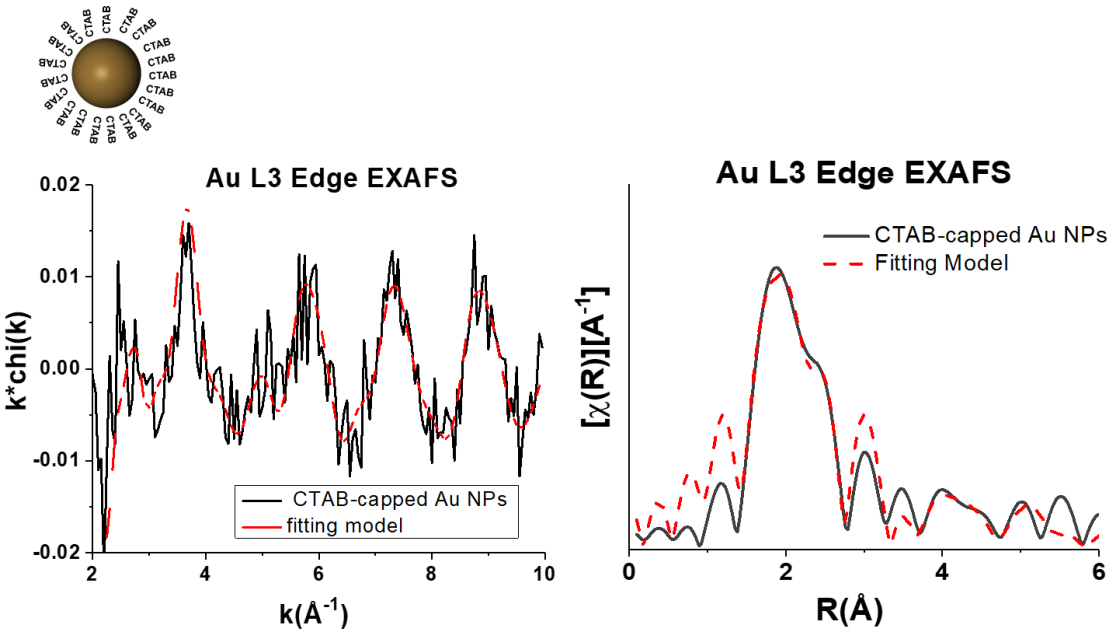

Figure A6.4.1 EXAFS data and fitting model for started Au-NPs with 50 mM CTAB. A fitting range from 1.5 to 3.0 Å and a k-range from 2 to 10 $Å^{-1}$ was used. The R-factor parameter associated with the goodness of fit for this model was 0.028.

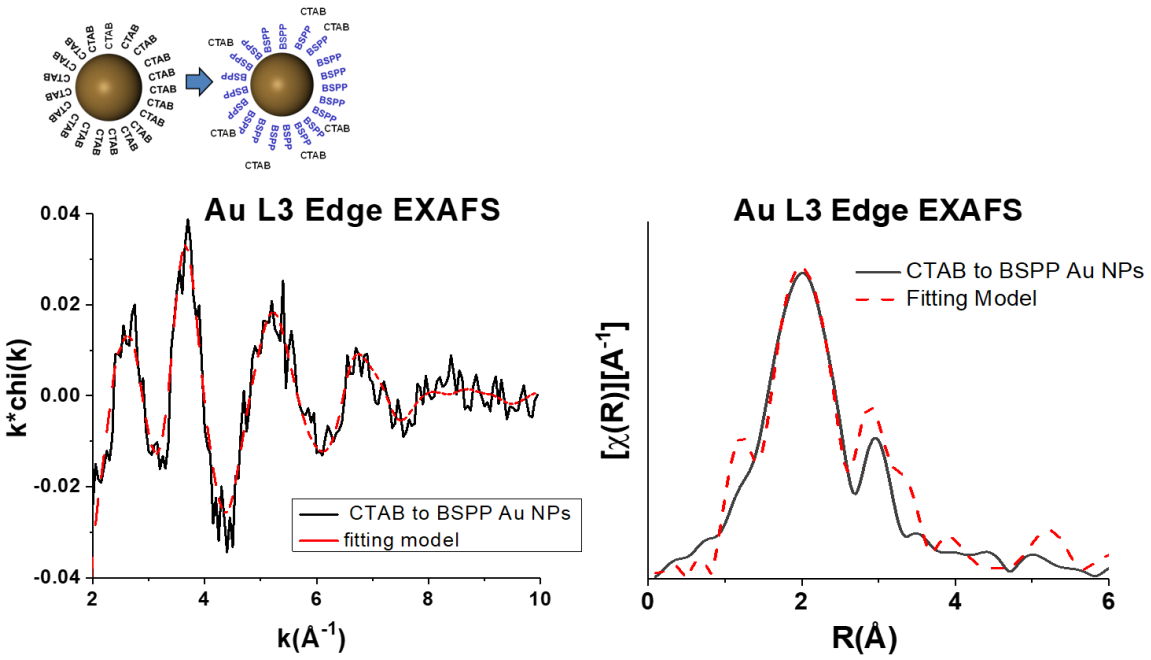

Figure A6.4.2 EXAFS data and fitting model for started Au-NPs with 50 mM CTAB and 50 mM BSPP introduced. A fitting range from 1.5 to 3.0 Å and a k-range from 2 to 10 $Å^{-1}$ was used. The R-factor parameter associated with the goodness of fit for this model was 0.035.

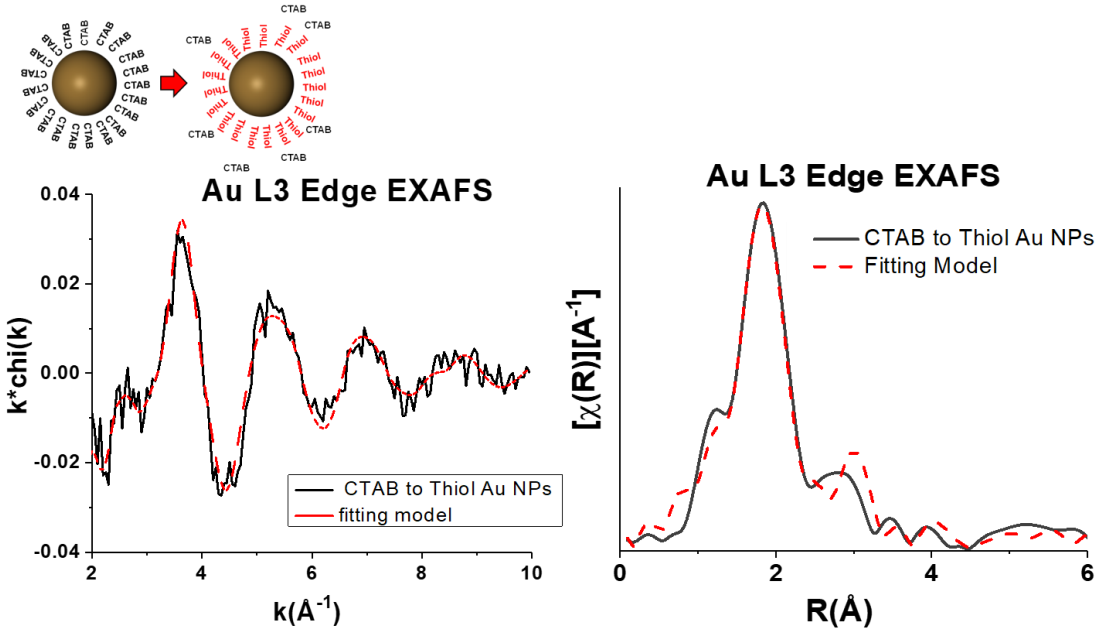

Figure A6.4.3 EXAFS data and fitting model for started Au-NPs with 50 mM CTAB and 50 mM PEG-thiol introduced. A fitting range from 1.5 to 3.0 Å and a k-range from 2 to 10 $Å^{-1}$ was used. The R-factor parameter associated with the goodness of fit for this model was 0.035.

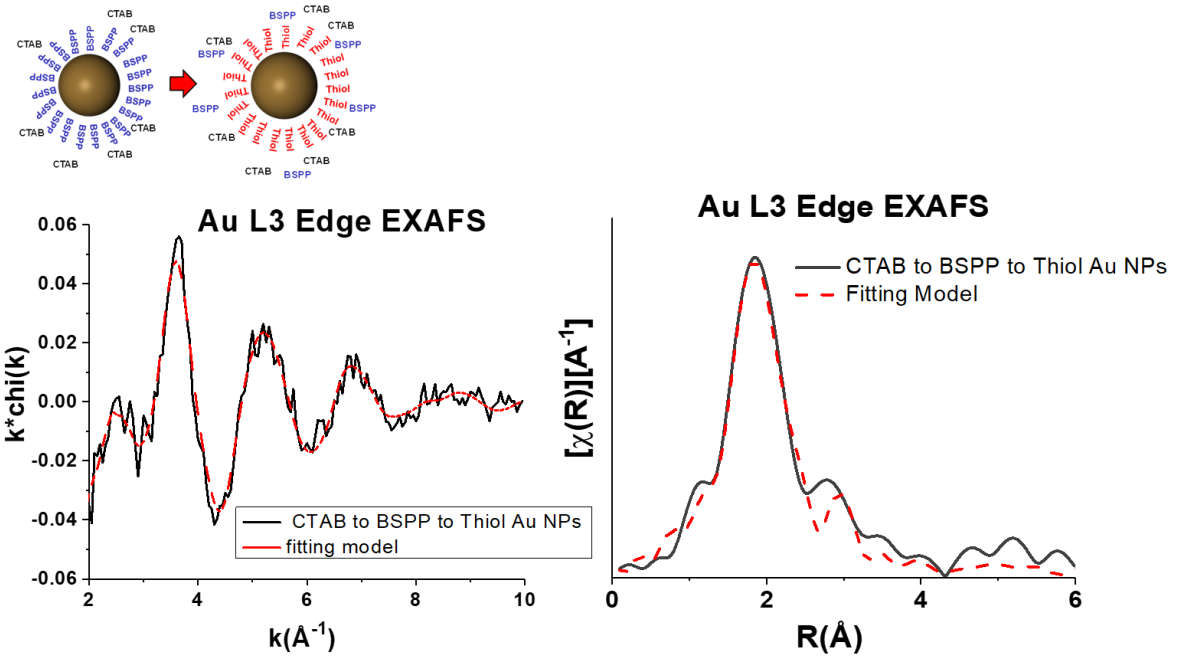

Figure A6.4.4 EXAFS data and fitting model for started Au-NPs with 50 mM CTAB and 50 mM BSPP, then 50 mM PEG-thiol introduced. A fitting range from 1.5 to 3.0 Å and a k-range from 2 to 10 $Å^{-1}$ was used. The R-factor parameter associated with the goodness of fit for this model was 0.024.

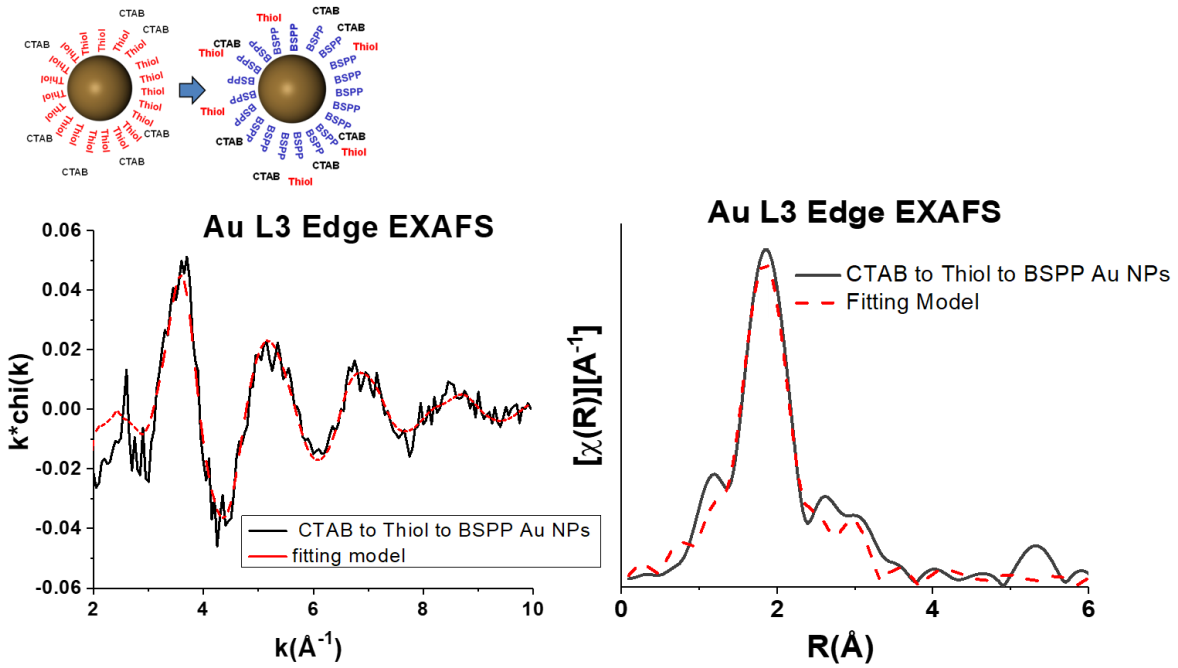

Figure A6.4.5 EXAFS data and fitting model for started Au-NPs with 50 mM CTAB and 50 mM PEG-thiol, then 50 mM BSPP introduced. A fitting range from 1.5 to 3.0 Å and a k-range from 2 to 10 $Å^{-1}$ was used. The R-factor parameter associated with the goodness of fit for this model was 0.020.

Appendix B XAFS processing and analysis using the IFEFFIT software package

B.1 Introduction

The purpose of this appendix is to provide a guide towards approaching XAFS analysis using the IFEFFIT software package.[116] This should prove a helpful document for future students working with local structure analysis. This appendix, however, is not meant to be a replacement for learning the fundamentals of XAFS, and for this purpose I would direct the reader to the following texts. As a first introduction, the XAFS section from the textbook "Physical Methods in Bioinorganic Chemistry: Spectroscopy and Magnetism" proves particularly helpful.[47] It provides a very qualitative description and is particularly useful for an individual approaching XAFS from a chemistry background. This text by Robert Scott is a very incomplete picture of XAFS and leaves out important mathematic details, however is a good first text due to its informative and brief qualitative description and thorough connection towards problems that XAFS can be particularly useful for.

A more thorough text by Grant Bunker, "Introduction to XAFS", provides a detailed description of XAFS theory, data collection and analysis methods.[28] I would highly recommend reading this text before diving into XAFS experimental design and data analysis. A third text by Scott Calvin, "XAFS for Everyone" is preferred by some due to its use of cartoon animals with different personalities and experimental systems of preference to explain XAFS concepts. This text is surprisingly clear and detailed despite this unconventional and rather fun twist.[184] These are only a few recommendations in a large volume of literature, however provide a starting place, in

addition to several key publications that I found useful in approaching XAFS analysis for the first time.[49-52, 161] The website xafs.org and IFEFFIT listserve and archives also prove valuable resources and have links to useful lectures from the XAFS school and related workshops.

After familiarizing oneself with XAFS theory and analysis concepts, a helpful exercise is fitting a model to a known structure, such as a bulk metal foil. This provides a means to learn the software basics while making sure that this process leads to the expected result as a means to self-check the analysis procedure. In addition, processing and fitting a foil of the absorbing atom element through the same measured edge energy is standard procedure for the purpose of calibrating the edge position and extracting the amplitude reduction factor S_0^2. The rest of this appendix will step through a general procedure for XAFS data processing and analysis using the IFEFFIT software package (Demeter, version 0.9.25). This is accomplished by going through the process step by step of fitting an Au foil.

B.2 Downloading the IFEFFIT software package

The IFEFFIT software package can be downloaded from the following website: http://bruceravel.github.io/demeter/

The most recent version of the package, which contains Hephaestus (a module that contains reference tables related to XAFS measurements that are searchable by element), Athena (data processing) and Artemis (data fitting) modules, is referred to as the “Demeter” package. The software is free for download and available for Linux, Windows, or Mac computers.

B.3 Data processing using Athena

B.3.1 Importing data into Athena

Raw data from the beamline is generally in the form of an ascii or similar file. Such files can generally be opened directly in Athena or Artemis whether or not there is a header for the data (I have not had trouble directly opening files from data collected at 5-BMD, for instance). If the file will not open, it may be helpful to first save the data as a text file so that the file form will be recognized. To open the data in Athena, go to File → Import data, and find the data file. When the file is opened, the screen should take you to a separate page:

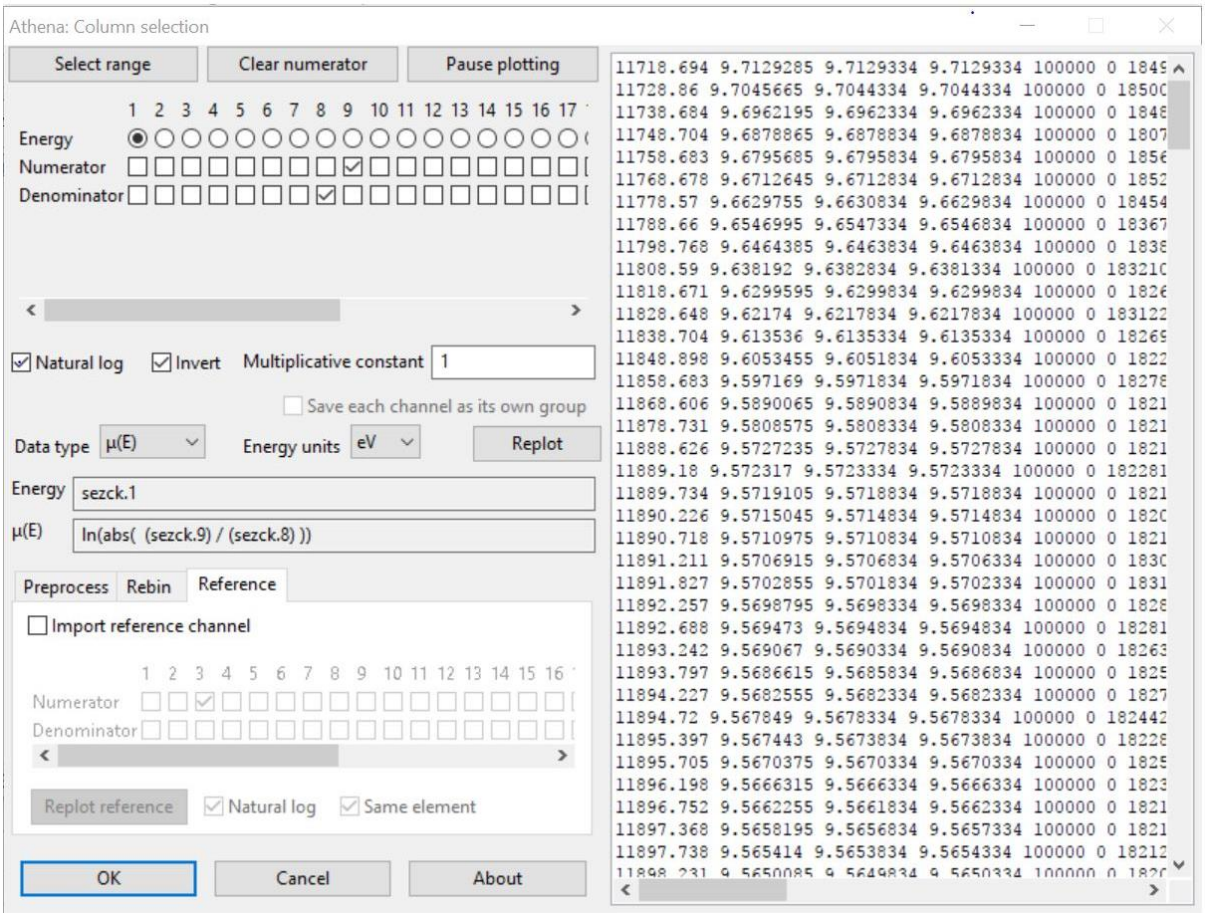

Figure B.1 Athena import page

Here a data file for an Au foil collected at the Au L_3 absorption edge has been imported into Athena. This file can be seen on the right-hand side of the page. The first task is to let the program know which columns from the data file are needed to plot the absorption spectrum. For this purpose, it is necessary when at the beamline and setting up an experiment to write down what is contained in each of the data file columns. This varies from experiment to experiment depending on the specific experimental details. In this particular case, the foil was collected in transmission geometry, meaning that we will want to plot $-\ln(\frac{I_t}{I_0})$ as a function of energy, where I_t is the intensity measured from the ion chamber after the sample and I_0 is the intensity measured from the ion chamber placed before the sample. At the top left of the page, where it says "energy", "numerator" and "denominator", the columns that contain the desired information are indicated. Typically, as in this case, energy is in the first column of the data file, hence we see the "1" indicated there. In this data file, I_t was in column 9 and I_0 in column 8, which is why 9 is checked for the numerator and 8 for the denominator. Since the total expression is the negative natural log, the boxes "natural log" and "invert" are also checked in the boxes below. The function resulting from the checked boxes can be seen in the μ(E) box in the middle of the page. It should be noted that for the case of fluorescence-mode XAFS, the function for μ(E) is different. In that case, the dead-time corrected fluorescence intensity columns should be checked in the numerator and I_0 in the denominator. If more than one detector is used, all columns that contain fluorescence data can be checked in the numerator, which will result in addition of these values.

Continuing down the page, raw data files should be imported as μ(E), since the data has not yet been normalized or processed. While data is generally in data files as eV, eV or keV should be chosen as appropriate depending on units of the data file energy column. The bottom left meu on

the page labeled “preprocess”, “rebin” and “reference” can generally be ignored. I have personally found it easier to simply input and process reference data as a separate file. At this point, we are ready to move on from the data import page, and can press “OK”.

B.3.2 Edge position determination and calibration

From the Athena main page (Figure B.2), there are several dropdown menus in order to perform different preprocessing operations. The default window is referred to as the “main window”. When the software is opened, Athena will automatically determine a set of default parameters based on the imported data (shown in Figure B.2). While these parameters require optimization, if there is not a large amount of noise in the data, they are generally sufficient to take a quick look at the data, add multiple scans and compare datasets while taking measurements at beamtime. The first step is to make sure that the correct element and edge are selected from the dropdown menus. The energy shift is defaulted at zero, however if a standard shows a shift in the edge of 1 eV from the theoretical value, for example, then an energy shift of 1 can be applied to sample data sets to account for this offset from theory.

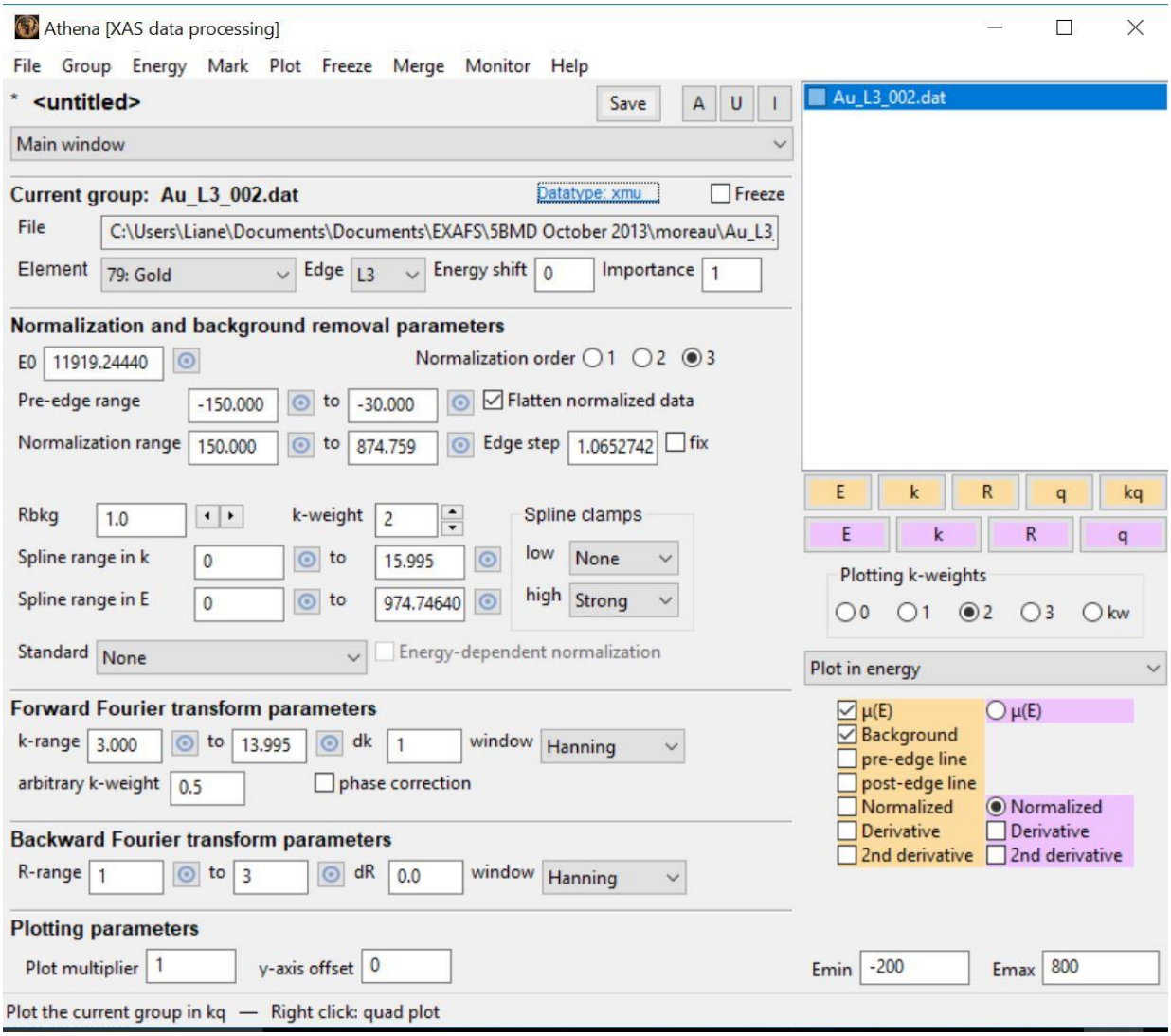

Figure B.2 Athena main window

Typically, there are two different ways to determine the position of the edge. It is important that when comparing to spectra in literature, or between samples, that the edge position is defined by the same operation. Some determine the edge position as the value of energy at the point half-way up the absorption edge. A more common way, and the way that I have typically used, is to define the edge position as the maximum value of the first derivative of the spectrum, or the first

inflection point. In order to apply one of these edge-determining operations, the drop-down menu can be used to navigate from the “main window” to “calibrate data” page (Figure B.3). The “display” pulldown enables plotting of the raw data, first or second derivatives. A point for the edge position can be selected using the “select a point” function, and the position of the selected point will be displayed in the “E0” box. If a standard has an edge position that is off from the theoretical value, it can be calibrated to the theoretical value by typing the theoretical value for the edge position (such as 11919 eV for the Au L_3 edge case) into the “calibrate” box and pressing the “calibrate” icon.

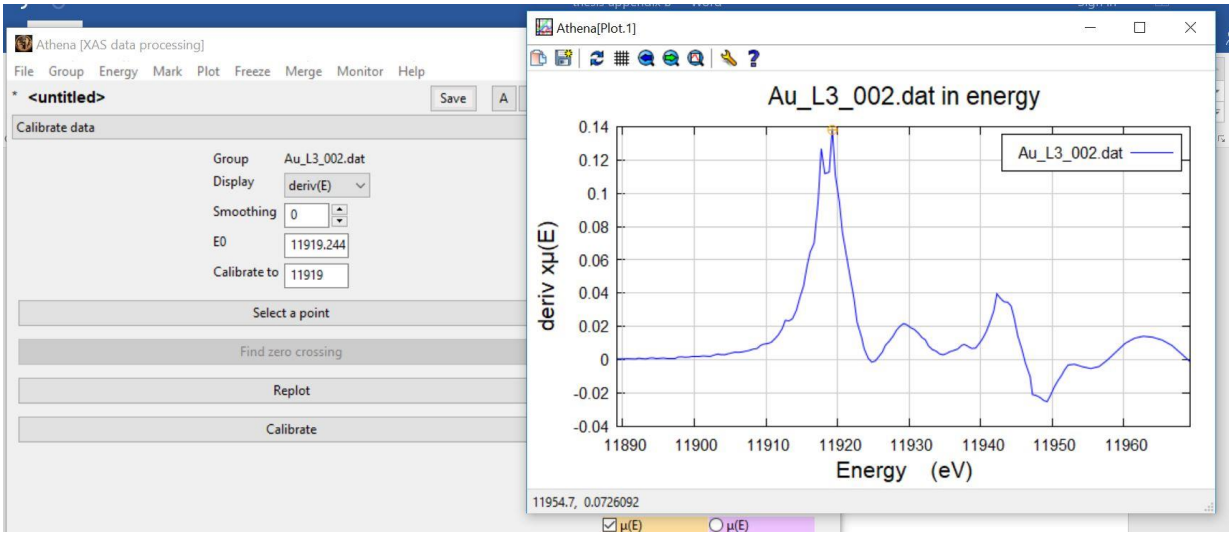

Figure B.3 Athena calibration window

If a standard requires calibration, then all samples should apply an E0 shift as previously described on the main menu page to account for this difference. In order to ensure an accurate edge determination, it is generally a good idea to place a standard foil between the ion chamber after the sample and a third ion chamber. This allows for simultaneous collection of a reference spectra, in the case that there is a shift in the mono energy over time. In my experience, this has not been a

problem within the 1 eV resolution of the measurement (using a 1 eV step size), however this may not always be the case.

B.3.4 Data alignment and summation

It is common, especially in the case of dilute nanoparticle samples as presented in this thesis, that multiple data scans will need to be collected for each sample. These will need to be added together to create a sample spectrum with reduced error. Before this can be done, the edge positions from the individual scans should be aligned if there is any offset. This can be done using the "align data" pulldown menu. If "align marked data" is chosen from this panel, marked data sets will be aligned to the same E_0 value as the selected sample or standard from the "standard" pulldown menu. These data sets can then be added together using the "data summation" page accessible from the main pulldown menu (Figure B.4).

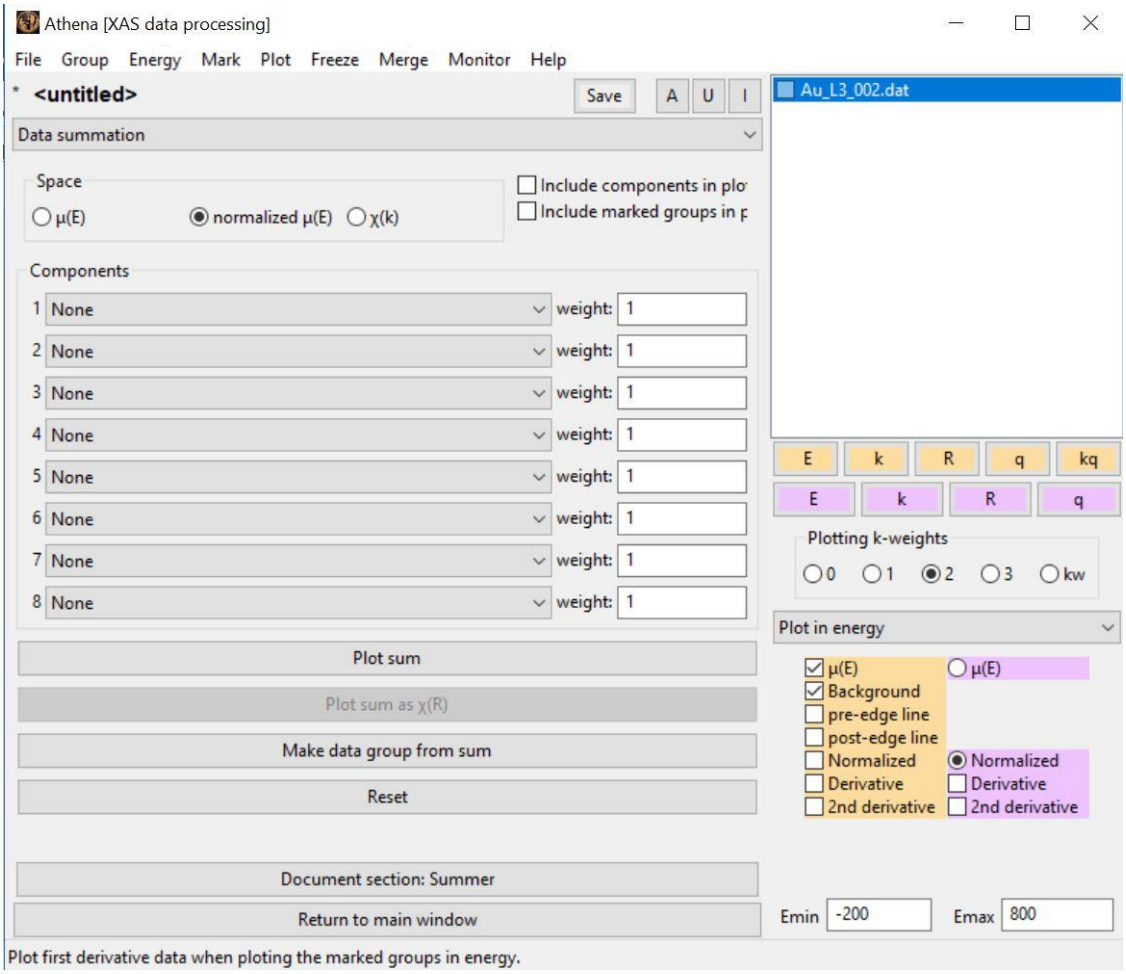

Figure B.4 Data summation page

Athena enables summation of the raw data (μ(E)), normalized data, or background subtracted data (χ(k)). I prefer to sum the raw data, in which case it is absolute intensity that is being added and therefore weighting is not required- rather data sets with a greater absolute intensity (more counts) automatically contribute more as appropriate to the overall data set. Only data from the same sample should be summed together. This can be done through either marking the groups intended for summation on the right side of the page. Or selecting them as components and checking either “include marked groups in plot” or “include components in plot” respectively. By

selecting “make data group from sum”, a data set will be created from the sum of the individual spectra, to be used moving forward through the analysis process.

B.3.5 Data normalization

For μ(E) to truly represent the probability of creating a core-hole, the background must be subtracted and data normalized such that the y-axis values go from 0 to 1. To achieve this, a line is fit to the pre-edge and through the post-edge regions of the spectrum. These two lines should be parallel, since both should scale as $\frac{1}{E^3}$. However, if the two points each defined on the pre and post-edge regions are not appropriate, this will not be the case, as observed from the Athena-program default lines shown in Figure B.5 below.

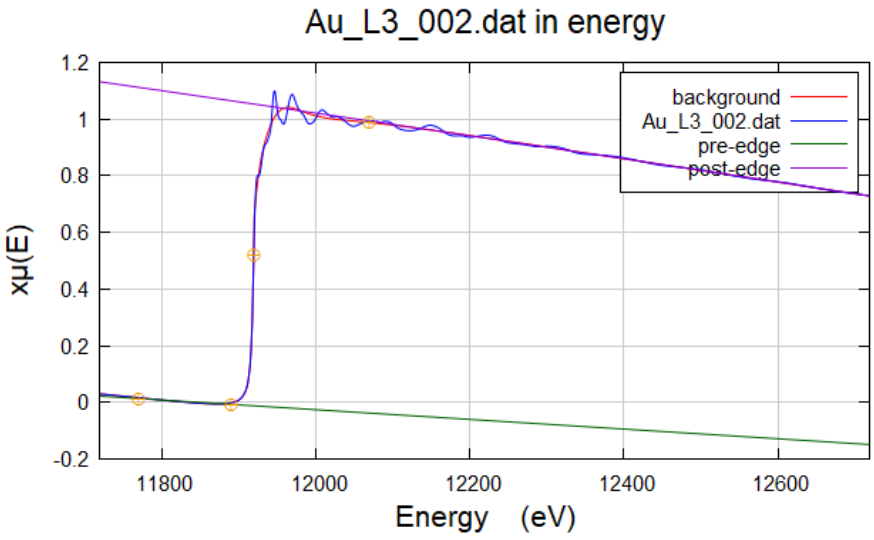

Figure B.5 Pre- and post-edge lines prior to setting appropriate normalization ranges

Regions for the pre-edge line fits are determined from a user-defined start and endpoint. These may need to be optimized in order to make the pre- and post-edge lines parallel to each other. In particular, the post-edge line slope may be particularly affected by the lower-energy point, if the

point is placed on the crest or trough of an oscillation rather than through the middle of the data. Note from figure Also, if the higher-energy point defining the pre-edge is too close to the edge position, it may be in an increase region rather than where μ is decreasing as $\frac{1}{E^3}$. Values can be input into the pre-edge range and post-edge range boxes. It is important to also ensure that the value used for the lower-energy side of the normalization (post-edge) range should be at least 50 to 100 eV above the edge position such that it is in the EXAFS region. Figure B.6 shows the optimized ranges and associated parallel pre- and post-edge lines. A normalization order of 3 was used in this case, and is generally standard.

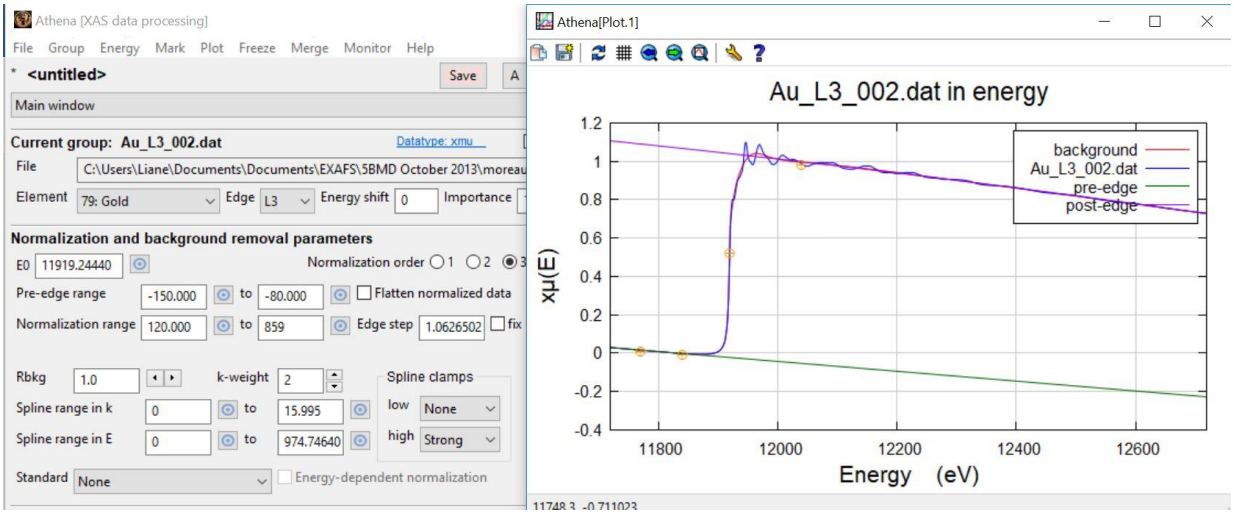

Figure B.6 Optimizing background removal parameters

B.3.6 Plotting in Athena

At this point, it is worthwhile to mention the plotting capabilities of Athena. At the right of the main page (see Figure B.2), there are yellow and purple buttons, and underneath, associated yellow and purple checkboxes. The yellow features correspond to the highlighted data and work

to plot a single spectrum. The buttons correspond to the plotting space, and from the check boxes, the pre- and post-edge lines can also be plotted, in addition to other features which will be discussed later, such as the background and window. The purple features enable plotting of all spectra that are marked with a check and is useful for comparing multiple spectra. Athena and Artemis were not meant to be graphing software and there is not much tunability in plotting preferences. For this purpose, it makes more sense to export the data sets after processing and plot in a graphing program of choice. This will be described in a later section of this appendix.

B.3.7 Background subtraction

In addition to defining pre-edge and post-edge regions for normalization, there are a few other conditions which need to be set for background subtraction of the XAFS data. By default, Athena uses the AUTOBK algorithm for this procedure. To learn more specifics about the algorithm and how it works, I refer the reader to the original publication of this development.[185] One parameter to be defined is the R_{bkg} parameter. Its name comes from the concept that it vaguely defines the region below which the data is suppressed in R-space, removing stray contributions not relevant to bonding structure of interest. As a result, since the XAFS modulations are in reciprocal space, wider oscillations correspond to data that will show up as lower values in R space. Thus, a lower value of R_{bkg} will result in a background that goes through the data without following the features (Figure B.7, left) and a higher value of R_{bkg} will follow the data closely through the primary oscillations that generally correspond to first-shell data (Figure B.7, right).

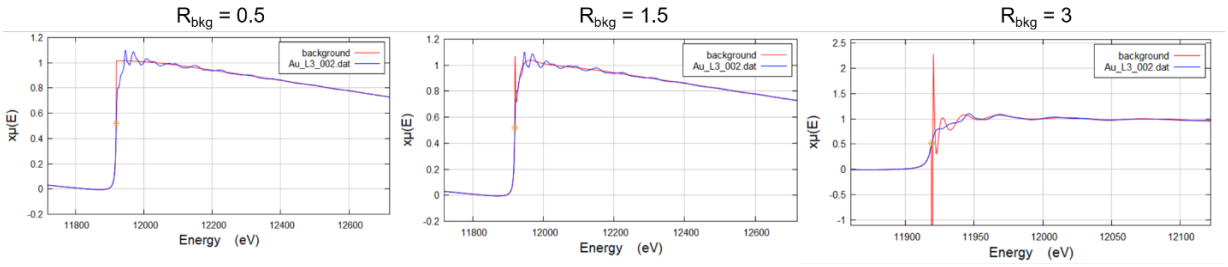

Figure B.7 Background with different R_{bkg} parameters

Figure B.7 shows backgrounds plotted using three different values of R_{bkg}. It is important that the previously described cases are not used. A good value of R_{bkg} goes sharply through the edge and follows the overall curve of the data, without following the shape of the individual oscillations (which would subtract the desired EXAFS signal from the data). A good rule-of-thumb is for R_{bkg} to be roughly half of the first nearest-neighbor distance (and not much higher, given that peaks in R-space generally appear at smaller R values than the true distances due to a phase shift, and because the R-space data is a Fourier transform, and not a radial distribution function. Since in FCC Au, the nearest neighbor distance is expected at 2.884 Å, a R_{bkg} parameter of 1.5, which appears appropriate (Figure 2.7, center) is used.

Another parameter that needs to be set is a k-weight. A k-weight is selected based on the region of the EXAFS spectrum that needs to be emphasized in order to create an even spectrum in k-space. This k-weight is the same that should be applied when plotting the EXAFS spectrum in k or R-space. Functionally, a k-weight of 1 corresponds to multiplication by k, a k-weight of 2 to a multiplication by k^2 and a k-weight of 3 to a multiplication by k^3. This is highly based on the identity of the scattering atoms. For example, or oxides and other bonds to lighter elements (even if the absorbing atom is heavy) a k-weight of 1 may be appropriate, whereas if there are heavier scatterers, higher k-weights are more appropriate. Figure B.8 shows plots of the EXAFS data in k-space with different k-weights. Observe that for a k-weight of 1 (Figure B.8, left) and for a k-

weight of 3 (Figure B.8, right), the data is not even through the k-range of interest, making these k-weights not appropriate. Rather, a k-weight of 2 results in a correctly-shaped spectrum (Figure B.8, middle). Thus, a k-weight of 2 is the appropriate choice.

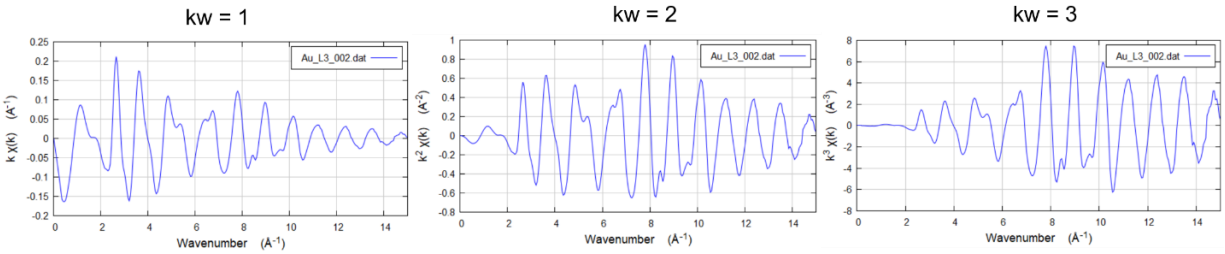

Figure B.8 k-space spectra with different k-weighting

Spline clamps are also set. However, the procedure is not particularly sensitive to the spine clamp used. It is standard to use a low spline clamp for the lower region, and a stronger one for the higher region. The spline range should extend to further out than the region in k that is intended for analysis.

B.3.8 Forward Fourier transform parameters

To transform the k-space EXAFS oscillations to R-space, parameters for the Fourier transform must be set. Namely, this includes a range in k to use, as well as a window function. As far as a range in k, the wider the k-range used, the more accurate the Fourier transform, therefore the end of the specified range should be as high of a k value as possible with the collected data that the data is sufficiently free of noise that the oscillations are well-defined, although it is not a bad idea to leave a bit of area at the end, depending on the shape of the window function used. It is also a good idea to use the same range for a standard as for the samples, for a better comparison. Here, a k-range of 2-12 $Å^{-1}$ is used (Figure B.9). This is generally the range that I use for

nanoparticle samples, since features tend to die into noise after 12 $Å^{-1}$ due to the amorphous-like nature of nanoparticle surface atoms.

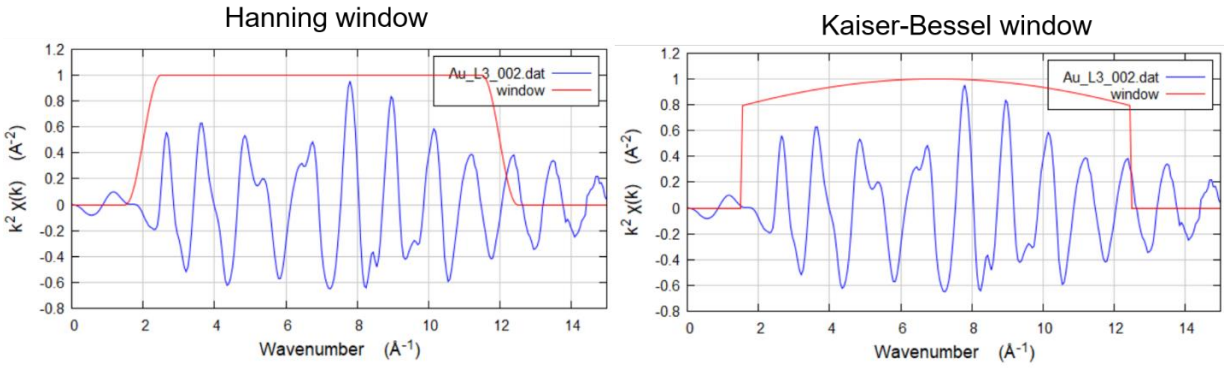

Figure B.9 different window functions for forward Fourier transform

A window function is used for the forward Fourier transform. One can choose the function of preference, the main defining factor being how the function dies out at the ends, with a slope, as in the Hanning window (Figure B.9, left) or abruptly (Figure B.9, right). The Hanning window is used by default and is what I have used for the cases in my thesis work.

B.3.9 The reverse Fourier transform

Just as it is necessary to define a region in k-space for the forward Fourier transform, a region in R-space need be defined for the reverse Fourier transform. This process is referred to as Fourier filtering, and may be helpful in k-space fitting by considering only the region of R-space of interest, rather than the raw k-data, which includes features for all distances. It is often helpful to plot both the k and q-space data together using the "kq" plotting feature.

B.3.10 Other noteworthy features of Athena

Figure B.10 shows the Athena main window with values that have been optimized through the previous sections for an Au foil. While this pre-processing is sufficient for an Au foil, and produces the spectra in k, R and q-space (for R = 1 to 3 Å) shown in Figure B.11, Athena has additional functions that are useful for analysis of multiple spectra and these will be briefly discussed here.

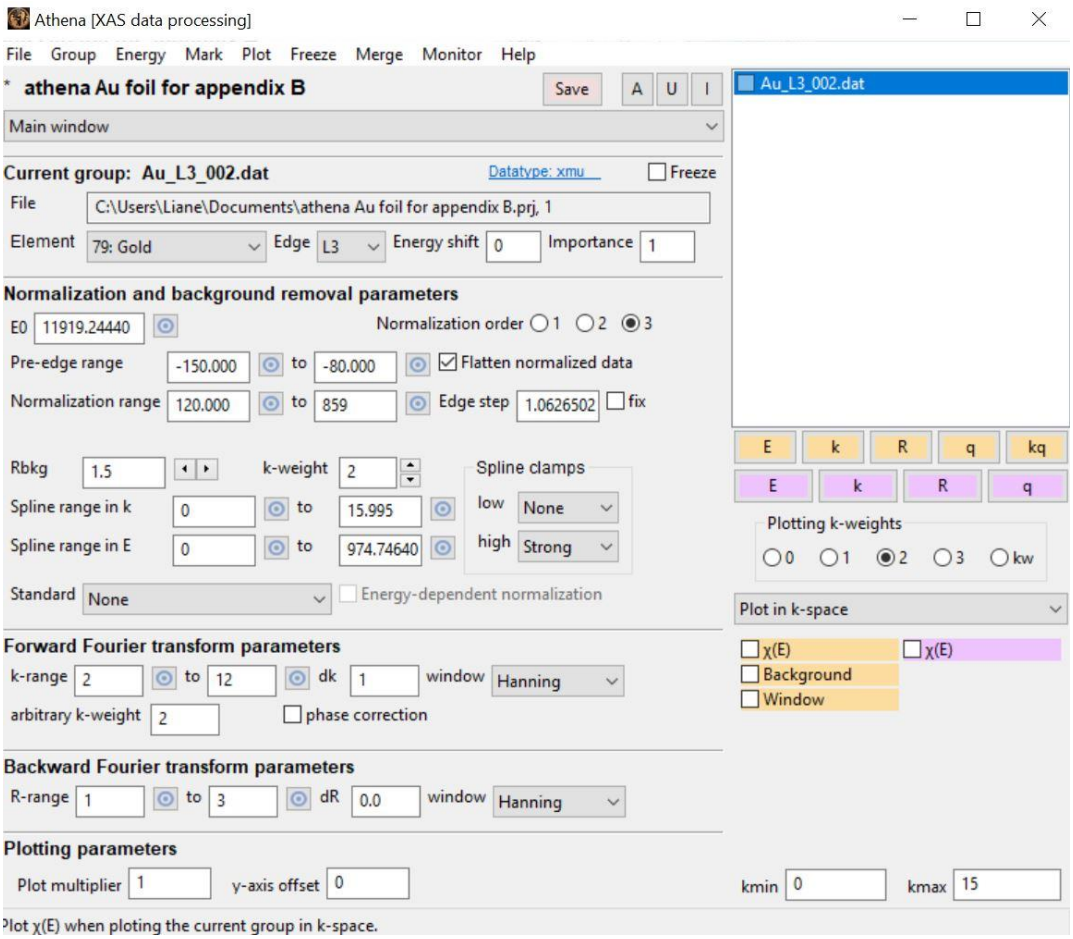

Figure B.10 Athena main window with optimized pre-processing parameters

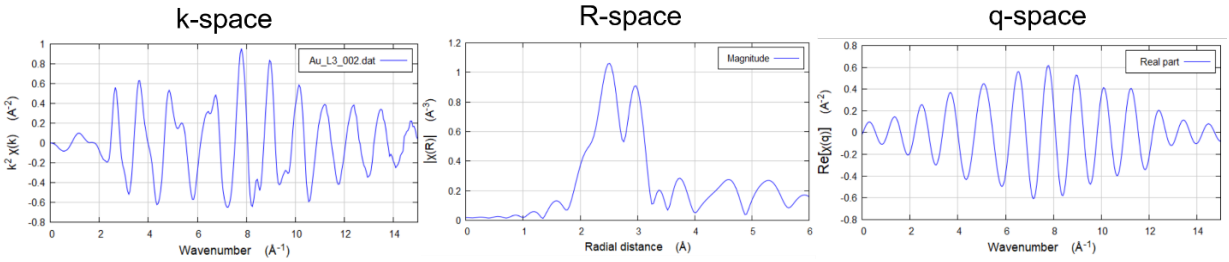

Figure B.11 k-space, R space and q-space data using optimized pre-processing parameters

B.3.10.1 Deglitching

From the main pulldown menu, there is a deglitching window, which may be useful in the cases where there are zingers in the data to be removed. These can appear in the data for a number of regions. Before deglitching, however, it should be considered whether the glitch is a single point or multiple points. A multiple-point glitch may make the data features unclear and therefore it will not be useful to use this function since the original spectral features cannot be recovered. Within this menu there is the option to remove a single point from the data, and I have used that function to remove single-point glitches.

B.3.10.2 Smoothing

There is a smoothing window in the main pulldown menu. I have never used this function for the reason that a better way to remove the noise in the data is to collect for longer times or sum a larger number of spectra for each sample. Personally, from trying out this feature briefly, I am afraid that important features would be lost and the true spectrum not reproduced using this feature. I would leave it up to the reader's cautious judgment as to whether they may find this feature useful to remove noise from data.

B.3.10.3 Linear combination fitting

Another pulldown option from the main menu enables linear combination fitting of a sample spectrum with two or more known standards. This is a common method of analysis for XANES spectra for cases where suitable standards may well describe the data. This may be helpful for cases where multiple oxidation states are possible, and the data may show an intermediate state between the two that would be helpful to evaluate. While I have found this useful in my undergraduate work for larger nanoparticles, I have found it not reliable to use linear combination fitting of nanoparticle samples using bulk spectra when nanoparticles are smaller, due to the sensitivity to surface structure, which affects the shape of the spectrum.

B.3.10.4 Principal component analysis (PCA)

Principal component analysis (PCA) is another common means of quantitatively analyzing XANES data, in particular with respect to pre-edge features that arise for the case of L or M edges. Due to discussion with several XAFS experts who have suggested that quantitative XANES analysis is not particularly accurate. In brief, this method determines the minimum number of principal components needed to reproduce the spectral features. For further reading, I would refer to literature that uses this method.[186-187]

B.3.10.5 Self-absorption correction

Athena also has capability for self-absorption correction using several different algorithms. This may be useful for cases where in fluorescence-mode XAFS, the sample is too thin or too concentrated for the absorption coefficient to be approximated as proportional to the fluorescence yield from the absorbing element. This effect is discussed in Chapter 2 of the thesis. Self-

absorption correction is generally more accurate for the EXAFS than for the XANES region, due to the greater effect on the large increase in XANES than the EXAFS data, since the oscillations only represent a few percent of the overall intensity. References for the individual correction algorithms can be found in the Athena documentation.

B.3.11 Exporting processed data

Processed data in E, k, R or q-space can be exported in a text file that can be opened in most spreadsheet programs, including Excel to plot the data columns in preferred plotting software. This can be done by going to File → save marked groups as and selecting the plot of interest. This way, all of the marked spectra will be saved. Different files need to be saved for different plots and do not include all plotting spaces, only the one specified.

B.4 Data analysis in Artemis

Data saved as an Athena file can be opened in Artemis for EXAFS modeling analysis. Primarily, Artemis is used for fitting a spectrum using the EXAFS equation, which is described in chapter 2 of this thesis, where particular parameters are set as variables and allowed to float during the fit in order to extract them. Since the EXAFS spectrum is modeled as a summation over individual scattering pathways, pathways from theory must be input to use in the fitting model. This can be done using one of the menus on the right-hand side of the Artemis data window, shown below in Figure B.12.

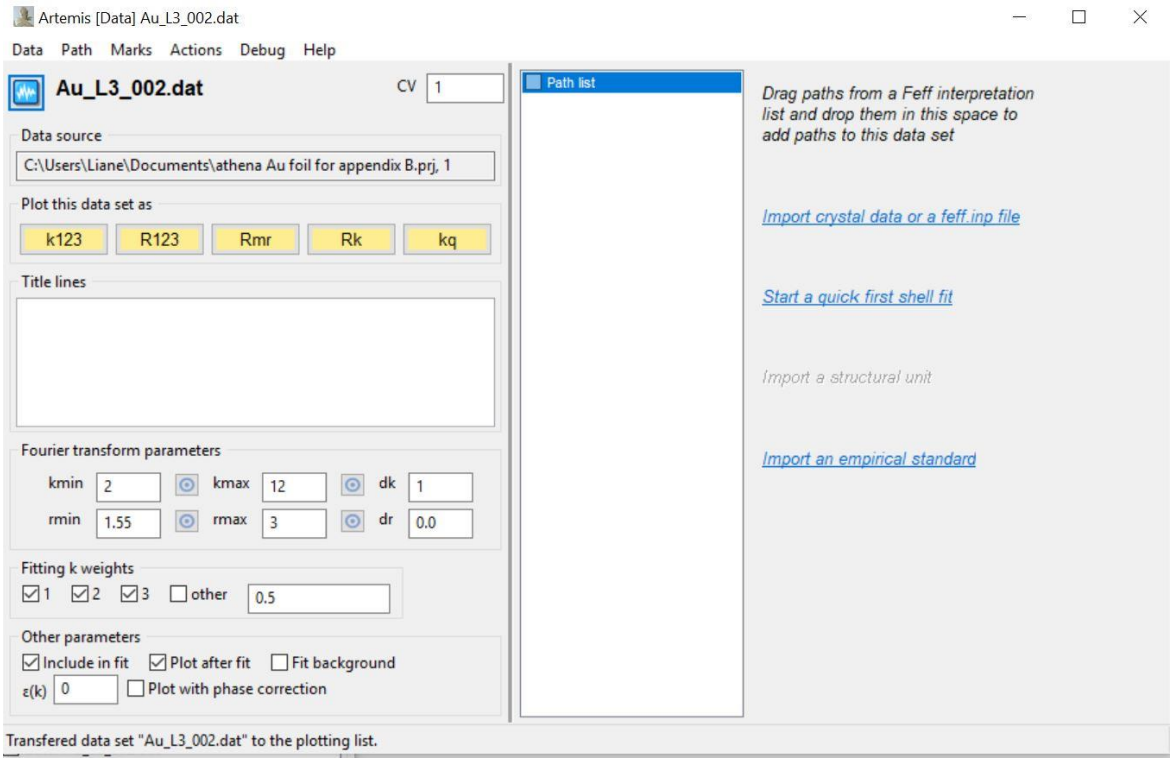

Figure B.12 Artemis data window

B.4.1 Importing theoretical pathways into Artemis

Perhaps the easiest way to generate a pathway is to use a quick first shell fit. It is best to generate a structure if the crystal structure or a similar structure is known using a FEFF calculation. However, for some cases, or to get a quick idea of what pathways might be present, using the quick first shell fit function is appropriate. For example, for the cases of probing nanoparticle surface ligand structure, as in Chapters 5 and 6, a crystal structure would not be appropriate and creating individual pathways representative of Au-ligand bonds is useful. A first-shell pathway can be generated using the "Start a quick first shell fit link" from the data page (Figure B.13).

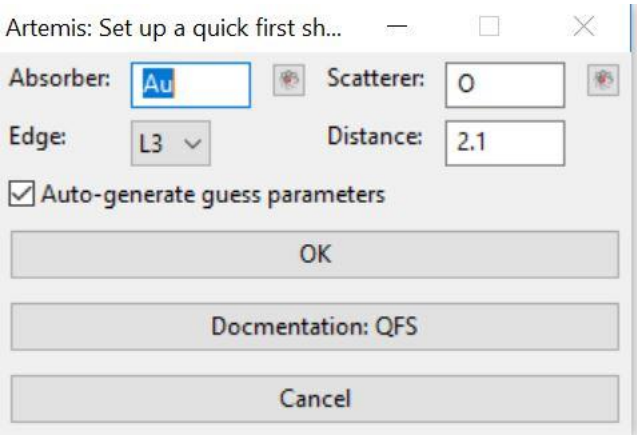

Figure B.13 Artemis quick first shell fit

To set up a first-shell path using the quick first shell fit function, the user defines the absorbing atom and associated edge for the data and scattering atom for the path. An appropriate distance (R) is also defined. It is important that the R value is very close to the value of R + ΔR that will be generated during the fit (within a few tenths of an angstrom), otherwise the calculated potential will not be accurate. If large ΔR values are generated as best-fit values, then it is necessary to create a new pathway at a more appropriate distance to use instead.

If a theoretical crystal structure exists that should be close to the expected structure for a sample, a more appropriate way to generate pathways is to either import a CIF file (generally these exist for the case of molecular crystal structures) or create pathways from a list of atomic coordinates using the ATOMS program[160] that is also included in the Demeter package and is downloaded with the rest of the software. Once opened, the ATOMS program main page appears as in Figure B.14.

For the case of fitting an Au foil, using an ATOMS-generated set of pathways is the appropriate route to take, since an FCC crystal structure for Au is expected. To generate these pathways, several inputs are required. The absorbing element and relevant absorption edge must

be specified, in addition to the space group for the structure. For the case of FCC Au, which has a space group of $Fm\bar{3}m$, this can be input into ATOMS as Fm-3m. This space group is then used to generate pathways when the atomic coordinates of the basis are identified. Since FCC Au contains only one type of atom, only one site needs to be specified and Au x = 0, y = 0, z = 0 is defined as the core. Polarization or shift vectors may be useful in defining a minimum set of atomic coordinates required to generate all of the atomic coordinates in the structure using the space group for translation, but in this case, these were set to zero. In addition to the space group, the lattice constants and angles need to be defined (in this case, as shown in Figure B.14, since Au has a cubic unit cell, a = b = c = 4.08 Å and $\alpha = \beta = \gamma = 90°$). From these inputs, atomic coordinates will be generated up to a defined cluster size or longest path, whichever corresponds to the shortest path length.

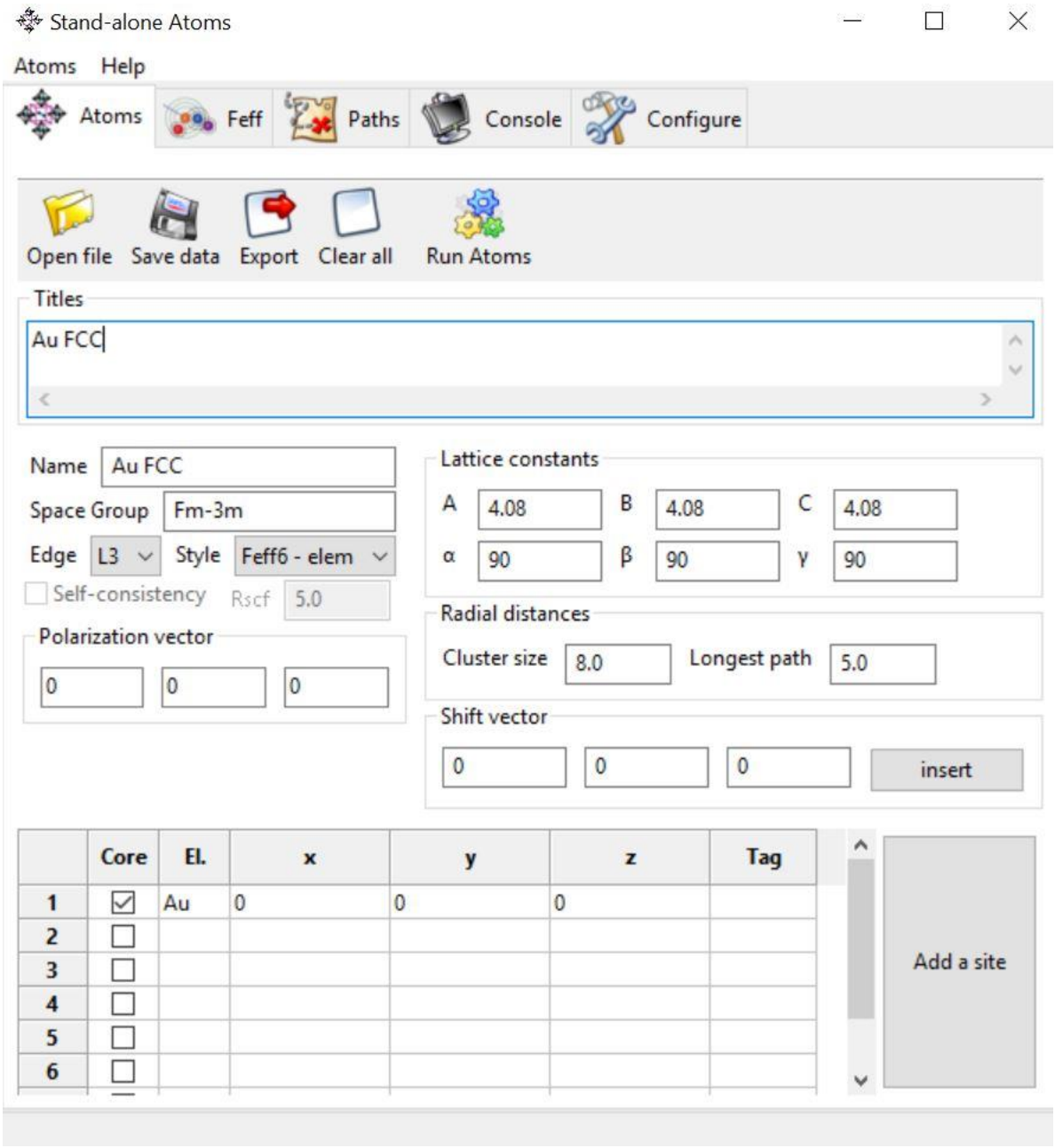

Figure B.14 ATOMS input page with Au FCC input values

After appropriate values are filled on the ATOMS input page, a FEFF calculation is run by pressing the “run atoms” icon and then going to the FEFF tab at the top of the page. The FEFF input file is generated, creating a list of all atomic coordinates within the path length specified. This list for our Au FCC calculation is shown in Figure B.15.

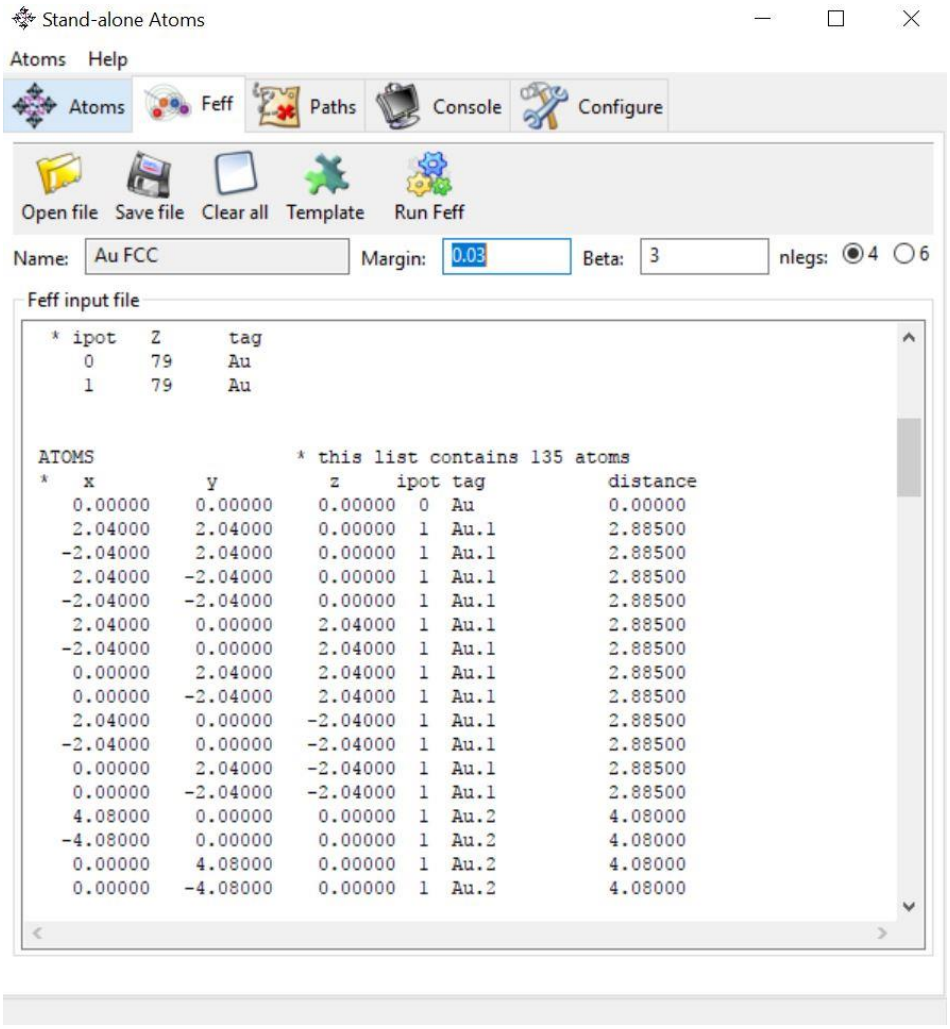

Figure B.15 FEFF input file

From the FEFF input file, the program calculates the scattering pathway distances, types and amplitudes, as shown in the paths tab in Figure B.16.

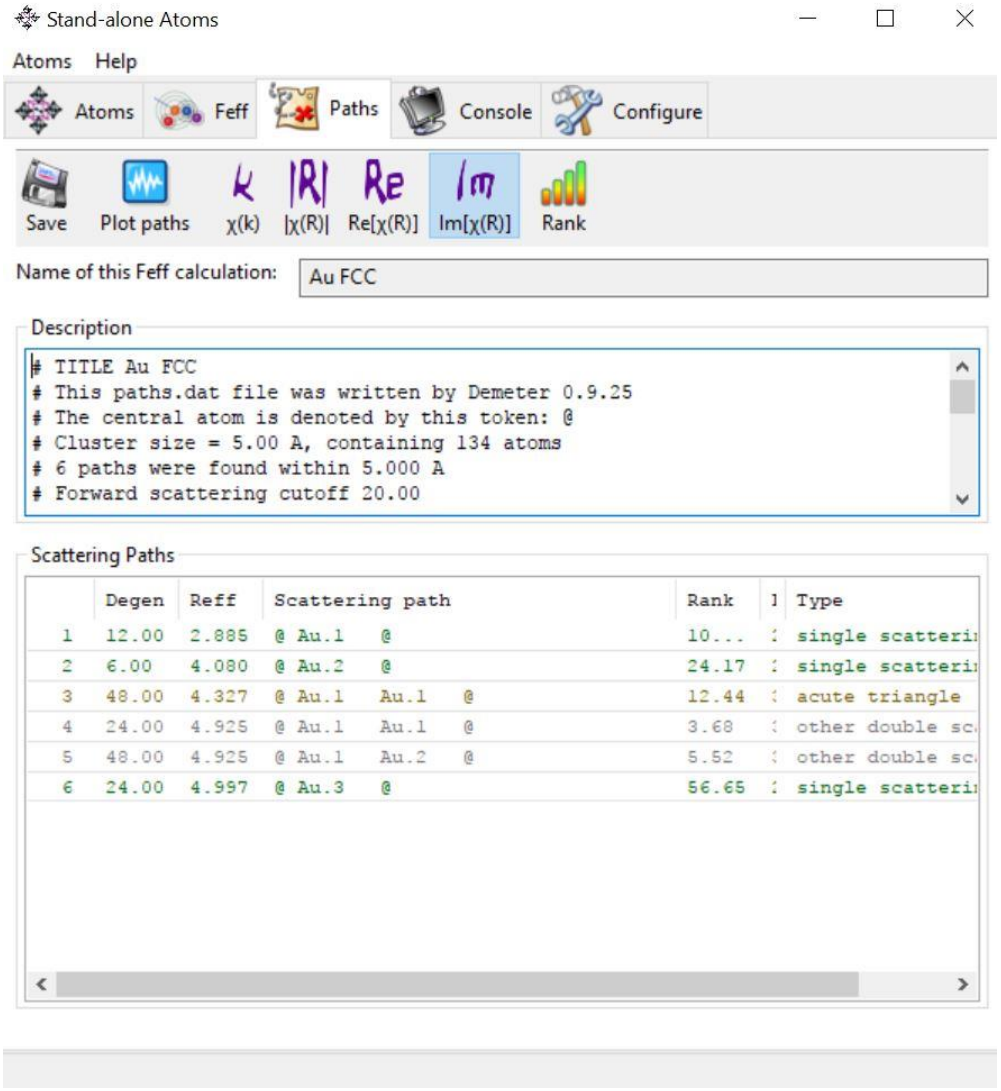

Figure B.16 Atoms-generated scattering pathways

Single scattering pathways (green) and multiple scattering pathways are generated from the FEFF calculation. While single scattering pathways alone can generally fit a structure well due to their dominance (shown in rank as a higher number), however depending on the analysis problem, inclusion of multiple-scattering pathways may be necessary. Once the pathways are generated and the file saved, the calculated pathways can be imported into Artemis using the “import crystal data or a defining file” link.

B.4.2 Defining pathways and variables

When opened in Artemis, all of the pathways generated for a given structure will be imported, and can be viewed in the central panel (see Figure B.17). Pathway properties will be shown on the right pane when a particular pathway is highlighted. The different atomic coordinates are shown, as well as the respective interatomic spacing (Reff) and degeneracy, often referred to as the coordination number (12). The boxes underneath represent variables to be used in the model. One can either put a value to use, or define a variable for each of these parameters. When the box is left empty, then by default Artemis sets the value equal to zero.

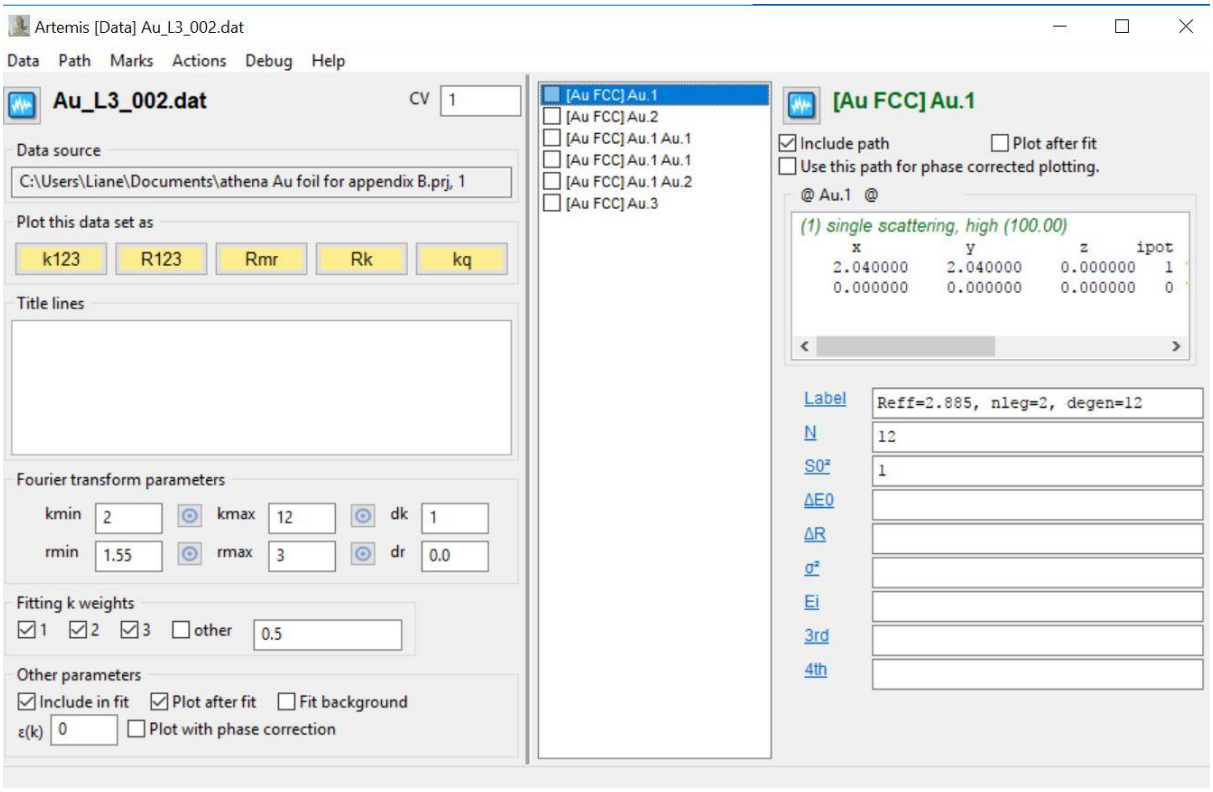

Figure B.17 Au imported pathways and path information

Values for N, the coordination number, $S0^2$, the amplitude reduction factor, ΔE_0, the deviation from the theoretical potential (not to be confused with the position of the absorption edge), ΔR,

the deviation from the pathway interatomic spacing (such that the interatomic distance is equal to Reff + ΔR) and σ^2 (mean-squared disorder) need to be defined with values or variables. E_i (the imaginary deviation in potential), 3rd and 4th (cumulants, representing deviation of the mean-squared disorder from a Gaussian distribution) can in general cases be ignored, and it is therefore fine to leave them set as zero unless there is some physical reason why such approximations might be thought unreasonable.

For the case of a standard, such as an Au foil, the coordination numbers should be the same as bulk and can be fixed at the bulk values. This is how for the systems studied in this thesis, the amplitude reduction factor S_0^2 was calculated, since these parameters were paired. The value of S_0^2 should be the same for each path and should have a value between 0.7 and 1. Thus a variable was defined for S_0^2 to extract that value in this case. For the case of a sample, the value of S_0^2 extracted from a standard is fixed and a variable set for N for each path to extract the coordination number.

The value of E_0 should be the same for pathways from the same scattering atom, therefore one variable should be defined as E_0 for all pathways. Different variables should generally be defined for ΔR and σ^2 for each pathway. However, it should be noted that not all of the variables will be allowed to float during the fitting process. This process will be further described in the following section. Also, since for the case of bulk, multiple-scattering contributions can contribute, yet since in this case the Reff values for these are similar, the same value of ΔR and σ^2 are set for all multiple-scattering pathways. A summary of the defined variables for our Au foil case is shown in Figure B.18. Values for these variables are evaluated using the GDS panel and discussed in the next section.

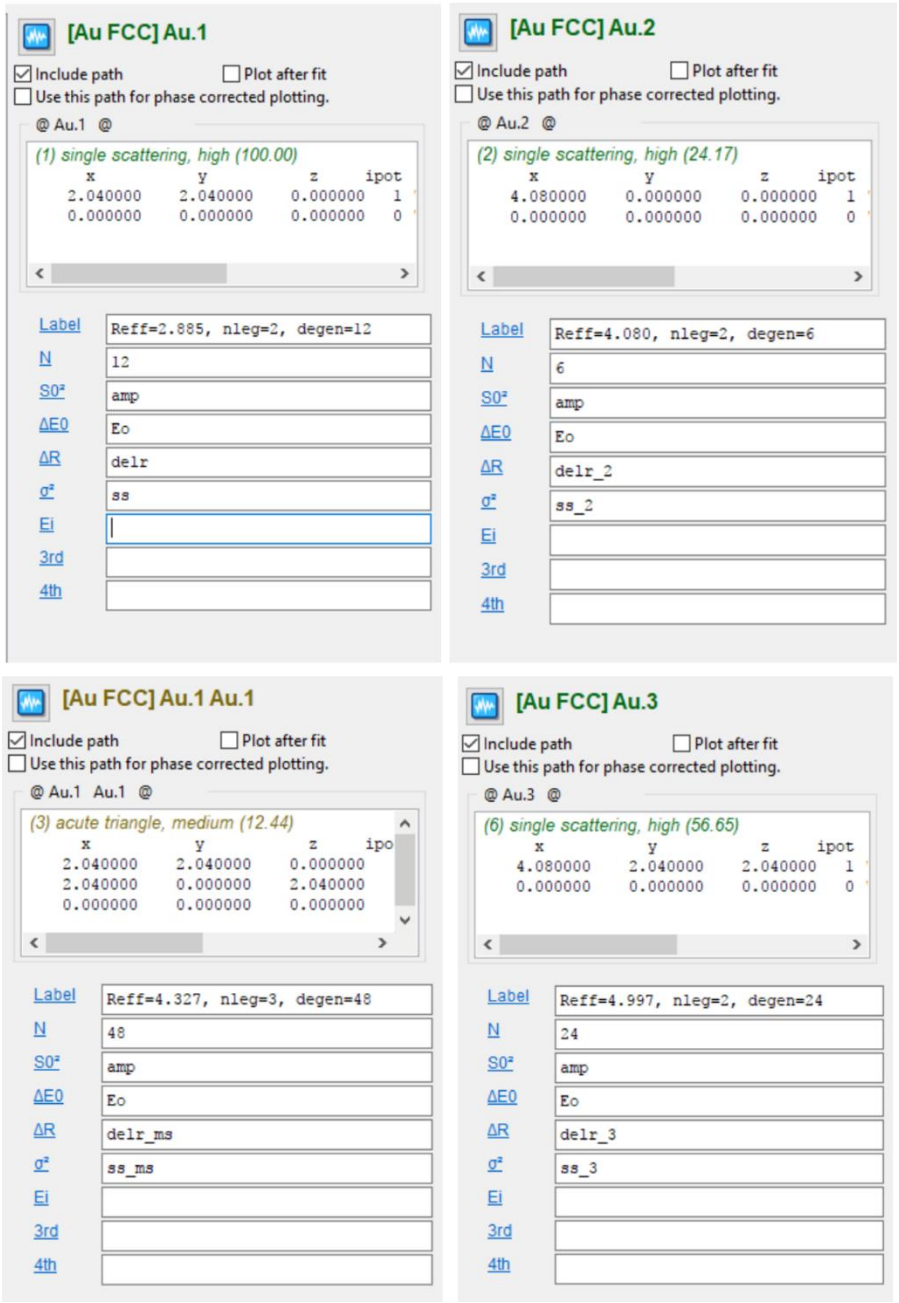

Figure B.18 Defining variables for pathways

B.4.3 Determining variable settings

Once variables are defined for pathways in the Artemis data window, settings and associated variable values are defined using the GDS screen accessible from the fitting window. This screen and defined variables with initial set values are shown in Figure B.19, top. Each variable defined in a pathway should be defined under “name” and given a type and initial value. EXAFS analysis using Artemis is meant to be ab-initio. This means that rather than allowing all of the variables to float, the variables are first optimized based on knowledge of the system as initial values. Several variable types can be used. However, I generally like to use the “set” and “guess” and occasionally the “restrain” types. “Set” variables are not allowed to float during a fit, and rather take on the value of the math expression defined. “Guess” variables are allowed to float during the fit in order to find the value of the variable that results in the best statistical fit. “Restrain” variables are similar to “guess” variables, however acceptable ranges are set such that a penalty is incurred if the variable exceed these ranges.

While there are a variety of ways to approach EXAFS modeling and the reader will eventually find their preferred approach, I will describe how I generally go about starting the modeling process. I first begin with fitting in k-space. Because the k-space spectrum results from pathways across all of R-space, more than just the first shell is used to optimize parameters. In an approach that was suggested to me by Dr. Matt Newville, higher shell pathways are optimized in k-space and then finally when R-space data is fit, only first shell pathways are allowed to float, and the range in R includes only these pathways. This way the higher order shells are used only to inform the first shell information, but are not actually included in the fitting range, therefore minimizing the number of variables used and simultaneously improving their accuracy.

To start fitting in k-space (it is generally a good idea to check boxes to fit with a k-weight of 1, 2 and 3 to try multiple k-weight fitting such that the k-weight selected does not influence the model substantially), I generally start with optimizing set parameters based on values that might be close to those expected as the math expression values. Initial parameters to start I set E_0 and ΔR values to zero, since these values would be expected to be minimal for a known bulk structure, amp (S_0^2) to 1, since this value should be between 0.7 and 1, and σ^2 (ss) values as increasingly larger for longer pathways, given that the radial disorder should increase. As a rule of thumb, for metallic bulk pathways, a mean-squared disorder value of 0.006 to 0.008 presents a good first guess for the first shell, and for ionic bonds, a value of 0.003 tends to be an appropriate first guess for this parameter. Variable values and the associated resulting fit are shown in Figure B.19.

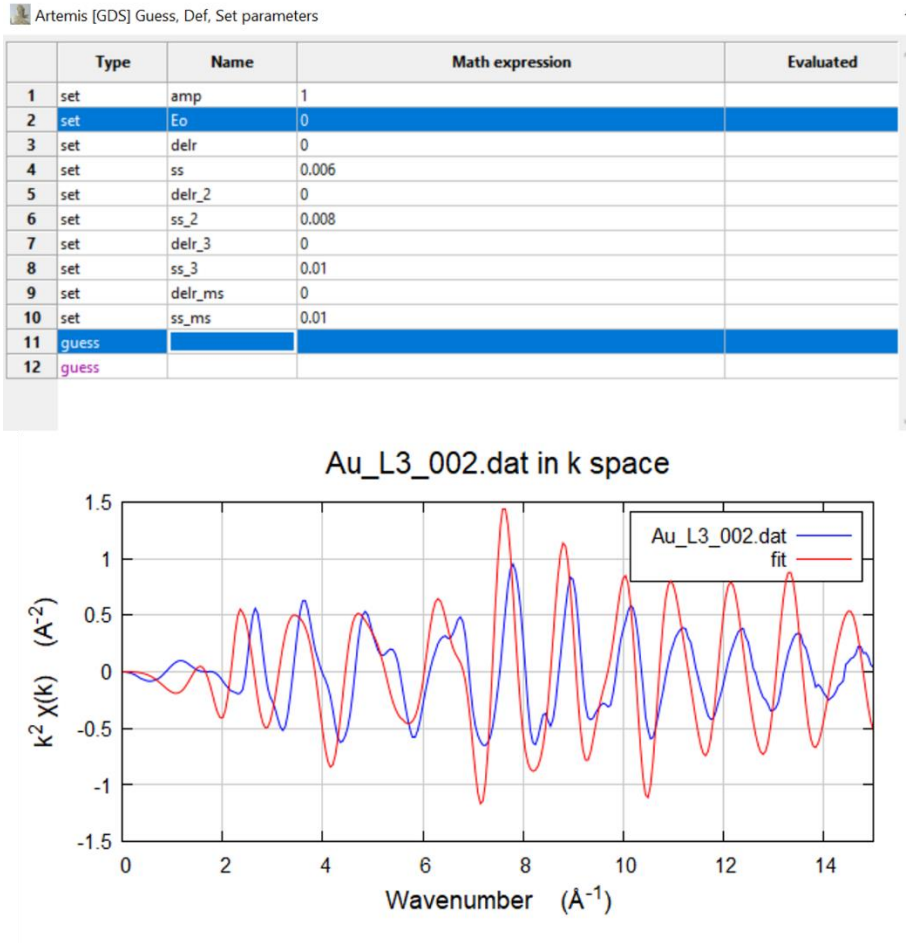

Figure B.19 Initial model using only "set" parameters

The fit was run by clicking "fit" in the fitting panel (Figure B.20). A fit will not be run even in k space if the R-space region specified is smaller than the longest path included in the model. This can be bypassed using the Fit → disable sanity checks option.

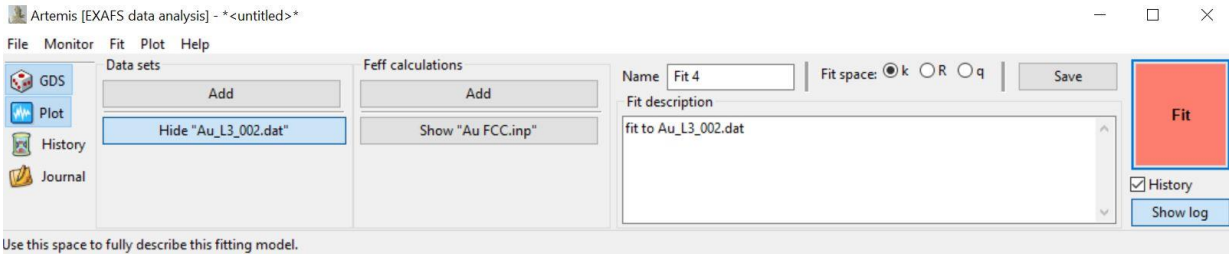

Figure B.20 Artemis fitting panel

After a fit is run, the fitting log (Figure B.21) can be viewed. This includes a sum of the parameters used in the fit, any values obtained from the fit if "guess" values are used. In addition, goodness of fit parameters, including χ^2 and R-factor values are shown. From the values shown for the fit from initial set parameters shown in Figure B.19, the values need to be minimized further, as shown from the values in the fitting log (Figure B.21). It should be noted that the XAFS community tends to use the R-factor value rather than χ^2 to evaluate the goodness of fit, because the χ^2 values are inaccurate due to the underestimate on data error bars. While a value for $\varepsilon(k)$ can be specified to correct this problem, only one value is allowed, whereas in reality, each different point has a different associated error bar. To circumvent this problem, R-factor minimization has generally been considered the standard comparison between data sets.

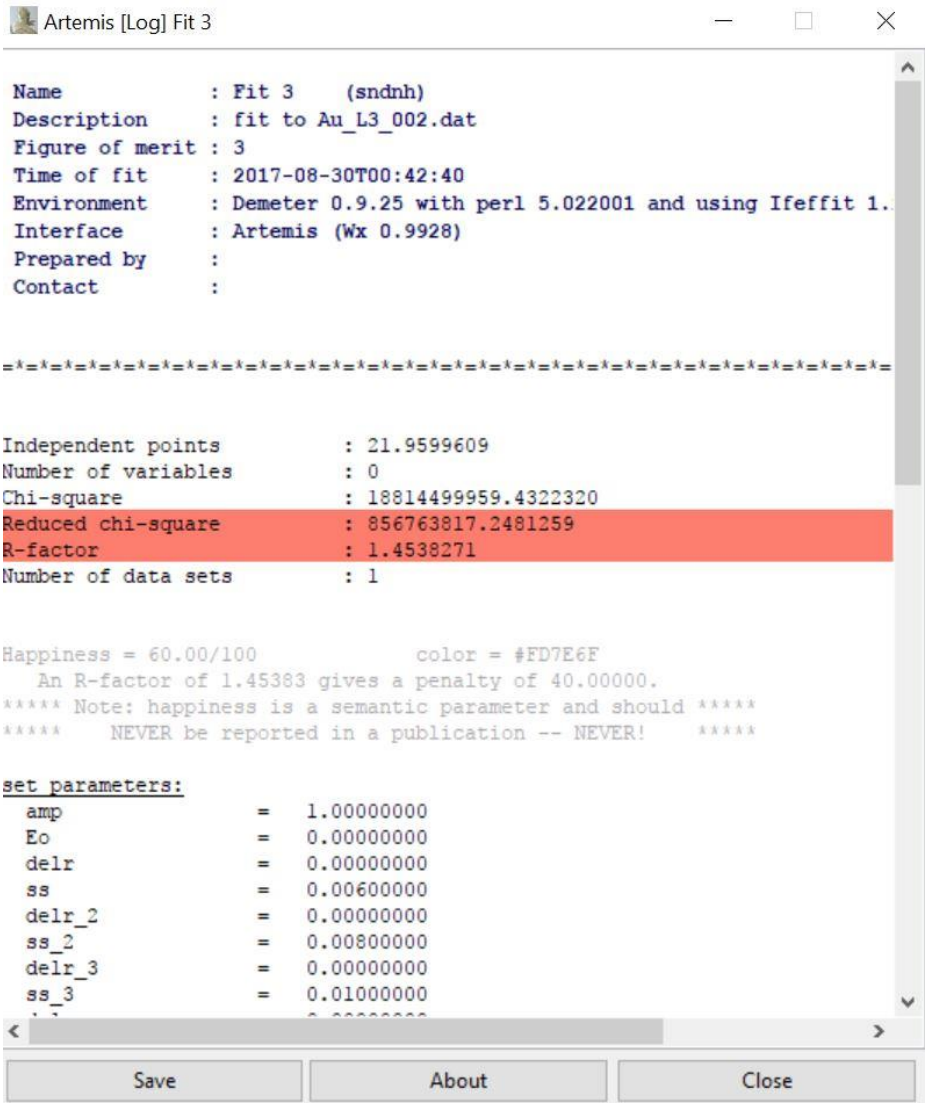

Figure B.21 Artemis fitting log

B.4.4 Fitting model optimization

One can see from the model in Figure B.19 that these initially set parameters capture most of the main oscillatory features in the data, however additional optimization is required. To this end, variables were allowed to float in order to find the best-fit values. Rather than allowing all variables to float at once, which can result in variables taking on un-physical values, one variable was

allowed to float at a time for optimization. For pathways of the same type, an increase in coordination number or $S0^2$ corresponds an increase in oscillation amplitude and a change in ΔR or E_0 corresponds to a difference in the oscillation period. A change in σ^2 also has an effect on the oscillation amplitude, with greater values corresponding to amplitude dampening.

Generally, I begin by allowing E_0 to float. This value should be within -10 to 10 eV and should not be nearly that large for the case of a foil, where calculated potentials should not be too far off. An E_0 value that is very large in magnitude generally suggests that the pathway has not been well defined or that a different distance or chemical species may be more representative. Figure B.22 shows the fitting log after E_0 was allowed to float. The fitting log contains the parameter value extracted from the best fit model and the associated error bar. Error bar calculation will be discussed in a later section.

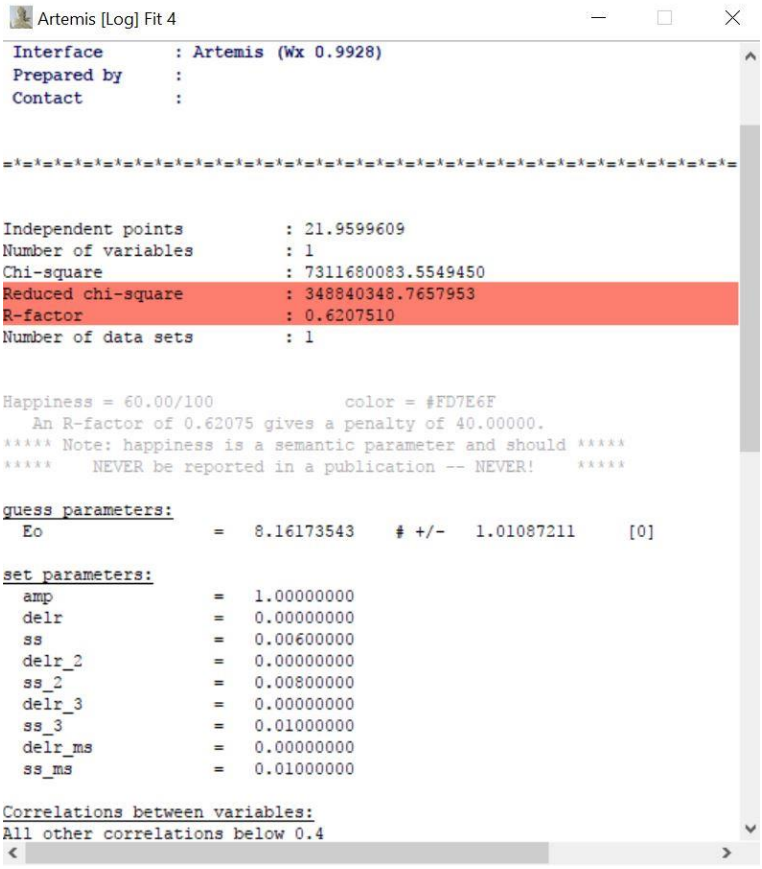

Figure B.22 Guess parameter fitting summary

The value of the E_0 parameter as determined by the best-fit model is a bit larger than would be expected for a standard, likely due to the lack of optimization of the other parameters. Nevertheless, the parameter takes on a larger quantity. Thus, I take the course of action of making the set E_0 value somewhere between 0 and the acquired value (5 eV) and continue optimizing the other parameters.

I next work towards optimizing ΔR values. These should not be very large for a bulk standard. Values should not be expected to exceed a few hundredths of an angstrom. If the best fit value is larger than this, a smaller value is selected with the same sign as the determined value. The amplitude reduction factor (amp variable) is optimized next. If a value less than 0.7 or greater than

1 is obtained, the value is changed within the range towards the lower or upper bound that is closer to the best-fit determined value. σ^2 values are optimized last, and should never be negative. For nanoparticles or amorphous structures, the values tend to be larger than for bulk due to the greater degree of radial disorder. It is also the case that higher shell pathways should have larger values for this parameter than first shell pathways. If not, this proves unphysical. After each of these parameters goes through one iteration of this process, this process is continued until a physical and well-fitting model is achieved. An optimized k-space model and associated parameters are shown in Figure B.23. Note that the parameters are physical according to the previously described conditions and that deviations of the model from the k-space spectrum are mostly with the narrow features, which correspond to larger values of R not included in the model.

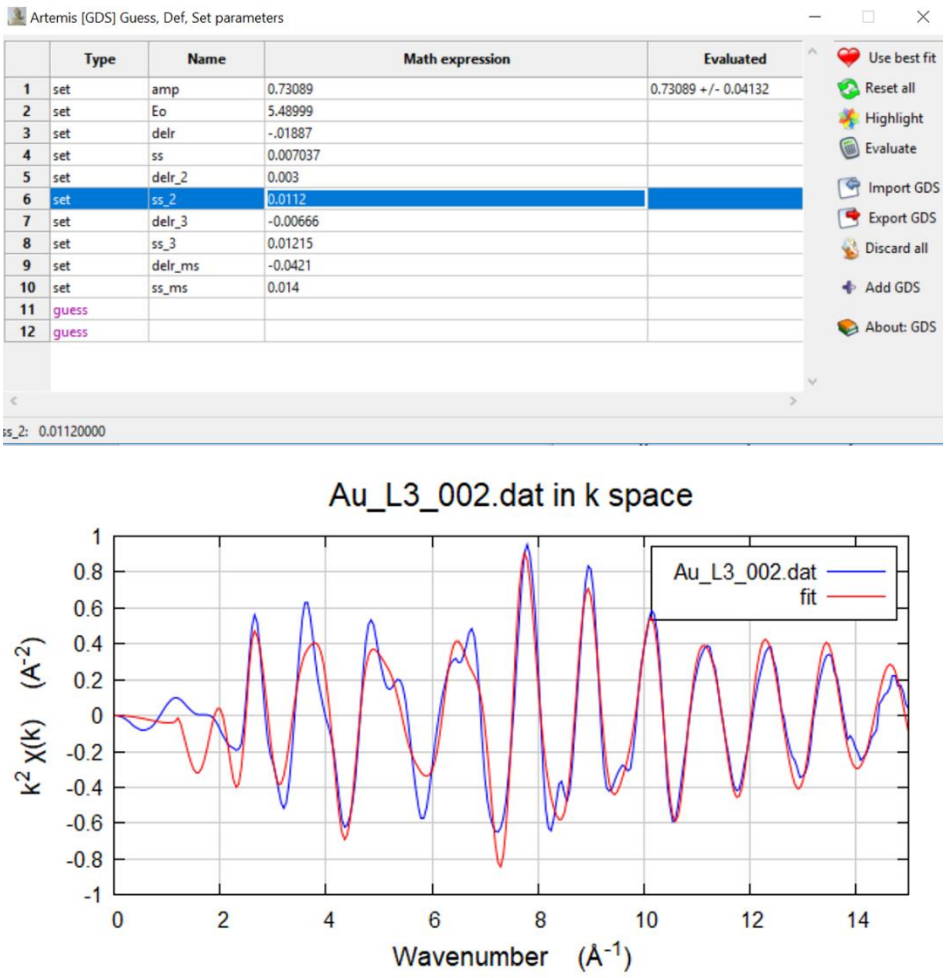

Figure B.23 Model optimized in k-space

Once a reasonable k-space model is obtained, best fit values for first-shell parameters allowing parameters to float can be achieved in R-space, where the higher order shells are kept as set parameters, and the fitting range confined to simply the first shell (1.5 to 3.5 Å presents a reasonable range for the fit, and 2 to 12 $Å^{-1}$ in k-space). When deciding which pathways should be allowed to float, the pathways should be within the fitting range specified and the number of variables should not exceed the number of independent points (this is very important and the number of independent points can be found in the fitting log for quick reference. In this case, the number of variables was 4 and the number of independent points 12.6 for the fitting ranges

specified). Following this procedure, we see that once physical values have been converged upon for the guess parameters, the values determined by the fit are physically reasonable. Generally, I have found that while there are many possibilities that will provide a good statistical fit to the data, there really is only one in most instances that is a good statistical fit and is within the realm of physical reasonability. It is this factor that has most greatly convinced me of the reliability of this method of quantitative analysis.

Parameters from the best fit model and the fitting model and raw data are shown in Figure B.24. Error bars and evaluated best-fit parameters are shown in the “evaluated” box. The error bars are reasonable. If the model is not appropriate, often this can be indicated by larger error bar values, due in part to the high degree of correlation between error bars, since the calculated error bars take into account the correlation matrix. The plot at the bottom of Figure B.24 shows that the fit well matches the experimental data.

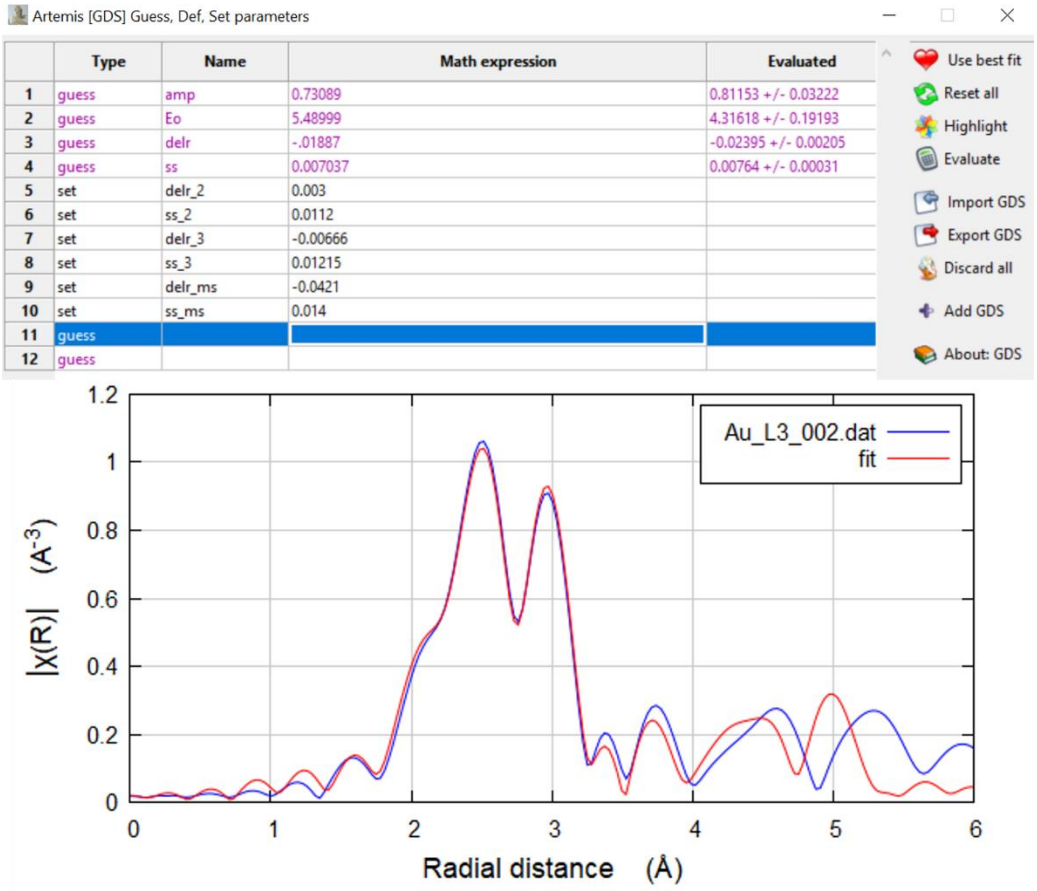

	Type	Name	Math expression	Evaluated
1	guess	amp	0.73089	0.81153 +/- 0.03222
2	guess	Eo	5.48999	4.31618 +/- 0.19193
3	guess	delr	-.01887	-0.02395 +/- 0.00205
4	guess	ss	0.007037	0.00764 +/- 0.00031
5	set	delr_2	0.003	
6	set	ss_2	0.0112	
7	set	delr_3	-0.00666	
8	set	ss_3	0.01215	
9	set	delr_ms	-0.0421	
10	set	ss_ms	0.014	
11	guess			
12	guess			

Figure B.24 Best-fit model in R-space

The fitting log (Figure B.25) also shows the values of the best-fit parameter, as well as the associated goodness-of fit parameters. As a rule of thumb, a fit is considered good with R factor values of 0.05 or less, which is observed here. If going on to fit sample data, the amp value extracted for S_0^2 can be applied for a more accurate determination of the coordination numbers.

```
Independent points          : 12.6318359
Number of variables         : 4
Chi-square                  : 8295.0583464
Reduced chi-square          : 960.9842456
R-factor                    : 0.0037876
Number of data sets         : 1


Happiness = 100.00/100              color = #D8E796
***** Note: happiness is a semantic parameter and should *****
*****    NEVER be reported in a publication -- NEVER!    *****

guess parameters:
  amp               =   0.81153445    # +/-   0.03222366     [0.73089]
  Eo                =   4.31617727    # +/-   0.19193403     [5.48999]
  delr              =  -0.02394592    # +/-   0.00205032     [-.01887]
  ss                =   0.00763605    # +/-   0.00031316     [0.007037]

set parameters:
  delr_2            =   0.00300000
  ss_2              =   0.01120000
  delr_3            =  -0.00666000
  ss_3              =   0.01215000
  delr_ms           =  -0.04210000
  ss_ms             =   0.01400000

Correlations between variables:
                ss & amp                --> 0.8226
              delr & eo                 --> 0.6237
All other correlations below 0.4
```

Figure B.25 Best-fit model fitting log

B.4.5 Exporting data and associated fitting model

Data and fitting models can be exported from Artemis for plotting in a different software, similar to data exporting in Athena. From the data page, both the experimental data and associated fit can be saved under "Data" → "Save data + fit" option. It is also possible to save the data and individual pathways. This can sometimes be a good way to compare from sample to sample as well. I previously used this strategy in a publication to show how different pathways were evolving as a function of reaction time.[99] One caveat to exporting the data in Artemis is that by default, depending on the absorbing atom, data is automatically exported with a k-weight determined by the program. For example, for the case of Au, data is automatically exported with a k-weight of 3,

even if plotting preferences specify a different k-weight. Thus, if plotting with a k-weight of 2 is desired, the data and fit values in the exported file will need to be divided by k.

B.4.6 Error analysis in Artemis

It was already discussed that the EXAFS community tends to use minimization of the R-factor as an indication of a good statistical fit of the model to experimental data and why χ^2 is not standardly used. As far as error bars on individual parameters are concerned, for this purpose χ^2 for the fit is assumed to be approximately 1. I have found that if an $\varepsilon(k)$ value is provided that is representative of the average error bar magnitude on the experimental EXAFS oscillations, that this assumption is reasonable, since the reduced χ^2 value turns out to be close to 1 for good fitting models. From this, the error bar reported for an individual parameter is determined as the amount the parameter needs to be changed to increase the χ^2 value by 1 (or a confidence interval of 1σ, or 68 %). While in reality this would result in both positive and negative error bars of differing magnitude, only one average value is reported. For most systems, the error in the coordination number or mean-squared disorder is generally on the order of 10 % and 5 % for E_0 and ΔR.

B.5 Conclusion and Outlook

This brief description and advice concerning using Athena and Artemis in the XAFS analysis process provides a starting point towards approaching XAFS analysis problems. Obviously, there are many additional topics that could be discussed that are beyond the scope of this tutorial and will require further reading. However, the process of modeling a standard, navigating the software and estimating reasonable parameters should be more clearly defined. Keep in mind that there are

a variety of software and methods used for analysis, however the general procedures and physical considerations of parameters are the same and should always be the primary consideration in evaluating models developed by the reader and those presented in literature. Hopefully this peek into the world of XAFS analysis has inspired the reader to more confidence and a critical eye in designing XAFS experiments around proper analysis considerations.

REFERENCES

1. National Research, Council.; Committee on Materials Science.; Engineering: Forging Stronger Links to Users., **1999**.

2. Lu, W.; Lieber, C. M., *Nat. Mater.* **2007,** *6,* 841-850.

3. Biswas, A.; Bayer, I. S.; Biris, A. S.; Wang, T.; Dervishi, E.; Faupel, F., *Adv. Colloid Interface Sci.* **2012,** *170,* 2-27.

4. Moore, G. E., *Electronics* **1965,** *38,* 114-117.

5. Kelly, K. L.; Coronado, E.; Zhao, L. L.; Schatz, G. C., *J. Phys. Chem. B* **2002,** *107,* 668-677.

6. Tian, N.; Zhou, Z.-Y.; Sun, S.-G.; Ding, Y.; Wang, Z. L., *Science* **2007,** *316,* 732-735.

7. Shipway, A. N.; Katz, E.; Willner, I., *ChemPhysChem* **2000,** *1,* 18-52.

8. E Sapsford, K.; Russ Algar, W.; Berti, L.; Boeneman, K.; Casey, B.; Oh, E.; H Stewart, M.; L Medintz, I., *Functionalizing Nanoparticles with Biological Molecules: Developing Chemistries that Facilitate Nanotechnology*. 2013; Vol. 113.

9. Mirkin, C. A.; Letsinger, R. L.; Mucic, R. C.; Storhoff, J. J., *Nature* **1996,** *382,* 607-609.

10. Kreuter, J., *Adv. Drug Delivery Rev.* **2001,** *47,* 65-81.

11. Jones, M. R.; Osberg, K. D.; Macfarlane, R. J.; Langille, M. R.; Mirkin, C. A., *Chem. Rev.* **2011,** *111,* 3736-3827.

12. Link, S.; El-Sayed, M. A., *J. Phys. Chem. B* **1999,** *103,* 8410-8426.

13. Murphy, C. J.; Thompson, L. B.; Alkilany, A. M.; Sisco, P. N.; Boulos, S. P.; Sivapalan, S. T.; Yang, J. A.; Chernak, D. J.; Huang, J., *J. Phys. Chem. Lett.* **2010,** *1,* 2867-2875.

14. Liz-Marzán, L. M.; Grzelczak, M., *Science* **2017,** *356,* 1120-1121.

15. Yin, Y.; Rioux, R. M.; Erdonmez, C. K.; Hughes, S.; Somorjai, G. A.; Alivisatos, A. P., *Science* **2004,** *304,* 711.

16. Sun, Y.; Xia, Y., *J. Am. Chem. Soc.* **2004,** *126,* 3892-3901.

17. Son, D. H.; Hughes, S. M.; Yin, Y.; Paul Alivisatos, A., *Science* **2004,** *306,* 1009-1012.

18. Tang, Z.; Kotov, N. A.; Giersig, M., *Science* **2002,** *297,* 237-240.

19. Walsh, M. J.; Barrow, S. J.; Tong, W.; Funston, A. M.; Etheridge, J., *ACS Nano* **2015,** *9,* 715-724.

20. Parker, J. F.; Kacprzak, K. A.; Lopez-Acevedo, O.; Häkkinen, H.; Murray, R. W., *J. Phys. Chem. C* **2010,** *114,* 8276-8281.

21. Hong, R.; Fischer, N. O.; Verma, A.; Goodman, C. M.; Emrick, T.; Rotello, V. M., *J. Am. Chem. Soc.* **2004,** *126,* 739-743.

22. Woehrle, G. H.; Hutchison, J. E., *Inorg. Chem.* **2005,** *44,* 6149-6158.

23. Chen, L. X.; Liu, T.; Thurnauer, M. C.; Csencsits, R.; Rajh, T., *J. Phys. Chem. B* **2002,** *106,* 8539-8546.

24. Zhang, P.; Sham, T. K., *Appl. Phys. Lett.* **2002,** *81,* 736-738.

25. Hurst, S. J.; Lytton-Jean, A. K. R.; Mirkin, C. A., *Anal. Chem.* **2006,** *78,* 8313-8318.

26. Jackson, A. M.; Hu, Y.; Silva, P. J.; Stellacci, F., *J. Am. Chem. Soc.* **2006,** *128,* 11135-11149.

27. Walter, M.; Akola, J.; Lopez-Acevedo, O.; Jadzinsky, P. D.; Calero, G.; Ackerson, C. J.; Whetten, R. L.; Grönbeck, H.; Häkkinen, H., *Proc. Natl. Academy Sci.* **2008,** *105,* 9157-9162.

28. Bunker, G., *Introduction to XAFS: a practical guide to X-ray absorption fine structure spectroscopy*. Cambridge University Press: Cambridge, 2010; p 260.

29. Yadong, Y.; Alivisatos, A. P., *Nature* **2005,** *437,* 664.

30. Thanh, N. T. K.; Maclean, N.; Mahiddine, S., *Chem. Rev.* **2014,** *114,* 7610-7630.

31. Kwon, S. G.; Hyeon, T., *Small* **2011,** *7,* 2685-2702.

32. Kimling, J.; Maier, M.; Okenve, B.; Kotaidis, V.; Ballot, H.; Plech, A., *J. Phys. Chem. B* **2006,** *110,* 15700-15707.

33. Wang, Y.; Zheng, Y.; Huang, C. Z.; Xia, Y., *J. Am. Chem. Soc.* **2013,** *135,* 1941-1951.

34. Jana, N. R.; Gearheart, L.; Murphy, C. J., *Adv. Mater.* **2001,** *13,* 1389-1393.

35. Nikoobakht, B.; El-Sayed, M. A., *Chem. Mater.* **2003,** *15,* 1957-1962.

36. Langille, M. R.; Personick, M. L.; Zhang, J.; Mirkin, C. A., *J. Am. Chem. Soc.* **2012,** *134,* 14542-14554.

37. Yacamán, M. J.; Ascencio, J. A.; Liu, H. B.; Gardea-Torresdey, J., *J. Vac. Sci. Technol. B* **2001,** *19,* 1091-1103.

38. Personick, M. L.; Langille, M. R.; Zhang, J.; Mirkin, C. A., *Nano Lett.* **2011,** *11,* 3394-3398.

39. Sun, Y.; Xia, Y., *Science* **2002,** *298,* 2176-2179.

40. Millstone, J. E.; Wei, W.; Jones, M. R.; Yoo, H.; Mirkin, C. A., *Nano Lett.* **2008,** *8,* 2526-2529.

41. Ghosh, S.; Nath, S.; Kundu, S.; Esumi, K.; Pal, T., *Solvent and Ligand Effects on the Localized Surface Plasmon Resonance (LSPR) of Gold Colloids*. 2004; Vol. 108.

42. Polte, J.; Ahner, T. T.; Delissen, F.; Sokolov, S.; Emmerling, F.; Thünemann, A. F.; Kraehnert, R., *J. Am. Chem. Soc.* **2010,** *132,* 1296-1301.

43. Als-Nielsen, J.; McMorrow, D., *Elements of modern X-ray physics*. Wiley: Hoboken, 2011.

44. Fabricius, A.-L.; Duester, L.; Meermann, B.; Ternes, T. A., *Anal. and Bioanal. Chem.* **2014,** *406,* 467-479.

45. Thompson, A. C.; Vaughan, D.; for, X. r. o.; advanced light source, C., *X-ray Data Booklet*. 2000.

46. Puri, S.; Chand, B.; Mehta, D.; Garg, M. L.; Singh, N.; Trehan, P. N., *Atomic Data and Nuclear Data Tables* **1995,** *61,* 289-311.

47. Scott, R., *Physical Methods in Bioinorganic Chemistry: Spectroscopy and Magnetism*. University Science Books: 2000.

48. Pfalzer, P.; Urbach, J. P.; Klemm, M.; Horn, S.; denBoer, M. L.; Frenkel, A. I.; Kirkland, J. P., *Phys. Rev. B* **1999,** *60,* 9335-9339.

49. Koningsberger, D. C.; Mojet, B. L.; van Dorssen, G. E.; Ramaker, D. E., *Top. Catal.* **2000,** *10,* 143-155.

50. Stern, E. A., *Contemp. Phys.* **1978,** *19,* 289-310.

51. Stern, E. A., *Phys. Rev. B* **1974,** *10,* 3027-37.

52. Ravel, B.; Kelly, S. D., *AIP Conf. Proc.* **2007,** *882,* 150-152.

53. Pérez-Juste, J.; Pastoriza-Santos, I.; Liz-Marzán, L. M.; Mulvaney, P., *Coord. Chem. Rev.* **2005,** *249,* 1870-1901.

54. Mohl, M.; Kumar, A.; Reddy, A. L. M.; Kukovecz, A.; Konya, Z.; Kiricsi, I.; Vajtai, R.; Ajayan, P. M., *J. Phys. Chem. C* **2010,** *114,* 389-393.

55. Moon, G. D.; Choi, S.-W.; Cai, X.; Li, W.; Cho, E. C.; Jeong, U.; Wang, L. V.; Xia, Y., *J. Am. Chem. Soc.* **2011,** *133,* 4762-4765.

56. Yavuz, M. S.; Yiyun, C.; Jingyi, C.; Cobley, C. M.; Qiang, Z.; Rycenga, M.; Jingwei, X.; Chulhong, K.; Song, K. H.; Schwartz, A. G.; Wang, L. V.; Xia, Y., *Nat. Mater.* **2009,** *8,* 935-939.

57. Cho, E. C.; Kim, C.; Zhou, F.; Cobley, C. M.; Song, K. H.; Chen, J.; Li, Z.-Y.; Wang, L. V.; Xia, Y., *J. Phys. Chem. C.* **2009,** *113,* 9023-9028.

58. Ma, Y.; Li, W.; Cho, E. C.; Li, Z.; Yu, T.; Zeng, J.; Xie, Z.; Xia, Y., *ACS Nano* **2010,** *4,* 6725-6734.

59. Skrabalak, S. E.; Chen, J.; Au, L.; Lu, X.; Li, X.; Xia, Y., *Adv. Mater.* **2007,** *19,* 3177-3184.

60. Toshima, N.; Yonezawa, T., *New J. Chem.* **1998,** *22,* 1179-1201.

61. Lim, B.; Jiang, M.; Camargo, P. H. C.; Cho, E. C.; Tao, J.; Lu, X.; Zhu, Y.; Xia, Y., *Science* **2009,** *324,* 1302-1305.

62. Wang, D.; Li, Y., *Adv. Mater.* **2011,** *23,* 1044-1060.

63. DeSantis, C. J.; Weiner, R. G.; Radmilovic, A.; Bower, M. M.; Skrabalak, S. E., *J. Phys. Chem. Lett.* **2013,** *4,* 3072-3082.

64. Chen, J.; McLellan, J. M.; Siekkinen, A.; Xiong, Y.; Li, Z.-Y.; Xia, Y., *J. Am. Chem. Soc.* **2006,** *128,* 14776-14777.

65. Skrabalak, S. E.; Au, L.; Li, X.; Xia, Y., *Nat. Protoc.* **2007,** *2,* 2182-90.

66. Oh, M. H.; Yu, T.; Yu, S.-H.; Lim, B.; Ko, K.-T.; Willinger, M.-G.; Seo, D.-H.; Kim, B. H.; Cho, M. G.; Park, J.-H.; Kang, K.; Sung, Y.-E.; Pinna, N.; Hyeon, T., *Science* **2013,** *340,* 964-968.

67. Niu, K.-Y.; Kulinich, S. A.; Yang, J.; Zhu, A. L.; Du, X.-W., *Chem. Eur. J.* **2012,** *18,* 4234-4241.

68. Sun, Y.; Xia, Y., *Anal. Chem.* **2002,** *74,* 5297-5305.

69. Rosi, N. L.; Mirkin, C. A., *Chem. Rev.* **2005,** *105,* 1547-1562.

70. Au, L.; Zheng, D.; Zhou, F.; Li, Z.-Y.; Li, X.; Xia, Y., *ACS Nano* **2008,** *2,* 1645-1652.

71. Mahmoud, M. A.; El-Sayed, M. A., *J. Am. Chem. Soc.* **2010,** *132,* 12704-12710.

72. Novo, C.; Funston, A. M.; Mulvaney, P., *Nat. Nano.* **2008,** *3,* 598-602.

73. Xu, W.; Kong, J. S.; Yeh, Y.-T. E.; Chen, P., *Nat. Mater.* **2008,** *7,* 992-996.

74. Wittstock, A.; Zielasek, V.; Biener, J.; Friend, C. M.; Baumer, M., *Science* **2010,** *327,* 319-22.

75. Calver, C. F.; Dash, P.; Scott, R. W. J., *Chemcatchem* **2011,** *3,* 695-697.

76. Song, G. L.; Atrens, A., *Adv. Eng. Mater.* **1999,** *1,* 11-33.

77. Gonzalez, E.; Arbiol, J.; Puntes, V. F., *Science* **2011,** *334,* 1377-1380.

78. Bi, Y.; Hu, H.; Lu, G., *Chem. Commun.* **2010,** *46,* 598-600.

79. Sun, Y.; Mayers, B.; Xia, Y., *Adv. Mater.* **2003,** *15,* 641-646.

80. Zhang, Y.; Sun, S.; Zhang, X.; Tang, L.; Song, X.; Yang, Z., *Phys. Chem. Chem. Phys.* **2014,** *16,* 18918-25.

81. Métraux, G. S.; Cao, Y. C.; Jin, R.; Mirkin, C. A., *Nano Lett.* **2003,** *3,* 519-522.

82. Personick, M. L.; Langille, M. R.; Wu, J.; Mirkin, C. A., *J. Am. Chem. Soc.* **2013,** *135,* 3800-3803.

83. Jang, H.; Min, D.-H., *ACS Nano* **2015,** *9,* 2696-2703.

84. Bi, Y.; Ye, J., *Chem. Commun.* **2010,** *46,* 1532-4.

85. Chen, J.; Wiley, B.; McLellan, J.; Xiong, Y.; Li, Z.-Y.; Xia, Y., *Nano Lett.* **2005,** *5,* 2058-2062.

86. Jiang, Z.; Zhang, Q.; Zong, C.; Liu, B.-J.; Ren, B.; Xie, Z.; Zheng, L., *J. Mater. Chem.* **2012,** *22,* 18192-18197.

87. Xu, C.; Liu, Y.; Wang, J.; Geng, H.; Qiu, H., *ACS Appl. Mater. Interfaces* **2011,** *3,* 4626-4632.

88. Sarkar, A.; Manthiram, A., *J. Phys. Chem. C* **2010,** *114,* 4725-4732.

89. Schwartzberg, A. M.; Olson, T. Y.; Talley, C. E.; Zhang, J. Z., *J. Phys. Chem. B* **2006,** *110,* 19935-19944.

90. Stamenkovic, V. R.; Mun, B. S.; Arenz, M.; Mayrhofer, K. J. J.; Lucas, C. A.; Wang, G.; Ross, P. N.; Markovic, N. M., *Nat. Mater.* **2007,** *6,* 241-247.

91. Erlebacher, J.; Aziz, M. J.; Karma, A.; Dimitrov, N.; Sieradzki, K., *Nature* **2001,** *410,* 450.

92. Kim, M. H.; Lu, X.; Wiley, B.; Lee, E. P.; Xia, Y., *J. Phys. Chem. C* **2008,** *112,* 7872-7876.

93. Cobley, C. M.; Xia, Y., *Mater. Sci. Eng. R* **2010,** *70,* 44-62.

94. Yin, Y.; Erdonmez, C.; Aloni, S.; Alivisatos, A. P., *J. Am. Chem. Soc.* **2006,** *128,* 12671-12673.

95. Choi, Y.; Hong, S.; Liu, L.; Kim, S. K.; Park, S., *Langmuir* **2012,** *28,* 6670-6676.

96. Smigelskas, A. D. K., O., *Trans. AIME* **1947,** *171,* 130.

97. Au, L.; Lu, X.; Xia, Y., *Adv. Mater.* **2008,** *20,* 2517-2522.

98. Fan, H. J.; Gösele, U.; Zacharias, M., *Small* **2007,** *3,* 1660-1671.

99. Ha, D.-H.; Moreau, L. M.; Bealing, C. R.; Zhang, H.; Hennig, R. G.; Robinson, R. D., *J. Mater. Chem.* **2011,** *21,* 11498-11510.

100. Ha, D.-H.; Moreau, L. M.; Honrao, S.; Hennig, R. G.; Robinson, R. D., *J. Phys. Chem. C* **2013,** *117,* 14303-14312.

101. Anderson, B. D.; Tracy, J. B., *Nanoscale* **2014,** *6,* 12195-12216.

102. Xia, X.; Xia, Y., *Front. Phys.* **2014,** *9,* 378-384.

103. Snyder, J.; Livi, K.; Erlebacher, J., *J. Electrochem. Soc.* **2008,** *155,* C464-C473.

104. Goris, B.; Polavarapu, L.; Bals, S.; Van Tendeloo, G.; Liz-Marzan, L. M., *Nano Lett.* **2014,** *14,* 3220-6.

105. Smith, J. G.; Yang, Q.; Jain, P. K., *Angew. Chem. Int. Ed.* **2014,** *53,* 2867-2872.

106. Li, H.; Xia, H.; Wang, D.; Tao, X., *Langmuir* **2013,** *29,* 5074-5079.

107. Pinkhasova, P.; Yang, L.; Zhang, Y.; Sukhishvili, S.; Du, H., *Langmuir* **2012,** *28,* 2529-2535.

108. Petri, M. V.; Ando, R. A.; Camargo, P. H. C., *Chemical Physics Letters* **2012,** *531,* 188-192.

109. Prevo, B. G.; Esakoff, S. A.; Mikhailovsky, A.; Zasadzinski, J. A., *Small* **2008,** *4,* 1183-1195.

110. Knecht, M. R.; Weir, M. G.; Frenkel, A. I.; Crooks, R. M., *Chem. Mater.* **2008,** *20,* 1019-1028.

111. Shibata, T.; Bunker, B. A.; Zhang, Z.; Meisel, D.; Vardeman, C. F.; Gezelter, J. D., *J. Am. Chem. Soc.* **2002,** *124,* 11989-11996.

112. Mikhlin, Y.; Karacharov, A.; Likhatski, M.; Podlipskaya, T.; Zubavichus, Y.; Veligzhanin, A.; Zaikovski, V., *J. Colloid Interface Sci.* **2011,** *362,* 330-336.

113. Skrabalak, S. E.; Au, L.; Li, X.; Xia, Y., *Nat. Protocols* **2007,** *2,* 2182-2190.

114. Guinier, A.; Fournet, G., *Small-Angle Scattering of X-Rays*. John Wiley and Sons: New York, 1955.

115. Als-Nielsen, J. M., D., *Elements of Modern X-Ray Physics*. 2 ed.; John Wiley: Chichester, U.K., 2011.

116. Ravel, B.; Newville, M., *J. Synchrotron Radiat.* **2005,** *12,* 537-541.

117. Lu, X.; Tuan, H.-Y.; Chen, J.; Li, Z.-Y.; Korgel, B. A.; Xia, Y., *J. Am. Chem. Soc.* **2007,** *129,* 1733-1742.

118. Calvin, S.; Miller, M. M.; Goswami, R.; Cheng, S.-F.; Mulvaney, S. P.; Whitman, L. J.; Harris, V. G., *J. Appl. Phys.* **2003,** *94,* 778-783.

119. Xia, H.; Bai, S.; Hartmann, J.; Wang, D., *Langmuir* **2010,** *26,* 3585-3589.

120. Murshid, N.; Gourevich, I.; Coombs, N.; Kitaev, V., *Chem. Commun.* **2013,** *49,* 11355-11357.

121. Jang, G. G.; Hawkridge, M. E.; Roper, D. K., *J. Mater. Chem.* **2012,** *22,* 21942-21953.

122. Yang, Y.; Liu, J.; Fu, Z.-W.; Qin, D., *J. Am. Chem. Soc.* **2014,** *136,* 8153-8156.

123. Polavarapu, L.; Zanaga, D.; Altantzis, T.; Rodal-Cedeira, S.; Pastoriza-Santos, I.; Pérez-Juste, J.; Bals, S.; Liz-Marzán, L. M., *J. Am. Chem. Soc.* **2016,** *138,* 11453-11456.

124. Tyson, W. R.; Miller, W. A., *Surf. Sci.* **1977,** *62,* 267-276.

125. Wang, A.-Q.; Liu, J.-H.; Lin, S. D.; Lin, T.-S.; Mou, C.-Y., *J. Catal.* **2005,** *233,* 186-197.

126. Young, K. L.; Ross, M. B.; Blaber, M. G.; Rycenga, M.; Jones, M. R.; Zhang, C.; Senesi, A. J.; Lee, B.; Schatz, G. C.; Mirkin, C. A., *Adv. Mater.* **2014,** *26,* 653-659.

127. Ross, M. B.; Ku, J. C.; Lee, B.; Mirkin, C. A.; Schatz, G. C., *Adv. Mater.* **2016,** *28,* 2790-2794.

128. Auyeung, E.; Li, T. I. N. G.; Senesi, A. J.; Schmucker, A. L.; Pals, B. C.; de la Cruz, M. O.; Mirkin, C. A., *Nature* **2014,** *505,* 73-77.

129. Giljohann, D. A.; Seferos, D. S.; Prigodich, A. E.; Patel, P. C.; Mirkin, C. A., *J. Am. Chem. Soc.* **2009,** *131,* 2072-2073.

130. Millstone, J. E.; Hurst, S. J.; Métraux, G. S.; Cutler, J. I.; Mirkin, C. A., *Small* **2009,** *5,* 646-664.

131. Kim, F.; Song, J. H.; Yang, P., *J. Am. Chem. Soc.* **2002,** *124,* 14316-14317.

132. Jones, M. R.; Macfarlane, R. J.; Lee, B.; Zhang, J.; Young, K. L.; Senesi, A. J.; Mirkin, C. A., *Nat. Mater.* **2010,** *9,* 913-917.

133. Macfarlane, R. J.; O'Brien, M. N.; Petrosko, S. H.; Mirkin, C. A., *Angew. Chem. Int. Ed.* **2013,** *52,* 5688-5698.

134. Langille, M. R.; Zhang, J.; Personick, M. L.; Li, S.; Mirkin, C. A., *Science* **2012,** *337,* 954-957.

135. Jana, N. R.; Gearheart, L.; Murphy, C. J., *J. Phys. Chem. B* **2001,** *105,* 4065-4067.

136. Wu, Z.; Chen, J.; Jin, R., *Adv. Funct. Mater.* **2011,** *21,* 177-183.

137. Whetten, R. L.; Khoury, J. T.; Alvarez, M. M.; Murthy, S.; Vezmar, I.; Wang, Z. L.; Stephens, P. W.; Cleveland, C. L.; Luedtke, W. D.; Landman, U., *Adv. Mater.* **1996,** *8,* 428-433.

138. Garg, N.; Scholl, C.; Mohanty, A.; Jin, R., *Langmuir* **2010,** *26,* 10271-10276.

139. Sau, T. K.; Murphy, C. J., *Philos. Mag.* **2007,** *87,* 2143-2158.

140. Petukhova, A.; Greener, J.; Liu, K.; Nykypanchuk, D.; Nicolaÿ, R.; Matyjaszewski, K.; Kumacheva, E., *Small* **2012,** *8,* 731-737.

141. Kinnear, C.; Dietsch, H.; Clift, M. J. D.; Endes, C.; Rothen-Rutishauser, B.; Petri-Fink, A., *Angew. Chem. Int. Ed.* **2013,** *52,* 1934-1938.

142. Liu; Guyot-Sionnest, P., *J. Phys. Chem. B* **2005,** *109,* 22192-22200.

143. Kolb, D. M.; Przasnyski, M.; Gerischer, H., *J. Electroanal. Chem.* **1974,** *54,* 25.

144. Herrero, E.; Buller, L. J.; Abruña, H. D., *Chem. Rev.* **2001,** *101,* 1897-1930.

145. Carbó-Argibay, E.; Rodríguez-González, B.; Gómez-Graña, S.; Guerrero-Martínez, A.; Pastoriza-Santos, I.; Pérez-Juste, J.; Liz-Marzán, L. M., *Angew. Chem. Int. Ed.* **2010,** *49,* 9397-9400.

146. Park, K.; Drummy, L. F.; Wadams, R. C.; Koerner, H.; Nepal, D.; Fabris, L.; Vaia, R. A., *Chem. Mater.* **2013,** *25,* 555-563.

147. Almora-Barrios, N.; Novell-Leruth, G.; Whiting, P.; Liz-Marzán, L. M.; López, N., *Nano Lett.* **2014,** *14,* 871-875.

148. Jackson, S. R.; McBride, J. R.; Rosenthal, S. J.; Wright, D. W., *J. Am. Chem. Soc.* **2014,** *136,* 5261-5263.

149. Orendorff, C. J.; Murphy, C. J., *J. Phys. Chem. B* **2006,** *110,* 3990-3994.

150. Giannici, F.; Placido, T.; Curri, M. L.; Striccoli, M.; Agostiano, A.; Comparelli, R., *Dalton Trans.* **2009,** 10367-10374.

151. *Chem. Commun.* **2005,** 4181.

152.Niidome, Y.; Nakamura, Y.; Honda, K.; Akiyama, Y.; Nishioka, K.; Kawasaki, H.; Nakashima, N., *Chem. Commun.* **2009,** 1754-1756.

153. Fenger, R.; Fertitta, E.; Kirmse, H.; Thunemann, A. F.; Rademann, K., *Phys. Chem. Chem. Phys.* **2012,** *14,* 9343-9349.

154. Wang, L.; Chen, X.; Zhan, J.; Chai, Y.; Yang, C.; Xu, L.; Zhuang, W.; Jing, B., *J. Phys. Chem. B* **2005,** *109,* 3189-3194.

155. Millstone, J. E.; Park, S.; Shuford, K. L.; Qin, L.; Schatz, G. C.; Mirkin, C. A., *J. Am. Chem. Soc.* **2005,** *127,* 5312-5313.

156. Leonov, A. P.; Zheng, J.; Clogston, J. D.; Stern, S. T.; Patri, A. K.; Wei, A., *ACS Nano* **2008,** *2,* 2481-2488.

157. Wijaya, A.; Hamad-Schifferli, K., *Langmuir* **2008,** *24,* 9966-9969.

158. Cortesi, R.; Esposito, E.; Menegatti, E.; Gambari, R.; Nastruzzi, C., *Int. J. Pharm.* **1996,** *139,* 69-78.

159. Nikoobakht, B.; El-Sayed, M. A., *Langmuir* **2001,** *17,* 6368-6374.

160. Ravel, B., *J. Synchrotron Radiat.* **2001,** *8,* 314-316.

161. Ravel, B.; Newville, M.; Cross, J. O.; Bouldin, C. E., *Physica B* **1995,** *208 & 209,* 145-7.

162. Johnston, R. L., *Atomic and Molecular Clusters*. Taylor & Francis: 2002; Vol.

163. Cheng, G.; Carter, J. D.; Guo, T., *Chem. Phys. Lett.* **2004,** *400,* 122-127.

164. Frenkel, A. I.; Yevick, A.; Cooper, C.; Vasic, R., *Annual Review of Analytical Chemistry* **2011,** *4,* 23-39.

165. Tsunoyama, H.; Ichikuni, N.; Sakurai, H.; Tsukuda, T., *J. Am. Chem. Soc.* **2009,** *131,* 7086-7093.

166. Jones, P. G., *Gold Bulletin* **1981,** *14,* 102-118.

167. Kryachko, E. S.; Remacle, F., *J. Chem. Phys.* **2007,** *127,* 194305.

168. Wang, Z.; Yuan, J.; Zhou, M.; Niu, L.; Ivaska, A., *Appl. Surf. Sci.* **2008,** *254,* 6289-6293.

169. Jung, H. T.; Coldren, B.; Zasadzinski, J. A.; Iampietro, D. J.; Kaler, E. W., *Proc. Natl. Academy Sci.* **2001,** *98,* 1353-1357.

170. Prince, N. P.; Seymour, D. L.; Woodruff, D. P.; Jones, R. G.; Walter, W., *Surface Science* **1989,** *215,* 566-576.

171. Heald, S. M.; Chen, H.; Tranquada, J. M., *Phys. Rev. B* **1988,** *38,* 1016-1026.

172. Bedzyk, M. J.; Gibson, W. M.; Golovchenko, J. A., *J. Vacuum Sci. and Technol.* **1982,** *20,* 634-637.

173. Balazs, A. C.; Emrick, T.; Russell, T. P., *Science* **2006,** *314,* 1107.

174. Rajh, T.; Chen, L. X.; Lukas, K.; Liu, T.; Thurnauer, M. C.; Tiede, D. M., *J. Phys. Chem. B* **2002,** *106,* 10543-10552.

175. Ghosh, S. K.; Nath, S.; Kundu, S.; Esumi, K.; Pal, T., *J. Phys. Chem. B* **2004,** *108,* 13963-13971.

176. Sapsford, K. E.; Algar, W. R.; Berti, L.; Gemmill, K. B.; Casey, B. J.; Oh, E.; Stewart, M. H.; Medintz, I. L., *Chem. Rev.* **2013,** *113,* 1904-2074.

177. Ilavsky, J., *J. Appl. Crystallography* **2012,** *45,* 324-328.

178. Hirose, K., *Journal of inclusion phenomena and macrocyclic chemistry* **2001,** *39,* 193-209.

179.Niidome, T.; Yamagata, M.; Okamoto, Y.; Akiyama, Y.; Takahashi, H.; Kawano, T.; Katayama, Y.; Niidome, Y., *J. Controlled Release* **2006,** *114,* 343-347.

180. Jang, B.; Park, J.-Y.; Tung, C.-H.; Kim, I.-H.; Choi, Y., *ACS Nano* **2011,** *5,* 1086-1094.

181. Millstone, J. E.; Georganopoulou, D. G.; Xu, X.; Wei, W.; Li, S.; Mirkin, C. A., *Small* **2008,** *4,* 2176-2180.

182. Michalowicz, A.; Vlaic, G., *J. Synchrotron Radiat.* **1998,** *5,* 1317-1320.

183. Tanuma, S.; Powell, C. J.; Penn, D. R., *Surface and Interface Analysis* **1994,** *21,* 165-176.

184. Calvin, S., *XAFS for Everyone*. Taylor and Francis: 2013.

185. Newville, M.; Līviņš, P.; Yacoby, Y.; Rehr, J. J.; Stern, E. A., *Phys. Rev. B* **1993,** *47,* 14126-14131.

186. Soderholm, L.; Antonio, M. R.; Williams, C.; Wasserman, S. R., *Anal. Chem.* **1999,** *71,* 4622-4628.

187. Ressler, T.; Wong, J.; Roos, J.; Smith, I. L., *Environ. Sci. Technol.* **2000,** *34,* 950-958.